



UNIVERSITAT
POLITÈCNICA
DE VALÈNCIA

Design and Development of an Acoustic Calibrator
for Deep-Sea Neutrino Telescopes
and First Search for Secluded Dark Matter
with ANTARES

Silvia Adrián Martínez

Tesis Doctoral

Marzo 2015

Director: Dr. Miguel Ardid Ramírez
Co-director: Dr. Manuel Bou Cabo

A mis padres

Contents

Resumen.....	5
Resum.....	9
Summary	13
1 Framework of the thesis: ANTARES Neutrino Telescope	17
1.1 Why Neutrino Astrophysics?.....	17
1.2 ANTARES: The first Undersea Neutrino Telescope.....	22
1.2.1 Detection principle.....	23
1.2.2 Detector overview.....	25
1.2.3 The AMADEUS system	28
1.2.3.1 System overview.....	29
1.2.3.2 Acoustic Storeys.....	31
1.3 KM3NeT.....	33
Part I: Design and Development of an Acoustic Calibrator for Deep-Sea Neutrino Telescopes	37
2. Part I Introduction: Acoustic detection of Neutrinos.....	39
2.1 Acoustic Detection of Ultra-High Energy Neutrinos.....	40
2.1.1 The Thermo-Acoustic Model.....	43
2.1.2 Acoustic Neutrino signature	45
2.1.3 Underwater conditions in the Mediterranean Sea.	48
2.1.3.1 Attenuation	48
2.1.3.2 Sound speed.....	52
2.1.3.3 Background in acoustic neutrino detection in the Mediterranean Sea....	54
2.2 Calibrator for Acoustic Detection of Ultra High Energy Neutrinos in Underwater Telescope.....	57
2.3 Parametric Acoustic Sources	58

3. Evaluation of the Parametric Technique for the Compact Acoustic Calibrator	65
3.1 Planar Transducers	65
3.1.1 Experimental Setup	66
3.1.2 Methods, Analysis and Results	67
3.2 Cylindrical Transducers	70
3.2.1 Experimental Setup	71
3.2.2 Methods, Analysis and Results	73
3.3 Array Configuration Evaluation	81
4. Prototype of the Versatile Compact Array.....	87
4.1 Design philosophy.....	87
4.2 Transducer versatility.....	89
4.3 Mechanics	92
4.4 Electronics.....	96
4.4.1 Electronic Emission Board.....	96
4.4.1.1 <i>Basic block diagram</i>	97
4.4.2 Register System.....	102
4.5 Tests with the Array	104
4.5.1 Array characterization.....	104
4.5.2 Low frequency tests	105
4.5.2.1 <i>Laboratory tests</i>	106
4.5.2.2 <i>Field tests</i>	111
4.5.3 High frequency tests.....	113
4.6 Current state and future steps	117

Part II: First Search for Secluded Dark Matter.....119

5. Part II Introduction: Dark Matter and Secluded Dark Matter121

5.1 Dark Matter..... 121

5.1.1 Indirect Evidences 123

5.1.1.1 *Galactic Rotation Curves* 123

5.1.1.2 *Galaxy Clusters* 124

5.1.1.3 *Gravitational Lensing*..... 124

5.1.1.4 *Velocity Dispersions of Galaxies and Mass to Light Ratio* 126

5.1.1.5 *Cosmic Microwave Background*..... 127

5.1.2 WIMP as the Dark Matter Candidate..... 129

5.2 Dark Matter Detection Methods 130

5.2.1 Direct Detection..... 130

5.2.2 Indirect Detection 132

5.3 Dark Matter Searches with ANTARES Neutrino Telescope..... 135

5.3.1 The Galactic Center 136

5.3.2 The Earth 137

5.3.3 The Sun..... 138

5.3.3.1 *Standard Dark Matter search*..... 138

5.3.3.2 *Search for Secluded Dark Matter in the Sun* 139

5.3.3.2.1 *DM annihilation in the Sun.* 141

5.3.3.2.2 *Mediator decay products and bounds from neutrino detection.* 142

5.3.3.2.3 *Decay probabilities* 146

6. Tools and Methods149

6.1 Signal expectations 150

6.1.1 Di-Muon Generator (*DiMuGen*)..... 155

6.1.1.1 *Inputs and outputs* 156

6.1.1.2 *Code description*..... 157

6.1.1.2.1 *Primary (mediator) direction* 158

6.1.1.2.2	<i>Inside decay</i>	159
6.1.1.2.3	<i>Outside decay</i>	162
6.2	Background obtained using the scrambled data	171
6.3	Optimization of the event selection criteria	173
6.4	Other interesting cases in Secluded Dark Matter	175
6.4.1	Di-muon decay into neutrino.....	175
6.4.2	Mediator decay into neutrino	176
7.	Analysis and Results	179
7.1	Flux sensitivities	179
7.2	Unblinding Strategy	182
7.3	Sensitivity in terms of annihilation rates	185
7.4	Cross Section Sensitivities	190
7.5	Final Results after unblinding the data.....	192
7.5.1	Unblinding results following MultiLine reconstruction strategy	193
7.5.2	Unblinding results following SingleLine reconstruction strategy.....	194
7.6	Limits obtained for Secluded Dark Matter models	196
7.6.1	Annihilation Rates.....	197
7.6.2	Limits on Cross Sections for SDM	199
	Conclusions	203
	Bibliography	207
	Acknowledgements / Agradecimientos	225
	Table List.....	227
	Figure List.....	229
	Acronyms	241
	Annex A.....	243

Resumen

La astronomía de neutrinos es un campo en auge dentro de la Física de Astropartículas. Los neutrinos ofrecen grandes ventajas como sondas para estudiar el Universo lejano y de alta energía. En la comunidad científica es extensamente aceptado que mediante la combinación de la información que proporcionan los neutrinos junto a la obtenida mediante fotones de alta energía (rayos gamma) y partículas cargadas (rayos cósmicos) se podría obtener una imagen más completa de los procesos astrofísicos fundamentales que tienen lugar a lo largo de nuestro Universo. Además, los neutrinos también proporcionan el único medio de entender algunos aspectos de la Física de Partículas. La prueba experimental de que los neutrinos tienen masa y de que sufren mezcla de sabores procede de observaciones realizadas en los primeros telescopios de neutrinos.

La razón fundamental por la que los neutrinos son tan altamente valorados como mensajeros es la baja interacción con el medio que los rodea. Al ser partículas sin carga interactúan muy débilmente con la materia, por ello pueden escaparse de la

fuelle donde se han producido y, al contrario de lo que ocurre con el resto de mensajeros, pueden llegar a la Tierra sin ser desviados por los campos magnéticos y sin prácticamente pérdida de energía. Esta misma razón que los hace tan valorados es a su vez la que los hace tan difíciles de detectar. Dada su baja interacción con la materia se impone la necesidad de construir detectores con grandes volúmenes de detección, del orden del km^3 , altamente instrumentados. Para ello se utilizan medios naturales (en el fondo del mar, en lagos o en enterrados en el hielo de la Antártida) aprovechando el agua (o hielo) como material diana donde se espera que interactúe el neutrino. ANTARES (Astronomy with a Neutrino Telescope and Abyss environmental RESearch) es el primer telescopio submarino de neutrinos construido en el fondo del mar Mediterráneo. Fue desarrollado por un consorcio internacional y financiado con fondos europeos y de los distintos países colaboradores. ANTARES está optimizado para la detección óptica de la luz Cherenkov inducida por los muones relativistas producidos en la interacción de neutrinos de alta energía en los alrededores del detector. La información de la carga, posición y tiempo de llegada de los fotones a los fotomultiplicadores que componen el detector permite tanto la reconstrucción de la trayectoria del neutrino, con una alta resolución angular, como el conocimiento de su energía. Además, ANTARES acoge el experimento AMADEUS (Antares Modules for Acoustic DETection Under Sea) mediante el cual se está investigando y testeando la detección acústica de neutrinos de muy alta energía que, al interactuar en el agua, producen un pulso termo-acústico que se pretende registrar con una red de hidrófonos.

El trabajo desarrollado en esta tesis se engloba bajo el marco del experimento ANTARES, por ello es el tema desarrollado en el Capítulo 1 a modo de contextualización. Como es común en las tesis desarrolladas en este experimento, el trabajo se ha dividido en dos áreas diferenciadas: por un lado, una parte de enfoque más tecnológico y, por otro lado, una parte analítica de datos tomados por el telescopio. Por su contexto y el carácter de las actividades realizadas ha sido necesaria

la formación en distintos campos: telescopios de neutrinos, astropartículas, física de partículas. Además, se ha desarrollado diversas capacidades y destrezas en diversos ámbitos como instrumentación, aplicaciones informáticas, técnicas de simulación, análisis masivo de datos.

La primera parte de la tesis está centrada en el desarrollo de un calibrador capaz de reproducir la señal acústica que se emite en la interacción de un neutrino de alta energía con un núcleo de agua que, generalizando, es un pulso bipolar altamente directivo. El disponer de un buen calibrador es clave a la hora de testear la detección acústica en el telescopio y poder sintonizar y “entrenar” los receptores para este tipo de señales.

En el Capítulo 2 se describen los procesos que intervienen en la emisión acústica del neutrino y las condiciones de propagación y ruido ambiental presentes en el *site* de ANTARES. Asimismo se introduce el concepto de fuentes acústicas paramétricas que será el punto de partida para el diseño del calibrador. En el Capítulo 3 se describen y se presentan los test iniciales realizados para evaluar la posibilidad de usar la técnica de fuentes paramétricas para reproducir el característico pulso acústico generado por el neutrino. Este trabajo supuso realizar estudios pioneros de generación paramétrica en casos con simetría cilíndrica y señales transitorias y demostraron el potencial de esta técnica para el desarrollo de un calibrador compacto para detección acústica de neutrinos. En el Capítulo 4 se presenta el prototipo desarrollado, un *array* de tres elementos ensamblados en una estructura compacta, y los test realizados al mismo. Éste es capaz de operar en dos rangos frecuenciales aumentando así su funcionalidad pudiéndose utilizar tanto desde el fondo del mar como operado desde un barco.

La segunda parte de la tesis, con carácter de análisis de datos, se ha centrado en el análisis de datos registrados por ANTARES con el fin de contrastar posibles modelos astrofísicos para la búsqueda de materia oscura. Este trabajo ha focalizado en la detección de los productos de la aniquilación de materia oscura atrapada en el centro

del Sol. En concreto, se ha testado el modelo de *Secluded Dark Matter* (SDM) a través de la detección de di-muones (pareja de muones co-lineales) y neutrinos en la dirección del Sol. A grandes rasgos, este modelo se basa en la idea de la existencia de un mediador resultado de la aniquilación de materia oscura que posteriormente decaería en partículas del modelo estándar como muones o neutrinos. Estos modelos han sido propuestos con el fin de explicar ciertas ‘anomalías’ experimentales observadas, tales como el espectro del flujo de positrones detectado en satélites, medido recientemente con gran precisión por AMS-II. El estudio realizado en esta tesis constituye la primera búsqueda de evidencias experimentales de este tipo de modelos en telescopios de neutrinos.

En el Capítulo 5 se resumen las evidencias de la presencia de materia oscura en el Universo así como los actuales métodos de detección de la misma. También se recogen las búsquedas de materia oscura realizadas con ANTARES, entre otras en el Sol, y se introducen las características del modelo de SDM. El Capítulo 6 está dedicado a la descripción de la metodología y herramientas utilizadas para este análisis. Se detalla el funcionamiento del código creado para la simulación de la generación de di-muones provenientes del decaimiento del mediador y su detección por ANTARES con objeto de conocer la respuesta del detector a este tipo de señal. Para finalizar, el Capítulo 7 recoge el proceso de análisis de los datos y su interpretación en términos de búsqueda indirecta de SDM. Dado que los resultados obtenidos en el análisis no indican un exceso de señal significativo se han establecido experimentalmente los primeros límites a modelos SDM en telescopios de neutrinos. Los límites impuestos a estos modelos son los más restrictivos que existen en la actualidad para un buen rango de valores de los parámetros a considerar: masa de la materia oscura, masa del mediador y vida media de este último. Así pues, estos resultados mejoran y/o complementan límites realizados por otros métodos, tales como la detección directa de materia oscura o detección indirecta a través de la búsqueda de positrones o rayos gamma.

Resum

L'astronomia de neutrins és un camp en auge dins la Física d'Astropartícules. Els neutrins ofereixen grans avantatges com a sondes per estudiar l'Univers llunyà i d'alta energia. En la comunitat científica està extensament acceptat que mitjançant la combinació de la informació proporcionada pels neutrins junt a la obtinguda mitjançant fotons d'alta energia (rajos gamma) i partícules carregades (rajos còsmics) es podria obtenir una imatge més completa dels processos astrofísics fonamentals que es donen al llarg del nostre Univers. A més, els neutrins també proporcionen l'únic mitjà d'entendre alguns aspectes de la Física de Partícules. La prova experimental de que els neutrins tenen massa i de que pateixen mescla de sabors prové de les observacions realitzades als primers telescopis de neutrins.

La raó fonamental per la qual els neutrins són altament valorats com a missatgers és la baixa interacció amb el medi que els envolta. Al ser partícules sense càrrega interactuen molt dèbilment amb la matèria, per això poden escapar-se de la font on s'han produït i, al contrari del que ocorre amb la resta de missatgers, poden arribar a

La Terra sense desviar-se pels camps electromagnètics i sense pràcticament pèrdua d'energia. Aquesta mateixa raó que els fan tan valorats és al mateix temps la que els fa tan difícil de detectar. Degut a la seua baixa interacció amb la matèria s'imposa la necessitat de construir detectors amb grans volums de detecció, de l'ordre del km^3 , altament instrumentats. Per això s'utilitzen medis naturals (al fons de la mar, en llacs, al gel de l'Antàrtida) aprofitant l'aigua (o el gel) com a material diana on interaccionen el neutrins. ANTARES (Astronomy with a Neutrino Telescope and Abyss environmental RESearch) és el primer telescopi submarí de neutrins construït al fons de la mar Mediterrània operat per un consorci internacional, finançat amb fons europeus i dels diferents països col·laboradors. ANTARES està optimitzat per a la detecció òptica de la llum de Cherenkov induïda pels muons relativistes produïts en la interacció de neutrins d'alta energia als voltants del detector. La informació de la carrega, posició i temps d'arribada dels fotons als fotomultiplicadors que componen el detector permet tant la reconstrucció de la trajectòria del neutrí, amb gran resolució angular, com el coneixement de la seua energia. A més, ANTARES acull l'experiment AMADEUS (Antares Modules for Acoustic DETection Under Sea) mitjançant el qual s'està investigant i testejant la detecció acústica de neutrins de molt alta energia, que, al interaccionar a l'aigua produeixen un pols termo-acústic que es pretén registrar amb una xarxa d'hidròfons.

El treball dut a terme en esta tesi s'engloba baix el marc de l'experiment ANTARES, per això es el tema desenvolupat en el Capítol 1 a mode de contextualització. Com es comú en les tesis desenvolupades en aquest experiment, el treball s'ha dividit en dues àrees diferenciades: per una banda una part d'enfocament mes tecnològic i, d'altra banda, una part analítica de les dades preses pel telescopi. Pel seu context i el caràcter de les activitats realitzades, ha sigut necessària la formació en distints camps com: telescopis de neutrins, Física d'Astropartícules, etc. A més a més s'han desenvolupat diverses capacitats i destreses en diferents àmbits com la instrumentació, aplicacions informàtiques, tècniques de simulació, anàlisi massiu de dades, etc.

La primera part de la tesi està centrada en el desenvolupament d'un calibrador capaç de reproduir la senyal acústica que es genera en la interacció d'un neutrí d'alta energia amb un nucli de l'aigua que, generalitzant, és un pols bipolar altament directiu. Disposar d'un bon calibrador es clau a l'hora de testejar la detecció acústica al telescopi i poder sintonitzar i "entrenar" els receptors a aquest tipus de senyals.

Al Capítol 2 es descriuen els processos que intervenen en l'emissió acústica del neutrí i les condicions de propagació i soroll ambiental presents al *site* d'ANTARES. Així mateix, s'introdueix el concepte de fonts acústiques paramètriques que seran el punt de partida per al disseny del calibrador. En el Capítol 3 es descriu i es presenten els tests inicials realitzats per avaluar la possibilitat d'utilitzar la tècnica de fonts paramètriques per a reproduir el característic pols acústic generat per el neutrí. Aquest treball va suposar realitzar estudis pioners de generació paramètrica en casos amb simetria cilíndrica i senyals transitòries. En el Capítol 4 es presenta el prototip desenvolupat, un *array* de tres elements assemblats en una estructura compacta, i els tests realitzats al mateix. Aquest és capaç d'operar en mode de baixa i alta freqüència per augmentar la funcionalitat tant per al seu ús en telescopis de neutrins com des de campanyes marines operat des del vaixell.

La segona part de la tesi, amb caràcter d'anàlisi de dades, s'ha centrat en l'anàlisi de les dades registrades per ANTARES amb el fi de contrastar possibles models astrofísics per a la recerca de matèria fosca. Aquest treball es centra en la detecció dels productes d'anihilació de matèria fosca atrapada al centre del Sol. En concret, s'ha testejat el model de *Secluded Dark Matter* (SDM) a través de la detecció de dimuons (parell de muons co-lineals) i neutrins en la direcció del Sol. A grans trets, aquest model es basa en la idea de l'existència d'un mediador resultat de l'anihilació de matèria fosca que posteriorment decauria en partícules del model estàndard com muons o neutrins. Aquests models han sigut proposats amb la fi d'explicar certes "anomalies" experimentals observades, tals com l'espectre del flux de positrons detectat en satèl·lits, mesurat recentment amb gran precisió per AMS-II. L'estudi

realitzat en esta tesi constitueix la primera recerca d'evidències experimentals d'aquest tipus de models en telescopis de neutrins.

Al Capítol 5 es resumeixen les evidències de la presència de matèria fosca a l'Univers així com els actuals mètodes per a detectar-la. També es recullen les recerques de matèria fosca realitzades amb ANTARES, entre altres al Sol, i s'introdueixen les característiques del model de SDM. El Capítol 6 està dedicat a la descripció de la metodologia i ferramentes utilitzades en l'anàlisi. Es detalla el funcionament del codi creat per a la simulació de la generació de di-muons provinents del decaïment del mediador i la seua detecció per ANTARES amb l'objecte de conèixer la resposta del detector a aquest tipus de senyal. Per a finalitzar, el Capítol 7 recull el procés d'anàlisi de les dades i la seua interpretació en termes de detecció indirecta de SDM. Donat que els resultats obtinguts de l'anàlisi no indiquen un excés de senyal significatiu, s'han establert experimentalment els primers límits a models SDM en telescopis de neutrins. Els límits imposats a aquests models són els més restrictius que existeixen en la actualitat per a un bon rang de valors dels paràmetres a considerar: la massa de la matèria fosca, la massa del mediador i la vida mitjana d'aquest. Així doncs, aquests resultats milloren i/o complementen els límits realitzats per altres mètodes, tals com la detecció directa de matèria fosca o la detecció indirecta a través de detecció de positrons o rajos gamma.

Summary

Neutrino astronomy is a booming field in astroparticle physics. Due to the particular characteristics of neutrinos, these particles offer great advantages as probes for the study of the far and high-energy Universe. Moreover, it is extensively accepted by the scientific community that a multi-messenger approach with the combination of information provided by neutrinos, photons and charged particles (cosmic rays) is possible to obtain a more complete image of the fundamental astrophysics processes taking place in our Universe. Furthermore, neutrinos also provide a unique way to understand some particle physics principles. As an example, the evidences that neutrinos have mass and flavour mixing did come from observations in the first neutrino telescopes.

Since neutrinos are neutral and very weak interacting particles they can reach the Earth from astrophysical sources without deflection by magnetic fields and almost without energy losses and absorption, contrarily to the rest of messengers. The other side of the coin of neutrino properties is that detection of neutrinos is very challenging

and big highly instrumented detection volumes are needed. Natural media (deep sea, lakes or ice in the Antarctica) host this kind of experiments using the water (or ice) as target material where the neutrino interaction is produced. ANTARES (Astronomy with a Neutrino Telescope and Abyss environmental RESearch) is the first undersea neutrino telescope, located at 2475 m depth in the Mediterranean Sea. It has been built by an international collaboration with funds from European Union and participating countries. ANTARES is optimized for optical detection of the Cerenkov light induced by relativistic muons produced by high energy neutrino interactions near the detector. The charge, position and arrival time of the photons to the optical modules which compose the detector allows the muon track reconstruction, and thus, knowing the neutrino coming direction with high angular resolution. Some information of the event energy is also derived. In addition, ANTARES is also hosting the AMADEUS (Antares Modules for Acoustic DETection Under Sea) experiment which is investigating the feasibility of the acoustic detection of Ultra-High Energy (UHE) neutrinos.

The framework of this thesis is the ANTARES experiment. In this sense, Chapter 1 describes the telescope and is dedicated to contextualize the work. As commonly done in the thesis developed in this experiment (and in this field), the work has been divided in two different areas. On the one hand, a part more devoted to technological aspects related to the detector and, on the other hand, a part dedicated to ANTARES data analysis. For the context and the characteristics of the activities performed, training in different fields has been necessary: neutrino telescopes, astroparticle physics, etc. Moreover different skills have been developed as well, such as instrumentation, computer applications, simulation techniques, massive data analysis, etc.

The first part of the thesis is focused in the development of a calibrator able to reproduce the acoustic signal generated in the UHE neutrino interaction with a water nucleus which, roughly speaking, generates a highly directive bipolar acoustic pulse.

Having a good calibrator is crucial to test and tune the telescope response for this kind of signals.

Chapter 2 describes the processes that intervene in the acoustic emission due the UHE neutrino interaction, the propagation conditions and background noise existing in the ANTARES site. The concept of parametric acoustic sources is also introduced as starting point for the calibrator design. The initial tests performed to evaluate the parametric acoustic technique for the generation of the characteristic acoustic neutrino pulse are presented in Chapter 3. These works were pioneering in the parametric generation of transient signals using cylindrical symmetry transducers and demonstrated the applicability of this technique for the development of a compact acoustic neutrino detection calibrator. Chapter 4 is devoted to describe the design and tests of the prototype developed, a three element array assembled in a compact structure. It is able to operate in low and high-frequency modes to increase the functionality for both possible uses: in deep-sea or being operated from a vessel.

The second part of the thesis, the data analysis part, is centred in the analysis of the ANTARES data in order to constrain possible Dark Matter models. This work is focused on the detection of products resulting of the Dark Matter annihilation trapped in the centre of the Sun. Specifically, the Secluded Dark Matter (SDM) model has been tested by the detection of di-muons (co-linear muon pair) and/or neutrinos coming from Sun direction. Broadly speaking, this model is based on the idea of the existence of a mediator resulting of the Dark Matter annihilation which, subsequently, would decay into standard model particles as muons or neutrinos. These models have been proposed in order to explain some experimental “anomalies” observed, such as the electron-positron ratio spectrum detected in satellites, measured recently with high accuracy by AMS-II. The study of this thesis constitutes the first search of experimental evidences of this kind of models in neutrino telescopes.

The evidences of the Dark Matter in the Universe and the methods to detect it are reviewed in Chapter 5. Dark Matter searches in ANTARES have been summarized,

among others, the ones using the Sun as source. The SDM model characteristics are also introduced. Chapter 6 describes the methodology and tools used in this analysis. A dedicated code has been developed for the simulation of di-muon generation from mediator decay, and its detection in ANTARES, in order to know the detector response to this kind of signal. To finalize, Chapter 7 deals with the data analysis process and the interpretation in terms of indirect SDM search. Since the conclusion of the analysis is that there is not a significant signal excess, limits to SDM models in neutrino telescopes have been established being the first time that these models are constrained in neutrino telescopes. The imposed limits to these models are the more restrictive ones for a wide range of values of the parameters to consider: Dark Matter mass and mass, and lifetime, of the mediator. Therefore, these results improve and/or complement the limits obtained by different methods, such as Dark Matter direct detection or positron and gamma ray indirect detection searches.

1

Framework of the thesis: ANTARES Neutrino Telescope

In this Chapter the importance of the neutrinos and its detection for the knowledge of the Universe will be reviewed. The ANTARES neutrino telescope, as a framework of the work carried out during this thesis, will be presented. Its scientific aims and the detection methods will be described, including the infrastructure dedicated to test the acoustic detection of neutrinos. To finalize, the KM3Net neutrino telescope, which is currently being deployed and has been developed with the knowledge acquired in the previous experience in the Mediterranean Sea with ANTARES, will be presented. In the future, it will be the biggest neutrino telescope in the northern hemisphere.

1.1 Why Neutrino Astrophysics?

Most of the knowledge of the Universe comes from the observation of photons. These messengers have many advantages because they provide valuable information about the chemical and physical properties of the source. Moreover they are copiously produced, stable, electrically neutral and easy to detect over a wide energy range. Unfortunately, the properties of the hot dense regions which form the central engines

of stars, active galactic nuclei and other astrophysical energy sources are completely opaque to photons, for this reason, they cannot be investigated by direct photon observation, but only by indirect inference. Furthermore, high energy photons interact with photons of the infrared background radiation and with the cosmic microwave background to create electron-positron pairs; this is the Greisen-Zatsepin-Kuz'min effect (GZK) (R. J. Gould & Schreder, 1966; Greisen, 1966; Zatsepin & Kuz'min, 1966), which suppresses any possibility of exploring the sky over distances greater than 100 Mpc with high energy (>10 TeV) gamma rays.

Another possibility is the observation of the proton component of the cosmic rays, which can provide information about the sources but, since they are charged, they can be deflected by the galactic magnetic fields and lose the directional information being impossible point back to their source.

In order to observe the inner workings of the astrophysical objects and to obtain a description of the Universe over a larger range of energies a messenger electrically neutral, so that its trajectory will not be affected by magnetic fields, stable, so that it will reach us from distant sources, and weakly interacting, so that it will penetrate regions which are opaque to photons, is needed. The only candidate currently known is the neutrino. Fig 1.1 shows the different messengers that could be used for studying astrophysical sources and its interaction with the medium along the way to reach the Earth.

The neutrino was proposed by Pauli in 1930 in order to explain the energy conservation and linear momentum during β disintegration: $n \rightarrow p + e^- + \bar{\nu}_e$. It was described as a sub-atomic fermion particle without electrical charge, zero mass and very small cross section $\sigma \sim 10^{-44} \text{ cm}^2$. Its interaction probability was considered so low that its own proponent bet that the neutrino never could be detected. Fortunately, there were scientists who did not cease in its efforts. Years after, in 1956, Cowen and Reines presented the first measurement of neutrinos coming from fragments of

nuclear fission through the observation of inverse β disintegration of protons. This work, besides to make Pauli losing his bet, became Reines Nobel Prize in 1995, after the death of his colleague in 1974.

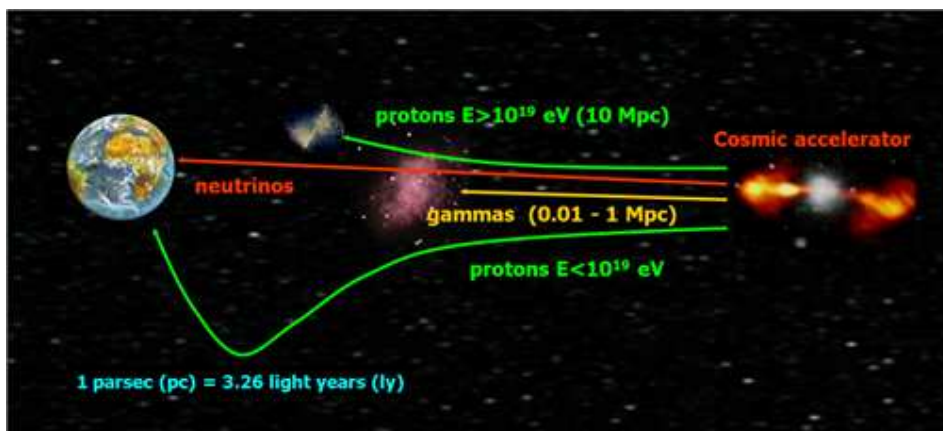


Fig 1.1. Scheme of the different messengers that can reach the Earth from astrophysical sources and its possible interaction with the medium during their travel.

Today, it is known that the neutrino has a very little mass but is not zero, and there exist three kinds of neutrinos according to the three leptonic families (ν_e, ν_μ, ν_τ) and its corresponding antiparticles ($\bar{\nu}_e, \bar{\nu}_\mu, \bar{\nu}_\tau$).

After decades of study and experimentation, some astrophysical sources are known for emitting neutrinos (of low energy range, a few tens of MeV). Hydrogen fusion produces electron neutrinos as by-products. Solar neutrino astronomy has a 30 years long history, the proton-proton chain is the most frequently reaction set that occurs in the Sun and converts hydrogen in helium, in this process an amount of energy is released in form of photons and neutrinos. The conversion of iron nuclei to neutrons when a neutron star is formed in the heart of a supernova produces a burst of neutrinos (augmented by the thermal production of neutrino-antineutrino pairs), and one such burst was observed by Kamiokande (Hirata et al., 1988) and IMB (Irvine–Michigan–Brookhaven) (Vander Velde, Personal web) detectors for Supernova 1987A in 1987

being the first observation of neutrinos from outside of the Solar System. Cosmology predicts a low-energy relic neutrino background similar to the low-energy relic photons of the Cosmic Microwave Background, but these would have an effective temperature of around 1.9 K and are very difficult to observe.

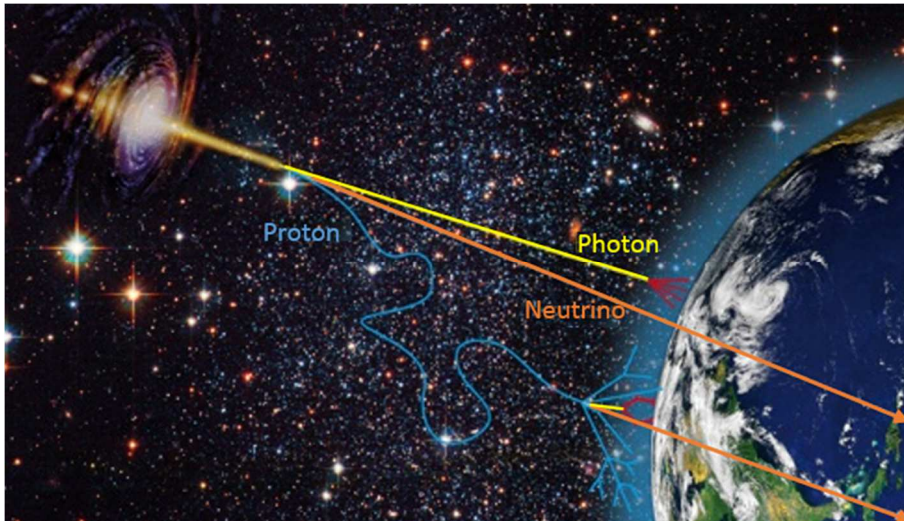


Fig 1.2. Infographic view of the two different origin of the neutrinos detected on the Earth: atmospheric neutrinos and astrophysical neutrinos.

Furthermore, on the Earth, high energy neutrinos can be detected from two different origins (Fig 1.2). The first ones are atmospheric neutrinos that are mainly produced in the decay of pions and kaons emerging from reactions of cosmic rays or gamma-rays in the upper atmosphere. The second ones are astrophysical neutrinos that originate from either galactic or extra-galactic astrophysical processes.

Astrophysical sources of high-energy neutrinos have not been observed directly, but their existence can be deduced by the properties of cosmic rays. Moreover, IceCube has recently claimed the discovery of high-energy cosmic neutrinos based on the excess of events observed with respect to the expected ones due to atmospheric neutrinos (IceCube Collaboration, 2013). Primary cosmic rays are protons, with some admixture of heavier nuclei; the energy spectrum (Fig 1.3) is a power law which

extends to extremely high energies, values exceeding 10^{20} eV having been observed in recent years. Protons themselves have limited use as astrophysical information carriers because they are charged, and therefore subject to deflection by cosmic magnetic fields: only the very highest energy cosmic rays are likely to retain any memory of the source direction. The exact source of the high-energy cosmic rays is thus unknown, although supernova remnants and active galactic nuclei have been proposed. Whatever the source, it is clear that accelerating protons to such high energies is likely to generate a large associated flux of photo-produced pions, which decay to yield gamma rays and neutrinos. These will remember the source direction, and so the existence of a general flux of very high energy cosmic-ray protons implies the existence of sources of high-energy neutrinos.

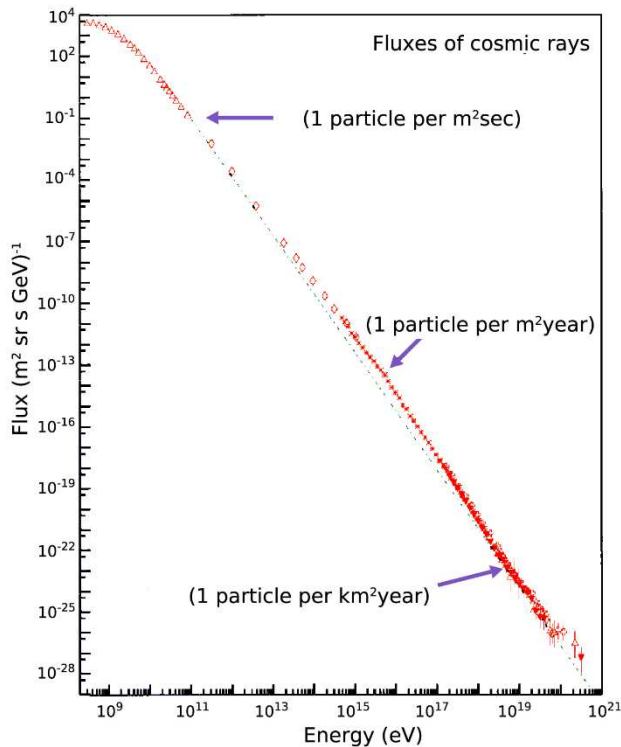


Fig 1.3. Spectral Flux of Cosmic Rays observed on Earth. Figure adapted from (Cronin, Gaisser, & Swordy, 1997).

Neutrino astronomy thus offers the possibility of observing sources which correspond to the central engines of the most energetic astrophysical phenomena. It also provides long baselines for neutrino oscillation studies, and can explore useful regions of supersymmetric parameter space in the context of dark matter. The drawback, of course, is that the weak interactions of neutrinos imply that a very massive detector with extremely good background rejection is required to observe a measurable flux.

Nowadays the existing neutrino telescopes NT200+ in lake Baikal (Aynutdinov et al., 2008; Kuzmichev et al., 2006), IceCube at the South Pole (IceCube Collaboration, 2014) and ANTARES (Ageron et al., 2011), the first undersea neutrino telescope, in the Mediterranean Sea are continuously reconstructing the muon tracks from the interactions of atmospheric muon neutrinos. An irrefutable evidence of neutrino signature from astrophysical sources would either be a reconstructed energy beyond $\sim 10^{14}$ eV for a significant number of events or a clustering of reconstructed neutrinos from a particular direction. Another determinant evidence would be the coincidence of its direction with a potential neutrino source identified through gamma-ray detectors by imaging atmospheric Cherenkov telescopes (H.E.S.S. (H.E.S.S. Collaboration, 2014), MAGIC (MAGIC Collaboration, 2015), VERITAS (VERITAS Collaboration, 2014) or by direct observation of the air shower particles (MILAGRO (MILAGRO Collaboration, 2007)). It is assumed that only a multi-messenger approach, combining observation of neutrinos, high energy photons (gamma rays) and charged particles (cosmic rays) will deliver a complete picture of the fundamental astrophysical processes taking place in the Universe.

1.2 ANTARES: The first Undersea Neutrino Telescope

ANTARES detector is located in the Mediterranean Sea, at 40 km of the south coast of France at 2475 m depth. Its location makes it sensitive to a large part of the southern sky, including the Galactic Centre region. It was completed in May 2008 making the largest neutrino telescope in the Northern hemisphere and the first

operated in deep sea. Data taking started in 2007 with the first deployed detection lines.

The main goal of ANTARES is the observation of astrophysical objects like Active Galactic Nuclei (AGN), Gamma Ray Bursts (GRBs), Microquasars, or Supernova Remnants. In fact, astrophysical objects that are able to accelerate protons and nuclei in a wide range of energy are candidates to be neutrino sources due to a possible interaction of these accelerated cosmic rays with matter or radiation located in the surroundings of the source. Other interesting studies carried out with ANTARES are led to the indirect detection of Dark Matter (DM) looking for neutrinos generated in the annihilation of Weakly Interacting Massive Particles (WIMPs) captured by celestial bodies like Earth, Sun, Galactic Center, etc. (See Chapter 5). In the field of particle physics, studies performed in ANTARES are trying to understand some processes concerning to the neutrino, among others, neutrino oscillations (Adrián-Martínez, Al Samarai et al., 2012) or neutrino interaction cross-sections. In addition, and due to the particular location of underwater neutrino telescopes, these infrastructures offer the possibility to extend the scientific program beyond the astroparticle physics by including in the facility different sensors for Earth and Sea sciences. The continuous monitoring of these sensors in real time is a powerful tool for environmental studies, and to bring some light in the understanding of different multidisciplinary problems such as ocean dynamics, climate change, etc.

1.2.1 Detection principle

The telescope is optimized to detect upward going high energy neutrinos by observing the Cherenkov light produced in sea water by secondary charged leptons originated in charged current interactions of the neutrinos with the matter around the instrumented volume. Due to the long range of the muon, neutrino interaction vertices tens of kilometers away from the detector can be observed. Other neutrino flavours are also detected, though with lower efficiency and worse angular precision because

of the shorter range of the corresponding leptons. To detect the Cherenkov light, the neutrino telescope comprises a matrix of light detectors, in the form of photomultipliers (PMTs) contained in glass spheres, called Optical Modules (OMs). These OMs are positioned on flexible lines anchored to the seabed. The muon track is reconstructed using the arrival time measurements of the Cherenkov photons on the OMs of known positions. With the chosen detector dimensions, the ANTARES detector has a low energy threshold of about 20 GeV for well reconstructed muons. The incoming neutrino direction, almost collinear with the secondary muon at high energy, can be determined with an accuracy better than 0.3° for energies above 10 TeV. Fig 1.4 illustrates the neutrino detection principle in an undersea telescope.

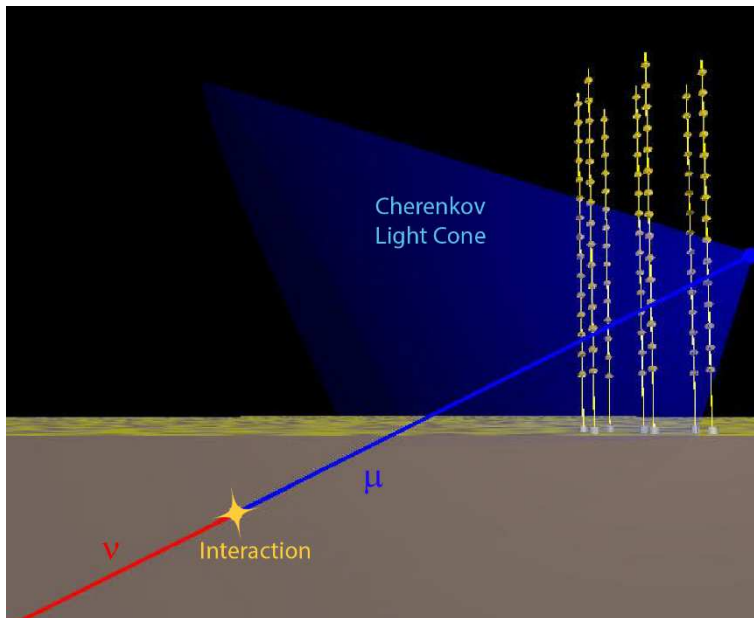


Fig 1.4. Detection principle of high energy muon neutrinos in an underwater neutrino telescope. The incoming neutrino interacts with the material around the detector to create a muon. The muon gives Cherenkov light in the sea water which is then detected by a matrix of light sensors. The original spectrum of light emitted from the muon is attenuated in the water such that the dominant wavelength range detected is between 350 and 500 nm.

This detection technique requires discriminating upward going muons against the much higher flux of downward atmospheric muons (Fig 1.5). To simplify the discrimination, the detector should be installed in a deep site where a layer of water or ice would shield it.

Another detection technique is being tested in ANTARES in order to complement the optical detection. This is the acoustic detection based on the thermo-acoustic model (See Chapter 2). For this purpose, the AMADEUS (ANTARES Modules for the Acoustic DEtection Under the Sea) system was installed in the general infrastructure (See Section 1.2.3).

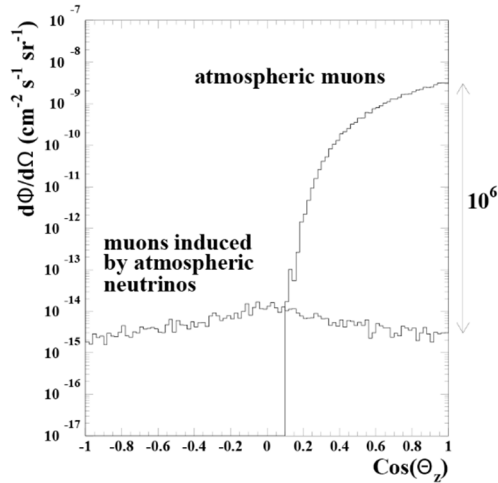


Fig 1.5. Zenith angular distribution of the muon flux above 1 TeV from atmospheric muons and atmospheric neutrino induced muons at 2300 m water equivalent depth.

1.2.2 Detector overview

The detector infrastructure is composed by 12 mooring lines holding the optical modules. These are a set of photomultipliers designed for measuring neutrino induced charged particles based on the detection of Cherenkov light emitted in water. There

are 885 OMs which composes the ANTARES detector. The arrangement of the OMs in space was optimized initially by simulation in order to have the best neutrino detection efficiency in terms of effective detection volume and angular resolution for the tracks. The optimal distances between OMs are correlated with the absorption length in water (maximum is about 60 m). Time coincidence conditions between close OMs (< 1 m) allows to reduce the optical background in sea water. The Fig 1.6 shows a schematic view of the detector configuration, composed of OM triplets distributed on vertical lines. These lines are flexible structures attached to the sea bottom by a heavy anchor and kept in tension by a buoy on the top of each line.

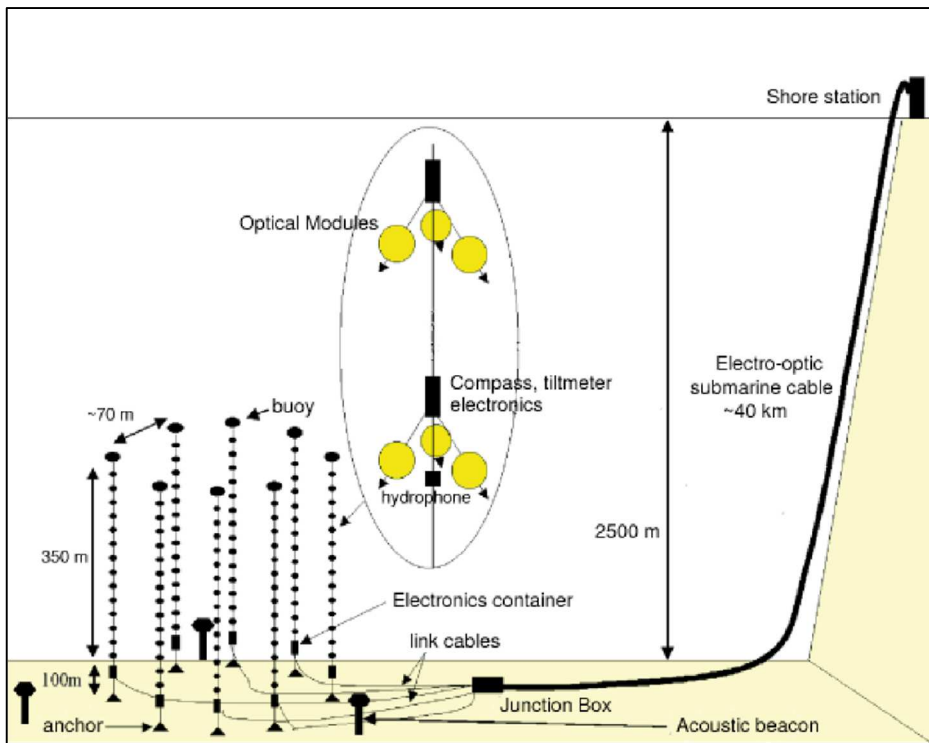


Fig 1.6. Schematic view of the ANTARES detector which consists in 885 OMs set along 12 lines connected to shore by an electro-optical cable.

Each line is separated about 65 m between each other. Any line can be deployed independently from others and released to the surface for maintenance. This simplifies operations at great depth. The lines are connected to the common junction box with 40 km cable which connects it to the shore station located in La Seyne-sur-Mer (France) where the ANTARES control room is located. The lines are divided in storeys, a mechanical structure to place three OMs to point downwards at 45° with respect to the vertical, each line has 25 except one which has hydrophones instead of OMs in the five top storeys (See Section 1.2.3). The downward orientation aim is optimizing the *upgoing* particles detection. Additionally, there are different kinds of sensors and instrumentation (LED beacons, hydrophones, compasses/tiltmeters) for time and position calibration of the OMs. Storeys in the same line are separated 14.5 m. The first storey is placed 100 m above the anchor. This distance is the optimized distance from the ground where the Cherenkov cone from the up-going particles is developed. The disposition of the lines and storeys results in a neutrino telescope that spreads over an area of about 0.1 km^2 and an active height of about 0.3 km.

ANTARES achieves very good angular resolution ($< 0.3^\circ$ for muon events above 10 TeV). The pointing accuracy of the detector is determined largely by the overall timing accuracy of each event. This is a quadratic sum of terms due to: a) the precision with which the spatial positioning and orientation of the optical modules is known; b) the accuracy of the arrival time of photons at the optical modules measurement; c) the precision with which local timing of individual optical module signals can be synchronized with respect to each other.

In order to determine accurately these parameters, positioning (Adrián-Martínez et al., 2012) and timing calibration (J. A. Aguilar, Samarai, Albert, André et al., 2011) systems are needed. The reconstruction of the muon trajectory is based on the differences of the arrival times of the photons between optical modules. As such, it is sensitive to the distances between the optical modules. In order to avoid degrading during the reconstruction, it is necessary to monitor the position of each optical

module with a precision of 10 cm (light travels 22 cm per ns in water). The reconstruction of the muon trajectory and the determination of its energy also require knowledge of the optical module orientation with a precision of a few degrees. The precise absolute positioning of the whole detector has to be guaranteed in order to point to individual sources. To attain a suitable precision on the overall positioning accuracy constant monitoring of relative positions of the various detector elements with respect to absolutely positioned acoustic beacons and emitters is necessary (Ardid, 2009).

The relative time resolution between OMs is of utmost importance for the muon trajectory reconstruction. It is limited by the transit time spread of the signal in the PMTs (about 1.3 ns) and by the scattering and chromatic dispersion of light in sea water (about 1.5 ns for a light propagation of 40 m). The electronics of the ANTARES detector is designed in order to contribute less than 0.5 ns to the overall time resolution. Time calibration should aim at a precision below the nanosecond level. To this end, several complementary time calibration systems are implemented in the ANTARES detector in order to measure and monitor the relative times between different components of the detector due to, e.g. cable lengths and electronics delays (J. A. Aguilar, Samarai, Albert, André et al., 2011).

1.2.3 The AMADEUS system

The AMADEUS project was carried out for performing a feasibility study for a potential future large-scale acoustic neutrino detector (acoustic detection principle will be described in Chapter 2). Following this purpose, an array of dedicated acoustic sensors was integrated into the ANTARES neutrino telescope. Initially, the purposes to follow by this project were:

- a) Performing long-term background investigations (levels of ambient noise, spatial and temporal distributions of sources, rate of neutrino-like signals);

- b) Investigation of spatial correlations for transient signals and for persistent background on different length scales;
- c) The development and test of data filters and reconstruction algorithms;
- d) The investigation of different types of acoustic sensors and sensing methods;
- e) The study of hybrid (acoustic and optical) detection methods.

In particular the knowledge of the rate and correlation length of neutrino-like acoustic background events in order to have an estimation of the sensitivity of a future acoustic neutrino detector.

1.2.3.1 System overview

The AMADEUS sensors are integrated in the form of acoustic storeys that are modified versions of the ANTARES storeys (Section 1.2.2) in which the OMs have been replaced by custom-designed acoustic sensors. These sensors work using dedicated electronics for digitization and pre-processing of the analogue signals. In particular these acoustic storeys are emplaced in detection line number 12 (L12) and in the Instrumentation Line. (IL) (Fig 1.7). IL is equipped with instruments for monitoring the environment. It holds six storeys and, in this line, for two pair of consecutive storeys the vertical distance is increased to 80 m. The AMADEUS system comprises a total of six acoustic storeys (with six acoustic sensors each). Three are located in the IL which started to take data in December 2007 and three more in L12 which was connected in May 2008. During their deployment, due to pressurization two acoustic sensors were damaged, so the AMADEUS fully and functional has been taking data with 34 sensors. The acoustic storeys on the IL are located at 180 m, 195 m, and 305 m above the sea floor. On Line 12, acoustic storeys are positioned at heights of 380 m, 395 m, and 410 m above the sea floor. Initially, IL was anchored at a horizontal distance of about 240 m from the L12. With this setup, the maximum distance between two acoustic storeys was 340m. AMADEUS hence covered three length scales: spacing of the order of 1m between sensors within

a storey (i.e. an acoustic cluster); intermediate distances of 14.5m between adjacent acoustic storeys within a line; and large scales from about 100m vertical distance on the IL up to 340m between storeys on different lines. The sensors within a cluster allow for efficient triggering of transient signals and for direction reconstruction. The combination of the direction information from different acoustic storeys yields (after verifying the consistency of the signal arrival times at the respective storeys) the position of an acoustic source.

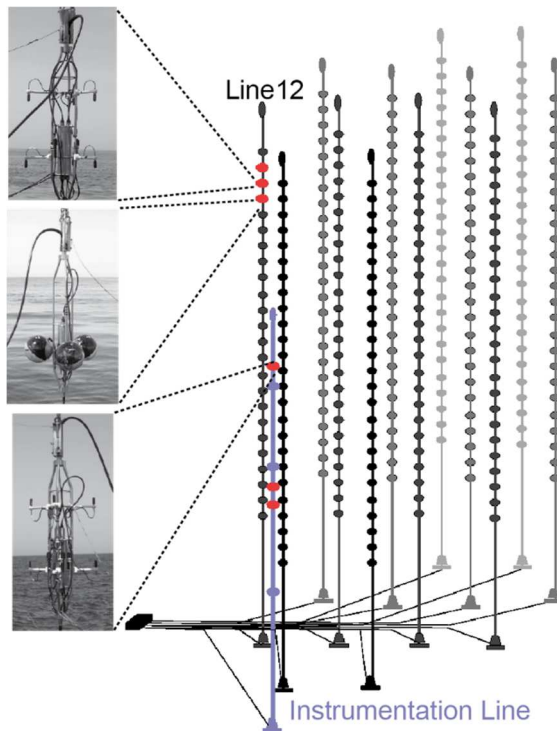


Fig 1.7. Schematic view of the ANTARES detector. The six acoustic storeys are highlighted and their three different setups are shown. This is the configuration after the last redeployment of the IL in November 2013.

Since the beginning of the project to nowadays some changes in the configuration have been performed. Some acoustic sensors in the IL have been replaced. Also the location of the IL was modified, after the disconnection for recovery in May 2011,

and last redeployment in November 2013. The distance between the IL and L12 is about 115 m.

The AMADEUS system includes time synchronization and continuous operating data acquisition setup that is scalable to a large-volume detector.

1.2.3.2 Acoustic Storeys

The family of sensors tested along the AMADEUS project can be divided in two types: hydrophones and Acoustic Modules (AMs). In both cases, the sensing principle is based on the piezo-electric effect. For the hydrophones, the piezo elements are coated in polyurethane, whereas for the AMs, piezos are glued inside of standard glass spheres which are normally used for Optical Modules in ANTARES. Fig 1.8 shows the design of a standard acoustic storey with hydrophones. In the IL, the acoustic storeys only have hydrophones, whereas the lowermost acoustic storey of L12 holds AMs. For more information and details about the whole system refer to (J. A. Aguilar, Samarai, Albert, Anghinolfi et al., 2011).

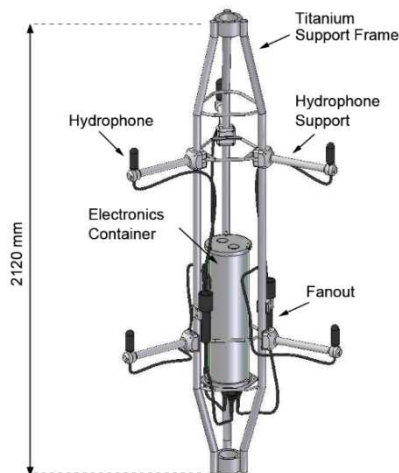


Fig 1.8. Drawing of a standard acoustic storey with hydrophones in the AMADEUS system.

The hydrophones are mounted to point upwards, except for the central acoustic storey of L12, where they point downwards. Fig 1.9 shows the three different designs of acoustic storeys installed in AMADEUS. The sensitivity of the hydrophones is largely reduced at their cable junctions and therefore shows a strong dependence on the polar angle. The different configurations allow for investigating the anisotropy of ambient noise, which is expected to originate mainly from the sea surface. Initially, three of the five storeys holding hydrophones are equipped with commercial models, dubbed HTI hydrophones (High Tech. Inc.©), and the other two with dedicated hydrophones developed and produced at the Erlangen Centre for Astroparticle Physics (ECAP). After the IL recovery in May 2011, in floor 3 the hydrophones produced at ECAP were replaced because they had reached end of life time. The new ones were developed for KM3Net by UPV (Universitat Politècnica de València) and INFN-LNS (Istituto Nazionale di Fisica Nucleare - Laboratori Nazionali del Sud). This fact provided a big opportunity to be tested on deep sea.

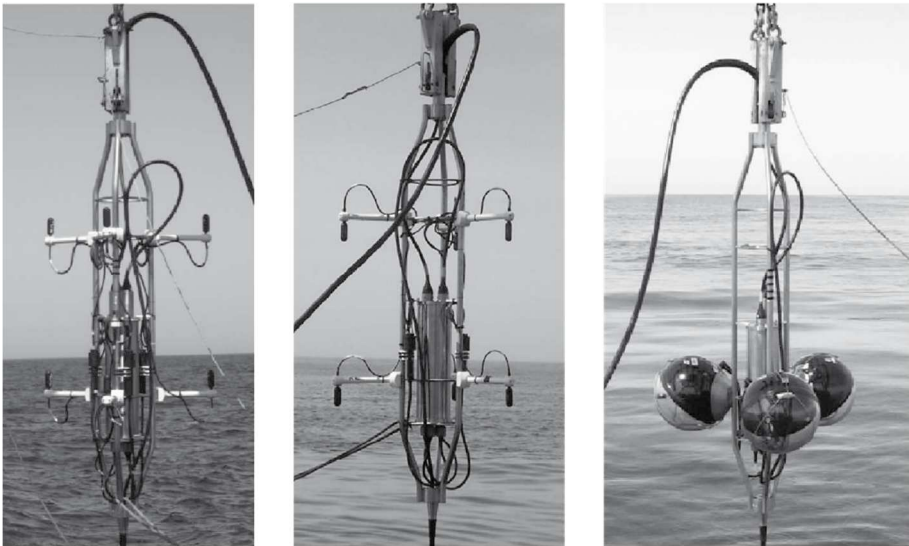


Fig 1.9. Images of the three different storeys of the AMADEUS system during its deployment. On the left a standard storey equipped with hydrophones pointing up is shown. In the middle the acoustic storey on L12 with the hydrophones pointing down. On the right the lowermost acoustic storey on L12 equipped with Acoustic Modules.

1.3 KM3NeT

The successful construction and operation of the ANTARES detector has demonstrated the feasibility of deep-sea neutrino telescopes. The experience acquired during the ANTARES operation and the privileged location of the Mediterranean Sea for Galactic Center visibility have meant a push to build a new large research infrastructure. It will consist of a network of deep-sea neutrino telescopes in the Mediterranean Sea, being a multidisciplinary laboratory also for Earth and Sea sciences (Lahmann, 2012).

The main objectives of KM3NeT are the discovery and subsequent observation of high-energy neutrino sources in the Universe and the determination of the mass hierarchy of neutrinos. Further on, it will be possible to include the acoustic detection of neutrinos from interactions of ultra-high energy cosmic rays with the cosmic microwave background, whereby is paramount to have a calibrator system able to reproduce the acoustic signal induced by neutrino interaction. At the end of the deployment, KM3NeT will dispose of a few km³ of detection volume, about 100 times more than its precursor ANTARES. A cost effective technology for (very) large water Cherenkov detectors has been developed based on a new generation of low price 3-inch photo-multiplier tubes. Following the successful deployment and operation of two prototypes, the construction of the KM3NeT research infrastructure has started.

For the second objective of KM3NeT, ORCA (Oscillation Research with Cosmics in the Abyss) (Katz, 2014), a detailed feasibility study addressing the prospects of measuring the neutrino mass hierarchy with KM3Net is being performed. With the ORCA detector it is possible to determine the mass hierarchy using oscillations of atmospheric neutrinos in the Earth. This mass hierarchy is, together with the CP-violating phase and possible Majorana nature of the neutrino, an outstanding unknown of the Standard Model of Particle Physics. Also ORCA presents sensitivity

to low-mass dark matter (via annihilation in e.g. the Sun) and possibly also to the composition of the Earth interior (via neutrino tomography).

Concerning to the technology, a new generation of 3-inch photo-multiplier tubes (PMTs) has been developed for KM3NeT. These PMTs combine good timing (RMS less than 2 ns), relatively high quantum efficiency (around 30%) and low price (comparing with 10-inch PMTs). The PMTs and the readout electronics are enclosed in pressure-resistant glass spheres. These optical modules are distributed in space along flexible strings, one end of which is fixed to the sea floor and the other end is held close to vertical by a buoy. An optimal building block consists of 115 such strings. The concept of building blocks is modular. Hence, the construction and operation of the research infrastructure allows for a phased and distributed implementation.

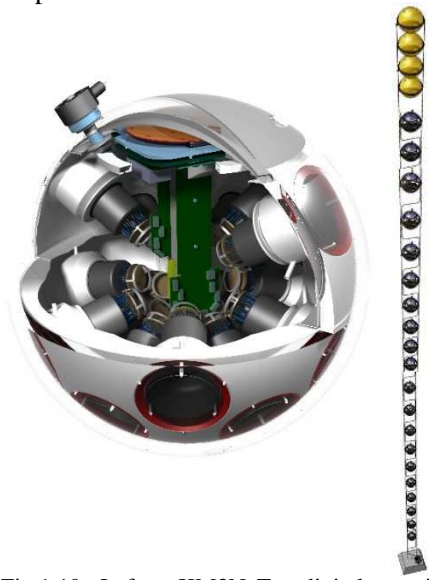


Fig 1.10. Left: KM3NeT digital optical module. Right: Detection Unit of KM3NeT.

sphere. The front part of each PMT is surrounded by a light concentrator ring to further increase the light collection area. The DOM also contains calibration sensors like acoustic piezo sensors, compass and tiltmeters and a nanobeacon. All readout electronics for PMTs and calibration sensors are confined inside the glass sphere of the DOM which has only one penetrator for connection to the backbone cable of the detection unit. The KM3NeT detection unit consists of 18 KM3NeT-DOMs supported by two parallel ropes. The distance between DOMs is 36 m. The lowest DOM is positioned at 120 m above the seabed. A backbone cable runs the full length of the detection unit and connects the DOMs with the seafloor network. The total height of the KM3NeT detection unit is about 700 m.

The innovative Digital Optical Module (DOM) is a stand-alone sensor module with 31 3-inch PMTs in a 17 inch glass

Recently, the collaboration started the first construction phase (Phase-1). During 2015-2016, 31 strings equipped with 558 optical modules will be assembled and deployed at the French and Italian sites.

The resulting arrays will be different in size, the setup at the Italian site being significantly larger and providing the equivalent of about 10% of the size of the IceCube detector (and more than 3 times the size of the ANTARES detector). This detector configuration is optimal for the discovery of high-energy neutrino sources in the Universe. The strings at the French site will be configured according to the outcome of the ORCA feasibility study, a densely instrumented detector, and as such prove the viability of a detector designed for the measurement of the neutrino mass hierarchy.

The ultimate goal is to fully develop the KM3NeT research infrastructure which comprises a distributed installation at three foreseen sites (Italy, France and Greece), with almost 700 strings equipped with 12,400 optical modules in total (Phase-2). The sensitivity of the Phase-2 neutrino telescope will not only exceed that of the current IceCube detector by a substantial factor, but also will bring possible neutrino sources in our Galaxy within reach. The neutrino signal reported by IceCube (Aartsen, Abbasi, Abdou, Ackermann, Adams, Aguilar, Ahlers, M., Altmann, Auffenberg, & Bai, 2013a) has led the collaboration to plan an intermediate step (Phase-1.5). The Phase-1.5 detector will allow for an independent measurement of this signal with different methodology, better angular resolution and complementary field of view. In addition, the predicted angular resolution of cascade events offers the breakthrough capability of doing all flavour neutrino astronomy.

Part I

Design and Development of an Acoustic Calibrator for Deep-Sea Neutrino Telescopes

2

Part I Introduction: Acoustic detection of Neutrinos

Neutrino detection in the high energy range supposes opening a new window in the study of extragalactic sources. Due to the small expected fluxes, neutrino detection in that energy range carries a significant challenge in terms of infrastructure and detection methods. Following the classical optical method for detecting these energetic neutrinos, collecting the Cherenkov light emitted by the muon resulting of neutrino interaction, it would be practically impossible in terms of scaling the infrastructure. It would be necessary more than 10 km^3 of optical instrumented volume for detecting a significant rate of Ultra High Energy (UHE) neutrinos implying a technically very complex design and a very high cost to develop it. In this Chapter the fundamentals of the acoustic detection of neutrinos will be reviewed. The underwater conditions for sound propagation of the ANTARES site will be summarized. To finalize, the need for a calibrator, in order to improve the acoustic neutrino detection in underwater neutrino telescopes, will be introduced together with the parametric acoustic sources technique, which has been used in the calibrator development.

2.1 Acoustic Detection of Ultra-High Energy Neutrinos

The acoustic detection method was predicted for Askaryan (Askaryan, 1957) and is based on the thermo-acoustic effect, described in the following section. Broadly speaking, when a UHE neutrino interacts with a nuclei in water (or ice) a hadronic cascade is generated. The cascade energy is deposited fast and locally in a narrow region of the medium which induces a local heating producing a rapid expansion of the surrounding water (or ice). As a result of this expansion a pressure wave is propagated perpendicularly to the cascade direction. One of the most relevant advantages of the acoustic detection over the optical detection is the attenuation length which is more than one order of magnitude higher for acoustic signals (~km) produced for cascades than for the Cherenkov light (~50 m), comparing the main frequency band of each emission. This advantage allows to instrument a huge volume using a relative low number of sensors.

Besides of the AMADEUS project in the ANTARES Neutrino Telescope, for more than a decade different test sites have been collecting data in order to clarify the acoustic sensitivity for detecting signals from neutrino interactions of a possible detector with given environmental conditions. The main activities in this area are summarized in Table 2.1.

The first experiment was started in 2001 near the Bahamas. The SAUND (Study of Acoustic Ultra-high Neutrino Detection) (Vandenbroucke, Gratta, & Lehtinen, 2005) was composed by seven hydrophones from the military AUTECH (Atlantic Undersea Test and Evaluation Center) array located at about 1600 m depth, resulting in a detection volume of 15 km³. The first acoustic neutrino flux limit was established by the data collected during the first phase of this experiment. In a second phase, the number of hydrophones increased to 49 (1500 km³ of detection volume). Detailed studies about acoustic background were performed after 130 days of data taking (Kurahashi & Gratta, 2008). Two events were compatible with showers from neutrino

interaction above 10^{22} eV after a complex data reduction which contributed to an improvement in the neutrino flux limit (Kurahashi, Vandenbroucke, & Gratta, 2010).

<i>Project</i>	<i>Host</i>	<i>Location</i>	<i>Medium</i>	<i>Sensors</i>
AMADEUS	ANTARES	Mediterranean Sea (Toulon)	Sea water	36
OvDE	NEMO	Mediterranean Sea (Sicily)	Sea water	4
SPATS	IceCube	South Pole	Ice	80
Baikal	BDUNT	Lake Baikal	Fresh water	4
ACORNE	RONA military	North Sea (Scotland)	Sea water	8
SAUND	AUTEC military	Tongue of the Ocean (Bahamas)	Sea water	7/49

Table 2.1. Overview of the acoustic detection test sites.

Deployed in 2005 at 25 km offshore of Catania, in the Mediterranean Sea, NEMO-OvDE (Ocean Noise Detection Experiment) was monitoring the underwater noise during 5 minutes every hour. The average noise level in the 20-43 kHz frequency band was found $5.4 \pm 2.2_{\text{stat}} \pm 0.3_{\text{sys}}$ mPa of pressure level and it was strongly correlated with the environmental conditions at the Sea surface (Riccobene, 2009). Moreover, almost daily during the approximately two years duration of the experiment, the presence of sperm whales was detected when the major environmental agencies declared that these species were declining in the area (Nosengo, 2009). The analysis of the acoustic signal produced for sperm whales allows to derive the age and gender of the animal emitting it.

Between 2006 and 2008 the ACORNE (Acoustic Cosmic Ray Neutrino Experiment) group was taking data using eight hydrophones of the RONA military array in North-West Scotland. Besides the neutrino flux limit in the same range of SAUND result, information about signal attenuation and localization also were collected (S. Bevan, 2009; Danaher, 2007).

In Baikal Deep Underwater Neutrino Telescope (BDUNT) experiment, an antenna consisting of four hydrophones in a tetrahedral arrangement with equal interspacing between hydrophones (1.5 m) was placed in 2006 at 150 m depth in Lake Baikal (Siberia, Russia). In this experiment, the target material is fresh water which has the advantage over sea water that the attenuation length is roughly one order of magnitude larger in the frequency range of 10 to 100 kHz. However, conditions in Lake Baikal are not particularly favourable for acoustic neutrino detection. The thermal expansion coefficient is close to zero and the Grüneissen parameter (see next section) is low. Extensive environmental studies were done concluding that the observed noise level depends mostly on surface conditions. In the frequency range of 5 to 20 kHz it has a value below 5 mPa. From the analysis, one interesting neutrino-like event was observed, accepting only signals from the deep lake. In 2011 an acoustic string with three acoustic modules was deployed and data taking is ongoing (Aynutdinov et al., 2012).

In the upper empty part of holes drilled for the IceCube neutrino observatory was deployed the SPATS (South Pole Acoustic Test Setup) (Karg, 2012). A total of seven acoustic stations composed by transmitters and receivers have been positioned between 80 m and 500 m distance in the ice of the South Pole. Due to the shortage of previous experimental studies for acoustic properties in ice, since data taking started at 2007, results have been orientated to describe the environmental conditions of the site and its influence in the acoustic signal propagation: speed of sound, pressure and shear waves and their refraction versus depth, the acoustic attenuation length and the ambient noise level (R. Abbasi et al., 2010; R. Abbasi et al., 2011b; R. Abbasi et al., 2012). Using data from transient noise measurements, a neutrino flux limit above 10^{11} GeV was derived after eight months of observation.

2.1.1 The Thermo-Acoustic Model

The prediction of the hydrodynamic radiation production as ultrasonic pressure waves (Askaryan, 1957) prompted the development of the *thermo-acoustic model* in 1970s. This model describes the production mechanism of the bipolar acoustic signals measured in a proton beam experiment in a fluid media (Askariyan, Dolgoshein, Kalinovsky, & Mokhov, 1979; Learned, 1979). According to the model, the hadronic particle cascade, originated by UHE particle integrating in water, gives rise to a large energy deposition in a small volume in a very short time (instantaneous with respect to the hydrodynamic time scale). Due to the temperature change, the medium expands or contracts according to its volume expansion coefficient, β , causing a pressure pulse which develops orthogonal to the cascade and therefore the incident particle direction. The equation that describes the pulse is:

$$\bar{\nabla}^2 p(\vec{r}, t) - \frac{1}{c^2} \frac{\partial^2 p(\vec{r}, t)}{\partial t^2} = -\frac{\beta}{C_p} \frac{\partial^2 q(\vec{r}, t)}{\partial t^2} \quad (2.1)$$

where, $p(\vec{r}, t)$ denotes the hydrodynamic pressure at given place and time, c is the speed of sound in the medium, C_p is the specific heat capacity and $q(\vec{r}, t)$ is the energy deposition density of the particles. It is possible to group all dependent parameters of water properties (temperature, salinity and hydrostatic pressure), i.e., the environmental parameters, in a dimensionless one, the Grüneissen parameter $\gamma = \beta c^2 / C_p$ which indicates the conversion efficiency of the thermal energy into sound. This allows the comparison of signal strength (acoustic pulse relative intensity) for different oceans and seas at different depths. As shown in Fig 2.1, the efficiency of the thermo-acoustic conversion mechanism varies over the water volume due to the vertical stratified profile where the sound speed is depth depending. Also the differences are caused by the temperature and salinity conditions which vary from one sea to another. The signal strength, defined by γ , increases with salinity, temperature and depth. In the case of Mediterranean Sea the fact of being an ‘old’

and ‘closed’ sea attributes high salinity and warm temperature at large depth, close to 13°. This translates into an enhancement by a factor 2 of the acoustic emission strength with respect to the oceans.

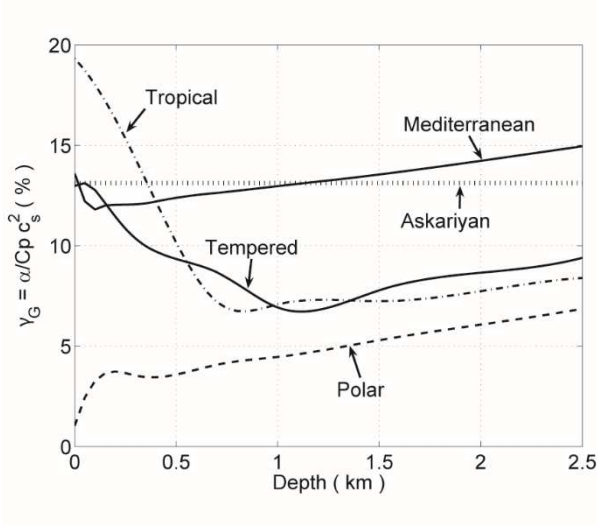


Fig 2.1. Grüneissen parameter γ for different oceans and seas as a function of depth. Polar areas (dashed), oceans in tropical (dash-dotted) and tempered (solid, bottom line) areas and the Mediterranean Sea (solid upper line). The dotted horizontal line indicates the value used by (Askariyan et al., 1979).

Equation (2.1) can be solved using the Kirchoff integral:

$$p(\vec{r}, t) = \frac{\beta}{4\pi C_p} \int \frac{dV'}{|\vec{r} - \vec{r}'|} \frac{\partial^2}{\partial t^2} q\left(\vec{r}', t - \frac{|\vec{r} - \vec{r}'|}{c}\right) \quad (2.2)$$

As the energy deposition is almost instantaneous, Eq.(2.2) can be simplified assuming:

$$\begin{aligned} q(\vec{r}, t) &= q(\vec{r})\theta(t) \\ \dot{q}(\vec{r}, t) &= q(\vec{r})\delta(t) \end{aligned} \quad (2.3)$$

being $\theta(t)$ and $\delta(t)$ the step and delta function respectively, the simplify equation would follow:

$$p(\vec{r},t) = \frac{\gamma}{4\pi} \frac{\partial}{\partial R} \int_s \frac{q(\vec{r}')}{R} d\sigma \quad (2.4)$$

Integration is carried out over spherical shells of radius $R=ct$ centred on \vec{r} , this means that the pressure in \vec{r} at time t is the sum of all contributions that can reach this point propagating at the speed of sound. Using this approach is neglected the pressure waves attenuation during the propagation form the source to \vec{r} , moreover linear propagation is assumed. Although the limitations induced by these assumptions this solution is very effective at short distances from the source (~ 100 m).

2.1.2 Acoustic Neutrino signature

UHE neutrinos are expected to interact by deep inelastic scattering with the nuclei of water molecules. This interaction results in hadronic fragmentation and, in the case of a charged current interactions (CC), in a charged lepton which acquires 80% of the energy of the primary neutrino (Gandhi, Quigg, Reno, & Sarcevic, 1998). The remaining energy is deposited into the water as hadronic shower aligned with the direction of the primary neutrino. The local heating resulting of this energy deposition causes an expansion of the medium which generates an acoustic pulse propagating perpendicular to the shower axis. While ν_μ and ν_τ neutrino generates hadronic shower, with travel paths of a few tens to a hundred kilometres, ν_e also generates and electromagnetic shower, which is superimposed on the hadronic one. The better event observable acoustically would be a ν_e charged current interaction where all the energy of the primary neutrino is dumped into cascades of short extend ($\sim 10 - 100$ m). On the other hand, in cases of neutral current interaction (NC) only about 20 % of the initial neutrino energy is available for acoustic detection trough hadronic shower.

The acoustic signal generated by the neutrino interaction in water is characterized by the high anisotropy of the source. The cascade, whose energy deposition is extended from a few meters to tens of metres in length with only a few centimetres in diameter, can be understood as the acoustic source. This strong anisotropy gives high directivity to the acoustic signal whose emission occurs in orthogonal directions of the cascade axis (Fig 2.2). Energy deposition is instantaneous, in terms of hydrodynamic scale, for this reason the signal has a bipolar shape in time, with a short and prominent compression peak followed by a longer, but weaker, rarefaction peak. In frequency domain it is a broadband signal whose spectrum differs depending on the distance to the source. The high frequency content of the spectrum, which is consequence of the instantaneous energy deposition, is suppressed by absorption or by the lateral spread of the energy deposition area, depending on the distance to the source.

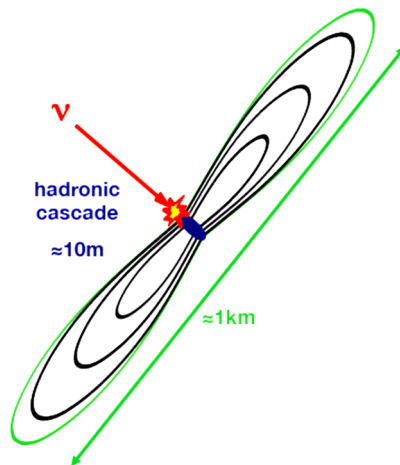


Fig 2.2. Illustration of the cascade produced by neutrino interaction in water and the directive pressure pulse generated. Typical dimensions of the implicated parts for acoustic detection are indicated.

Fig 2.3 shows the principal characteristics of the signal which vary depending on the cascade extension and the energy range. The parameters considered by several authors to describe the signal are the peak to peak duration, Δt , the half peak

amplitude, A_p , and the symmetry factor, R/C , which defines the ratio of compression and rarefaction peak amplitude.

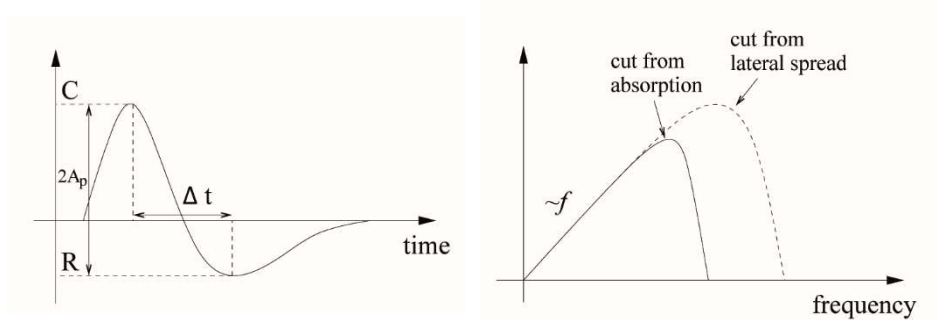


Fig 2.3. Sketch of a typical acoustic signal pulse. On the left the time pattern. On the right the frequency spectrum. From (Niess & Bertin, 2006)

The maximum pulse height will be proportional to the deposited energy, to the inverse of the square of the radial energy distribution, to the inverse of the distance and to the Grüneisen parameter, related with the properties of the medium. As an example, in Fig 2.4 the shape and spectrum of a bipolar pulse resulting from the simulation of a 10^{20} eV cascade are shown, from (Graf, 2008).

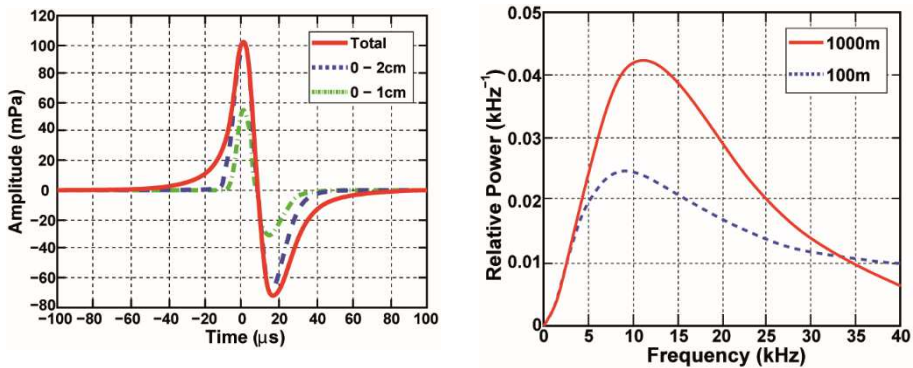


Fig 2.4. Simulated acoustic pulse for a 10^{20} eV shower at 1 km distance from the shower centre. Left: the contribution of the radial distribution for up to 1 cm and 2 cm from the shower core and for the contribution of the whole shower are shown, in time domain. Right: Relative power spectrum at 100 and 1000 m from the shower.

2.1.3 Underwater conditions in the Mediterranean Sea.

Acoustic propagation depends on the environmental characteristics of the propagation medium, in this case, seawater. Propagation is connected fundamentally to two concepts: sound propagation velocity and wave attenuation. Both depend directly to the physical and chemical properties of the medium. In the attenuation process there are two different causes: on one hand, attenuation is produced by the geometrical spread of the beam. On the other hand, the beam is attenuated due to the loss of energy through absorption, which is converted into heat. The absorption depends on the temperature of the medium, the salinity and the pressure (depth), also sound velocity propagation depends on these environmental parameters.

2.1.3.1 Attenuation

As previously advanced, the attenuation of an acoustic beam during its propagation is the result of two different mechanism. On one hand, as the wave-fronts travel outwards from the transducer they spread over a larger area. The total energy of the transmission is fixed, so the intensity (power transmitted through unit area) decreases as the beam spreads (Fig 2.5(a)).

In Fig 2.5 (b) it is distinguished two differentiated zones. It is known as far field the range, much larger than the transducer size, where the intensity varies with the range R according to the inverse square law:

$$I = \frac{I_0}{R^2} \quad (2.5)$$

In the pressure case, this is inversely proportional to the range.

$$|P| = \frac{|P_0|}{R} \quad (2.6)$$

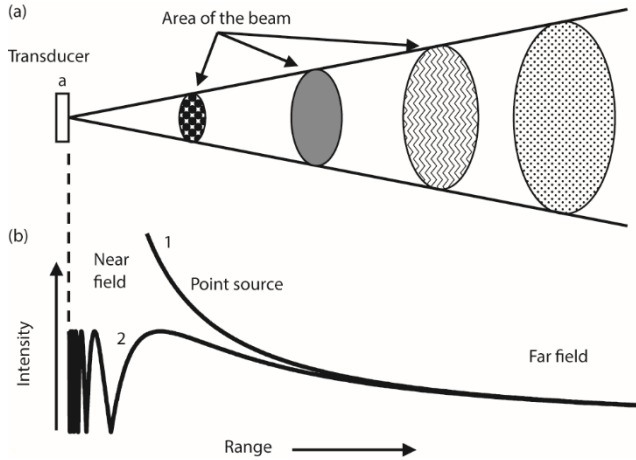


Fig 2.5. Illustration of acoustic energy propagating away from a transducer. (a) Spherical spreading reduces the intensity at large ranges. (b) This causes the intensity of a point source to follow the inverse-square law (curve 1) at any range. For a finite transducer near-field effect limits the intensity near the face of a finite transducer (curve 2). From (Simmonds & MacLennan, 2005)

Near field is the region immediately in front of the transducer where the range dependence of the intensity is more complicated, also called the Fresnel zone. In the near field, the intensity varies rapidly with the range in an oscillatory manner. This occurs at ranges where the wave-fronts produced by the transducer elements are not parallel, a state which alters the phase relationships compared to the far field. Only in far field (also known as the Fraunhofer zone), where the element wave-fronts are nearly parallel, beam is properly formed and the inverse square law applies. If a is the linear distance across the transducer face, the boundary between near and far fields in b is approximately at the range:

$$R_b = \frac{a^2}{\lambda} \tag{2.7}$$

The other mechanism that intervenes into the attenuation process is the sound absorption, it is the loss of acoustic energy which converts into heat. This causes

exponentially decrease with the distance, r , of the amplitude pressure of a plane wave along the propagation path.

$$|P| = |P_0| e^{-\alpha r} \quad (2.8)$$

where α is the absorption coefficient in nepers per meter (Np/m) or in dB/m, $\alpha_{dB/m} = 8.69\alpha_{Np/m}$.

Several mechanisms are responsible of the absorption. In both, fresh and saline water there are losses due to viscosity, frictional losses. This part of the absorption is proportional to the square of the frequency because at higher frequencies the particle velocities are faster and thus higher friction losses. In seawater there are additional losses due to the molecular relaxation of certain compounds. For relaxation it is understood the pressure-induced effect of the reduction of molecules to ions which takes a certain time to complete. In this case, as at high frequencies the sound pressure cycles too quickly, the reduction does not take place and thus no energy is absorbed by this process. In the frequency range of 2 - 500 kHz the magnesium sulphate ($MgSO_4$) relaxation dominates the absorption. At lower frequencies there is a further loss associated with boric acid $B(OH)_3$.

Although the frequency is the main variable for the absorption, it also depends on the water temperature and salinity. Equations for predicting the absorption coefficient at a given frequency, temperature, salinity and depth have been developed by diverse authors (Fisher & Simmons, 1977; Schulkin & Marsh, 1963). The most used is the one formulated by (Francois & Garrison, 1982a; Francois & Garrison, 1982b) who maintain that, assuming the exact knowledge of the temperature and other parameters, the predicted α is within 5% of the true value. A simplified expression of the Francois and Garrison formula easier to evaluate is also available (Ainslie & McColm, 1998). Previously to these formulations a possible phase shift during the propagation was predicted by (Liebermann, 1948). More recently, (Niess & Bertin, 2006) published a formulae for the complex absorption based on the predictions of

Liebermann and the parameterizations for the Mediterranean Sea conditions, through the Francois and Garrison results. Also regarding with the complex absorption, from the ACORNE collaboration a complex version of the Ainslie & McColm formulation where MgSO_4 and $\text{B}(\text{OH})_3$ contributions are complex was proposed (S. Bevan et al., 2009). Fig 2.6 has been extracted from (S. Bevan et al., 2009), it shows a comparative study of the absorption coefficient in sea water using different equations, including a result in ice.

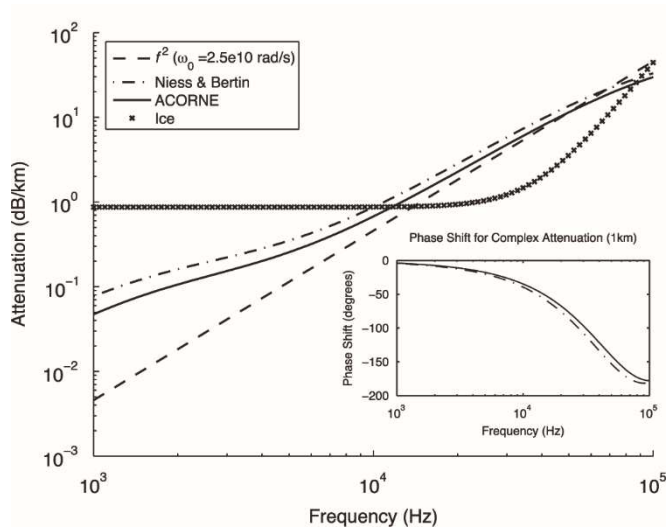


Fig 2.6. Sound attenuations in sea water for the SAUND/Learned (f^2 approximation, Niess and Bertin, Francois and Garrison, Ainslie and McColm and the ACORNE parameterisations). Since the Ainslie & McColm/ACORNE and Francois & Garrison results match very closely they are depicted as the same curve in the figure. The attenuation in Antarctic ice is shown for comparison. Inset: the phase shifts at 1 km for the two complex attenuation models. Plot extracted from (S. Bevan et al., 2009).

In Chapters 3 and 4, results for theoretical propagations will be presented. In these results, the small dispersion effects over distances of several hundred of meters resulting from complex attenuation have not been taken account.

2.1.3.2 Sound speed

As with the absorption coefficient, the sound speed c depends on the water temperature, salinity and depth. Since sound speed should to be determined from these variables, the best values are obtained using empirical formulations proposed by (Del Grosso, 1974) which have 19 terms, 18 of which have coefficients with 12 significant figures each, so not much “manageable”. A simplified formula was proposed by (Medwin, 1975) with less than 0.2 m/s error compared with Del Grosso’s result for $0 < T < 32$ °C and $22 < \text{Salinity } \text{‰} < 45$ for depths up to 1000 m:

$$c = 1449.2 + 4.6T - 0.55T^2 + 0.00029T^3 + (1.34 - 0.01T)(S - 35) + 0.016z \quad (2.9)$$

where c is the sound speed (m/s), T is the water temperature (°C), S is the salinity (‰, parts per thousand) and z is the depth (m). Years after, (Mackenzie, 1981) proposed a longer formula with 0.07 m/s error and with no restriction to depths less than 1000 m:

$$c = 1448.96 + 4.591T - 5.304 \cdot 10^{-2}T^2 + 2.374 \cdot 10^{-4}T^3 + 1.340(S - 35) + 1.630 \cdot 10^2 z + 1.675 \cdot 10^{-7} z^2 - 1.025 \cdot 10^{-2}T(S - 35) - 7.139 \cdot 10^{-13}Tz^3 \quad (2.10)$$

These formulas ((2.9),(2.10)) have been used to obtain the sound propagation velocity in the ANTARES site for calculations on this work.

Speed of sound was calculated for the ANTARES site as a function of the depth, taking into account the geographic position of the detector (40° 48’N 6°10’E) and the salinity and temperature values obtained during sea campaigns carried out in August of 2007 and in March of 2010. Around 100 m deep from the surface, water suffers seasonal temperature variations of maximally 0.5 °C. Beyond 700 m depth, temperature is quite stable and independent to the season with values between 13.1 °C and 13.6 °C. For this reason, near to the ANTARES site the sound channeling has

not significant effect. This is different at ocean situation where typically the uppermost kilometer of water suffers temperature decrease with depth.

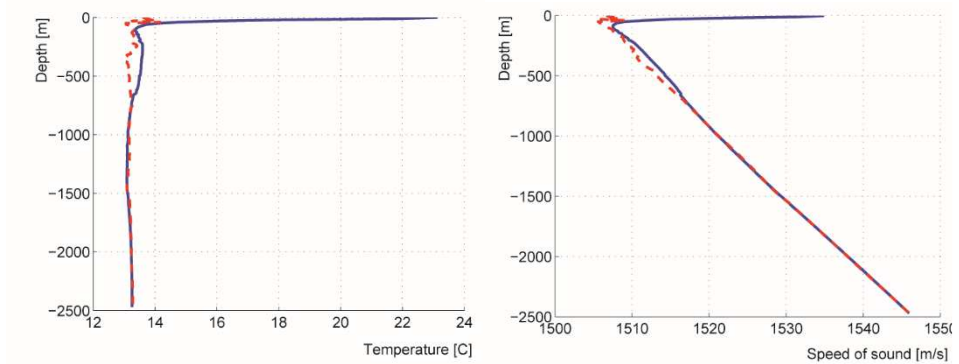


Fig 2.7. Left: temperature variation with the depth from sea surface. Right: Sound propagation velocity variation with the depth from sea surface. For both plots: measurement from the ANTARES site in August 2007 (solid blue line) and in March 2010 (dashed red line). Figure from (Lahmann, 2011)

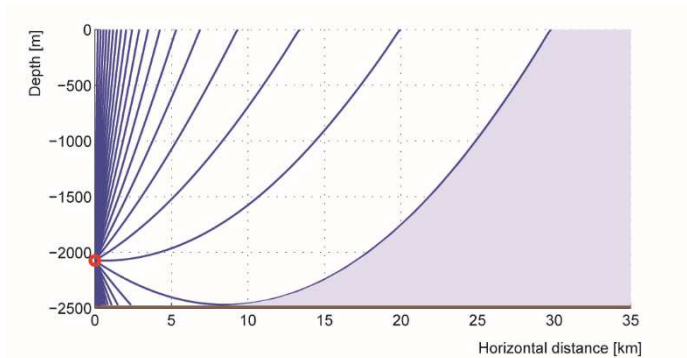


Fig 2.8. Ray tracing of acoustic signals for the speed of sound profile of Fig 2.7 (summer values). It is assumed open water models with a constant depth (2478 m). The shaded area indicates the region from which signals cannot reach the receiver located 410 m above sea floor.

Fig 2.7 shows the temperature variation with the depth and, as a consequence of it, the variation of sound propagation velocity. The stability of temperature is translated into a linear increase of the speed of sound with the depth. Fig 2.8 shows the paths of

acoustic signals. The furthest distance from which an acoustic signal originated in the surface can reach the AMADEUS device is about 30 km.

2.1.3.3 Background in acoustic neutrino detection in the Mediterranean Sea

The background noise in underwater environment can be divided in two main groups: ambient noise and transient signals. These, in turn, can be classified by the affected frequency band (See Fig 2.9).

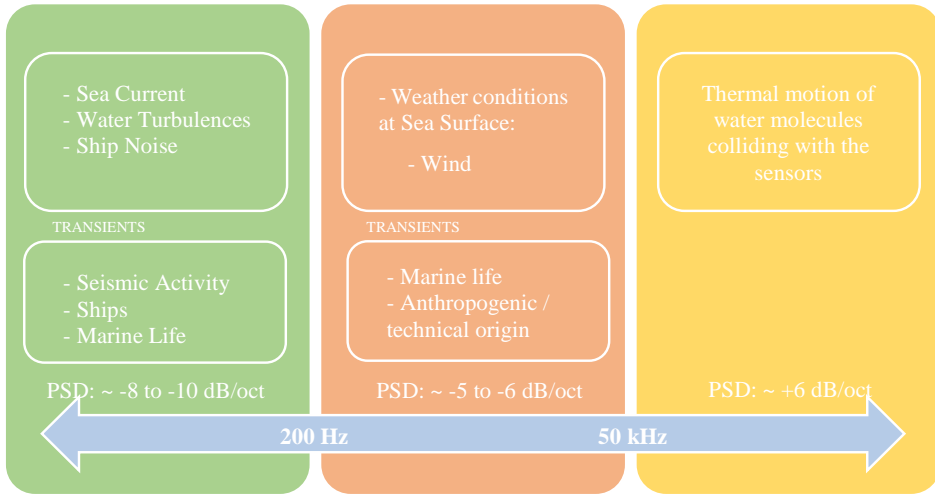


Fig 2.9. Summary of the principal background sources and the affected frequency band. The orange part is the most relevant one for neutrino detection.

Below 200 Hz, which is not relevant for acoustic detection, the sea current and the turbulences are the responsible of the ambient noise. Anthropogenic sources as ship noise also contributes in this band. Concerning to the transients, in this frequency range signals from seismic activity, ships and also marine life are expected. The more relevant band for neutrino detection is 200 Hz to 50 kHz. Fig 2.10 shows the power spectral density (PSD) of the ambient noise recorded by a sensor located on the topmost storey of the ANTARES IL for year 2008 (Lahmann, 2011). The authors have used an algorithm to remove strong transient signals (mostly coming from the emitters of the acoustic positioning system). The relics of such signals and electronics

noise show up as spikes between 45 and 75 kHz. They confirm that the lowest level of recorded noise in situ was confirmed to be consistent with the inherent noise of the system recorded in the laboratory prior to deployment. The observed in-situ noise can be seen to go below the noise level measured in the laboratory for frequencies exceeding 35 kHz. This is due to electronic noise coupling into the system in the laboratory that is absent in deep sea.

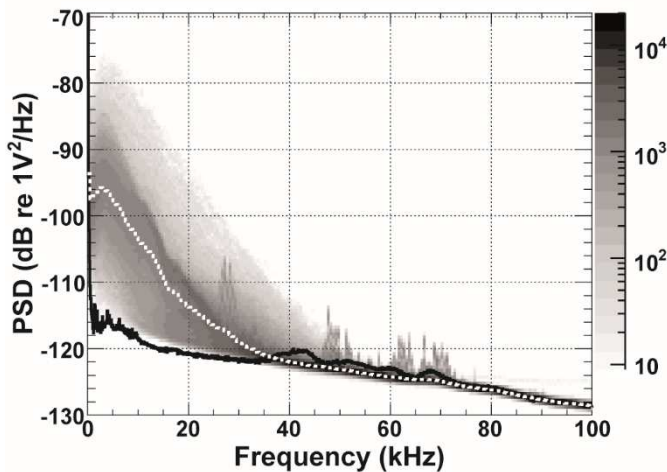


Fig 2.10. Power spectral density (PSD) of the ambient noise recorded with one HTI sensor on the topmost storey of the IL. Occurrence rate in arbitrary units (shades of grey), where dark colours indicate higher rates. Median value of the in-situ PSD (white dotted line) and the noise level recorded in the laboratory prior to deployment (black solid line).

Ambient noise is dependent on the weather conditions on the sea surface, most especially wind activity dominates the noise level at this band. Wind activity is responsible of motion of the sea surface, turbulences, surface wave interactions, spray and cavitation. There are a strong correlation between this noise and the data of the weather stations in this range. Fig 2.11 Left shows the qualitatively correlation with the weather station at Cap Cépet located at about 35 km north-west of the ANTARES detector. Quantitative measurements are affected by the large distance between the

weather station and the ANTARES site but it can be observed a large correlation. Fig 2.11 Right shows the noise values, relative to the mean noise over all samples, as a function of the time of the day. The peak observed at about 1 a. m. and 8 to 9 p. m. can be related with the shipping traffic in the zone.

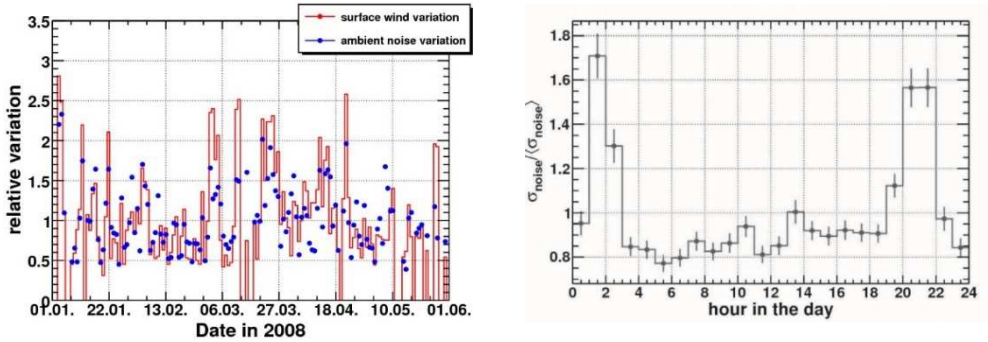


Fig 2.11. Left: Relative variation of the wind speed and of the ambient noise level at ANTARES site over the first half of 2008. Acoustic data measured on the topmost acoustic storey of the IL. The plot is the relative variation for better comparison. The values represent the daily averages divided by the yearly average. Right: Ambient noise in the 1-50 kHz frequency range as a function of the time of the day. It is shown the noise relative to the mean noise recorded during about two years.

At this band (200 Hz - 50 kHz) the transient signals are generated by marine life and also have an anthropogenic or technical origin. Marine mammals (and other environmental sources) are responsible of the transient signals which constitutes an important background for neutrino detection. In particular dolphins whistles which pulse shape is very similar to the bipolar neutrino pulse. The multidisciplinary character of the underwater neutrinos telescopes in the Mediterranean Sea allows work in parallel using the acoustic data from two different optics and generating synergies. The acoustic monitoring of the deep sea has a large potential for interdisciplinary research. Marine scientist are using the acoustic data for the study of marine mammals (Nosengo, 2009) whose knowledge helps to understand and reduce this kind of background. Above 50 kHz the noise spectrum are dominated by the thermal motion of water molecules colliding with the sensors.

2.2 Calibrator for Acoustic Detection of Ultra High Energy Neutrinos in Underwater Telescope

Searching for UHE neutrinos in presence of strong background of transient signals is a challenging task. Due the presence of this background it is necessary an efficient signal classification able to distinguish between transient background signals and the expected acoustic signals from neutrino interaction in water. During the last years, some works have focussed on the search of possible ways to classify acoustic signals produced by a neutrino interaction in presence of acoustic background (Neff, 2013). Simulation studies were performed to reproduce the acoustic signature of neutrino interaction and their propagation to the sensors within the detector. Also the transient background were studied. In this work, it was proposed a pre-selection scheme for neutrino-like signals based on matched filtering. An analysis chain consisting of reconstruction techniques for the arrival time, the incident direction of the pressure wave, and the source position of an acoustic signal was developed. In addition, a signal classification strategy, based on machine learning algorithms was implemented in the same work.

In spite of all sensors that conform the AMADEUS system have been calibrated in the lab it would be desirable to dispose of a compact calibrator that “in situ” may be able to monitor the detection system, to train the system and tuning it in order to improve its performance for testing and validating the technique and also for determining its reliability (Ardid, 2009). Moreover, the possibility of performing *in situ* measurements of neutrino-like signals generated from a known source (a calibrator) during sea campaigns or even integrating the source in the neutrino telescope, would permit to verify the simulation results and also to improve the signal classification.

An eight-hydrophone linear array (about 8 m length) has been developed by the Northumbria University group for the generation of emulated UHE neutrino-induced

pulses (Ooppakaew, Danaher, & Saldana, 2011). By means of this acoustic array, they pretend simulate the acoustic pulse created from a neutrino interaction in water generating a coherently emitted acoustic bipolar pulse. The calibrator was developed using signal processing methods. An eight channel PIC hydrophone array module was built for processing and control. A linear array simulation for the neutrino pulses production was performed in order to predict the shape and directivity. The Northumbria's device was tested during a sea campaign in September 2011 but, due to technical problems, results were not conclusive (Danaher, 2012).

In this work a different approach will be presented for a prototype calibrator for *in situ* evaluation of the acoustic detection technique. The main goal will be the development of an autonomous and optimized system able to reproduce the acoustic signal (shape and directivity) produced by neutrino interaction using the parametric acoustic sources technique.

2.3 Parametric Acoustic Sources

Parametric acoustic sources have been subject of considerable research since their introduction by (Westervelt, 1963) due to the rise of interest for applications in underwater communications. Parametric transduction offers a potential solution to several of the problems concerned with transmission to long range at low acoustic frequencies. The parametric effect occurs when two high intensity primary signals co-exist in the water. The nonlinear behaviour of the water results in the generation of sum and difference frequency components of these primary signals. The difference frequency component is of particular interest in underwater acoustics. This low frequency beam may be considered to be radiated from a virtual array of acoustic sources, distributed continuously throughout the water interaction region (Fig 2.12). In the process of conversion of the primary frequency waves to the difference frequency wave the source seems to be shaded exponentially, with increasing

distance from the transmitter. This is because of the attenuation produced by viscous friction and other effects in the water.

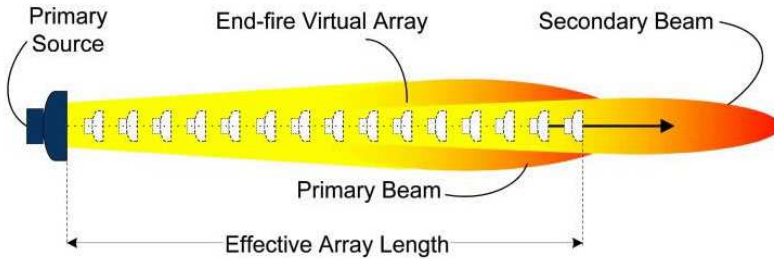


Fig 2.12. Illustration of the virtual array in the water interaction region of the two primary beams where the parametric effect takes place.

The resulting polar response is of narrow beam width, due to the aperture of the virtual array comprises many thousands of wavelengths. It also has the unusual but sometimes useful characteristic of being free of side lobes. Furthermore, the parametric conversion process provides great frequency agility. This is because, even though at the primary frequency the transducer may have only a modest proportional bandwidth, the parametric down-mixing process makes all this bandwidth available at the lower secondary frequency. In principle, this should enable parametric transduction to be used for high data rate communication, or for wide-band signal processing techniques.

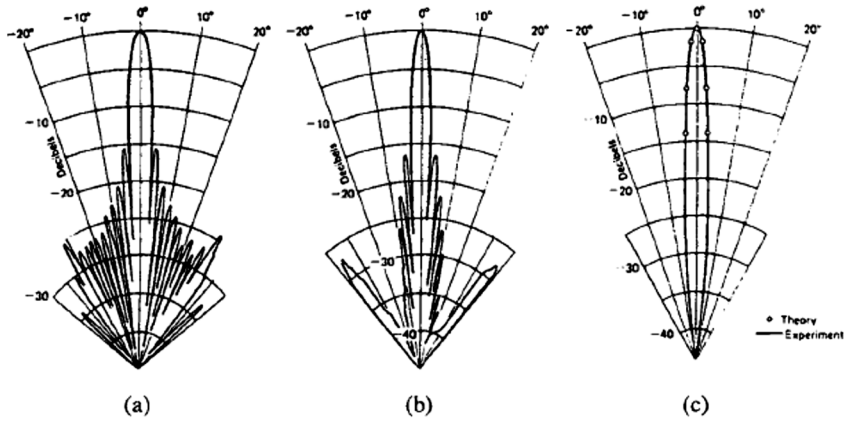


Fig 2.13. Directivity pattern of a parametric source. (a) Primary 418 kHz, (b) Primary 482 kHz, (c) Beam pattern of difference frequency, 64 kHz.

The parametric generation is a cumulative process. The difference frequency wave grows in the source volume made of the primary waves. The Westervelt model exemplifies this principle by considering perfectly collimated primary beams: the source volume is in fine interpreted as a virtual array whose length is only limited by the linear absorption of the primary waves. The parametric directivity is thus proportional to the square root of the array length. In addition, the beam pattern is devoid of side-lobe.

Since the Westervelt proposal many other models have been proposed for handling more realistic source distributions (Moffett & Mellen, 1977; Moffett, Mellen, & Konrad, 1978; Muir & Willette, 1972; Tjøtta & Tjøtta, 1980), i.e., by taking into account altogether diffraction, attenuation and saturation phenomena. In most applications, the width of the beams is relatively narrow all around the main axis (e.g., sub-bottom profilers). The paraxial approximation is thus convenient to model such transmitters. In the underwater domain, a classical application of parametric transmission is sub-bottom profiling: due to the large attenuation, only low frequency waves can penetrate the sediments; but narrow beams are also required to improve

the profile resolution. Recent projects have studied the feasibility to detect buried objects by means of high resolution imaging. The idea is to combine the parametric transmission and the synthetic aperture sonar techniques. The parametric beam must be narrow in one direction to achieve the required resolution in elevation, and sufficiently large in the perpendicular direction to perform the synthetic aperture process. The paraxial approximation is then no longer sufficient to model the parametric projector.

Most of the work cited till here has been directed toward what may be called the steady-state, or narrow-band, version of parametric source wherein two discrete primary-frequency components of equal amplitude interact in a nonlinear acoustic medium to form a difference-frequency component. Parametric generation can also be reached using transient, or broad-band, signals (Moffett & Mello, 1979). In this reference authors discuss the transient parametric source in which a modulated primary beam generates a transient signal related to the modulation envelope. For example, a primary beam consisting of a single high-amplitude pulse generates a secondary transient signal that can be associated with the up and down parts of the primary pulse. The transient version of the parametric array is sometimes referred to as self-demodulation because the result is similar to the demodulation of the original signal. The transient parametric array is a generalized form of the steady-state array. The latter is the result of a typical modulated waveform:

$$\cos\left(\omega_0 - \frac{\omega}{2}\right)t - \cos\left(\omega_0 + \frac{\omega}{2}\right)t = 2\sin\left(\frac{\omega t}{2}\right)\sin(\omega_0 t) \quad (2.11)$$

Where ω_0 is the primary frequency and ω is the parametric desired signal. Which is the same of a carrier frequency ω_0 modulated by an envelope of the form:

$$E(t) = \sin\left(\frac{\omega t}{2}\right) \quad (2.12)$$

Theory for parametric transient sources is based on the Westervelt formulations. Following (Moffett & Mello, 1979) the pressure distribution along the axis for a secondary beam generated parametrically emitting transient signals follows:

$$p(x,t) = \left(1 + \frac{B}{2A}\right) \frac{P^2 S}{16\pi\rho c^4 \alpha x} \frac{\partial^2}{\partial t^2} \left[f\left(t - \frac{x}{c}\right) \right]^2 \quad (2.13)$$

In this equation $(1 + B/2A)$ is the non-linear parameter of the medium, the values A and B are the coefficients of the first and second order terms of the Taylor series expansion of the equation relating the pressure and the density of the medium. For seawater is about 5.25 at 20° temperature and 35 ‰ salinity conditions (Hamilton & Blackstock, 1998). Where S is the area of the transducer surface, ρ , c are the density and the sound velocity in the medium respectively, α is the absorption coefficient of the medium. P is the pressure amplitude of the primary signal and $f(t - x/c)$ is the envelope of the primary transient signal which modulates the primary frequency. It is remarkable the temporal dependence of the parametric signal with the second time derivative of the square of the envelope function. This could be useful in order to design primary transient signals which generate parametric signals with a pre-determined characteristics. The pressure distribution out of the axis can be described by the next equation, in this case it follows the first time derivative and takes into account the angular distance to the axis:

$$p(x,\theta,t) = \left(1 + \frac{B}{2A}\right) \frac{P^2 S}{16\pi\rho c^2 \alpha x} \left(\sin \frac{\theta}{2}\right)^{-2} \frac{\partial}{\partial t} \left[f\left(t - \frac{x}{c}\right) \right]^2 \quad (2.14)$$

In both situations, steady-state and transients, the main disadvantage of parametric transduction is its low-power conversion efficiency, which is usually less than 1%; that is, equivalent to at least 20 dB of power loss. The low-power conversion efficiency may be offset, for long distance transmission, by the lower attenuation at the secondary frequency. Despite this, parametric acoustic source technique has some

properties that result very interesting to be exploited for the development of an acoustic calibrator for neutrino detection:

- a. It is possible to obtain narrow directional patterns at small overall dimensions of primary transducer.
- b. Absence or low level of side lobes in a directional pattern on a difference frequency.
- c. Provides broad band of operating frequencies of radiated signals.
- d. Since the signal has to travel long distances, primary high-frequency signal will be absorbed.

For all these reasons, and some more detailed in the next section, this technique could be interesting for the development of an acoustic compact calibrator.

3

Evaluation of the Parametric Technique for the Compact Acoustic Calibrator

In this Chapter a set of different experiments performed in order to validate and evaluate the parametric technique is described. These experiments follow an ascending trajectory, in terms of application of the technique and adaptation to the final goal: to apply it in the design of a compact calibrator able to mimic the acoustic signature generated for the UHE neutrino interaction in water. For this, as first approximation, a simple experiment using planar transducers was the starting point. The next step was the incorporation of the cylindrical symmetry in emission and the study of the ability to control the shape of the parametrically generated signal. To finish these first steps, a possible array configuration of cylindrical transducers was evaluated. The results and conclusions of these primary tests are detailed in this Chapter.

3.1 Planar Transducers

Initially, drawing on the work of (Ardid et al., 2009), studies and experiments were done with the aim of understanding the parametric generation and evaluating the feasibility of this technique in the generation of the particular acoustic neutrino

signature. In this first stage a simple configuration using planar transducers as emitters in a controlled laboratory environment was chosen. The aim of this study was to evaluate the technique and setting the basis for a first design of the calibrator using parametric generation.

3.1.1 Experimental Setup

First test was performed in the Ultrasonic's Laboratory of Escola Politècnica Superior de Gandia (EPSG). The experimental setup follows the classical scheme of confronted emitter and receiver transducers into a water tank of 1.10 x 0.85 x 0.80 m³ volume. Two fixed planar transducers TC3027 and TC3021 (Teledyne RESON©), with resonance frequencies of 1 MHz and 2 MHz respectively, were used as emitters. It was used a digital function generator PCI-5412 (14 bits, 100MS/s, National Instruments©) and a linear 55 dB RF amplifier ENI 1040L (ENI, Rochester©) to feed the emitter. As a receiver a TC4014 (Teledyne RESON©) hydrophone mounted on a micropositioning system LF-5-DC (MICOS GmbH©) with a precision better than 0.1 mm was used. This transducer is an omni-directional, broad-band spherical hydrophone with flat frequency response below 400 kHz and sensitivity around -186 dB (ref. 1V/μPa). Above 400 kHz the sensitivity decreases with the frequency but it is still enough sensitive to detect primary beams at 1 and 2 MHz. For parametric studies this sensitivity pattern results very convenient by the fact that it is enough sensitive to primary frequencies, allowing an easy and fast alignment of the system, and, on the other hand, it is more sensitive and has a flat range in the region where the parametric signal is expected. For the digitalization of the received signals NI PCI 5102 (8 bits, 20 MS/s, National Instruments©) was used. Fig 3.1 shows a schematic view of the experimental setup and the instrumentation that comprises it.

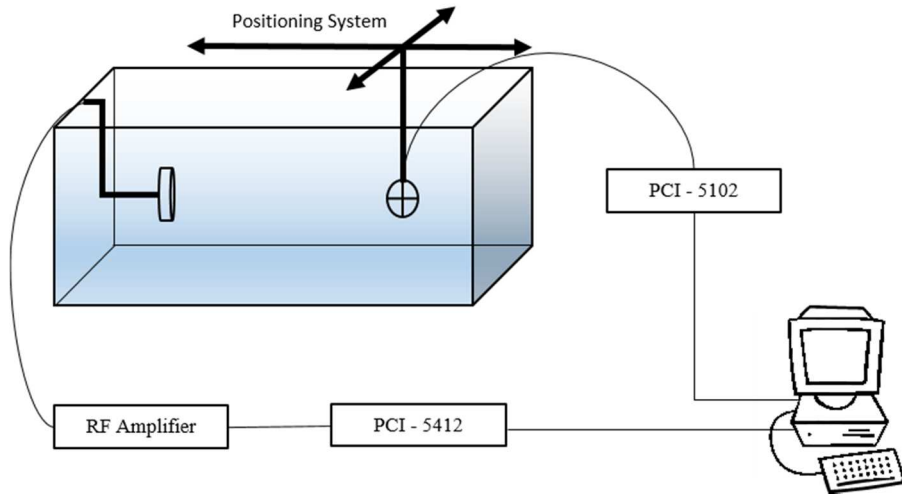


Fig 3.1. Experimental set-up

3.1.2 Methods, Analysis and Results

The goal of this study was to prove that it is possible to reproduce acoustic neutrino-like signals through the parametric effect. For this purpose the main characteristics of the acoustic neutrino signal, shape in time and directivity, were evaluated as well as the non-linear behaviour of the parametrically generated signal.

Applying the knowledge in transient parametric sources (Moffett & Mellen, 1977) the signal shape for emission which parametrically generates a bipolar pulse was calculated following the Eq.(2.13). Following this equation, it is concluded that the waveform of the secondary parametric beam is related with the second time derivative of the primary beam envelope. As the objective is generating a bipolar pulse, is easy to conclude that the envelope of the primary beam could be the integral of a Gaussian function, which will be parametrized by the Error Function.

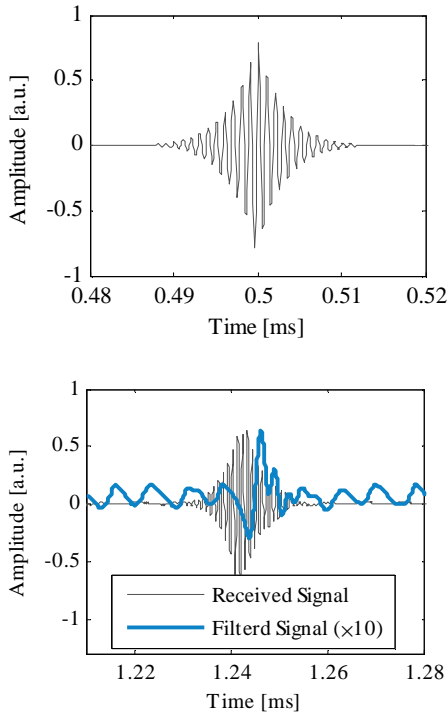


Fig 3.2. Top: Signal used for emission (1 MHz emitter). Bottom: Received signal (black line) and bipolar signal obtained after applying the low-pass filter (blue line)

For instance, Fig 3.2 top, shows the waveform used to feed the 1 MHz emitter before amplification (after amplification the peak amplitude used was around 120 V). On the bottom figure the received signal is shown, the primary signal is clearly visible at first sight (solid line). To distinguish better the parametric signal a low-pass Butterworth filter (200 kHz, 10th-order) was applied. Filtered signal is shown by the dashed line, where the bipolar signal is clearly seen. Considering that the sensitivity of the receiver at 1 MHz was 29 dB lower than the sensitivity for low frequency, the pressure amplitude of the bipolar signal in the water tank would be in the [0.1-1%] range of the amplitude of the received signal (primary beam). As expected, the shape of the bipolar signal was following approximately the second time derivative of the envelope of the 1 MHz modulated signal.

In order to make sure that the secondary beam has a non-linear behaviour, the amplitude of the parametric signal, as a function of the voltage applied to the transducer, was measured. Fig 3.3 shows the amplitude behaviour of the received signal, without filtering (main component is the 1 MHz, primary beam) and with the low-pass filtering (basically the parametric bipolar signal, secondary beam). Linear behaviour is observable for the amplitude of the primary beam. Whereas, for the secondary received signal (parametric bipolar signal) the amplitude behaviour is

proportional to the square of the amplitude of the input signal, showing the non-linearity of the effect.

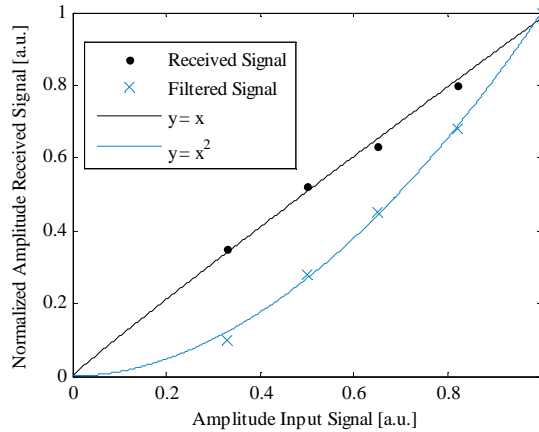


Fig 3.3. Amplitude of the received (primary beam) and filtered (bipolar, secondary beam) vs amplitude of the input signal.

The directivity of the parametric generation was measured and compared with the directivity of the transducer emitting the primary beam. The directivity patterns were measured in a perpendicular plane to the emission axis with a distance between emitter and receiver of about 80 cm, see Fig 3.4 (left). In order to compare both directivities (primary and secondary beams) data have been normalized to the maximum value in each case. In absolute numbers, the amplitude of primary beam is approximately 300 times larger than the amplitude of the secondary beam. Notice that, although the spectral content of the parametric signal (<200 kHz) is completely different to the primary one (1 MHz), both beams have a similar directivity pattern. To complete the tests with planar transducers, the amplitude dependence of the primary and secondary beams with the distance between the emitter and the receiver was measured along the radiation axis (Fig 3.4 right). As expected, pressure amplitude of primary beam decreases with the inverse of the distance. However, there is a softer decrease in the case of the parametric signal. These measurements are compatible with a decrease with the inverse of the square root of the distance.

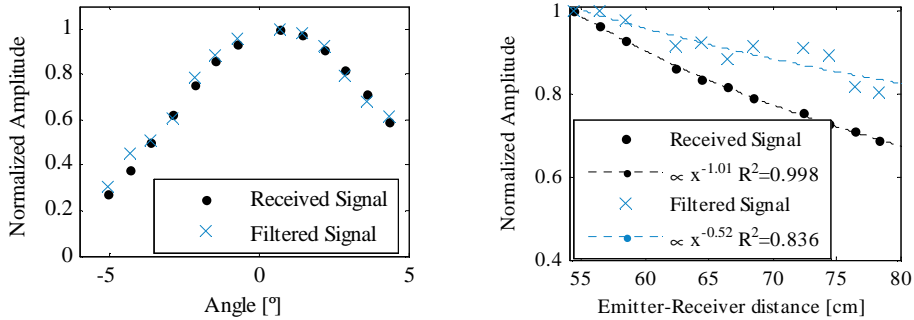


Fig 3.4. Directivity patterns (left) and distance dependence (right) of the primary and secondary (parametric) beams.

According to the results obtained in the study of the parametric generation technique using planar transducers it seems, *a priori*, possible to generate neutrino-like acoustic signals using this method. Following the bases on parametric generation and taking into account these results, as first approximation, it is possible to obtain directive low frequency beams with small transducers (high frequency transducers), which could be very convenient to reproduce the pancake directivity with few sources in a compact design.

3.2 Cylindrical Transducers.

Next step was an extension of the previous studies (Planar Transducers). In this case, evaluating the parametric acoustic source technique dealing with the cylindrical symmetry and studying the capability to control the shape of the parametrically generated signal (Ardid et al., 2012). Although the theory behind it is the same, to achieve the cylindrical symmetry is, in practise, a challenge due to the larger geometric attenuation, the scarcity of transducers available for it, and the lack of experiences and literature in the use of the parametric acoustic sources effect for transient signals by cylindrical transducers. In the next sections the experimental setup, the different studies performed and the analysis results are described.

3.2.1 Experimental Setup

As previously indicated, one of the novelties in these tests was the use of cylindrical emitter. A commercial Free Flooded Ring (FFR) transducer SX83 (Sensortech©) was selected as emitter.

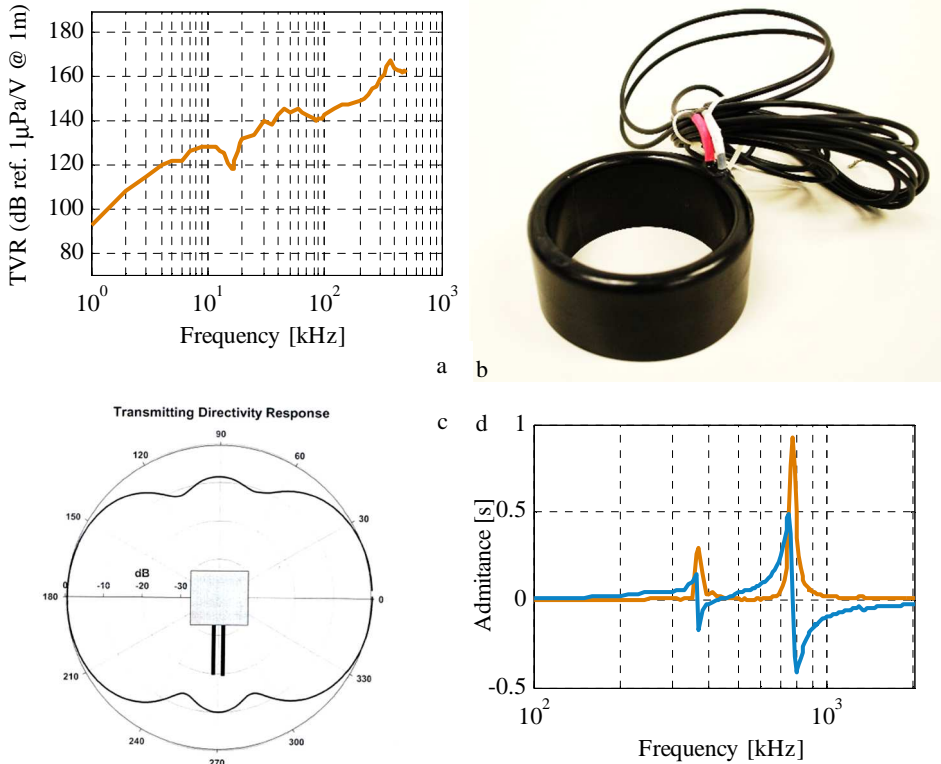


Fig 3.5. a) Transmitting voltage response. b) FFR SX83. c) Directivity pattern. d) Electrical admittance.

The FFR transducers have ring geometrical form maintaining the same hydrostatic pressure inside and outside the ring so reducing the change of properties of the piezoelectric ceramic under high hydrostatic pressure. For these reasons they are a good solution to the deep submergence problem (Sherman & Butler, 2007). The FFR-SX83 is an efficient transducer that provides reasonable power levels over wide range

of frequencies, and deep ocean capability. Its radiation pattern is omni-directional in the perpendicular plane to the ring axis, while the directivity in the other planes depends on the cylinder height, 5 cm (11.5 cm diameter). It presents a main resonance peak at 10 kHz and a secondary one at 380 kHz (Fig 3.5 d). The versatility in the frequency work range of this transducer allows designing a device able to carry out several acoustic-related tasks in an underwater neutrino telescope, this point will be extended in Chapter 4, section 4.2.

The experiment was carried out in the same Laboratory, confronting emitter and receiver transducers in a water tank (1.10 x 0.85 x 0.80 m³). The transducer was fed using a function generator PCI-5412 (National Instruments©) and a linear RF amplifier 1040L (55 dB, ENI©). To measure the acoustic waveforms a spherical omni-directional hydrophone ITC-1042 (International Transducer Corporation©) connected to a conditioning charge amplifier CCA 1000 (Teledyne RESON©) and a digitizer card PCI-5102 (National Instruments©) were used as receiver system. With this configuration the receiver presents an almost flat frequency response below 100 kHz with a sensitivity of about -180 dB, whereas it is 38 dB less sensitive than at 380 kHz. The election of the receiver system was motivated to be much more sensitive to the bipolar pulse (<100 kHz), generated parametrically, than to the primary beam (380 kHz). A three-axis micro-positioning system LF-5-DC (MICOS GmbH©) was used to move the receiver in three orthogonal directions with a nominal accuracy of 10 µm. All the signal generation and acquisition process was conducted by a National Instruments PCI-Technology controller NI8176, which also controls the micro-positioning system.

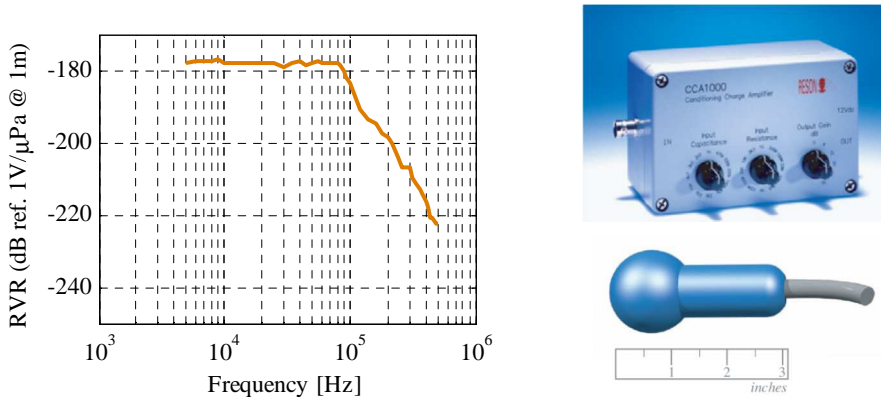


Fig 3.6. Left: Receiving voltage response (sensitivity) of the ITC-1042 + CCA1000 set using the measurement configuration (10 kHz, 10 nF, 20dB). Right top: CCA1000, bottom: ITC-1042.

3.2.2 Methods, Analysis and Results

With the aim to analyse the capability of controlling the shape of the parametric signal generated in the medium, measurements using different emitted signals were performed. Starting from the default bipolar signal given by the integral of a Gaussian function with a sigma of 5 μs , the envelope function $f(t-x/c)$ was calculated by integrating twice the expression. The shape of this signal was modified either using a different sigma (in the Gaussian function): 2.5, 5, 10 or 20 μs , or by separating the positive and negative parts of the bipolar pulse adding a constant amplitude cycles in the middle of the signal with lengths: 0, 5, 10, 20 or 50 μs . Fig 3.7 shows some of the signals used for emission.

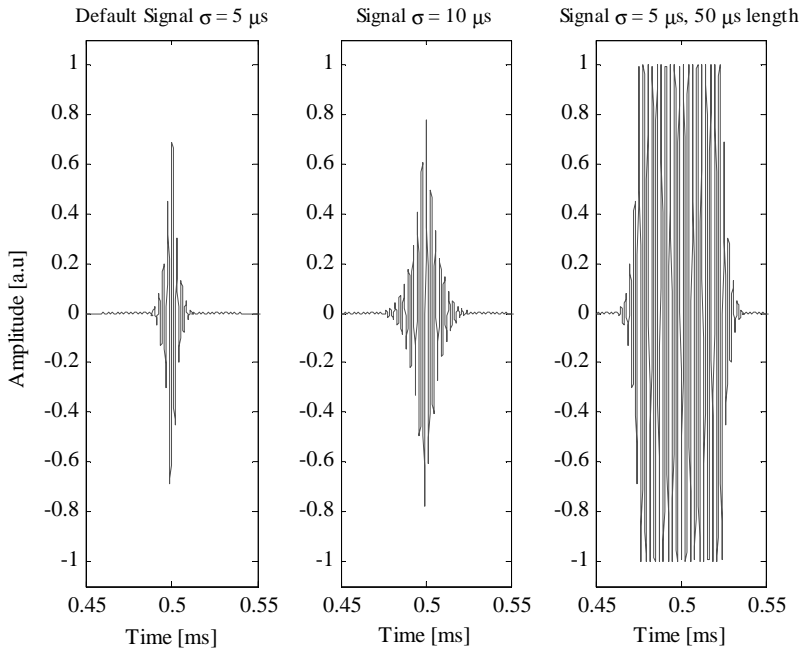


Fig 3.7. Examples of different signals used for emission to study the shape dependences of the secondary parametric bipolar pulse. Left: the default signal with $5 \mu\text{s}$ sigma. Centre: signal with $10 \mu\text{s}$ sigma. Right: signal with $5 \mu\text{s}$ sigma and with $50 \mu\text{s}$ length of constant amplitude in the middle.

The received signals were, in general, a mix of the primary beam at 380 kHz (main component) and the secondary signal produced by parametric effect. In order to distinguish these components, a band pass filter ([250 - 450] kHz) was applied for the primary beam, whereas a band pass ([5 - 100] kHz) filter was used for the secondary parametric beam. Fig 3.8 shows some examples of received signals, primary and secondary beams. An interesting parameter for this study is the time separation between the maximum and minimum of the signals, δt . As expected, δt increases with the sigma used, from 7-8 μs (for 2.5 and 5.0 μs sigma) to 10-11 μs (for 10 and 20 μs sigma). With respect to the constant amplitude added in the middle of the signal, for small lengths it results in a moderate increase of δt , but no clear separation between positive and negative parts is observed. However if the length is

very large ($50 \mu\text{s}$), this separation is clearly observed, as shown in Fig 3.8 (right). Therefore, from this study can be concluded that the shape of the parametric signal is, approximately, the second time derivate of the primary signal envelope, so there are some different possibilities to control the parametric signal generated.

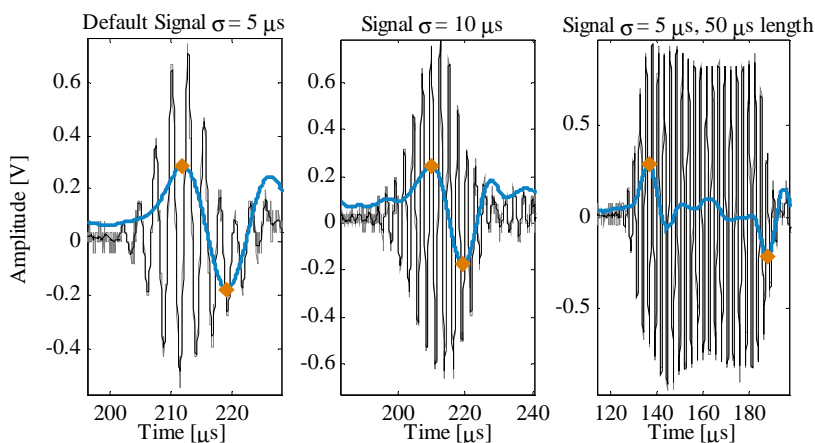


Fig 3.8. Received signals (gray), primary beam (black) and parametric secondary beam, i.e. bipolar signal (blue) for the emitted signals shown in Fig 3.7. Bipolar signal (blue) has been multiplied by a factor of three for a better visual comparison. The maximum and minimum of the bipolar signal used to calculate δt and δV are highlighted (orange). Notice that for the last signal, the constant amplitude between the rise and fall of the primary beam results in a separation of the positive and negative parts of the bipolar pulse.

As in previous section using planar transducers, the parametric generation in function of the emitted amplitude has been studied comparing the amplitude (peak-to-peak, δV) of the primary and secondary beams. From theory, a linear relationship for the primary beam and a nonlinear behaviour of the secondary beam (proportional to the square of the amplitude of the input signal) is expected. Fig 3.9 (left) shows the results of this study using the default signal, that is, the short signal with $5 \mu\text{s}$ sigma. Fitting the data to potential functions shown that the exponent for the secondary beam is twice the exponent of the primary beam, which agrees with theory. However, the exponent for the primary beam is slightly below one. The reason for this deviation is probably due to saturation effects in the transducer part.

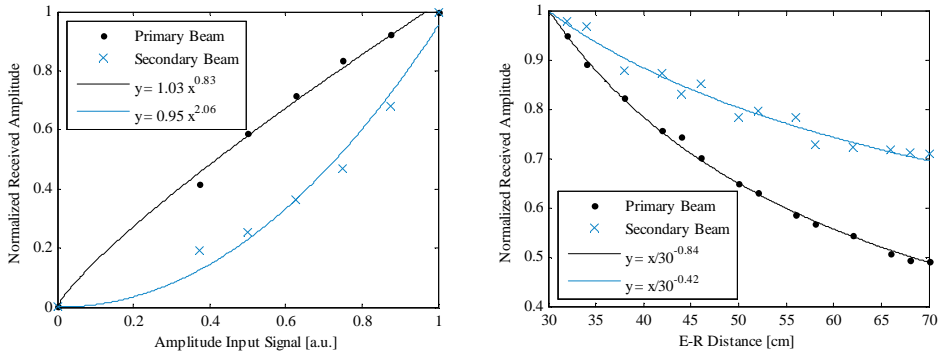


Fig 3.9. Left: Normalized amplitude of the received primary beam and the secondary (bipolar) signal as function of the input amplitude to fed the transducer. Right: Amplitude dependence with the distance of the primary and secondary (parametric) beams. The results of the data fits are also shown in both plots.

The dependence of the parametric signal with the distance from the transducer has been studied evaluating the decreasing amplitude of the primary and secondary beams in function of the distance (at 0 degrees, that is, aligned emitter and receiver). Results of this study using the default signal can be observed in Fig 3.9 (right). Potential functions have been fitted to the data with good agreement. For the primary beam, it is expected an exponent of -1 for an omni-directional (spherical) transducer, and -0.5 for an ideal non-diverging cylindrical transducer. Since the FFR SX83 transducer is cylindrical, but it is clearly diverging, the value of -0.84 seems reasonable. For the secondary beam it was expected a significantly smaller exponent since parametric generation is being produced in the medium, at least for small distances. At distances of about 1 m, the amplitude of the bipolar pulse is two orders of magnitude lower than the amplitude of the primary beam. However, considering the attenuation and the higher absorption at high frequency, at distances larger than a few hundred meters the bipolar pulse will be dominant. Therefore, for the application in underwater neutrino telescopes, it can be considered a ‘clean’ technique.

As it has already been highlighted in previous sections, the main advantage of using the parametric technique is the possibility of having broadband low-frequency

directive beams, which is an essential aspect to have bipolar signals with ‘pancake’ directivity. To finalize these tests the directivities obtained for primary and secondary beams have been compared. The results using the default signal are shown in Fig 3.10. It can be observed that, despite the differences in the spectral content, both, primary and secondary beams have similar directivity patterns.

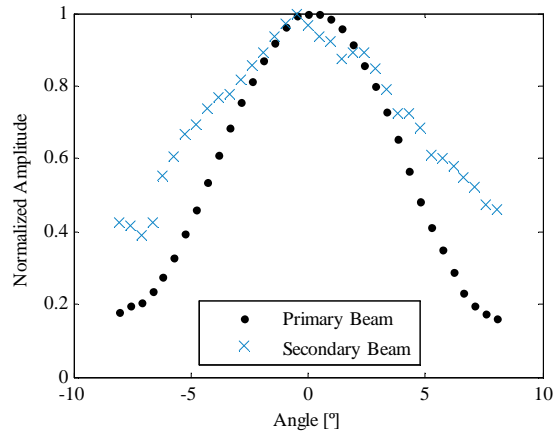


Fig 3.10. Directivity pattern of the primary beam and the secondary beam measured in the water tank at 60 cm distance between emitter and receiver.

The laboratory tests performed to understand the control of the bipolar shape (secondary parametric beam), the studies about amplitude dependence of secondary beam with the voltage applied to feed the transducer, also its dependence with the distance to the emitter, as well as, the measurement of the directivity pattern show that the acoustic parametric sources technique is a promising tool that could be used to generate neutrino like signals with good directivity using a cylindrical transducer (or a compact array with a few of them).

To verify the previous studies over longer distances, a new study using the same emission-reception systems but now submerged in a larger pool ($6.3 \times 3.6 \times 1.5 \text{ m}^3$) was performed in order to obtain the dependence of the pressure level as a function of the distance. It was also compared the directivity patterns with 2.3 m distance between emitter and receiver. Fig 3.11 summarizes the results of these studies. On

the left (distance dependence amplitude plot) a different behavior is observed between both, being a clear evidence of the generation of the secondary bipolar pulse by the parametric acoustic effect. Again, despite the differences in the spectral content, both, primary and secondary beams present similar directivity patterns.

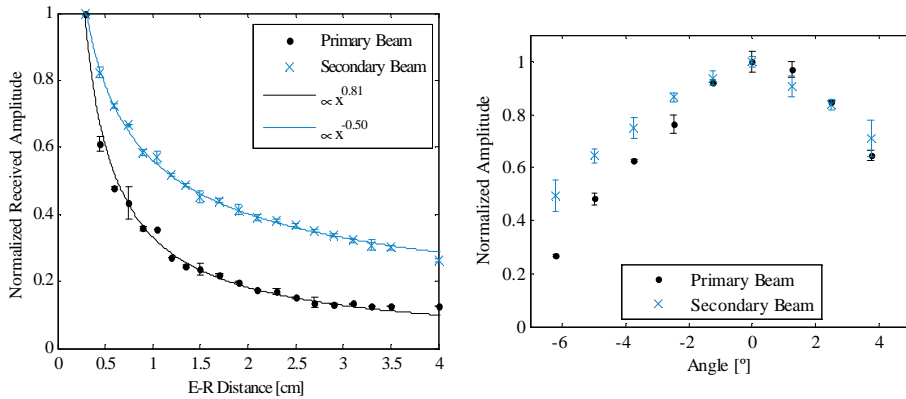


Fig 3.11. Amplitude of the primary and secondary signals as a function of the distance and directivity pattern for both beams. Normalization values (a) Primary beam: 166 kPa, Secondary beam: 200 Pa; (b) Primary beam: 27 kPa, Secondary beam: 80 Pa.

Finally, to estimate the effect of the propagation on the bipolar parametric signal, the received signals of the experimental measurements, performed using single cylindrical transducer in the pool, have been extrapolated to longer distances (on the km range). For this purpose, an algorithm that works in the frequency domain and propagates each spectral component considering the geometric spread of the pressure beams as $1/r$ and its absorption coefficient (S. Bevan et al., 2009; Francois & Garrison, 1982b) has been developed (Fig 3.12). The propagation code starts from the registered signal (Rx) (by the receiver ITC-1042+CCA-100) in time domain. From the received signal in frequency domain, and knowing the receiver sensitivity, the pressure amplitude of each spectral component is obtained and also the pressure amplitude at 1 m from the source. From there, each spectral component is propagated considering its absorption coefficient in the propagation medium. For this study, the

propagation was simulated for the sea conditions in the ANTARES site, Table 3.1 and Fig 3.13 contains the values of the different parameters used for the propagation simulation.

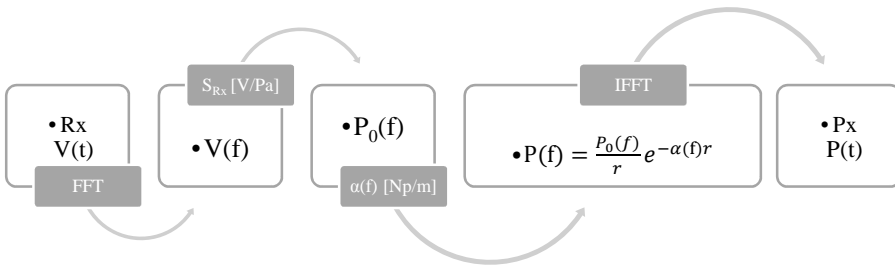


Fig 3.12. Schematic view of the propagation algorithm

Fig 3.14 shows the results of propagating the received signal (registered at 2.3 m distance E-R) over the propagation axis of the emitter. In this plot, no filter has been applied, the propagation medium acts as a natural filter. High frequencies of the primary beam are absorbed and, at km range, only low frequencies remain. From the theoretical propagation can be extracted that for a single element, it is expected to have a bipolar pulse with a 40 mPa amplitude peak-to-peak at 1 km, approximately.

Sea conditions ANTARES site

Depth (m)	2200
Sound Speed (m/s)	1541.7
Salinity (‰)	38.5
Temperature(°C)	13.2
pH	8.15

Table 3.1. Sea conditions in the ANTARES site used for the signal propagation.

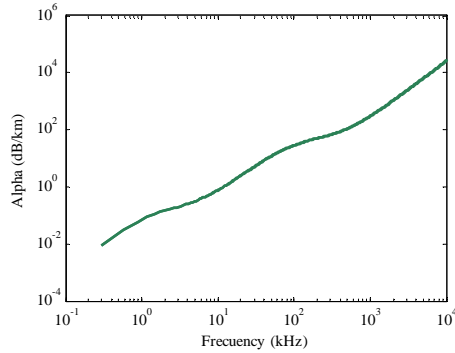


Fig 3.13. Sound absorption coefficient in the ANTARES site.

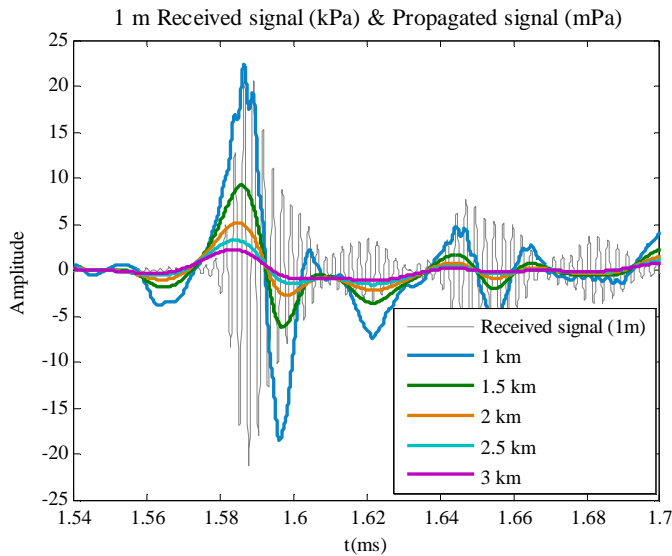


Fig 3.14. Signal obtained by the propagation of the received signal to distances beyond 1 km. Notice that received and propagated signal are shown in different units.

A possible drawback of the system is that the parametric generation is not very efficient energetically, but since bipolar acoustic pulses from UHE-neutrino interactions are weak, they can be afforded having reasonable power levels of

primary beams. Considering an array configuration, with three elements fed in phase, it is expected to have 0.13 Pa amplitude peak-to-peak, which is a good pressure reference for neutrino interaction calibration of the 10^{20} eV energy range (S. Bevan et al., 2009). Therefore, with the goal of reproducing the ‘pancake’ directivity, to cover long distances and improving the signal level of the non-linear beam generated in the medium, a three elements array configuration has been proposed as possible solution.

3.3 Array Configuration Evaluation.

Once the single cylindrical transducer had been characterized for bipolar pulse generation using the parametric technique, all the required inputs, for designing an array able to generate neutrino-like signals with ‘pancake’ directivity (with an opening angle of about 1°), are available. It is intended to obtain a more energetic and directive bipolar pulse by the interaction, at long distances, of the parametric beam generated for each element of the array. Fig 3.15 shows an example of the results for calculations performed by summing the contributions of different sensors for far distances at different angles. In this example, a linear array of 3 elements with 20 cm separation from each other could be enough to obtain an opening angle of about 1° .

Finally, to prioritize the handling by a compact design, an array composed by 3 FFR-SX83 transducers with a distance between centers of 7.5 cm, having the active part of the array a total height of about 20 cm, was proposed and tested. The three elements are maintained in a linear array configuration by using three bars with mechanical holders as is shown in Fig 3.16. In a primary stage the bars can also help to hold the array and orientate it in the tests.

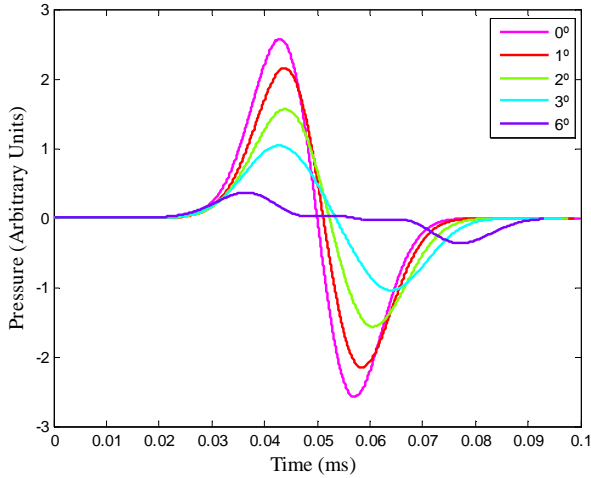


Fig 3.15. Pressure signal obtained at different angles for a three-element array.

Measurements for the array characterization were performed in an emitter-receiver configuration using a pool of 6.3 m length, 3.6 m width and 1.5 m depth. The emitter array, which was 70 cm depth, was fed using a function generator PCI-5412 (National Instruments©) and a linear RF amplifier 1040L (55 dB, ENI©). To measure the acoustic waveforms a spherical omni-directional hydrophone ITC-1042 (International Transducer Corporation©) connected to a conditioning charge amplifier CCA 1000 (Teledyne RESON©) and a digitizer card PCI-5102 (National Instruments©) were used as receiver system. With this configuration the receiver presents an almost flat frequency response below 100 kHz with a sensitivity of about -180 dB, whereas it is 38 dB less sensitive at 380 kHz. The larger sensitivity at lower frequencies is very helpful to better observe the secondary beam.

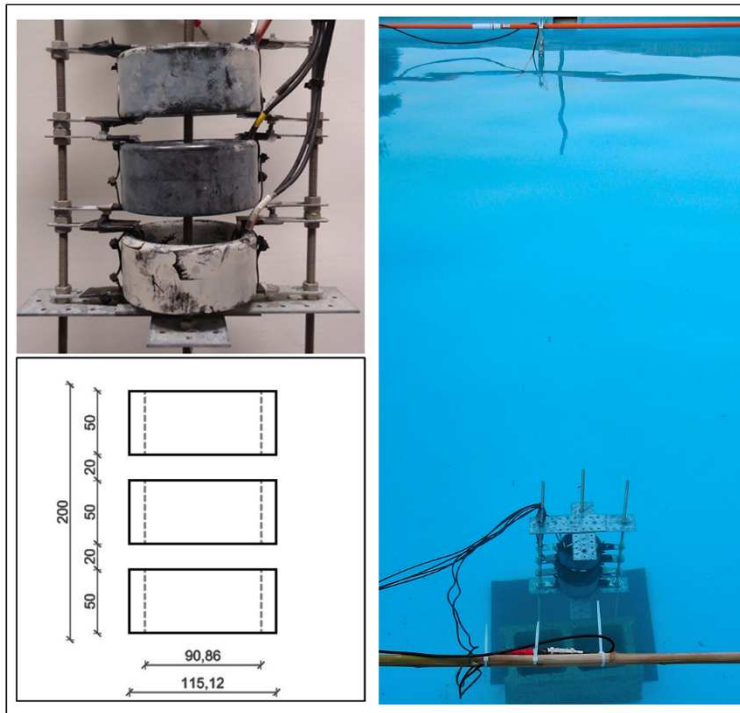


Fig 3.16. Photography of the array during the initial tests and geometric configuration of the array.

For these tests emitter and receiver were aligned and positioned manually with cm accuracy, which is enough for these purposes. The results obtained for the array tests are summarized in Fig 3.17. An example of a received signal (4.45 m) and the primary and secondary beams obtained after applying the bandpass filters (the secondary beam has been amplified by a factor of 3 for a better observation) are shown in Fig 3.17 Left. It is possible to see how the reproduction of the signal shape is achieved agreeing the results expected from theory and previous observations for a single element. The amplitude of the primary beam is less than in the single element test because the same linear RF amplifier 1040L (55 dB, ENI©) was used to feed the array of three elements, with the consequent power distribution and impedance change, resulting in lower feed tension for each transducer. Fig 3.17 Right shows the

directivity pattern measured at a longitudinal line defined by the array axis. The directivity measurements were performed with a 2.7 m separation between the array and the receiver. It is worth to mention that for the secondary beam the Full Width Half Maximum (FWHM) in the array configuration is about 7° ($\sigma=3^\circ$), for a single element the FWHM was about 14° ($\sigma=6^\circ$). Moreover, the pattern for the array should be a little more directive for far distances since the signals of the three elements will be better synchronized.

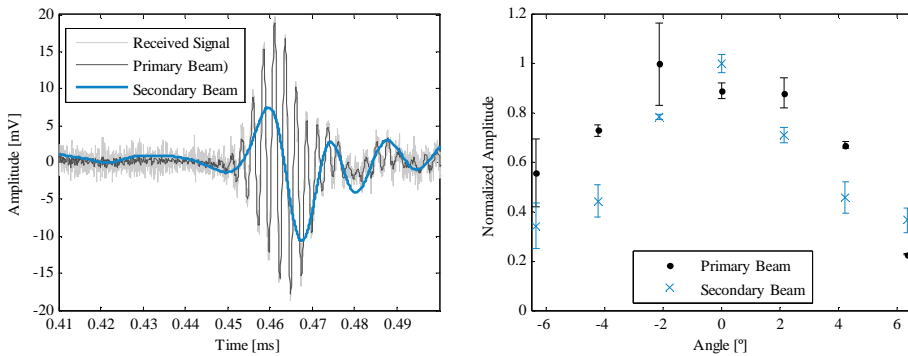


Fig 3.17. Left: Example of a received signal and the primary and secondary beams obtained after applying the band-pass filters (the secondary beam has been amplified by a factor 3 for a better observation). Right Directivity patterns of primary and secondary beam emitted with the array.

The same propagation exercise (Section 3.2.2) was carried out with the signals emitted with the array. Fig 3.18 shows the results of the propagation. It is possible to observe that, despite the primary beam is dominant at short distances, the secondary beam is larger for long distances due to the lower absorption.

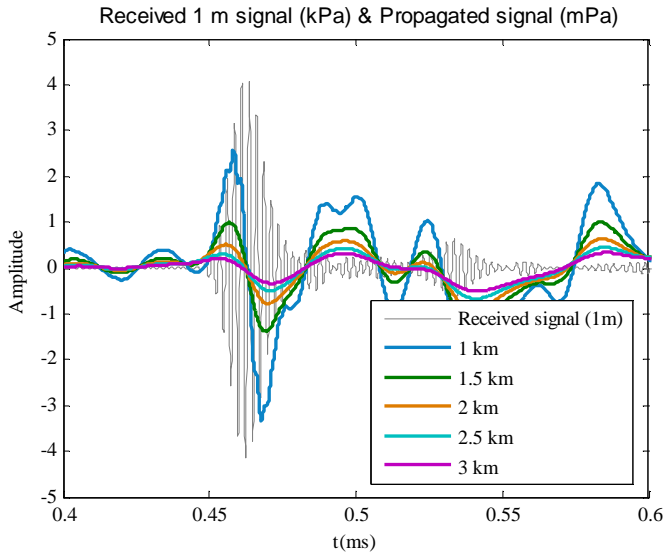


Fig 3.18. Signal obtained by the received signal (Fig 3.17a) propagation. Notice that the received and the propagated signal have different magnitude orders.

As previously indicated, the amplifier used is not very efficient to feed the three elements together due to a mismatch of electrical impedances and, therefore, each transducer provides a lower pressure beam. Thus, for the final array system, is it essential to work in parallel on electronics and have a dedicated amplifier for each transducer.

In the next chapter the work in the compact array design and its specific electronics for the feeding and operation will be detailed.

4

Prototype of the Versatile Compact Array

In this Chapter the design of the compact array calibrator prototype is presented. In the following sections the philosophy of the design, construction details and tests performed will be described. Finally, the status and some ideas for a possible second prototype will be argued.

4.1 Design philosophy

The aim of this work is the design of a compact transmitter for the calibration of acoustic neutrino detection arrays. The transmitter must be able to generate neutrino-like signals to check and train the feasibility of the UHE neutrino acoustic detection technique. As detailed previously, the use of parametric techniques presents good results to generate the bipolar directive pulse. The only drawback could be the low efficiency of the technique, but since bipolar acoustic pulses from UHE-neutrino interactions are weak, they can be emulated with reasonable power levels of the primary beams. For this first prototype, the detection threshold (20 mPa_p) of the AMADEUS system has been adopted as amplitude pulse limit. The positive results of the tests performed with the cylindrical transducer FFR-SX83, the fact that it can

work in two frequency ranges (Section 4.2) and its great robustness to work at deep Sea were determinant to choose it for the prototype. In particular, to deal the amplitude and directivity requirements, a set of three FFR-SX83 was proposed. The array disposition enhances the parametric beam. At long distances, the result of the interaction of the three parametric pulses, will be a more directive and energetic one. Moreover, it should be a compact transmitter which facilitates its handling during a Sea campaign or, in a future, to be integrated in underwater telescopes.

In the following sections some aspects that need to be dealt and solved will be detailed. Starting with the mechanical design of the array, including the assembly of the transducers in array and the required anchors to handle it during a Sea campaign. Special attention require the anchors design and the Sea campaign strategy. Due to the high directivity of the bipolar pulse is crucial to be able to orientate the emitter to the receivers for having a successful Sea campaign. For this reason rotating anchor plus a location register system (Section 4.4.2) and a test strategy have been designed to handle the transmitter from a vessel. The developed register system helps to orientate the emitter to a known receivers location and also generates a log with the position of the emitter and the current time of each emission. All of this information is essential during the post-processing tasks.

The versatility of the transducers that compose the array plays an important role in the test strategy, being possible tagging the parametric emission of the bipolar pulse by the emission of non-directive signals after and before of the bipolar directive pulse, and also by emitting long directive parametric signals which are easier to detect.

Dedicated electronics (Section 4.4.1) to drive the array of acoustic sensors, able to generate and amplify the signals in both different frequency ranges, is being developed to have an optimized system. For parametric generation, due the low efficiency of the effect and the little impedance at high frequency, this is very challenging.

4.2 Transducer versatility

The characteristics and benefits presented by the FFR-SX83 to be selected for an array prototype are listed in the previous Chapter (section 3.2.1). In particular the cylindrical geometry of the transducer is sought so that the emissions are as close as possible to that produced by the hadronic shower. The versatility in the frequency range of the selected transducer (FFR-SX83) opens up the possibility to carry out different tasks with the same device. Although the primary application of this transmitter is to generate the acoustic signature of a neutrino, the possibility of working in two frequency ranges ($\sim 5\text{-}20$ kHz and ~ 400 kHz) allows the system to carry out several acoustic-related tasks in an underwater neutrino telescope: the aforementioned acoustic detection calibration, receivers calibration and emitters monitoring of an acoustic positioning system and even acting as transceiver for such a system. Certainly, this could reduce the overall costs of the necessary calibration systems and facilitates the deployment and operation in the deep sea.

Another benefit to work in the two operation modes is the possibility to tag the bipolar pulse emissions when the array is used as acoustic detection calibrator, this could be essential during a Sea Campaign. The detection of this weak directive signal, emitted from a boat, by the AMADEUS system several kilometres away is very challenging. For this reason, a measurement strategy has been developed taking into account the array versatility. A three step calibration (Fig 4.1) is foreseen, increasing progressively the difficulty. Firstly, a long broadband low frequency non directive signal (sweep signal for example) can be emitted. Since it is directly emitted (not by parametric generation) it could be of high amplitude. Moreover, as it is a low frequency signal, the attenuation will be small and it will be non-directive, so the orientation should be easy. In addition it has broadband, so processing techniques (as cross-correlation) could be applied. For all of this it should be quite easy to detect it. In a second step, a long parametric signal could be emitted. Incorporating the directivity challenge and dealing with higher frequencies, i.e., due to the low

efficiency of the parametric effect and as absorption consequence, lower amplitudes. In this second step and, despite the difficulties due to the amplitude of the received signal, it could be still taken the advantage of processing techniques. Finally, the parametric bipolar signal, that is transient and directive, could be emitted. The emission of the last one might be tagged, that is preceded and followed by signals of the previous modes. In this way it will be easier to look for the bipolar signal during the post processing, looking at the correlation peaks of the received signal and the known expected tag signals.

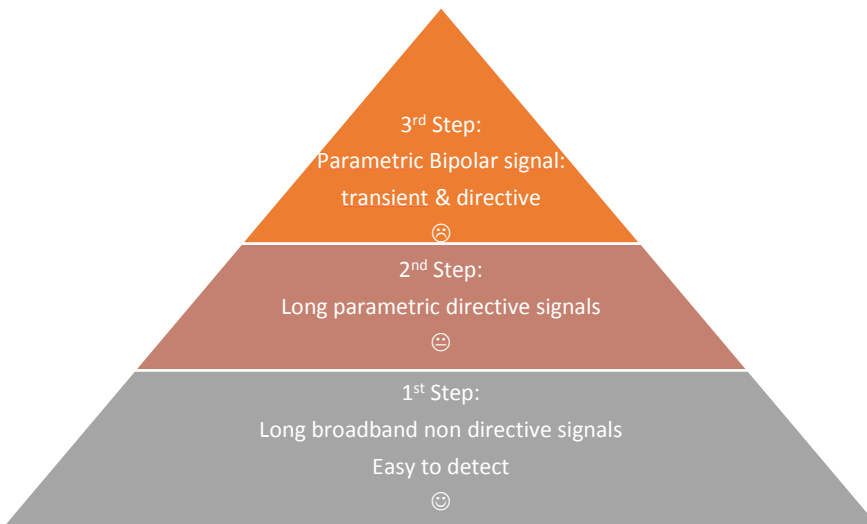


Fig 4.1. Diagram of the three step calibration strategy.

The transducer was tested using these long broadband signals. This kind of signals can be used in both modes of operation: generated directly at low frequency, or generated parametrically at 400 kHz. Fig 4.2 shows some tests with a parametric sweep (400 kHz signal modulated by a 10-50 kHz sweep signal). Using this signal it is possible to obtain a low frequency sweep signal from parametric generation, which is highly directive. On the left side of the figure, it is shown the emitted signal (top) and the expected parametric signal (signal to be used for the cross-correlation) (bottom). On the right, the received signal (top) and the signal obtained after

correlation (bottom) are shown. The main peak in the correlated signal indicates the time of detection. Knowing the sound velocity it is easy to determine the emitter-receiver distance (this will be the reference peak in positioning tasks), the remaining peaks are due to reflections on the pool walls and on the surface. The time for the different peaks agrees with the geometric dimensions of the setup. The measurements were made in a pool of 6.3 m length, 3.6 m width and 1.5 m depth. A FFR-SX83 transducer was used as emitter, and the receiving hydrophone used to measure the acoustic waveforms was a FFR-SX30 (Sensortech©). The distance between emitter and receiver was 4.3 m. The following DAQ system was employed for emission and reception. To drive the emission, a 14-bits arbitrary waveform generator PXI-5412 (National Instruments©) was utilized with a sampling frequency of 10 MHz. A linear RF amplifier (1040L, 400W, +55 dB, Electronics & Innovation Ltd. ©) was handled to amplify the emitted signal. For the reception, an 8-bit digitizer PXI-5102 (National Instruments©) was used with a sampling frequency of 20MHz.

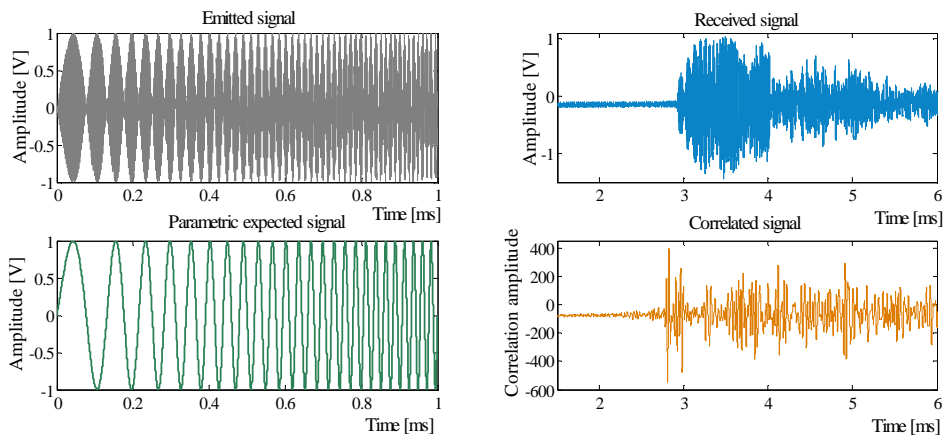


Fig 4.2. Emitted and received signal for the parametric sweep test. The correlated signal is the result of correlation between parametric expected signal and received signal.

Fig 4.3 shows the result of a comparative directivity study of the different signals used: Sweep signal from 5 kHz to 25 kHz (low frequency signal), parametric sweep

signal, i.e. 400 kHz signal modulated by a 10-50 kHz sweep signal (the low frequency directive signal is generated parametrically in the medium), and a bipolar pulse generated parametrically (transient and directive signal). Both parametric signals have a clear directive pattern whereas the direct sweep signal is non-directive since the transducer is not directive for low frequencies. The results must be taken with caution due to the geometric limitations of the tank, especially for the sweep case. For this case, since the receiver hydrophone is not a directive transducer and the tests were done using long emitted signals, the reflections on the bottom and on the water surface might affect the correlation results. The different behavior of parametric and non-parametric signals is evident, however. The possibility of having different kinds of signals will allow to perform different kind of calibrations and/or to do calibration in different steps.

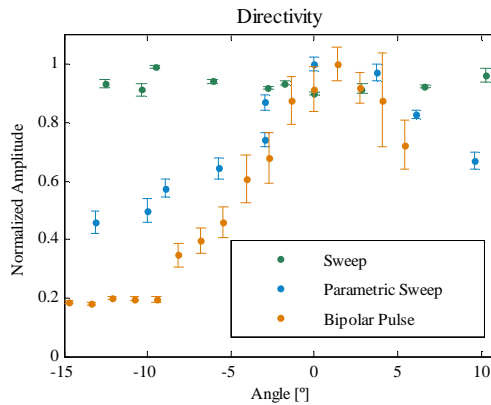


Fig 4.3. Directivity comparison of the three different kind of signals generated with the selected transducer. These signals are proposed for the different steps of the strategy for a Sea Campaign.

4.3 Mechanics

For the prototype, the transducers have been fixed around an axis using flexible polyurethane (EL110H, Robnor resins Limited©) as assembly material. This polyurethane offers water resistance and electrical insulation for high frequency and high voltage applications due to the nature of the cured polymer. EL110H also

provides excellent resistance to thermal and mechanical shock and may be used in applications to -55°C . Fig 4.4 shows the compact array prototype.

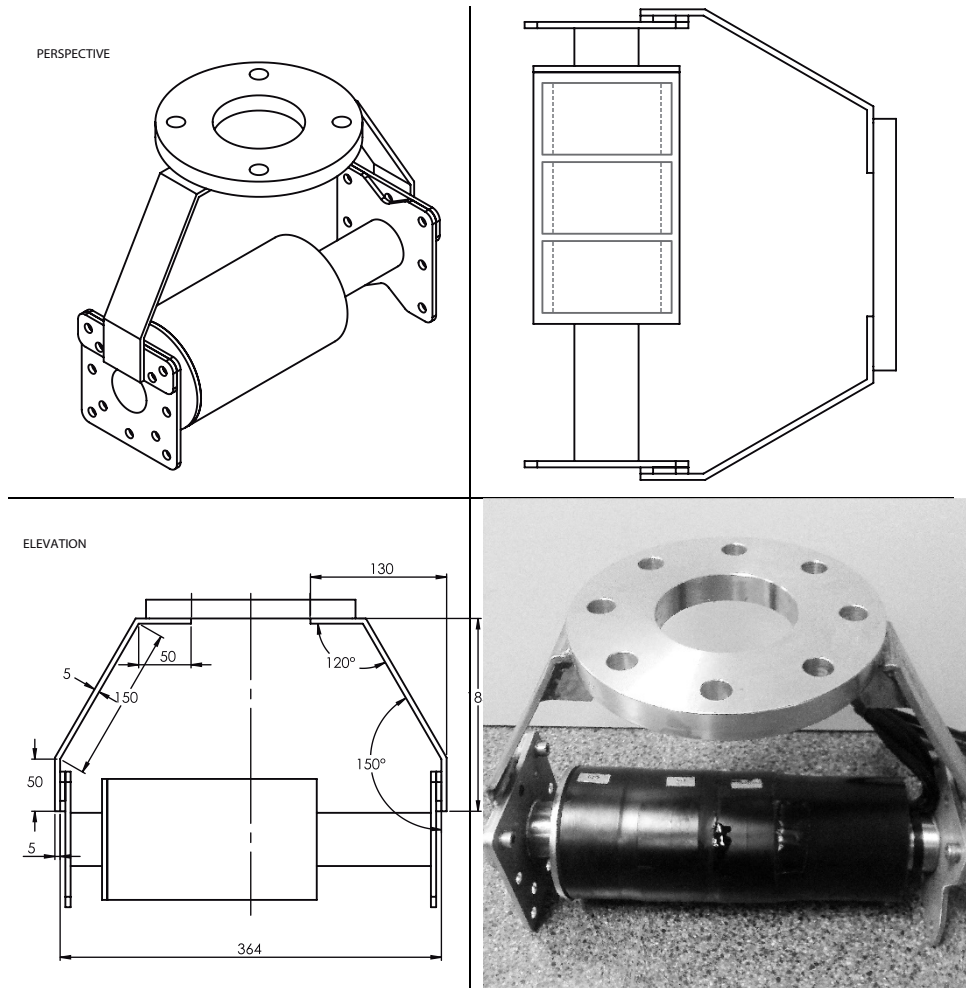


Fig 4.4. Constructional drawings and photo of the array with the holding system. Dimensions in mm.

Its compact design is remarkable, with an active surface length of about 20 cm. A holding system was designed with the aim to test the prototype in a Sea campaign, therefore, to be operated from a vessel. The perforated ring shown in Fig 4.4 (top-

left) is the piece that holds the array to a fastening structure which, in turn, acts as a rudder and allows to rotate the device around a perpendicular axis to the geometrical array axis. The last item is significant due to the high directivity of the bipolar pulse. It is very important to be able to orientate the emitter to the receivers. Fig 4.5 shown a simulated view of the array operated from a vessel and supported with the fastening structure.



Fig 4.5. Artistic view of the array operated from a boat during a Sea campaign calibration.

The designed fastening structure was built by Mediterraneo Señales Marítimas S.L and facilitates operating the device from a vessel besides offering control of the rotation angle. This structure is composed of two differentiated parts. On the one hand the head (Fig 4.6), that ensures the device to the boat and enables the management of

the rotation through its rudder. On the other hand the modular arm, that allows immerse the device up to 20 m deep. The mechanical arm is modular in steps of 3 m, so it is possible select the depth by adding more or less 3 m arms (6 in total) to the head of the structure.

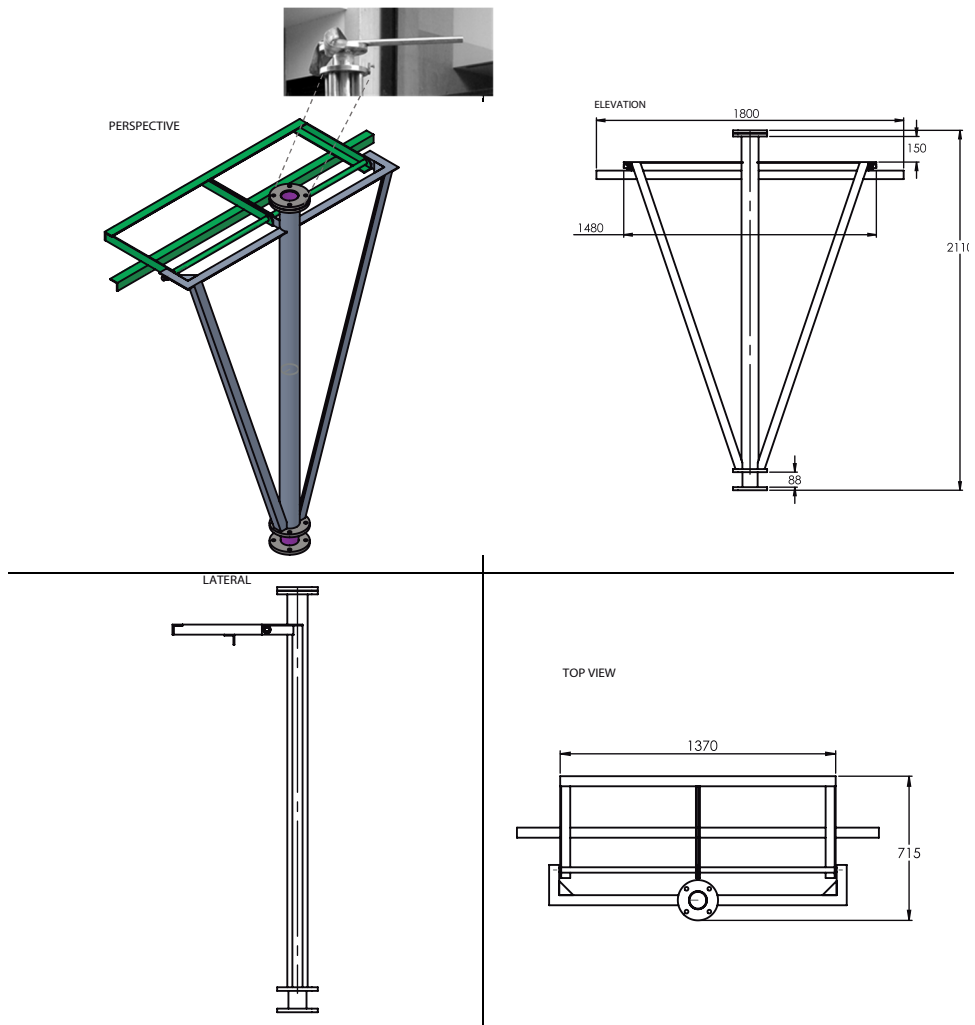


Fig 4.6. Constructional drawings of the head of the fastening structure. Real view of the rudder is shown in the perspective view. Dimensions in mm.

4.4 Electronics

4.4.1 Electronic Emission Board

The final goal in the development of the compact calibrator is building an autonomous and optimized system. For this reason, it was necessary to work on the associated electronics of the acoustic array able to generate and amplify the required signals in both frequency ranges. This topic is being developed as a part of a doctoral thesis (C. D. Llorens, In process).

In the initial stage of design process it was decided to follow the same philosophy carried out by the IGIC-UPV group in the electronics for the acoustic transceivers developed for positioning systems in underwater neutrino telescopes (Ardid et al., 2012; Larosa et al., 2013; C. D. Llorens et al., 2012). These transceivers are integrated, and have been positively tested, in the IL13 of ANTARES and in KM3NeT Italy detection tower (NEMO-Phase II) in Capo Passero, Sicily. The main, and novel, characteristic in the Electronic Emission Board (EEB) design is the use of the Pulse Width Modulation (PWM) technique (Barr, 2001). PWM is a modulation technique that generates variable-width pulses to represent the amplitude of the desired signal with the desired specifications.

Some of the advantages offered by this technique are:

- The system efficiency is improved respect to classical solutions due the use of class D amplification, this means that the transistors work in switching mode, suffering less power dissipation in terms of heat, and therefore offering a superior performance.
- Simplicity of design. Analog - Digital converters are not needed. It is possible to feed directly the amplifier with the digital signals modulated by the PWM technique.
- It is not necessary to install large heat sinks at amplifier transistors, reducing the weight and volume of the electronic system and, consequently, of the whole

calibrator. Analog systems, such as linear power supplies, tend to generate a lot of heat since they are basically variable resistors carrying a lot of current. Digital systems do not generally generate as much heat. Almost all the heat generated by a switching device is during the transition (which is done quickly).

- In waiting mode, the power amplifier has a minimum power at idle state that allows storing the energy for the next emission in the capacitor very fast and efficiently.

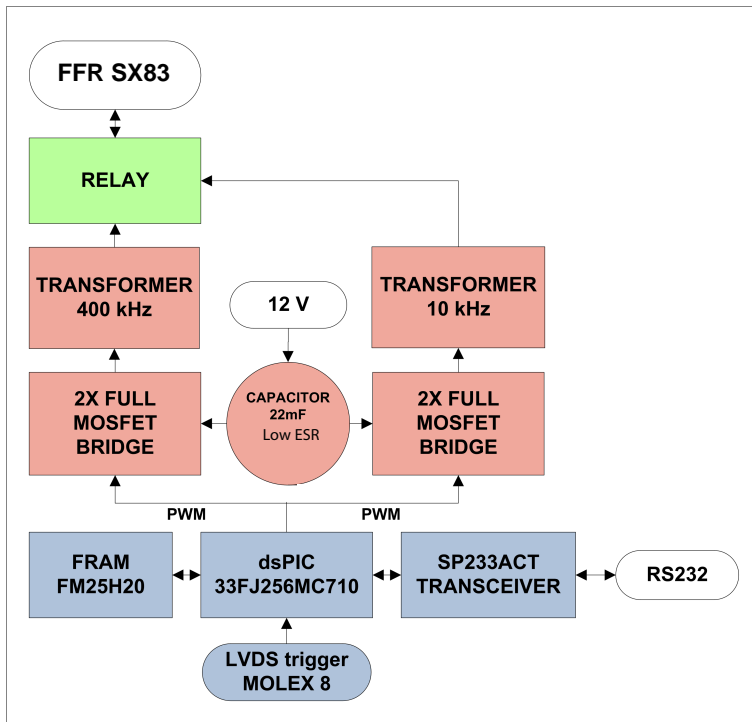


Fig 4.7. Conceptual block diagram of the EEB.

4.4.1.1 Basic block diagram

In Fig 4.7 the basic block diagram of the EEB is shown. The transducer is located at the top of the diagram. The relay block (green) allows the transducer connection to the low or to the high frequency amplifier, depending on the operation mode. The transducer is connected to the power amplifier through an impedance matching

network with a transformer. Limited power availability to feed the EEB has been assumed, in a similar way than in neutrino telescope infrastructures. Since 12 V_{DC} power is not enough to excite the transducer to cover long distances and for parametric emission, it has been necessary to implement an energy storage block (red). In the lower part of the block diagram the signal generator, which drives the power amplifier, is shown (blue). It has two inputs, one for the low bitrate communication port (RS232) and one for the trigger signal.

Capacitors are used to store the required transmission energy. This solution allows fast charging, consequently, short time delays between successive emissions (in calibration or positioning task the usual mode of operation is a high power emission of a few ms duration every few seconds). The solution also offers a long life expectancy.

The power amplifier solution adopted is a class D amplifier formed by a full bridge. One of the advantages to choose the full bridge power amplifier is that it must be fed with squared signals like a MLS (Maximum Length Sequence), which is a signal extensively used in electro-acoustic measurements. The main characteristic of this signal are the flat spectrum and the non-correlation with any other signal. For these peculiarities it is widely used to obtain the impulse response of an entire emitter-receiver system and for time of flight measurements used in positioning tasks. Moreover, if the desired signals to emit are the standard sinusoidal (or arbitrary) ones, it is possible emitting a square signal in the desired band and, due to the transducer and the transformer are good band pass filters, all higher frequencies that are out of the working band will be removed.

The best technique, to send arbitrary signals by generating squared signals, is using PWM with a modulation frequency outside of the main band. To implement PWM it should vary the width of the square signal in direct relation to the amplitude of the desired signal (0-100% Pulse width). The classic way to obtain the related square

signal is comparing the desired signal with a triangular or sawtooth signal (Fig 4.8). After the amplification, the desired signal is integrated (filtered by the transformer and the transducer) and the median value of the square signal is obtained. This median value is the desired signal.

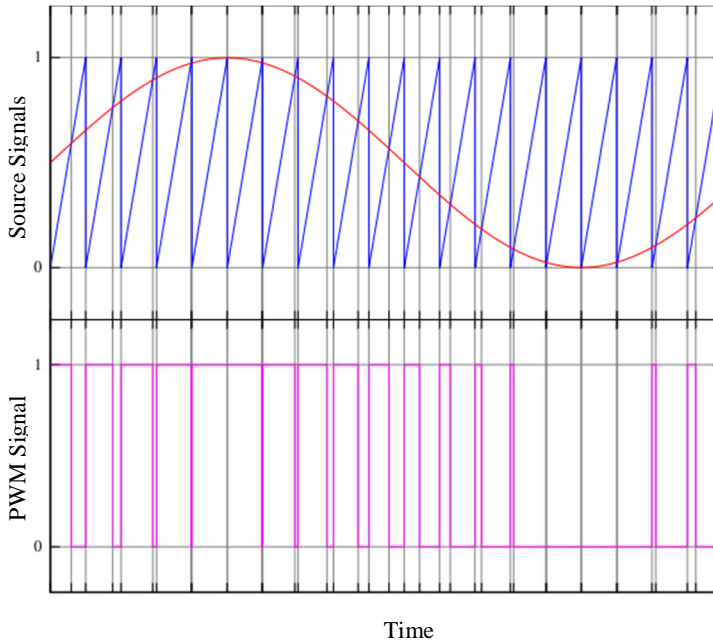


Fig 4.8. A simple method to generate the PWM pulse train corresponding to a given signal is the intersective PWM: the signal (here the red sinewave) is compared with a sawtooth waveform (blue). When the latter is less than the former, the PWM signal (magenta) is in high state (1). Otherwise it is in the low state (0).

For the signal generator it was decided to use a Microchip “Motor Control” function inside most of the DSPic microcontroller series. The “Motor Control” function is basically a digital counter that works with the main frequency of the microcontroller (40MHz). This device disposes of all necessary components to work with full MOSFET bridges (symmetric outputs, dead time generators, etc.), and for this reason matches perfectly for the purposes.

With the aim of test the feasibility of applying the PWM technique to emit the necessary signal for parametric bipolar pulse generation, a simulation of the electronic board has been done. Pulse width modulated theory, works with the envelope of the desired signal used to feed the transducer. This envelope is shown in Fig 4.9. After applying PWM modulation it is possible to obtain the square signal that parameterize the signal before feeding the amplifier (Fig 4.10). Finally, the result of the simulation shows the theoretical signal expected at the amplifier output (Fig 4.11).

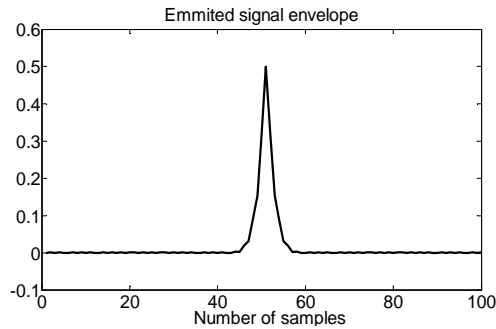


Fig 4.9. Envelope of the signal to be used for emission

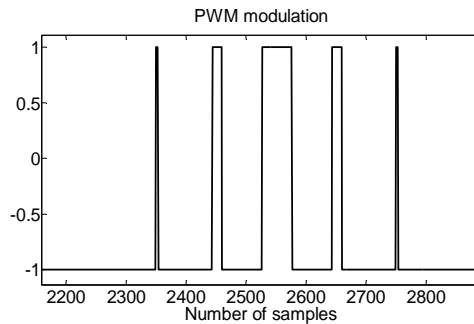


Fig 4.10. Square signal after applying PWM modulation.

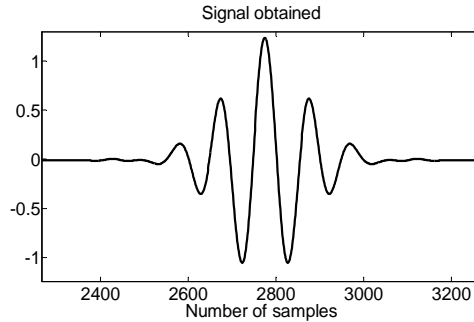


Fig 4.11. Expected signal at the amplifier output.

Seen the required emitted signals for the calibrator (Section 3.2.2) and the result obtained by the simulation of the electronic board design, PWM technique seems to be a good candidate in order to be implemented in the electronic board that will control the array. Moreover is endorsed by the in situ experience of other acoustic devices.

The proposed design a priori seemed to be the most suitable for the purposes of generating and amplifying the signals in both frequency ranges. Unfortunately, in practice, it was not trivial to amplify the high frequency signal to generate the parametric bipolar signal. Due to the very low impedance of the transducer in the high frequency range, the high requirements of current, voltage and frequency, some electronic components did not support more than a few emissions. This made very difficult building a robust and durable solution required for any device that pretends to be integrated into an infrastructure such as underwater neutrino telescope ANTARES. New designs are being developed and tested to drive the array for parametric generation (C. D. Llorens, In process). There are mainly two lines under study: the first one is based in the idea of applying a higher supply voltage in the class D amplifier and lower turns ratio in the transformer. The second one is based in the possibility of, in addition to the higher supply voltage in the class D amplifier,

replacing the transformer with a single inductor to adapt the impedance in a narrow band of frequencies.

4.4.2 Register System

As advanced in the Section 4.3, in order to facilitate the point to the receivers and to provide all related with the set of measurements info, a register system was developed. This register system monitors, for each emission, the time of emission, the emitted signal, location and orientation information of the array. All this information plays an important role during the post-processing tasks. Moreover, it is possible to manage and program the emissions through the register system.

The register system is composed by a smartphone with android© technology which is located in the array holding arm and a computer with wireless connection. Through an easy free APP called SensorUdp (Takashi SASAKI©) it is possible sending, by User Datagram Protocol (UDP), the positioning data of the smartphone to the pc (as long as both are connected to the same network).

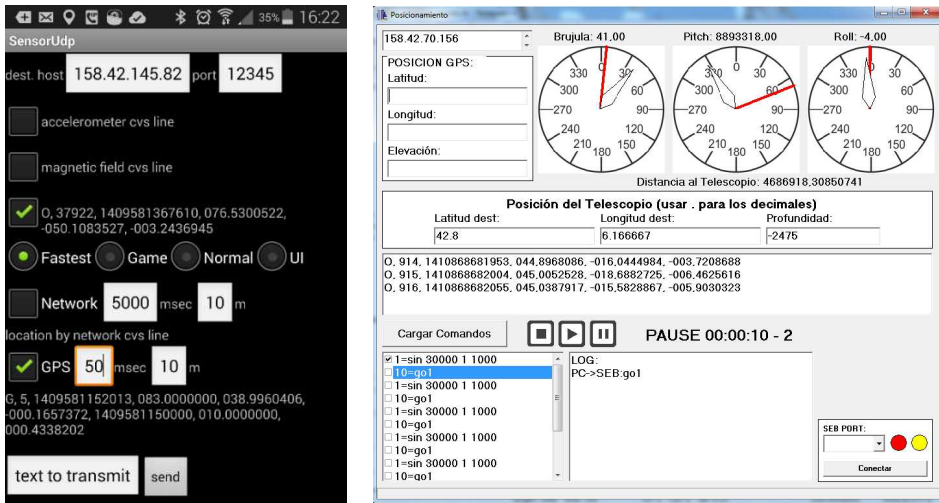


Fig 4.12. Screenshots of the APP and the register system.

An intuitive graphic interface has been designed to visualize, in real time the positioning data, and to manage the emissions of the array (Fig 4.12 right). Moreover the interface includes, in a graphical way, the compass, pitch and roll info. The red marks help to orientate the array to the selected point (where the receivers would be located) knowing its GPS coordinates. On the bottom of the graphic interface there is the management of the EEB. The MODBUS commands are loaded from a text file on the left, to generate the desired signals. The log of the emissions and the port and status connection with the EEB are in the middle and right windows respectively.

A register report is generated automatically for each emission with the time of emission, the direction of the emission: PC-EEB (sending the MODBUS commands to generate signals) or EEB-PC (with the location info), command sent, location info about the array position (longitude, elevation, compass, pitch and roll). In the next table an example of a register report is shown.

TIME	DIRECT	COMMAND	LAT	LONG	ELEVATION	COMPASS	PITCH	ROLL
16:30:02.76	EEB->PC	EMITTED	0.000000	0.000000	0.000	0.000000	0.000	0.000
16:57:07.24	PC->EEB	sin 10000 0.6 2000	38.994.415	-0.158742	5.000	197.999.985	-7.000	0.000
16:57:09.75	EEB->PC	Gen:s sin 100 0.6 2000	38.994.415	-0.158742	5.000	186.627.808	-2.000	-4.000
16:57:09.95	EEB->PC	OK	38.994.415	-0.158742	5.000	185.515.366	-3.000	-4.000
17:02:21.91	PC->EEB	sin 10000 0.6 2000	38.994.415	-0.158742	5.000	77.150.116	-3.000	-4.000
17:02:23.94	PC->EEB	go1	38.994.415	-0.158742	5.000	77.150.116	-3.000	-4.000
17:02:24.46	EEB->PC	Gen:s sin 10000 0.6 2000	38.994.415	-0.158742	5.000	77.150.116	-3.000	-4.000
17:02:24.66	EEB->PC	OK	38.994.415	-0.158742	5.000	77.150.116	-3.000	-4.000
17:02:25.26	EEB->PC	OK-ready	38.994.415	-0.158742	5.000	77.150.116	-3.000	-4.000
17:02:25.71	EEB->PC	EMITTED	38.994.415	-0.158742	5.000	77.150.116	-3.000	-4.000
17:02:25.97	PC->EEB	go1	38.994.415	-0.158742	5.000	77.150.116	-3.000	-4.000
17:02:26.698	EEB->PC	OK-ready	38.994.415	-0.158742	5.000	77.150.116	-3.000	-4.000

Table 4. 1. Register report example

4.5 Tests with the Array

After the array assembly some test were performed to characterize it. Studies of impedance, transmitting voltage response, radiation patterns, etc. were done to know the behaviour of the new configuration, also using the EEB. Moreover, as the transmitter is able to work in different frequency ranges, it was tested for low frequency emission, evaluating the possibility of being used to carry out several tasks related to acoustics in underwater neutrino telescopes, in addition to emission of neutrino-like signals: calibration of sensor sensitivities and responses, emission of signals for positioning, etc.

4.5.1 Array characterization.

Transmitting voltage response (TVR) has been measured in both frequency ranges at 400 kHz it is about 164 dB (ref $\mu\text{Pa/V}$ at 1m). For the low frequency range the TRV of one element has been compared with the response of the array (three elements connected in parallel). The results are presented in Fig 4.13.

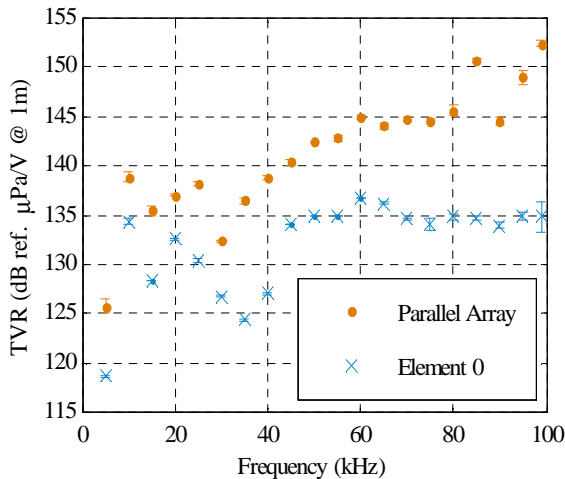


Fig 4.13. Transmitting voltage response of the array connected in parallel and for the central element for the low frequency range.

4.5.2 Low frequency tests

Besides the studies of acoustic parametric generation, some tests have been made to select signals to carry out all the acoustic tasks (See Section 4.2) and also, a signal detection method based on cross-correlation technique (Barr, 2001) has been evaluated in order to obtain, in an accurate way, the Time of Arrival (ToA) and the amplitude of the acoustic received signal (Adrián-Martínez et al., 2015). This detection method facilitates to have a good signal to noise ratio so allows improving the accuracy in the ToA determination in noisy environments or low signal level conditions. Typically, for positioning tasks pure sinusoidal signals are used. Usually, a band-pass frequency filter is applied, and the detection time is determined by reaching a threshold level (Adrián-Martínez et al., 2012). Doing this properly requires a very accurate calibration in order to determine the inertial delay of the hydrophone, and even so, it can give bad results in case of high noise or intense reflections nearby that can add to the waves constructively. In contrast, the cross-correlation of broadband signals is less sensitive to these effects. The inertial delay, which affects mainly to the start and end of the signal, is rendered less important by considering the whole duration of the signal. The effect of the reflections is reduced by distinguishing between different peaks of the cross-correlated signal, the first main peak being the one to consider. In cross-correlation techniques the use of signals with wide band frequency signals or non-correlated signals such as sine sweep or Maximum Length Sequence (MLS) signals, instead of pure sinusoidal signals may result in an improvement of the signal-to-noise ratio, and therefore resulting in an increase in the detection efficiency, as well as in the accuracy of the time of detection.

The Correlation between two signals x and y with the same N samples length is described by the following expression:

$$\text{Corr}\{x, y\}[n] = \sum_{m=1}^N x[m] \cdot y[m+n] \quad (4.1)$$

It is worth to note that, in the autocorrelation of one signal with itself, the correlation peak amplitude ($V_{max,corr}$) is equal to the half of samples of the signal in question (N). Therefore, it can be obtained the peak voltage of the signal (V_p) by Eq (4.2):

$$V_p = \frac{2V_{max,corr}}{N} \quad (4.2)$$

Furthermore, this ratio does not vary with the amplitude of the signal and is less susceptible to the presence of noise. In real applications, it is not trivial to tackle the problem because is completely crucial windowing temporarily the direct signal avoiding reflections to obtain a reliable value of its amplitude, which is not always possible.

Then, it would be important to obtain the corresponding relation between the maximum of the cross-correlation between received and emitted signal with the amplitude of the received signal avoiding reflections. This issue has been studied (Adrián-Martínez et al., 2015) and has been found that knowing the amplitude of the sent signal ($V_{p,env}$), its number of samples (n_{env}) and the maximum correlation value ($V_{max,corr}$), corresponding to the detection of this signal, it is possible to obtain the peak-amplitude voltage of the received signal applying the following expression:

$$V_{p,rec} = \frac{V_{max,corr}}{V_{p,env}} \frac{2}{n_{env}} \quad (4.3)$$

Obtaining this amplitude information could be very useful for *in situ* calibration of receivers and monitoring emitters of an acoustic positioning system.

4.5.2.1 Laboratory tests

The low frequency tests were done in a progressive way, starting in a controlled environment using a pool and finalizing taking measurements in Gandia's Harbour. For the first test, a set of measurements were made in a pool of 6.3 m length, 3.6 m width and 1.5 m depth. The compact array was used as emitter, EEB was used to

generate and amplify the different emitted signals. The receiver hydrophone used to record the acoustic waveforms was a FFR-SX30 (Sensortech©) with a NI PXI 5102 (8 bits, 20MS/s, National Instruments©) as a digitizer system.



Fig 4.14. Experimental setup (left), emitter (middle) and receiver (right) transducers.

In this study the results obtained using pure tones and broadband signals (sweep and MLS) to obtain the emitter-receiver distance have been compared.

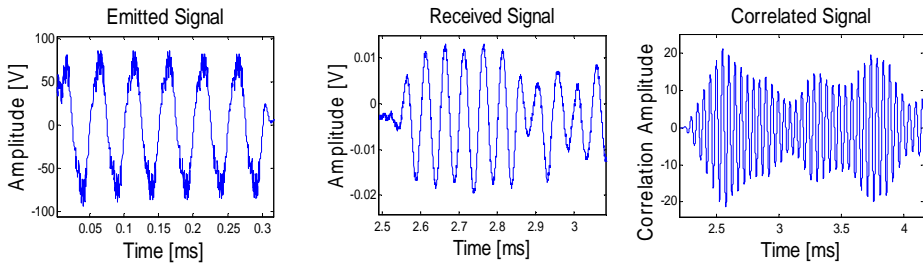


Fig 4.15. Pure tone emitted: 20 kHz, 0.3 ms duration signal (left). Received signal (middle).Emitted-received signal correlation (right).

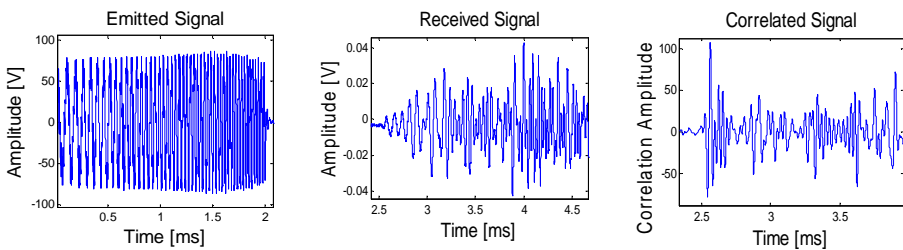


Fig 4.16. Sine sweep emitted: 10 kHz – 40 kHz, 2 ms duration (left). Received signal (middle).Emitted-received signal correlation (right).

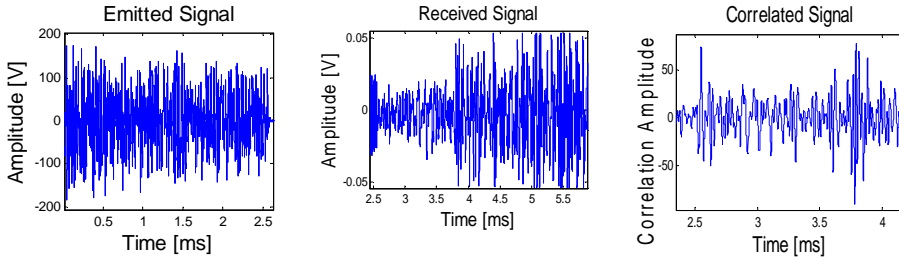


Fig 4.17. MLS emitted: 2.5 ms duration (left). Received signal (middle). Emitted-received signal correlation (right).

The plots of Fig 4.18 show the results obtained by comparing the voltages (left) and the S/N ratios (right) both in cross-correlation method and time-domain method.

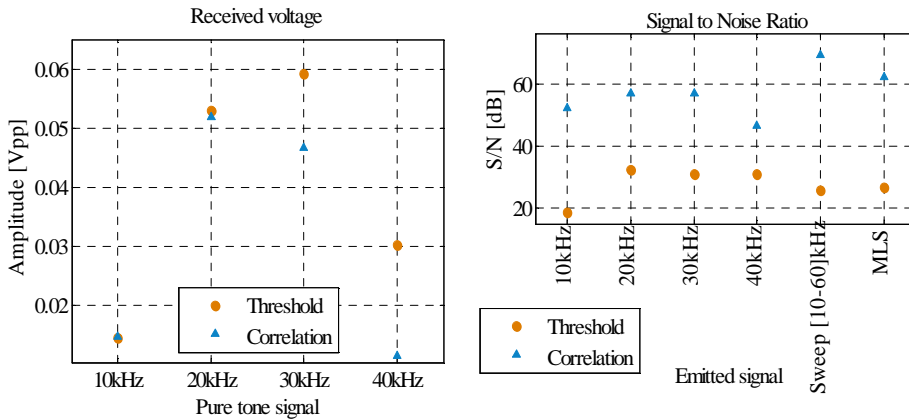


Fig 4.18. Left: Comparison of the received amplitude in time domain and using the cross-correlation method. Right: Comparison of the S/N ratio.

Looking at the waveforms can be concluded that sine of 40 kHz was clearly affected by a reflection. One of the reasons for the relatively large variation in the 30 kHz and 40 kHz measurements might be the interference between the three emitters of the array, which depends on the frequency. The use of broadband signals with the cross-correlation method may help to mitigate this problem since it will average the response of the different frequencies. Excepting these cases, as before, using the Equation (4.3) very similar results to the usual techniques are obtained. On the other hand, the S/N ratio increases considerably (at least 20 dB) for the set of signals used

using correlation method, in this case the main correlation peak has been compared to the noise level of the correlated signal. This improvement is crucial for a correct detection of the signals, especially in noisy environments or weak signals.

In order to know the reach of the device in low frequency range, the received signals have been extrapolated up to 3 km using the propagation algorithm (Section 3.2.2) Fig 4.19 shows the evolution of the amplitude during the propagation for the different studied signals. It shown that, excepting 40 kHz sine signal, all signals *a priori* could be detected up to 3 km distance of the AMADEUS receivers which have an amplitude threshold of about 20 mPa_p for this frequency range. The 40 kHz sine signal could be detected up to 2.5 km.

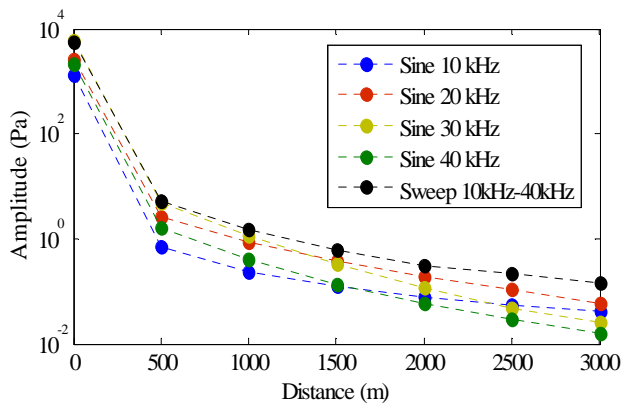


Fig 4.19. Evolution of the amplitude of the different received signals during propagation up to 3 km.

Signals could be masked by background noise. To study its effect, environmental background noise background, *in situ* measured, has been added to the propagated signals in order to know if these signals could be detected during a Sea Campaign. As receiver has been used the HTI-08 receptor located in the second floor of the IL13 in the AMADEUS system. The background noise added was registered by HTI-08 during its operation. Fig 4.20 shows the sensitivity of the HTI-08 and an example of background noise registered in the ANTARES site.

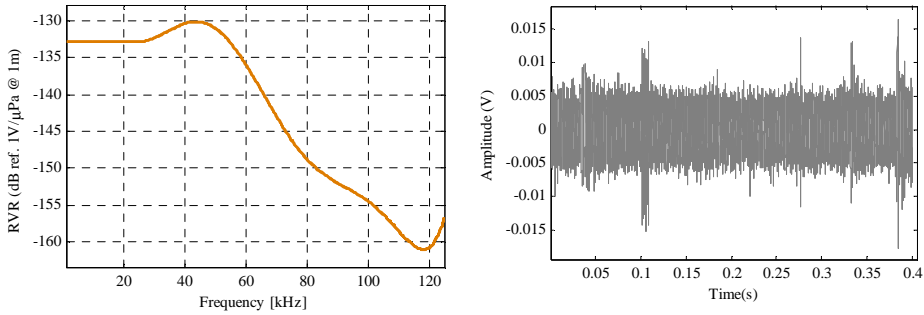


Fig 4.20. Left: HTI-08 Receiving Voltage Response. Right: Example of background registered by the same receiver.

The propagated signals have been added to different noise registers in different (up to 100) positions inside the same noise file. The objective of this work was, on one hand, to determine a possible deviation of the correlation method in the determination of the time of arrival. The results show that this is a robust method. No deviations were obtained in almost all cases. On the other hand, it was studied the signal to noise ratio of the received signals in order to compare it with their equivalent using the correlated signals.

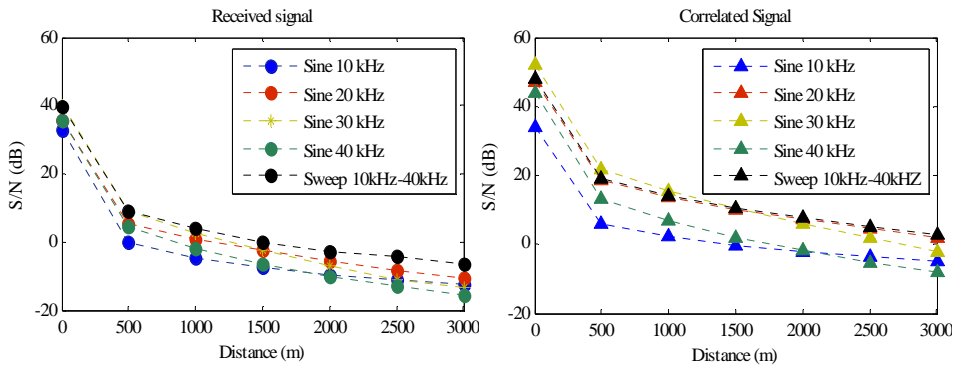


Fig 4.21. Signal to noise ratio of the received signals in time domain (left) and signal to noise ratio of the received signal after correlation (right).

Fig 4.21 shows the results for both cases, it can be seen that using the correlated signal the signal to noise ratio increases up to 10 dB in 20 kHz, 30 kHz sine signals and

sweep signal. This improvement achieved by the use of correlation techniques could be crucial for signal detection in noisy environments or low signal level conditions

4.5.2.2 *Field tests*

The more complex environment in which this study has been performed is the Gandias's Harbour. In this case, the distance between emitter and receiver was about 110 m and the S/N ratio was quite low. Fig 4.22 shows the location of the experimental setup. As emitter the array with its elements connected in parallel was used and by the dedicated electronics for low frequency mode it was fed. The receiver hydrophone used to record the acoustic signals was a FFR-SX30 (Sensortech©) connected to a conditioning charge amplifier CCA 1000 (Teledyne RESON©) and with a NI PXI 5102 (8 bits, 20MS/s, National Instruments©) as a digitizer system. In order to synchronize the emission with the reception a wireless trigger was used. For the Time of Arrival the delay introduced for the wireless trigger, which is of 8.23 ms, was considered. Pure tones and broadband signals (sweep and MLS) were evaluated using correlation technique.

Due to the activity of the harbour, the registered signals were totally masked by noise. Fig 4.23 shows an example of a waveform registered when a tone of 30 kHz and 4 ms duration was emitted. In Fig 4.23 (right) the result of the correlation between the emitted and the received signal is shown. It is remarkable the improvement in the signal to noise ratio using the correlation method.

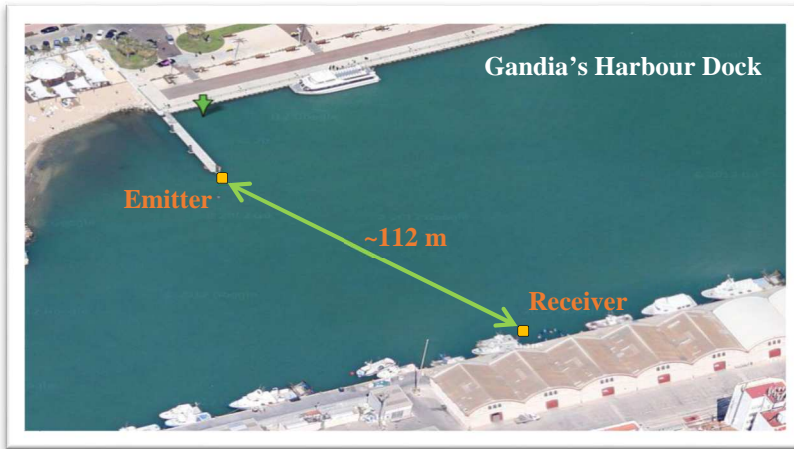


Fig 4.22. Aerial view of the experimental setup disposition.

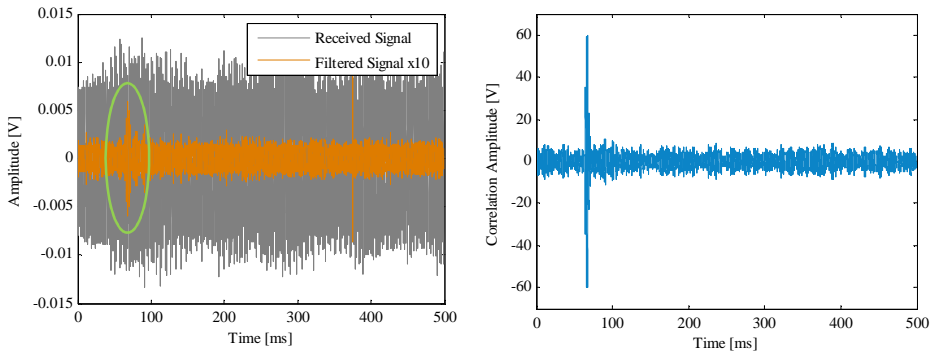


Fig 4.23. Left: Registered signal when the array had emitted a pure tone of 30 kHz and 4 ms duration. In grey is represented the registered signal (masked by noise), Band-pass filtered signal has been plotted in orange, also has been magnified for better visualization. Right: Result of the correlation between the emitted and the received signal.

The emitter-receiver distance was calculated through the time of arrival obtained for each emitted signal using the correlation method. Moreover the signal to noise ratio for each kind of signals has been compared. In this case, pure tones presents high signal to noise ratio because 10 kHz is the resonance frequency of each element of the emitter and 30 kHz is the resonance frequency of the receiver. The sound propagation velocity considered was 1500 m/s. These results, obtained in a very noisy

environment, corroborate the potential of the use of this correlation method to obtain the time of arrival and the amplitude of the received signals, last one very useful for in situ sensor calibration purposes. Different MLS were used: MLS 22 (10.2 ms duration), MLS 32 (20.4 ms duration), MLS 42 (40.9 ms duration).

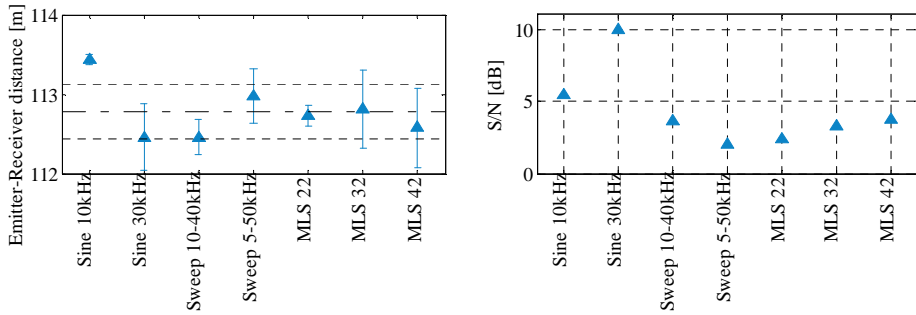
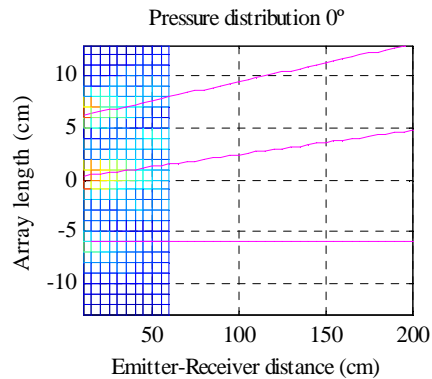
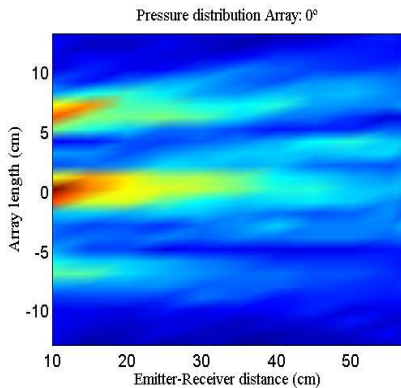


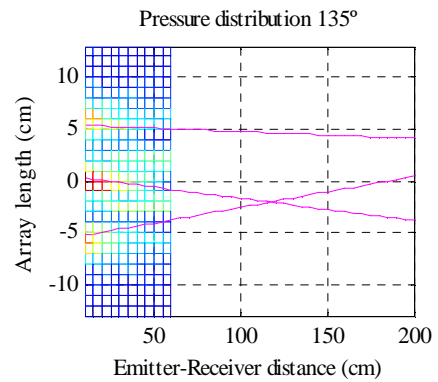
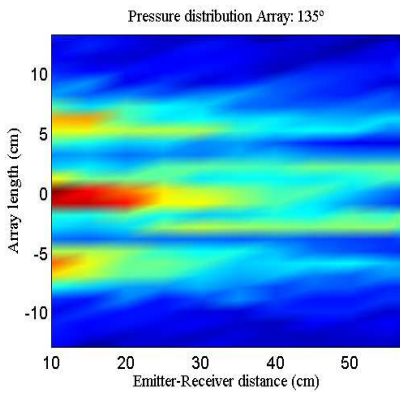
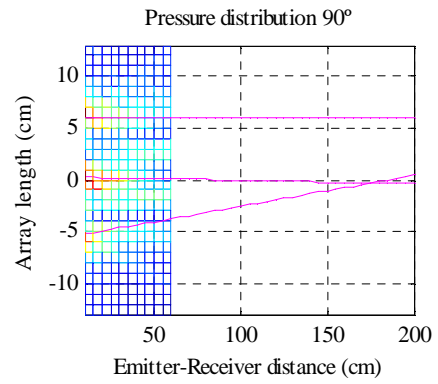
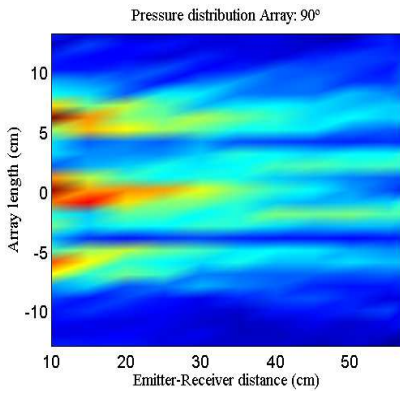
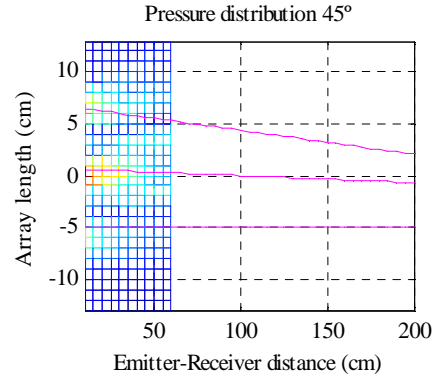
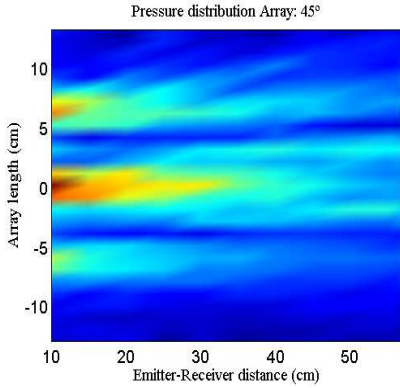
Fig 4.24. Left: Emitter-Receiver distance obtained with correlation method for each emitted signal tested. Dot-dashed line indicates the mean value and dashed lines indicates the deviation of the results obtained with all emitted signals. Error bars indicates the measurement uncertainty of each particular signal. Right: Signal to noise ratio of the correlated signal for each emitted signal tested.

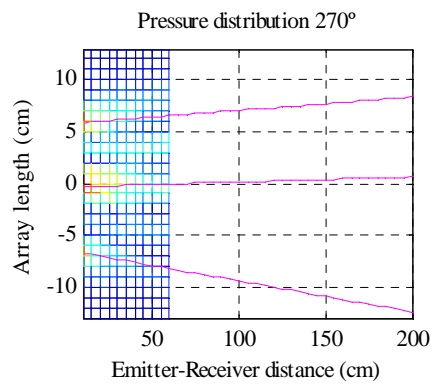
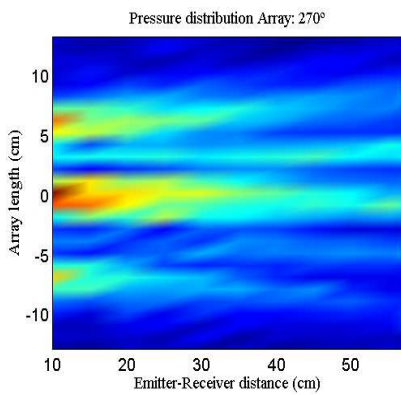
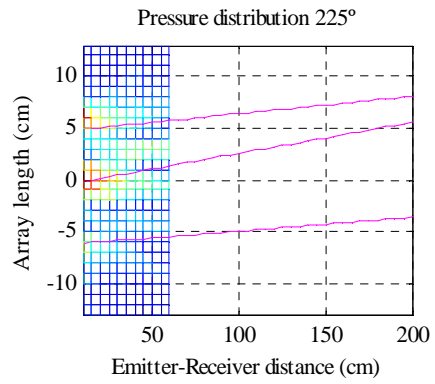
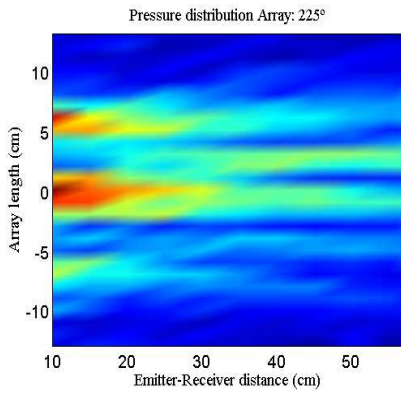
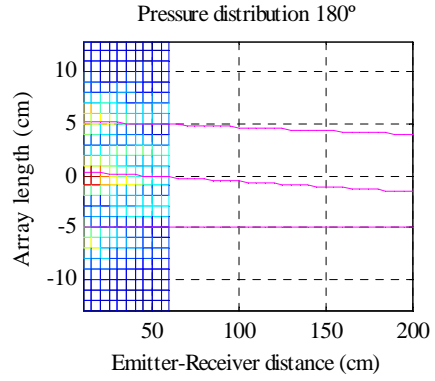
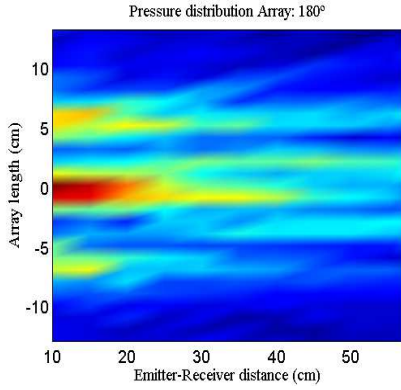
4.5.3 High frequency tests

A set of tests were performed with the array emitting high frequency for parametric generation. Firstly, for signal amplification, was used a commercial RF amplifier (1040L, 400W, +55 dB, Electronics & Innovation Ltd. ©) until the dedicated electronics was available. Using this amplifier it was decided connecting the three elements in series in order to have maximum power transfer since the serial impedance (50.64Ω) was near to 50Ω , the output impedance of the amplifier. On the other hand, the serial connection, offered less synchronization between emissions and less symmetry, but the power requirements for parametric generation was a more critical factor when choosing. The best solution would be to feed in phase each element by one amplifier, but, not having enough amplifiers, the aforementioned solution was decided in a first term. Numerous tests were performed using this

configuration, unfortunately parametric generation was not observed during the array emission, mainly for two remarkable reasons. One of them is related with the way of feeding the transducers. In the best case (identical transducers), each transducer is fed with 1/3 of the total power which, been higher than when a single element was fed (due the better impedance matching of the array), is not enough to reach the non-linear regime separately. Despite this, it was expected that the parametric generation takes place, as was observed in similar conditions in the works with the preliminary array (see Section 3.3). As in the previous results, it was expected, by the interaction of the three parametric beams, to have enough bipolar pulse amplitude to be detected. The test results presaged some kind of misalignment of the transducers during assembly, as was lately confirmed in a specific test. Radiation patterns of the array, and each element separately, were evaluated emitting at 400 kHz (primary beam in parametric generation) for the 360° of the emission surface in steps of 45° (See Fig 4.25). The best alignment would be one in which the three beams travel parallel. For this prototype, the best radiation surfaces are located at 315° so, the proposal is to use this orientation for the calibration tests with the new electronics.







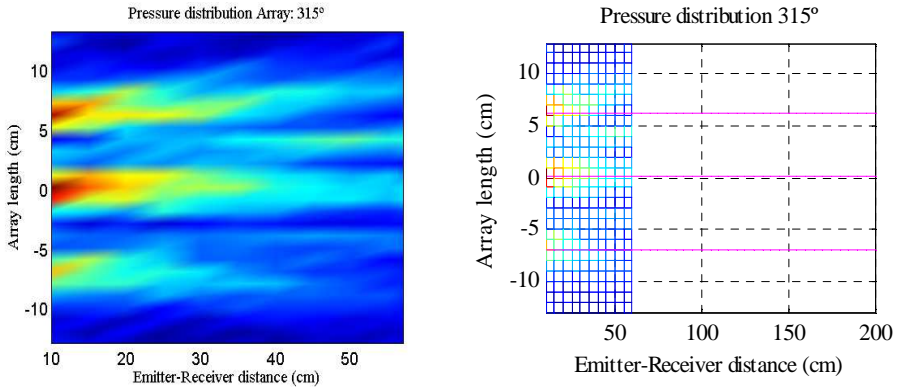


Fig 4.25. Left: Normalized pressure amplitude measured along a parallel plane to the array axis. Right: Extrapolation with the distance of the pressure maximum evolution offered by each element of the array.

4.6 Current state and future steps

To describe the current state of the device it is necessary to describe the status of the array in two blocks. On the one hand the status of the array to be used in low frequency applications and, on the other hand, to be used, as a parametric source, in the high frequency range.

The device (array + electronics) has been tested in positively way in different scenarios, working in laboratory environments and in noisy real environments as in Gandia's Harbour. It has been reported that, the device is able to generate, amplify and reproduce different low frequency signals (pure tones between 10 and 60 kHz, sweep signals and MLS) working on a wide range of distances and in very different environmental conditions. Acoustic detection through the technique of cross-correlation between the emitted and received signals has also been evaluated. This technique is more favourable for broadband signals (sweeps and MLS) because they have a narrower correlation peak and consequently they are easier to discern than others peaks. Furthermore, this technique is powerful in measurement conditions with a reduced S/N ratio, as in the case of marine environments over long distances

where the recorded signal is weak, or in environments with high background noise. All of these signals and processing techniques are very useful in order to carry out the designed strategy for a Sea Campaign described in Section 4.2.

Regarding to the high frequency application some aspects must be taken in caution. The assembly of the transducers is a critical aspect. Due to the low efficiency of the parametric generation, at long distances, the interaction of the parametric beams is crucial in order to reach enough amplitude levels. For better interaction of the three beams, all of them should travel parallel. This aspect forces the selection of the most favourable radiation surface or, in a future prototype, the elements re-assembly in order to have the same radiation behaviour along the entire cylindrical surface array. Taking into account the low impedance of this transducer at 400 kHz and, due to this, the high requirements of intensity to reach the desired power levels to bring on the parametric effect, the proposed electronic solution to amplify high frequency signals has been quite challenging and it is still being under development (C. D. Llorens, In process).

Part II

First Search for Secluded Dark Matter with ANTARES

5

Part II Introduction: Dark Matter and Secluded Dark Matter

In this section the evidences of the Dark Matter presence in the Universe and the direct and indirect techniques for its detection will be reviewed. Furthermore, the searches of dark matter with ANTARES will be summarized. To finalize, the particularities of the models which describe the mechanisms of Secluded Dark Matter and the effects on the Sun, as DM source, will be detailed.

5.1 Dark Matter

Since the 1930s in large astrophysical systems, with sizes ranging from galactic to cosmological scales, some “anomalies”, that can only be explained either by assuming the existence of a large amount of unseen matter or by assuming a deviation from the known laws of gravitation and the theory of general relativity, have been observed. After decades of slow accumulation of evidence, in the 1970s and 1980s were laid the basis of the existence of a kind of Dark Matter (DM), which does not interact with light (and ordinary matter), making it invisible, but its existence is attributed for the gravitational effects. Since then, the main goal for the scientific community in this topic is the knowledge of what DM is made of. Most astronomers,

cosmologists and particle physicists are convinced that at least 95% of the composition of the Universe is due to this non-luminous matter and its constitution today remains one of the most relevant and fascinating enigmas in modern physics. The relative abundances of the major components of the Universe are illustrated in Fig 5.1. Baryons, the commonly known matter, lightly sprinkle the Universe, as they constitute only about 4.6% of the total mass-energy density. Dark energy makes up the bulk of the Universe at the present epoch, about $\sim 72\%$. Dark matter comprises $\sim 23\%$ of the Universe. Dark matter holds baryons together to form galaxies, galaxy groups, and galaxy clusters.

UNIVERSE COMPOSITION

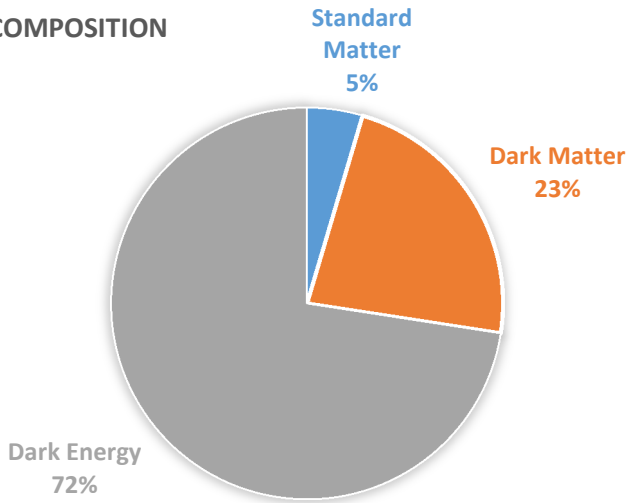


Fig 5.1. Estimated composition of the Energy-Matter of the Universe.

5.1.1 Indirect Evidences

5.1.1.1 Galactic Rotation Curves

The most convincing and direct evidence for dark matter on galactic scales comes from the observations of the rotation curves of galaxies, i.e., the graph of circular velocities of stars and gas as a function of their distance from the galactic centre. In 1933 Fritz Zwicky provided evidence that the mass of the luminous matter (stars) in the Coma cluster, which consists of about 1000 galaxies, was much smaller than its total mass implied by the motion of cluster member galaxies. Also, in 1959 a study on the radial velocity of the spiral galaxy M33 showed that the rotation curve of the galaxy does not agree with the mass density of visible matter (Volders, 1959). It was not until 1970's when the existence of dark matter began to be considered seriously and its presence in spiral galaxies was the most plausible explanation for the anomalous rotation curves of these galaxies. The rotation of stars in Andromeda galaxy were measured using more precise spectroscopy methods and shown that the rotation speed of the stars in spiral galaxies is roughly constant beyond the galactic bulge at the centre instead of decreasing at large radius (see Fig 5.2) (Rubin V.C. & Ford Jr., 1970). A complete study using twenty one spiral galaxies evidenced that the best way to explain the rotation curve of the stars was by means of assuming that the majority of the mass of the galaxy had to be in a form of an invisible matter in the galactic halo (Rubin, Thonnard, & Ford, 1980). Fig 5.2 shows the rotation curve for a nearby dwarf spiral galaxy M33, superimposed on the optical image. If there were no galactic matter outside the visible disk, the rotation velocity curve would have decreased as $1/\sqrt{r}$. Instead it continues to rise towards a constant value, way beyond the visible disk, suggesting that there is a lot of invisible matter in and around the galaxy. Similar rotation curves have been observed for about a thousand galaxies, including our own. And they suggest the mass of the invisible matter to be over one order of magnitude larger than the mass of visible matter.

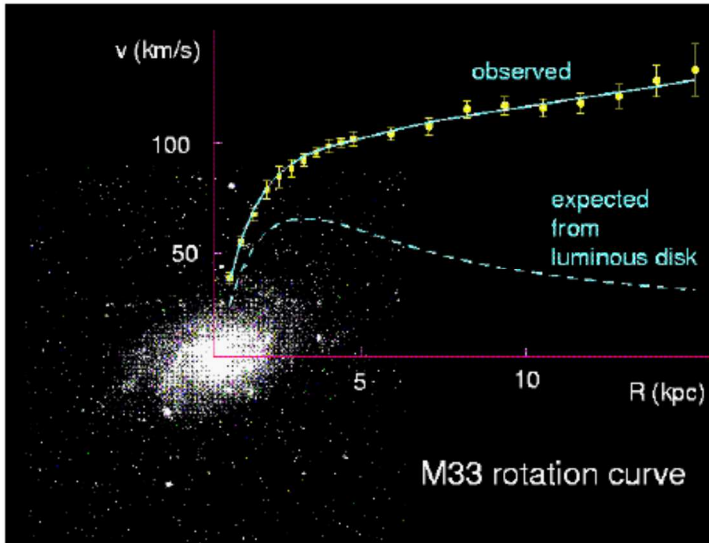


Fig 5.2. Observed rotation curve of the nearby dwarf spiral galaxy M33, superimposed on its optical image (from (Roy, 2000)).

5.1.1.2 Galaxy Clusters

Galaxy clusters are a large number of galaxies (up to 1000) confined by their gravitational effect. Typically they have a mass of $10^{14} M_{\odot} \sim 10^{15} M_{\odot}$ ¹ and stretching from 2Mpc² to 10Mpc. More proofs on the existence of DM have been provided by the study of these galaxy clusters. Chandra X-ray Observatory study of the Abell 2029 cluster (Vikhlinin et al., 2006) showed that about $10^{14} M_{\odot}$ cluster mass is contained in a form of invisible matter exerting gravitational forces on the galaxies.

5.1.1.3 Gravitational Lensing

Gravitational lensing is the phenomena in which the light from a very distant source is bent around a massive object (such as a black hole or a galaxy) between the source

¹ M_{\odot} is the solar mass, about $1.9 \cdot 10^{30}$ kg

² One parsec (pc) is about $3 \cdot 10^{16}$ m or 3.2 light-years

and the observer (Fig 5.3). This effect was first predicted in 1930's and its first observation, in 1979, occurred by studying the twin quasars SBS 0957+561 A & SBS 0957+561 B (Walsh, Carswell, & Weymann, 1979). In 1998 took place the first evidence from gravitational lensing hinting at invisible mass from the study of the galaxy cluster Abell 1689 (Taylor, Dye, Broadhurst, Benitez, & van Kampen, 1998). The development of new detection techniques in gravitational lensing (Refregier, 2003) contributed to obtain stronger evidences of the DM presence. In the study of two merging galactic clusters while the baryonic matter still separated it was shown, independently of any assumption on the laws of gravity, that the gravitational potential of the cluster traced the overall shape of the merging clusters and not that of the baryonic component (D. Clowe et al., 2006; D. Clowe, Gonzalez, & Markevitch, 2004). This proved that the mass peak was not located with the baryonic mass but with a dark halo combining the two clusters. Additionally, about 87.5% of the mass is invisible and the remaining 12.5% is baryonic. These two studies served to reinforce the existence of a particle component of dark matter versus the opposite theories which advocated to a deviation from the known laws of gravitation and the theory of general relativity as a solution to the missing mass (Milgrom, 1983).

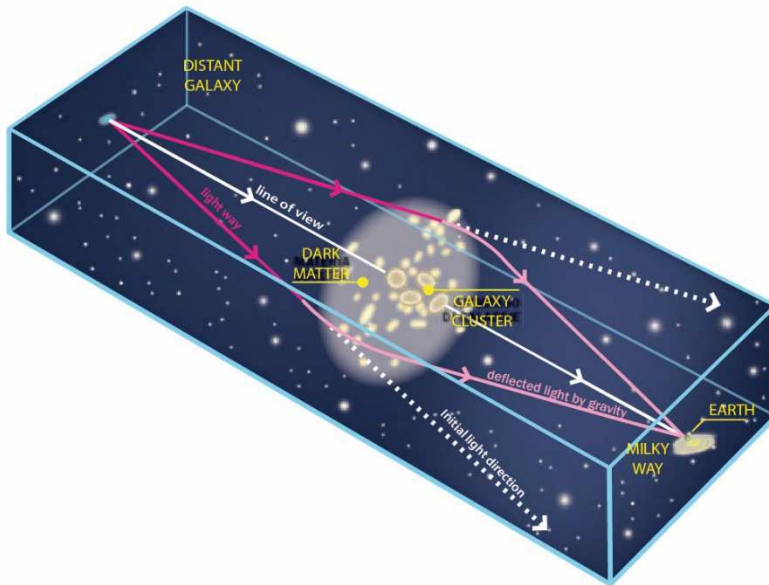


Fig 5.3. Gravitational Lensing phenomena diagram. Light coming from a faraway galaxy is deflected due the dark matter located in its travel path. Dark matter gravity acts as a lens and at the observer point (Earth) is appreciated various images of the same galaxy. (Figure adapted from ©Infn-Asimmetrie).

5.1.1.4 Velocity Dispersions of Galaxies and Mass to Light Ratio

The velocity dispersion is the statistical deviation (about the mean) of the velocities of objects bounded gravitationally, such as stars in a galaxy or galaxies in a galaxies cluster. It is defined as mass to light ratio the ratio between the mass of a specific volume and its luminosity. This is a well-known observable characteristic for objects such as stars and other astrophysical objects. For the measurements of entire galaxies, it is expected that the ratio should be approximately the average of individual ratios of the diverse luminous objects located inside. However, experimental measurements of these parameters in spiral and elliptical galaxies (Faber & Jackson, 1976) evidence a large missing mass component (Faber & Jackson, 1976; Faber & Dressler.A, 1977).

These studies showed that visible mass distribution found in galaxy clusters is not enough to determine the velocity dispersion revealing that a dark halo surrounding the clusters would have to contain the equivalent of more than five times the visible mass. Moreover, the measurement of the mass to light ratio showed that the value is much larger than the average of the individual components, indicating again that there is, at least, three times more invisible matter than visible.

5.1.1.5 *Cosmic Microwave Background*

The cosmic microwave background (CMB) is the thermal radiation assumed to be left over from the "Big Bang" of cosmology. The CMB is a cosmic background radiation that is fundamental to observational cosmology because it is the oldest light in the Universe, dating to the epoch of recombination (Fig 5.4). It was predicted by George Gamow, Ralph Alpher, and Robert Hermann in 1948 and accidentally discovered by Arno Penzias and Robert Wilson in 1965 when they observed a background temperature excess of 3.5° K in its radiograph built to radioastronomy and satellite communications experimentation. Penzias and Wilson were awarded with the Physics Nobel Prize in 1978 when they determined that the antenna temperature was induced by the cosmic microwave background. Since then, several experiments were built to measure the CMB radiation such as COBE experiment (National Aeronautics and Space Administration, 2008), WMAP (Wright, E.L. et al., 2003), and PLANCK (European Space Agency, 2014). The CMB cannot be considered as an evidence of the existence of DM but its importance is due to the fact that it validates the Λ CDM model (Lambda-Cold Dark Matter). The Λ CDM model is a parameterization of the Big Bang cosmological model in which the Universe contains a cosmological constant, denoted by Lambda (Λ), associated with dark energy, and cold dark matter (CDM), a form of matter introduced in order to account for gravitational effects observed in very large-scale structures (rotation curves of galaxies; the gravitational lensing of light by galaxy clusters; and enhanced clustering of galaxies). It is frequently referred to as the standard model of Big Bang cosmology,

since it is the simplest model that provides a reasonably good explanation of the following properties of the cosmos:

- the existence and structure of the cosmic microwave background (CMB)
- the large-scale structure in the distribution of galaxies
- the abundances of hydrogen (including deuterium), helium, and lithium
- the accelerating expansion of the Universe observed in the light from distant galaxies and supernovas

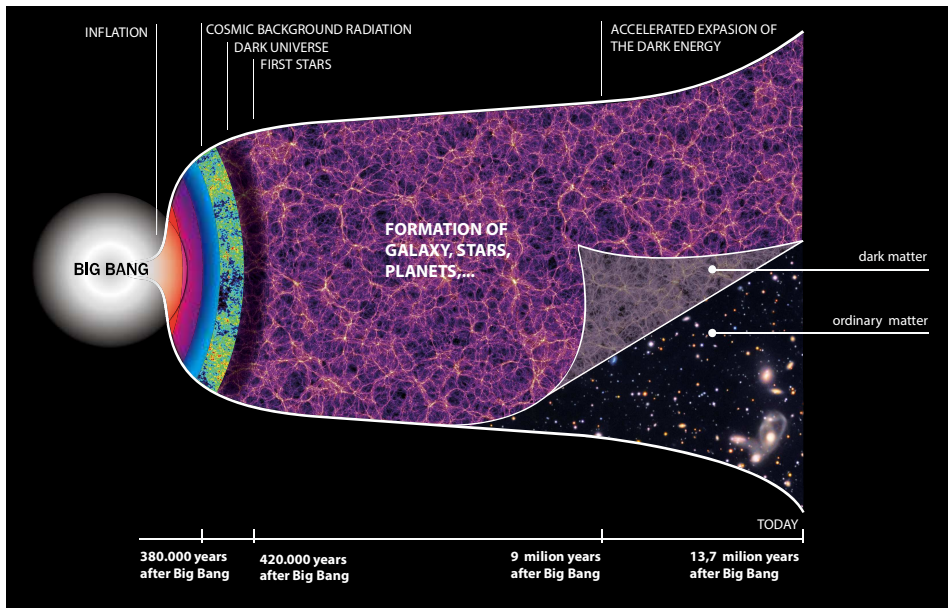


Fig 5.4. Schematic view of Universe evolution following the Standard Model in cosmology. On the bottom the temporal scale of the events since the Big Bang until now is shown. On the top flap the estimated DM distribution is represented. (Figure adapted from ©Infn-Asimmetrie)

The model assumes that general relativity is the correct theory of gravity on cosmological scales. The period when emerged this model (in the late 1990s) was marked by appearing of disparate properties of the Universe and mutually inconsistent, and there was no consensus on the composition of the energy density of the Universe. Model descriptions and also the fact that the model has been validated

by other measurement such as the Baryon acoustic oscillations (Percival et al., 2007), distance measurements by type Ia Supernovae (Kowalski et al., 2008), and the Lyman-alpha forest measurements (Viel, Bolton, & Haehnelt, 2009) have tipped the balance in favour of the existence of a particle component of dark matter versus the opposite theories which advocated to a deviation from the known laws of gravitation.

5.1.2 WIMP as the Dark Matter Candidate

Even though there are tens of DM candidates proposed in the bibliography (Bergstrom, 2000; Bertone, Hooper, & Silk, 2005), the most widely studied and often most likely DM candidates are WIMPs (Weakly Interacting Massive Particles). Following the idea that DM particles would be thermal relics from the Early Universe, they can remain from the earliest moments of the Universe in sufficient number to account for a significant fraction of relic dark matter density. In the simplest WIMP models, during the early Universe dark matter particles were in thermal and chemical equilibrium with the Standard Model particles, they were as abundant as photons in the beginning, being freely created and destructed in pairs when the temperature of the hot plasma was larger than their mass. However, after the temperature dropped below the mass of the WIMP, its density rapidly decreases as the Universe expands, until it becomes so low that WIMPs cannot self-annihilate anymore and they freeze-out from equilibrium, having the same density since then. Under some simplifying assumptions and following these arguments, the relic abundance of WIMPs in the Universe (that is, the number density of WIMPs in the local Universe in units of the critical density) can be simply computed in terms of the self-annihilation cross-section:

$$\Omega_{WIMP} \approx \frac{7 \cdot 10^{-27} \text{ cm}^3 \text{ s}^{-1}}{\langle \sigma_{ann} v \rangle} \quad (5.1)$$

where σ_{ann} is the cross section for annihilation of a WIMPs pair into Standard Model particles, v is the relative velocity between two WIMPs, $\langle \dots \rangle$ denotes thermal averaging and the value in the numerator is obtained using the value of the temperature of the cosmic background radiation, the Newton's constant, etc. (Bertone et al., 2005). The self-annihilation cross-section required in order to achieve the appropriate relic density is $\sigma_{ann} = 3 \cdot 10^{-26} \text{ cm}^3 \text{ s}^{-1}$, this is a value remarkably close to the cross-section typical of weak interactions in the Standard Model, hence the name of WIMPs. This is the hint that physics at the weak scale could provide a reliable solution to the dark matter problem. Moreover, since WIMPs interact with ordinary matter with roughly weak strength, their presence in galactic scales, and in particular in our galaxy, raises the hope of detecting relic WIMPs directly in a detector by observing their scattering on target nuclei through nuclear recoils.

5.2 Dark Matter Detection Methods

If WIMPs compose most of the DM not only will be present as background density in the Universe but also will be gravitationally accumulated in the galactic halos. Of course they will be present in the Milky Way, so it may be possible either detecting them directly in experiments located in the Earth or indirectly looking for their annihilation products in astrophysical sources.

5.2.1 Direct Detection

Direct DM detection is based on the energy detection of nuclei recoils struck by DM particles travelling through a detector, either through the measurement of the light (scintillation), the charge (ionization), through the phonons produced in the target material by the scattering event or in nucleation of superheated liquids. Fig 5.5 shows a summary of the different direct detection experiments classified by their detection mechanism. These different techniques exploited in direct experiments are performed using diverse target materials: Ge, Si, NaI, Xenon, C₃FI, C₃F₈. The physics in dark

matter nucleus interaction involves elastic scattering on nucleus. The elastic scattering of a WIMP off of a nucleus in a detector is simply the interaction of the WIMP with a nucleus as a whole, causing it to recoil, ideally often enough to measure the recoil energy spectrum in the target. WIMP scattering off nuclei is commonly discussed in the context of two classes of couplings, the different experiments of direct detection can be classified in base of these couplings:

- Scalar or spin-independent (SI): The SI experiments are designed to detect the coherent recoil of the nucleus caused by the DM scattering. For a heavy nuclear target, the coherent scattering increases the cross-section by the square of the Atomic Number. Experiments using heavy nuclei as target material, as Iodine, Germanium or Xenon like DAMA (Bernabei et al., 2013), Edelweiss (EDELWEISS Collaboration, 2011), SuperCDMS (Sander et al., 2013) and XENON (Aprile et al., 2012), LUX (Akerib et al., 2013) among others, are more sensitive to scalar interactions and their limits are mainly constrained by the spin-independent WIMP-nucleon cross-section.
- Axial or spin-dependent scattering (SD): The SD cross-section occurs through the axial vector coupling to the spin content of the nucleus; there is a $J(J + 1)$ enhancement from the nuclear spin J . Until recently, the SD cross section limits had been about 6 orders of magnitude weaker than for SI. Experiments which use target materials of light nuclei are more sensitive to spin-dependent WIMP-nucleon cross-section such as COUPP (Behnke et al., 2012), SIMPLE (Felizardo et al., 2014) or PICO (Amole et al., 2015; Bou-Cabo, RICAP).

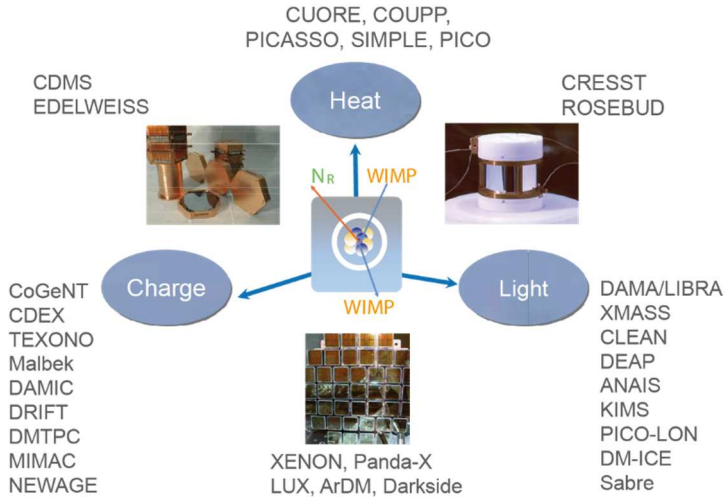


Fig 5.5. Summary of the direct detection experiments classified by their detection mechanism.

It is crucial for these experiments having a good background discrimination since cosmic rays with energies about keV to MeV range bombard the Earth’s surface producing in most cases nuclear recoils similar to those expected from WIMPs at a rate of about 10^3 events kg^{-1} per day^{-1} . This is the reason to carry the experiments out in the deep underground in order to minimize the background by orders of magnitude compared with the sea level intensity. Moreover, it must be extremely demanding with the protection against the natural radioactivity from the surroundings and the material of the detector itself.

5.2.2 Indirect Detection

Indirect detection is based in the fact that the DM passing through massive objects like the Galactic Centre, the Sun or the Earth may decrease its velocity under the scape velocity, due to the elastic scattering with the nuclei of the object, and consequently keeping trapped. DM Indirect detection experiments aim to detect the annihilation products of DM particles as products of Standard Model particles: charged particles (electrons and positrons, protons and antiprotons, deuterium and

antideuterium), photons (gamma rays, Xrays, synchrotron radiations) and neutrinos. As these particles are present for different processes, not only DM annihilation, the indirect searches focus on looking for channels and energy ranges where it is possible to distinguish from the background due to ordinary astrophysical processes. For this reason, searches for charged particles focus on fluxes of antiparticles (positrons, antiprotons and antideuterons) which are much less abundant in the Universe than the corresponding particles. Also, for photons and neutrinos it is usual to look at areas where the DM-signal to background ratio can be maximized. For a complete review on indirect DM searches see (Cirelli, 2012). The flux of such radiation is proportional to the annihilation rate, which in turn depends on the square of the dark matter density.

The study of electron and positron fluxes in different experiments (AMSII (Accardo et al., 2014; M. Aguilar et al., 2014), PAMELA (Adriani et al., 2010), Fermi (Abdo et al., 2009), ATIC-2 (Chang et al., 2008), PPB-BETS (Torii et al., 2008), HESS (Aharonian et al., 2008)) have offered various results which could indicate a rising in the positron-electron ratio at the TeV and sub-TeV scale. These signal excesses are striking because they imply the existence of a source of ‘primary’ e^+ (and e^-) other than the ordinary astrophysical ones. This unknown new source can well be itself of astrophysical nature (Serpico, 2012) but also it could be understood as a signature of DM.

Gamma rays fluxes have been studied by other experiments such as Fermi (Tempel, Hektor, & Raidal, 2012; Weniger, 2012), HESS (Aharonian et al., 2008), MAGIC (Elsaesser & Mannheim, 2005), and VERITAS (Vivier, 2011), emphasising on the Galactic Centre, dwarf galaxies and galaxy clusters that have a high mass to light ratio. Findings with Fermi are indicating a possible dark matter signal (4.5 σ of significance level) for a WIMP with a mass of 130 GeV (Bergström, Edsö, & Zaharijas, 2009). Nowadays, the origin of this excess has not been confirmed. In

addition to a possible DM signal, there are several interpretations of the Fermi results based either on a single large scale Galactic cosmic-ray electrons-plus-positrons component or by invoking additional electron-positron primary sources, e.g. nearby pulsars (Grasso et al., 2009).

Finally, in addition to e^+/e^- and gamma rays, neutrinos are an indirect messenger of DM presence. Neutrinos are produced in DM annihilations together with all the other particles. Neutrinos have the advantage of proceeding straight and essentially unabsorbed through the Galaxy. As detailed in Chapter 1 they can cross a long path with dense matter with little interaction. ANTARES (Ageron et al., 2011), ICECUBE (IceCube Collaboration, 2014), and Super-Kamiokande (SuperKamiokande Collaboration, 2013) search for dark matter through neutrinos coming from the Sun, Earth, Galactic-Centre (GC), Galactic-Halo(GH), and dwarf galaxies. The experiments, in order to minimize the background of cosmic muons coming from the atmosphere above the detector, must select only *upgoing* tracks, i.e., neutrinos which have crossed the Earth and interact near of the instrumented volume. These experiments look for neutrinos with different origins. From the GC or the GH, neutrino telescopes located at the South Pole have difficulties to ‘see’ the GC, which is essentially above horizon for them. The DeepCore extension of ICECUBE, however, avoids this limitation by using the outer portion of the experiment as an active veto. From galaxy clusters, in this case the sensitivities are not competitive with gamma rays (unless one considers very large DM masses). From the centre of the Sun (or even the Earth) as DM particles may become gravitationally captured by a massive body, lose energy via repeated scatterings with its nuclei and thus accumulate at its centre. The annihilations occurring there give origin to fluxes of high energy neutrinos. The detection of these high-energy neutrinos from the Sun would constitute a definitive evidence for DM, as there are no known astrophysical processes able to mimic it.

Due to lack of signal evidence, constraints have been imposed for the searches in each object. From the GC constraints in DM annihilation cross section in SuperKamiokande (Desai et al., 2004; Desai et al., 2008) have been imposed. ICECUBE have imposed constraints in DM annihilation cross section from the GH (R. Abbasi et al., 2011a), from the GC (R. Abbasi et al., 2012) and finally from dwarf galaxies and clusters of galaxies (Aartsen, Abbasi, Abdou, Ackermann, Adams, Aguilar, Ahlers, M., Altmann, Auffenberg, & Bai, 2013b). Also ANTARES has put constraints for the GC (ANTARES Collaboration, In preparation). For the Sun different experiments have imposed constraints on the scattering cross section of DM particles with nuclei, in SuperKamiokande (Tanaka et al., 2011), ICECUBE (IceCube Collaboration, 2012) and ANTARES (Adrián-Martínez et al., 2013). The neutrino flux due to WIMP annihilation in the Sun is highly dependent on the capture rate of WIMPs in the centre of the Sun which, in turn, is dominated by the SD WIMP-proton cross section. This is the reason why these indirect searches have better limits compared to direct search experiments (COUPP, SIMPLE). Contrary to the case of SI WIMP-nucleon cross section where, thanks to their target material, direct search experiments have better limits (XENON100, LUX).

5.3 Dark Matter Searches with ANTARES Neutrino Telescope

Together with the observation of astrophysical sources, the indirect detection of DM is one of the main goals of the ANTARES neutrino telescope. There are five potentially interesting DM sources to be explored with ANTARES: the Sun, the Galactic Centre, the Earth, dwarf galaxies and galaxy clusters. Each one presents advantages and disadvantages. Assuming that DM is made of WIMPs, like neutralinos, they can scatter in astrophysical objects like the Sun or the Earth and become gravitationally trapped. In this way their self-annihilation would produce directly or commonly indirectly high energy neutrinos. DM which form part of the

Galactic Halo could also annihilate and produce signal, in particular coming from the Galactic Centre direction, where is more abundant.

5.3.1 The Galactic Centre

A promising DM source for neutrino telescopes is the Galactic Centre. The apparent drawback due the large distance between the Earth and the GC is offset by the large mass involved. The main advantage of this source, contrary to what happens, for example, in the Sun, is that there is no absorption of neutrinos, which is relevant for high energy/mass and improves the effective area and angular resolution.

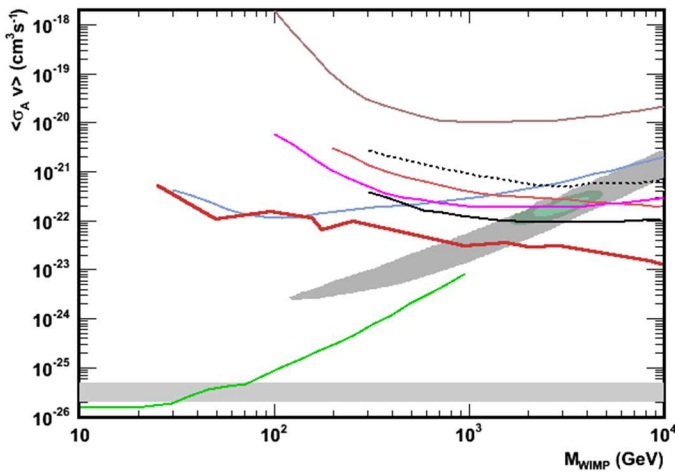


Fig 5.6. Preliminary limits on $\langle \sigma v \rangle$ for the Galactic Centre for the $\tau^- \tau^+$ channel (red solid line) with IceCube40 for the GC (brown solid line), IceCube59 for dwarf galaxies (dashed black line), IceCube79 for the Galactic Halo (magenta solid line), IceCube59 for the VIRGO cluster (black solid line), DeepCore+IceCube79 for the GC (blue solid line) and Fermi for dwarf galaxies (green solid line). The grey/green area represent leptophilic dark matter models which would explain the PAMELA (grey) and AMSII+Fermi+PAMELA+HESS (green) excess in the Galactic Centre. The grey band indicates the natural scale for which all the dark matter particles are considered as WIMPs only. Adapted from ((ANTARES Collaboration, In process)).

During the 2007-2012 analysed data period no significant excess was observed so limits were set in mean cross-section velocity product for dark matter $\langle \sigma v \rangle$ (See Fig

5.6) for Navarro–Frenk–White (NFW)³ halo profile and the $\tau^- \tau^+$ channel (ANTARES Collaboration, In preparation). These limits exclude leptophilic DM interpretation of the Fermi-PAMELA-HESS excess. It is remarkable that above $\sim 150 \text{ GeV}$ the best limits from neutrino telescopes are provided by ANTARES due to the fact that the visibility of the GC and the angular resolution is better in ANTARES than in Ice Cube.

5.3.2 The Earth

DM would accumulate within the Earth after scattering. The scattering is produced mainly on the heavy elements at the Earth core. For this reason, the limits are set on the spin-independent cross section of WIMP scattering. Limits (Fig 5.7) are particularly interesting for WIMP masses close to the masses of scattering nuclei (iron and nickel).

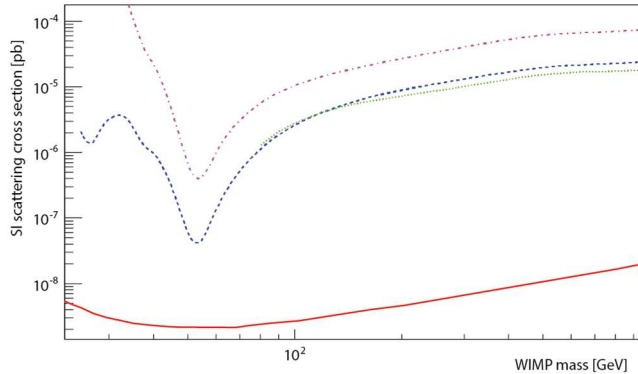


Fig 5.7. Preliminary Spin-independent cross section sensitivity (90% CL) for the Earth analysis, assuming $\langle \sigma v \rangle \sim 3 \cdot 10^{-26} \text{ cm}^3 \text{ s}^{-1}$ for three different channels: $\tau \tau^+$ (dash, blue), $W^+ W^-$ (dot, green) and $b \bar{b}$ (dash-dot, magenta). This sensitivity is also compared with the results of XENON-100 (solid, red). Plot from (Zornoza, 2014).

³ The Navarro–Frenk–White profile or NFW profile is a spatial mass distribution of dark matter fitted to dark matter haloes identified in N-body simulations by Julio Navarro, Carlos Frenk and Simon White (Navarro, Frenk, & White, 1996). The NFW profile is one of the most commonly used model profiles for dark matter halos

5.3.3 The Sun

DM searches in the Sun are very interesting since a potential signal would be free of astrophysical background and this is a big advantage over other indirect searches. The neutrinos produced through nuclear reactions in the Sun are of much lower energies. The background produced for cosmic rays interaction on the Sun corona is very low and the atmospheric one can be estimated from scrambled data with high accuracy. In this section two kind of DM searches coming from the Sun with ANTARES are described. On the one hand, *the standard DM search* in which WIMPs trapped in the Sun core self-annihilate into Standard Model particles. These particles could decay give rise to the production of energetic neutrinos which can escape from the Sun and be detected by ANTARES. The main disadvantage of this search is the absorption suffered by neutrinos over 100 GeV because they can interact with Sun nuclei and be absorbed before escaping the Sun. On the other hand *the search of Secluded Dark Matter*, which is one of the objects of this thesis.

5.3.3.1 Standard Dark Matter search

As related in previous sections, possibilities of DM detection have been motivated by its gravitational capture, in massive objects like the Sun, and subsequent annihilation. If as expected DM self-annihilates, the capture is balanced by the annihilation of DM particles. The intensity of the annihilation signal would be a probe of the DM scattering cross-section on nuclei. Neutrinos could be produced in the annihilations, also SM particles which interact strongly with the interior of the Sun being largely absorbed but, during this process, producing high-energy neutrinos which could escape and can be potentially seen by neutrino detectors as ANTARES.

Latest results on search for DM in the Sun were obtained after the analysis of 2007-2012 data (Zornoza, 2014). In this analysis no excess over the expected background was observed and limits on the neutrino flux limit and on the WIMP-nucleon cross section were set. Fig 5.8 shows the preliminary limits for spin-dependent and spin-

independent WIMP-proton scattering cross-section. Neutrino telescopes offer the best limits for spin-dependent cross-section compared to direct searches, since the Sun is made basically of protons. (Previous (2007-2008) official results in (Adrián-Martínez et al., 2013)).

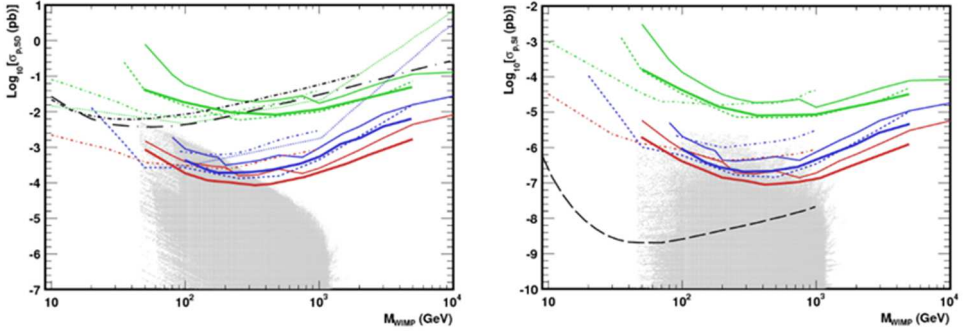


Fig 5.8. Preliminary Spin-dependent (left) and Spin-independent (right) cross-section limits for the search on the Sun: ANTARES 2007-2012 (thick solid) lines: $\tau \tau^+$ (red), W^+W^- (blue), $b\bar{b}$ (green), IceCube-79 (dashed lines), SuperKamiokande (colored dash-dotted lines), SIMPLE (black short dash-dotted line), COUPP (black long dash-dotted line) and XENON-100 (black long dashed line). The results are compared with a scan in MSSM-7. (Figure from (Zornoza, 2014)).

5.3.3.2 Search for Secluded Dark Matter in the Sun

Another possibility is based on the idea that DM annihilates first into metastable mediators (ϕ), some new gauge bosons, which subsequently decay into SM states, (Arkani-Hamed, Finkbeiner, Slatyer, & Weiner, 2009; Chen, Cline, & Frey, 2009; Pospelov, Ritz, & Voloshin, 2008; Pospelov & Ritz, 2009; Rothstein, Schwetz, & Zupan, 2009). In all of these models, the thermal relic WIMP DM scenario is considered as usual, while there is also the possibility to explain some astrophysical observations such as the rising in the positron-electron ratio observed by PAMELA (Adriani et al., 2010), Fermi (Abdo et al., 2009) and recently measured with high precision in AMS-II (Alpha Magnetic Spectrometer) (Accardo et al., 2014; M. Aguilar et al., 2014). These models try to describe the Secluded Dark Matter (SDM) scenario in which the presence of mediators, also called neutral long lived particles

(LOLIPs) in some references, as a communication way between DM and SM, can dramatically change the annihilation signature of DM captured in the Sun. This idea is based in the fact that if the mediators are long-lived enough to escape the Sun before decaying, they could produce detectable charged-particle or γ -ray fluxes (Batell, Pospelov, Ritz, & Shang, 2010; Schuster, Toro, Weiner, & Yavin, 2010) and also neutrinos that could reach the Earth and be detected. In many of the secluded dark matter models, ϕ can decay into leptons near the Earth. Some differences appear in the leptons created by the neutrino interaction and the leptons arising from ϕ decays. In the latter case, for kinematics, as the DM mass is greater than the ϕ mass the leptons may be boosted and parallel. If these leptons are muons the signature in the vicinity of the detector would be two muon tracks almost parallel. The di-muon signature could be interpreted as a single muon and it could be discriminated (or at least the cut selection could be optimized for these cases) from the atmospheric neutrino signal by its energy deposition topology. Even being short-lived and decaying inside the Sun energetic neutrinos would remain the only signature. Also in these situations the neutrino signal could be enhanced compared to the standard scenario where high energy neutrinos can interact with nuclei and be absorbed before escaping the Sun. The fact that the solar density decreases exponentially with radius facilitates that the neutrinos injected by ϕ at larger radii could propagate out of the Sun because they are subjected to much less absorption. As will be detailed in following sections, the experimental results in the search for SDM depend on the decay length and the production rate. There are several models that can accommodate the lifetimes required for the mediators to enhance the final signal in neutrino telescopes, which have been summarized in reference (Meade, Nussinov, Papucci, & Volansky, 2010). In this work some examples that contain LOLIPs which can have decay lengths in the 1 km to 10^{15} km range, providing the relevant formulae, are detailed.

In the following subsections the processes involved in the possibility of SDM detection will be described starting with the mediator production rate from DM

capture and annihilation in the Sun. To finalize the different scenarios of SDM, in terms of the mediator decay products which have been evaluated with ANTARES (Chapters 6 and 7) will be introduced.

5.3.3.2.1 *DM annihilation in the Sun.*

In the Sun, during the gravitational capture, DM particles suffer multiple scatterings and become trapped within a small region of size $\sim 0.01R_{\odot}\sqrt{100\text{GeV}/m_{\chi}}$ around the Sun's centre, where R_{\odot} is the solar radius. As the finite size of this region has a negligible effect on the neutrino spectra (Cirelli et al., 2005; A. Gould, 1987; Press & Spergel, 1985), DM annihilation can be assumed to take place in the centre of the Sun. The capture rate, C_{\odot} , depends on whether the DM interacts elastically with the nucleus (A. Gould, 1987; Jungman, Kamionkowski, & Griest, 1996) or, whether there are more complicated interactions, in inelastic scattering (Menon, Morris, Pierce, & Weiner, 2010; Nussinov, Wang, & Yavin, 2009). In this work only the elastic scattering for the capture rate has been considered, as assumed in many direct detection searches. The capture rate can be calculated from the scattering cross section, both spin-independent, σ_{SI} , and spin-dependent, σ_{SD} of the process dark matter-nucleon. Both types of processes are constrained by direct detection experiments, but the latter much less so. It is worth to mention that the capture rate relies on assumptions on the density and velocity distributions of dark matter particles in the Solar System, as well as on the composition and density distribution of the interior of the Sun. In this work the capture rate proposed by (Ibarra, Totzauer, & Wild, 2014) has been followed, approximately given by:

$$C_{\odot} \approx 10^{20} \text{ s}^{-1} \left(\frac{1\text{TeV}}{M_{\chi}} \right)^2 \frac{2.77\sigma_{SD} + 4.27 \cdot 10^3 \sigma_{SI}}{10^{-40} \text{ cm}^2} \quad (5.2)$$

In equilibrium, the DM annihilation rate is exactly half of its capture, generally given by ((Jungman et al., 1996)):

$$\Gamma_{ann} = \frac{1}{2} C_{\odot} \tanh^2(t/\tau_{eq}) \quad (5.3)$$

where τ_{eq} is the equilibrium time and $t \approx 10^{17} s$ is the dynamical time of the system. DM can typically scatter in the Sun on a much shorter timescale than it annihilates, in elastic scattering case. Hence, it thermalizes with the rest of the matter in the Sun and concentrates in the inner core as it approaches its equilibrium configuration.

5.3.3.2.2 *Mediator decay products and bounds from neutrino detection.*

As long as the mediator lifetime is long enough such that they can escape the Sun it will produce decay products between the Sun and the Earth. Depending on the mediator decay products different experiments may be able to detect them. For instance, mediator could decay into charged particles which will radiate photons on their way from the Sun to the Earth that could be detected by gamma ray experiments as Fermi (Abdo et al., 2009) or Milagro (Atkins et al., 2004). The decay products able to be detected by neutrino telescopes have been the studied in this work. If the mediator decays into di-muons anywhere between the Sun's surface and the earth, these muons can be observed in neutrino telescopes (ANTARES, IceCube) and also in underground neutrino detectors (Superkamiokande, BAKSAN). When the mediator decay product is a di-muon, the mediator lifetime, or its decay length, is crucial to know what is expecting in the detector. If the decay length of the mediator is long enough to reach the Earth before decaying, i.e., the mediator decays in the vicinity of the detector ($\leq km$) (See Fig 5.9) this muon pair may be observed directly through their Cherenkov radiation as nearby tracks.



Fig 5.9. Secluded scenario diagram where the mediator decays in the vicinity of the Earth as two co-linear muons which could be detected by neutrino telescopes.

In practice, these muons will not be separated enough to be identified as two individual muons, about few meters at most for the energy range explored, which translates into about 10 ns relative time delay for the emitted Cherenkov light. This time is comparable to the readout of the PMTs. These di-muons would be recognized as a single muon but the Cherenkov light yield along the track of a di-muon is higher (factor 2) than a single sub-TeV muon (Fig 5.10). Initially a di-muon event (Fig 5.10 black) could be recognised as an energetic single muon (Fig 5.10 blue) looking at its light emitted on top of the Cherenkov emission, but with the monitoring of the energy deposition along the track, which is mostly energy independent for di-muons, it could be possible to discriminate between single muons and di-muons.

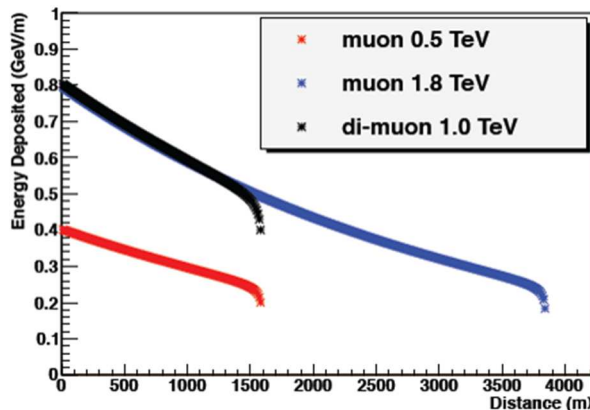


Fig 5.10. Energy deposited for stopping a di-muon event (black), a single muon (red) and a more energetic single muon (blue).

In this work a good discrimination between di-muons and single muon is not the priority, but to obtain the best efficiency to detect di-muons from secluded dark matter in the Sun.

On the other hand, if the mediator decays into di-muons far from the detector then the muons would yield high-energy neutrinos and anti-neutrinos, typically $e^-(e^+), \nu(\bar{\nu})$, which can be detected, like in standard neutrino detection, as they convert back into a muon in the rock or water (ice) near the detector (Fig 5.11).

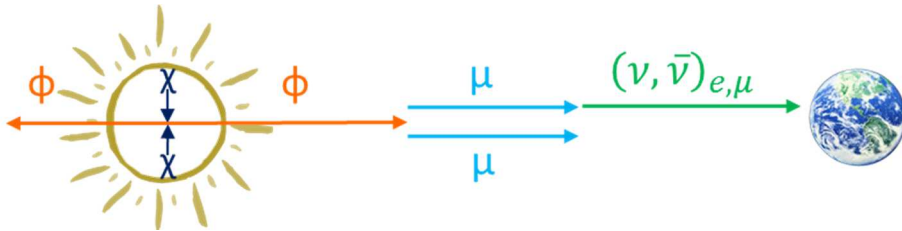


Fig 5.11. Secluded scenario diagram where the mediator decays far from the detector as two co-linear muons which, in turn, decay into neutrinos and could be detected by neutrino telescopes.

While a great deal of the parameter space for neutral LOLIPs is unexplored, some constraints already exist. The strongest bounds on the flux of upward going muons come from Super-Kamiokande (Desai et al., 2004). Fig 5.12 shows the bound on annihilation rate of DM into mediators that subsequently decay into muons which in turn yield high-energy neutrinos and the expected improvement in sensitivity with ANTARES and Ice-Cube.

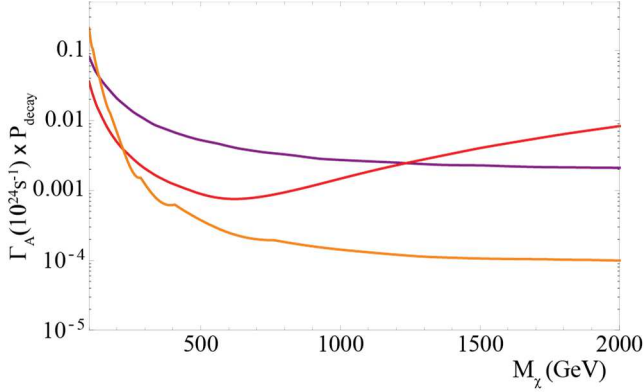


Fig 5.12. The purple curves show the current bounds from SuperKamiokande on the annihilation rate of DM in the Sun into mediators assuming 100% branching ratio and decaying into di-muons. The red (orange) curves are the expected bounds from ANTARES (Ice-Cube). (Plot adapted from (Schuster et al., 2010)).

Another possible scenario is composed by short-lived mediators that decay in the interior of the Sun or near its surface directly into neutrino (and antineutrino) (see Fig 5.13). In the standard scenario, in which neutrinos are produced at the center of the Sun, the neutrino energy spectrum is damped as $e^{-E_\nu/\varepsilon}$, with a critical energy of $\varepsilon \sim 100 \text{ GeV}$. This is because high energy neutrinos can interact with nuclei and be absorbed before escaping the Sun. However, as the solar density decreases exponentially with radius, if neutrinos are injected (by a mediator) at larger radii they suffer much less absorption and finally can propagate out of the Sun. Even for ϕ decay inside the Sun, the neutrino signal can be dramatically enhanced compared to the standard scenario. It is expected that the critical energy scale for absorption increases exponentially with the neutrino injection radius, increasing rapidly once the injection point is moved outside the dense core. In this work, it has been studied the neutrino signal at the Earth from annihilation of secluded DM in the Sun, for a range of DM masses and considering mediator lifetimes $\gamma\tau \geq 10 \text{ s}$. For this case the spectrum of neutrinos is flat with energies from 0 to the DM mass (Bell & Petraki, 2011). It is usually also assumed that the mediators decay with equal branching ratio

to the three neutrino flavors. They will reach the Earth with ratios 1:1:1. For the last two scenarios a detailed oscillations study has not been performed for the propagation of neutrinos, in this work the more conservative assumption has been taken into account in which, after oscillations, all neutrino flavours arrive to the Earth with the same ratio 1:1:1.

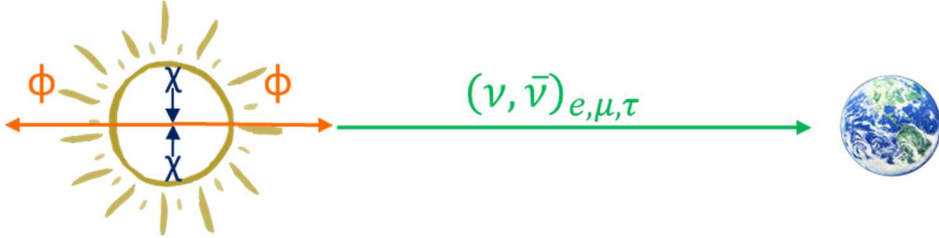


Fig 5.13. Secluded scenario diagram where the mediator decays inside or near the Sun's surface into neutrinos which could be detected by neutrino telescopes.

5.3.3.2.3 Decay probabilities

If the mediator product decay is a di-muon pair, the probability of a mediator with decay length $L = \gamma c \tau$, to decay inside a detector of size d (considering the size of the detector and the typical traveled range by the particles being detected, muons in this case) is given by (Meade et al., 2010):

$$P_{decay} = e^{D/L} (1 - e^{-d/L}) \approx \begin{cases} e^{-D/L} & L \ll D \\ d/L & L \geq D \end{cases} \quad (5.4)$$

D is the distance between the detector and the source. In the second equality above, has been considered two important limits, demonstrating that if the decay length is comparable to or larger than the distance to the source, the probability to observe the particle increases linearly with the size of the detector. This makes the neutrino telescopes very competitive in these searches because these are the largest volume detectors currently available. Conversely, if the mediator is short lived (compared to D), the probability for decaying inside the detector is exponentially small. P_{decay} is maximized when $D = L$. As a consequence, mediators can only be detected if

produced at relatively nearby sources, such as the LHC, the Earth or the Sun. Looking for LOLIPs from DM annihilation in the Galactic center suffer a suppression of at least $P_{decay}^{GC} \sim 10^{17} d / km$, which converts this source unusable for detection or for setting limits. Besides P_{decay} the other dependence on d, D comes in from the usual solid angle suppression $\Delta\Omega = A_{eff} / D^2$, so that when P_{decay} is maximized the total suppression is approximately V_{det} / L^3 where V_{det} is the detector volume.

In the cases which the final detected product is the neutrino the situation changes and, to increase the probability to be detected, the mediator should decay between the source and the detector, not around it. This will be detailed in Section 7.3.

In Chapters 6 and 7, an indirect search for SDM using the 2007-2012 data recorded by the ANTARES neutrino telescope is reported by looking at the different mediator decay products: a) di-muons (a good discrimination between di-muons and single muon is not the priority, but to obtain the best efficiency to detect di-muons from secluded dark matter in the Sun), b) di-muons which in turn, decay into neutrinos and c) neutrinos.

6

Tools and Methods

In this work, a search for SDM in the Sun has been performed using the data recorded by the ANTARES neutrino telescope during 2007 to 2012 period. In this analysis a blinding policy, in order to avoid biases in the event selection, has been followed. The values of some cuts have been selected before looking at the region where the signal is expected. This selection criteria have been chosen to maximize the selection of possible signals (di-muons and neutrinos) produced by mediator (from DM annihilation in the Sun) decay with respect to the atmospheric background. First step on the selection is the estimation, by simulation, of the expected flux on the detector. Once the flux is estimated and taking into account the background in the detector, which will be obtained through scrambled data, the pair of cuts which provides the best flux sensitivity will be selected. The final part of the analysis is the data unblinding, i.e., uncover the ANTARES registered data looking to this region where is expected the best flux sensitivity in order to ensure if there are some significant signal excess over the background (Chapter 7). In this chapter tools and methods for the search of SDM coming from the Sun will be detailed. For the signal expectation,

a new tool developed for simulating the di-muon flux will be described. Moreover, the different background sources implied and the ways to minimize their effects will be discussed. To finalize, the expressions to estimate the ANTARES, di-muon and neutrino flux sensitivities will be discussed.

6.1 Signal expectations

In order to know the di-muon flux ($\phi_{\text{di-}\mu}$), generated by mediators ($m_\phi=1$ GeV) decay, at the Earth surface (Fig 6.1) as a function of the energy of the annihilated WIMP, a new tool called *DiMuGen* has been developed. *DiMuGen* generates and propagates di-muons coming from decay of mediators resulting of dark matter annihilation. The output of this code follows the ANTARES *.evt* format (see Section 6.1.1.1) and acts as input for the Monte Carlo (MC) chain used to obtain the expected number of detected events (n_s).



Fig 6.1. Secluded scenario diagram where the mediator decays in the vicinity of the Earth as two co-linear muons. These could be detected by neutrino telescopes.

In this analysis, the mediators arrive from Sun direction following the zenith and azimuth info of the Sun during the period under study with respect to the ANTARES position. The different detector configurations and periods used in the analysis are presented in Table 6.1. Optimal data runs were selected after Data Quality selection based on external conditions (bioluminescence rates, sea current, etc.), the configuration and behavior of the detector during a given run (number of active units, thresholds, alignment, etc.), and the properties of the run itself (duration, number of

slices, trigger rates, etc.). After that, a total number of 13063 runs were selected which were performed during about 1321 days. Same periods and data of the standard dark matter search in the Sun analysis have been used (Ardid, 2014; Lambard, Zornoza, & Hernandez-Rey, 2013), so the same criteria of data selection and background from scrambled data have been taking into account.

Different background and detector trigger conditions have been applied. Usually one registered detector run condition for each month is used for the di-muon simulation. The number of detected events n_s obtained after each simulation (each year and detection configuration) are weighted taking into account the lifetime of each period.

Year	Direction	Geometry		
		Nº Lines	Runs	Days
2007	Sun	5	1466	192.3
2008	Sun	10	301	36.2
2008	Sun	9	346	45.3
2008	Sun	10	21	1.9
2008	Sun	12	1318	96.6
2009	Sun	12	36	2.4
2009	Sun	11	504	45.5
2009	Sun	10	392	48.05
2009	Sun	9	516	87.3
2009	Sun	8	49	8.5
2009	Sun	10	166	18.3
2010	Sun	10	1399	147
2010	Sun	9	399	41.9
2010	Sun	12	614	51.1
2011	Sun	12	3118	275.4
2012	Sun	12	2418	223.7
Total days				1321

Table 6.1. Different configuration periods used in the simulation and for background estimation using scrambled data

For track reconstruction the algorithm called *BBFit* (J. A. Aguilar et al., 2011) was used. *BBFit* provides a fast and robust reconstruction of neutrino induced upward-going muons and a discrimination of these events from downward-going atmospheric muon background in the data collected by the ANTARES neutrino telescope (See Section 6.2). From the position and time of the hits of the Cherenkov photons in the OMs a muon track is reconstructed. This reconstruction algorithm is based on the minimization of a χ^2 -like quality parameter, Q , which uses the differences between the expected and measured times of the detected photons plus a correction term that takes into account the effect of light absorption:

$$Q = \sum_{i=1}^{N_{hit}} \left[\frac{(t_\gamma - t_i)^2}{\sigma_i^2} + \frac{A(a_i)D(d_\gamma)}{\langle a \rangle d_0} \right] \quad (6.1)$$

where t_γ and t_i are respectively the expected and recorded arrival time of the photons from the track, and σ_i^2 is the timing variance. The second term takes into account the accumulation of high charges in storeys close to the track. This term uses the measured hit charge, a_i , the average hit charge calculated from all hits which have been selected for the fit, $\langle a \rangle$, and the calculated photon travel distance, d_γ , together with a normalization value, d_0 . The functions $A(a_i)$ and $D(d_\gamma)$ are detailed in (J. A. Aguilar et al., 2011).

Depending on the configuration of the detector (number of active lines) and the muon (anti-)neutrino energy, this algorithm yields an angular resolution on the *upgoing* neutrino direction between 1° and 8° .

Basic cuts are applied to the data previously to the χ^2 -like quality parameter minimization:

- Number of hits (storeys) used in the track fit $n_{hit} > 5$. Before starting any fit, the list of selected hits is examined. If the analog PMT signal crosses a preset

threshold, typically $1/3$ photoelectron (p.e.), its arrival time is measured together with its charge. The latter is obtained by integrating the analog PMT signal within a time window of 40 ns. Each such pair of time and charge is called a hit and the corresponding data for each hit are collected. Only events with more than 5 hits are accepted. If all selected hits are on a single detector line, a procedure for a single-line fit is started, otherwise a multi-line fit procedure is performed.

- Number of lines used in the track fit: $nline > 1$ for *MultiLine* (ML) analysis ($nline=1$ for *SingleLine* (SL) analysis).
- $|t_{costh}| < 0.9998$, it refers to cosine of the zenith angle of the fitted track. This cut excludes events for which the fit stopped at the boundary condition for the elevation angle.
- $Q < Q_b$. In the BBFit-like reconstruction two types of fits could be performed. The first one corresponds to the quality parameter of the *track fit*, Eq.(6.1), aimed at the reconstruction of a particle track and the second one to the *bright-point* fit defined for the search of point-like light sources. For each one a quality function is built based on the time differences between the hit times and the expected arrival times of photons from the track or bright-point, as in a standard χ^2 fit. The terms that depend on the measured hit charges and calculated photon travel distances are equally injected. From these, two so-called quality functions, Q and Q_b respectively, are available normalized by the number of degrees of freedom of the fit. As the Q is by definition more efficient for hadronic and electromagnetic showers produced by the downward going muons bundles this will be the fourth element in the basic quality cuts used for this analysis.

In this analysis for each year 10^5 di-muon events generated from $m\chi = 0.03, 0.05, 0.1, 0.2, 0.5, 1, 2, 5$ and 10 TeV, and $m\phi = 1$ GeV, arriving from Sun direction at random time have been simulated. For the higher DM masses ($m\chi = 0.2$ to 10 TeV)

mediator decay outside of the spherical can (Section 6.1.1) have been considered as well adding simulated events in this region following the same approach. To compare and to sum up the outside and inside decay expected signal, the considered volumes (Fig 6.2) should be taken into account in order to weight the number of events of each decay zone.

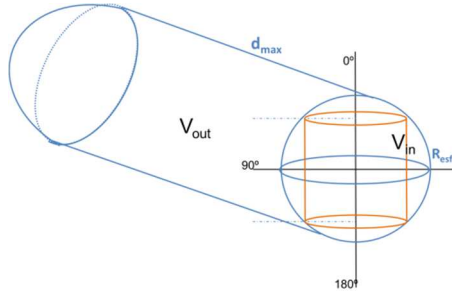


Fig 6.2. Schematic view of the different considered volumes for inside and outside decays.

$$n_s = n_{sin} + \frac{V_{out}}{V_{in}} n_{sout} \quad (6.2)$$

where:

$$V_{out} = \pi R_{sph}^2 d_{max} \quad (6.3)$$

$$V_{in} = \frac{4}{3} \pi R_{sph}^3 \quad (6.4)$$

and R_{sph} is the radius of the spherical can, d_{max} is the maximum travelled distance used in *DiMuGen* for a muon of $M_\chi/2$ energy before reaching the sphere to be detected. For example, the value for the case $M_\chi = 1$ TeV, $m_\phi = 1$ GeV (being $R_{sph}=394.4\text{m}$ and $d_{max}=1749$ m) is $V_{out}/V_{in} = 3.33$.

6.1.1 Di-Muon Generator (*DiMuGen*)

In this section the di-muon signal generator code is described. For simplicity, *DiMuGen* uses a spherical can that contains the typical cylindrical ANTARES detection volume, which surrounds the instrumented detector volume, and defines the limit of simple muon propagation plus Cherenkov light generation and propagation. The detection volume extends typically 3 attenuation lengths beyond the instrumented volume. Fig 6.3 illustrates the relevant numbers of these volumes.

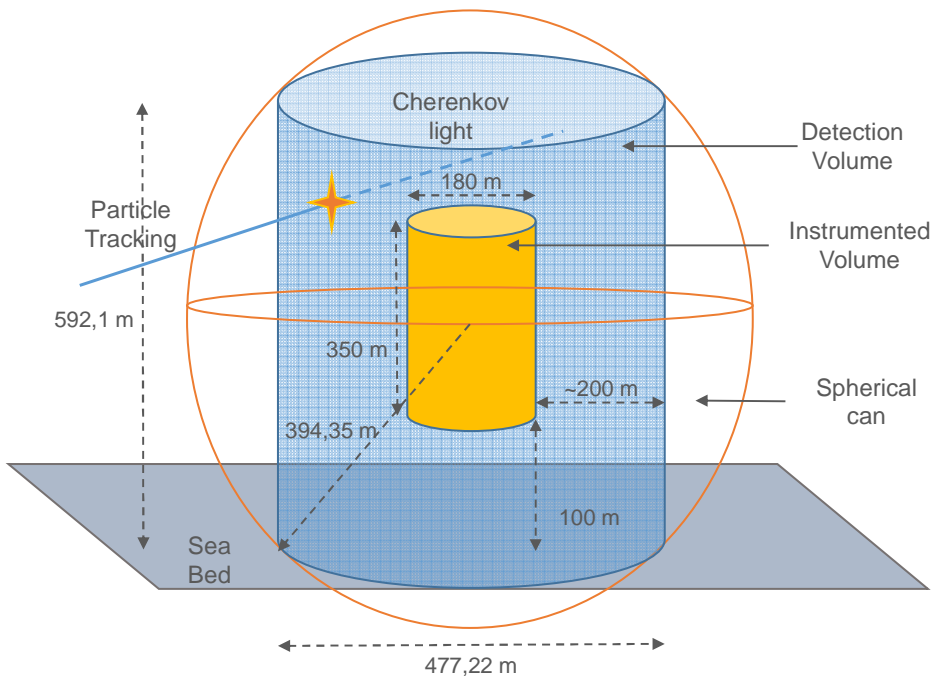


Fig 6.3. Relations between instrumented volume, detection volume and spherical detection can used in *DiMuGen*.

DiMuGen code has two main differentiated parts regarding whether decay occurs inside or outside of the spherical can. Both parts will be explained separately in the following sections. In order to visualize the whole process Fig 6.4 shows a block diagram of the code.

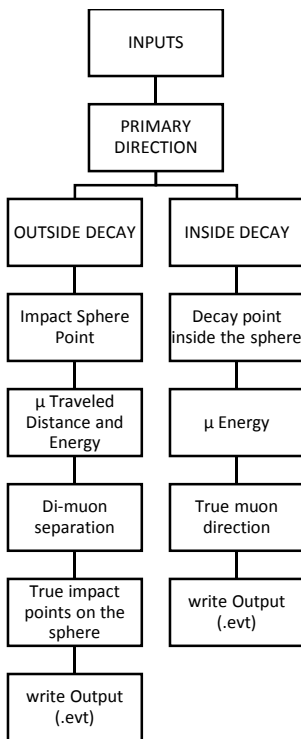


Fig 6.4. Block diagram of the *DiMuGen* main program

6.1.1.1 Inputs and outputs

The *DiMuGen* inputs are six. 1) The number of events to simulate, 2) the WIMP mass ($M\chi$). 3) The mediator mass (m_ϕ), for this analysis typically set to 1 GeV. 4) The decay zone, inside or outside of the spherical can. 5) The main arrival direction, i.e., if the mediators arrive from the Sun or from all incoming directions, the last option useful for diverse physics, systematics, etc.... In next releases could be included the option for mediator coming from the Earth center, this could be an interesting SDM case too. 6) The output directory where the *.evt* output file will be saved.

The output of this code follows the ANTARES *.evt* format. A file containing the list of di-muon tracks. This file consists of a general header, which contains info about

the simulation performed, followed by the list of physics events (Monte Carlo tracks).

Each track entry contains the following information:

```
start_event: 1 1
track_primary: 1 x y z v_x v_y v_z M_χ + (d / 15) t_delay zone
track_in: 1 x1 y1 z1 v_x1 v_y1 v_z1 E1 t_delay P_id
track_in: 2 x2 y2 z2 v_x2 v_y2 v_z2 E2 t_delay P_id
end_event:
```

start_event: indicates the beginning of an event and provides an event number.

track primary: includes the information of the primary track which corresponds to the mediator. x, y, z indicates the hypothetical impact point over the spherical can of the mediator. v_x, v_y, v_z are the director cosines which indicate the mediator direction. $M_χ + (d / 1^5)$ is a control value that indicates the DM mass and distance traveled by the di-muon. t_{delay} indicates whether it has been introduced some delay time. *zone* indicates if the mediator decays inside or outside of the spherical can.

track_in contains the information of each muon with the track number identification. x_1, y_1, z_1 are the coordinates of the impact point over the spherical can. The director cosines are indicated by v_{x1}, v_{y1}, v_{z1} . E_1 is the muon energy. P_{id} is the particle identification, in this case 5 for muons.

Three additional outputs are also available in form of single muon events: *muon1*, which contains only the single muon1 tracks but acquiring the primary direction; *muon2*, which contains only the single muon2 tracks; and *sum*, which contains single tracks with the primary direction and impact points but with energy sum of $E_1 + E_2$.

6.1.1.2 Code description

In the following sections the *DiMuGen* operation is illustrated with 10^5 simulated events of $M_χ = 1TeV$ and $m_φ = 1GeV$. This will be the reference case.

6.1.1.2.1 Primary (mediator) direction $v_0 = (v_x, v_y, v_z)$

The first step, common for inside and outside decays, is the assignment of the mediator direction. If the mediator arrives to the detector from all incoming directions:

$$V_0 = (v_x, v_y, v_z) = (\sin \theta \cos \phi, \sin \theta \sin \phi, \cos \theta) \quad (6.5)$$

where θ will be random between 0 and π weighted as $f(\theta) = \sin(\theta)$, and ϕ will be random between 0 y 2π (See Fig 6.5).

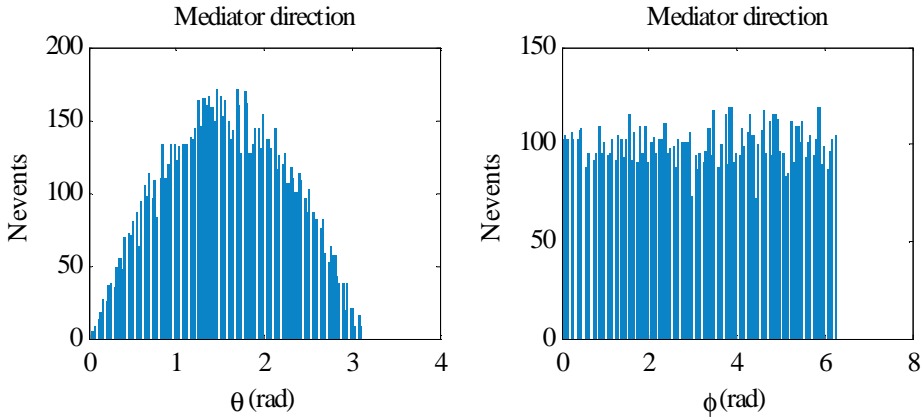


Fig 6.5. θ and ϕ distributions to assign the mediator direction arriving from all incoming directions.

Instead, if the mediator arrives from Sun direction, zenith and azimuth information about the Sun position, with respect to the ANTARES position are obtained in order to assign the Sun direction to the mediators. The matlab© function called *sun_position.m* is used for this purpose. This function computes the Sun position (zenith and azimuth angle) as a function of the observer local time and position. This function follows an algorithm based on numerical approximation of the exact equations. The authors of the original paper (Reda & Andreas, 2008) state that this algorithm should be precise at ± 0.0003 degrees. In *DiMuGen*, if mediator arrives

from Sun direction, it is considered $\theta = \text{zenith}$ and $\phi = -\text{azimuth} - UTM_{conv}$, ($UTM_{conv} = 1.9264\pi/180$ is the convergence angle of the UTM coordinates at the ANTARES site in rad) (Fig 6.6). Finally the direction cosines will be:

$$V_0 = (v_x, v_y, v_z) = -(\sin \theta \cos \phi, \sin \theta \sin \phi, \cos \theta) \quad (6.6)$$

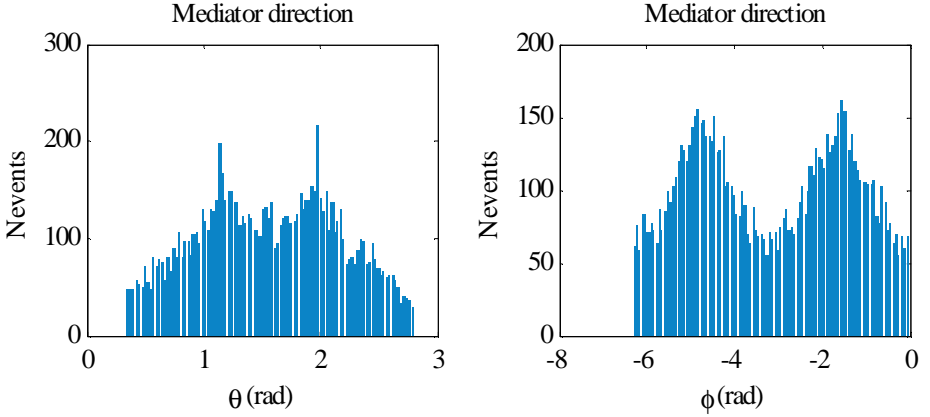


Fig 6.6. θ and ϕ distributions to assign the mediator direction arriving from Sun direction

From this point the code is different if the decay occurs inside or outside the sphere.

6.1.1.2.2 Inside decay

I. Decay point inside the sphere (x, y, z)

After the mediator direction assignment, a decay point inside the spherical should be assigned too (See Fig 6.7). Random values between -1 and 1 are generated for the x, y, z coordinates of the inside decay point. Accepting only internal points, of a sphere of radius 1 a.u., $\sqrt{x^2 + y^2 + z^2} \leq 1$. The decay point coordinates will be then multiplied by the sphere radius.

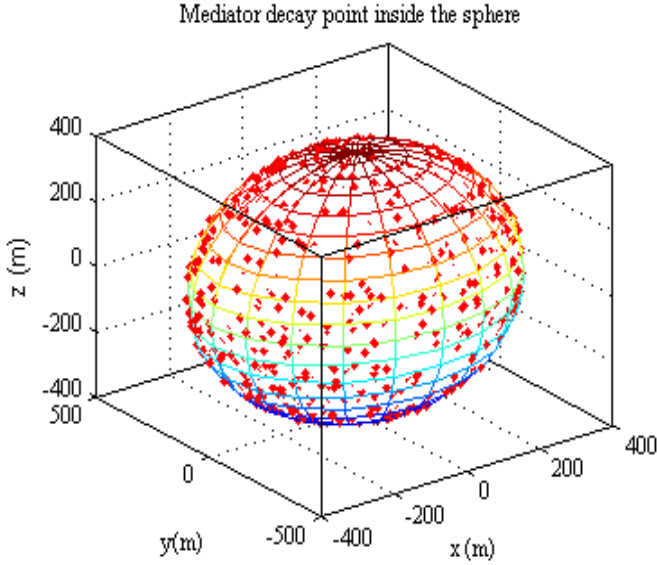


Fig 6.7. Random mediator's decay points inside the sphere.

II. Muon Energy (E_1, E_2)

Once the mediator direction and mediator decay point have been established, muon energy to the di-muon is assigned. In this case, where the decay occurs in the vicinity of the detector, no energy losses are taking into account, so each muon has the same energy, $M_\chi / 2$.

III. Muon direction (V_{01}, V_{02})

Due to the boost during the mediator decay, the two resulting muons suffer a little deviation with respect to the mediator trajectory. To determine the deviation angle with respect to the mediator direction, longitudinal (p_L) and transverse (p_T) momenta are calculated. As DM mass is much greater than mediator mass it is possible to consider $\tan \varphi = p_T / p_L$, where $p_L = E_0$ (in GeV) and $p_T = a_T m_\phi / 2$ (in GeV), being

$a_T = 1 - x_m^2 / \sqrt{x_m^2 + y_m^2 + z_m^2}$, where x_m, y_m and z_m (random values between -1 and 1) will

indicate the random direction of a muon in the mediator's rest frame. Finally, by means of two orthonormal vectors, V_1 and V_2 , to the mediator direction V_0 :

$$V_1 = \frac{(V_{0y}, -V_{0x}, 0)}{\sqrt{V_{0y}^2 + V_{0x}^2}} \quad (6.7)$$

$$V_2 = V_0 \times V_1$$

the final directions of the two muons will be assigned as:

$$V_{01} = V_0 + \tan \varphi (a_1 V_1 + a_2 V_2) \quad (6.8)$$

$$V_{02} = V_0 - \tan \varphi (a_1 V_1 + a_2 V_2)$$

where a_1 is a random value between -1 and 1, and $a_2 = (1 - a_1^2)^{1/2}$.

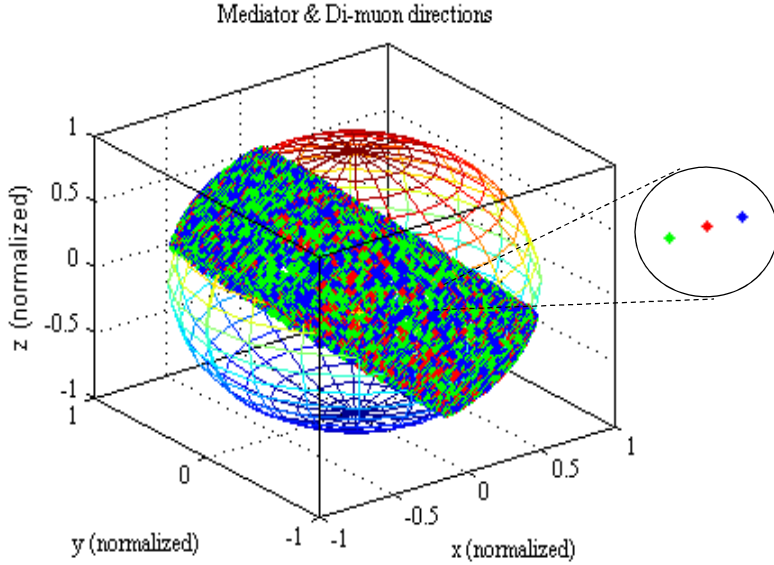


Fig 6.8. Mediator decay point (red) after the direction assignment. Blue and green points show the trajectory deviation of the two muons. In the detailed view, a 500X zoom has been applied.

Fig 6.8 shows the decay point into the sphere (red) and the hypothetical location of the two muons taking into account the deviated trajectory respect to the mediator direction. At this point it is available all the information to complete the output file: mediator's direction, mediator's decay point, muon energies and muon directions.

6.1.1.2.3 Outside decay

If the decay occurs outside of the spherical can, the process is a little bit more complex because of the muon propagation from the decay point to the can.

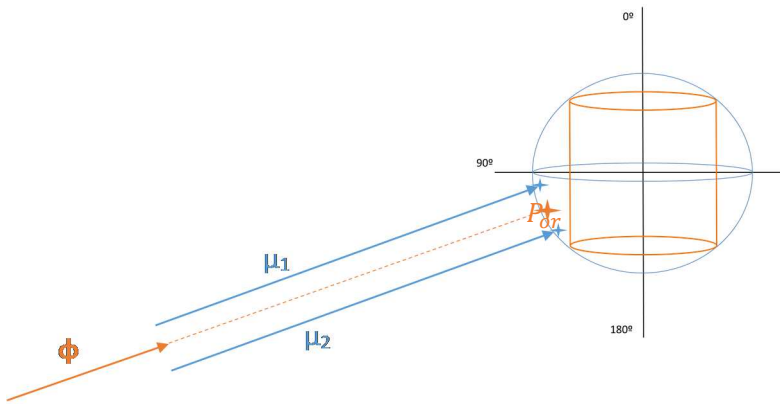


Fig 6.9. Schematic view of the outside decay case.

I. Muon direction (V_{o1}, V_{o2})

In the outside decay case, this occurs far away of the detector. The deviation due to the boost versus the travelled distance is negligible, for this reason, it is considered that the two co-linear muons arrive to the detector maintaining the mediator direction, $V_0 = V_{o1} = V_{o2}$.

II. Di-muon impact point over the sphere (P_o)

In order to know where the di-muons impact over the spherical can, first it is obtained the hypothetical impact point reached by the mediator (Fig 6.9).

$$P_{or} = R_{sph} [\sin \alpha \cos \beta \quad \sin \alpha \sin \beta \quad \cos \alpha] \quad (6.9)$$

being α random between 0 and $\pi/2$, weighted as $f(\alpha) = \sin \alpha$, and β random between 0 and 2π . ($\psi=0$) (See Fig 6.10).

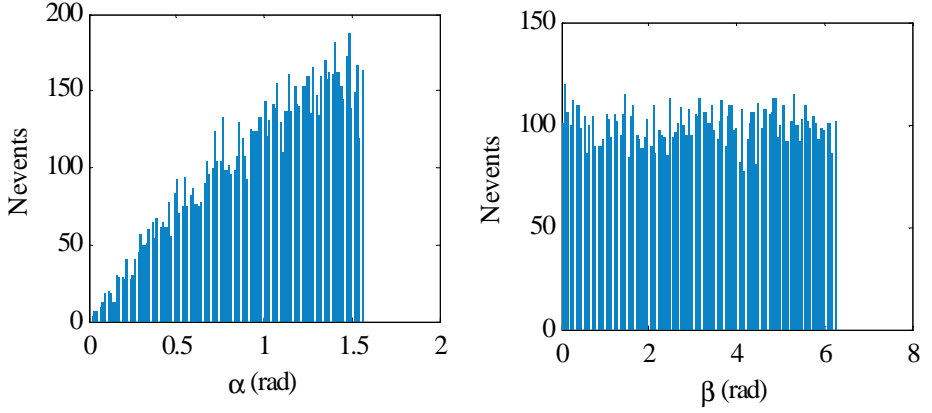


Fig 6.10. α and β distributions to assign the hypothetical mediator impact point over the sphere

This hypothetical impact point is defined with the z axis direction. In order to define it with the mediator direction it is necessary doing the corresponding rotation using the R matrix (Eq.(6.10)). After that, it is obtained the impact point in a perpendicular plane of the mediator direction taking into account the travelled distance and the deviation.

$$R = \begin{bmatrix} \sin-\phi & -\cos-\phi & 0 \\ \cos-\phi & \sin-\phi & 0 \\ 0 & 0 & 1 \end{bmatrix} \begin{bmatrix} 1 & 0 & 0 \\ 0 & \cos-\theta & \sin-\theta \\ 0 & -\sin-\theta & \cos-\theta \end{bmatrix} \begin{bmatrix} \cos\psi & \sin\psi & 0 \\ -\sin\psi & \cos\psi & 0 \\ 0 & 0 & 1 \end{bmatrix} \quad (6.10)$$

III. Traveled distance and energy (d , E_1 , E_2)

The traveled distance of the di-muon is a random number between 0 (that corresponds to mediator decay over the spherical can surface) and d_{max} , maximum distance allowed, usually related to the muon range, calculated by:

$$Rg = \frac{\log(1 + (E_o / E_{crit}))}{b} \quad (6.11)$$

where $E_o = M_\chi / 2$, $E_{crit} = 1029$, that is the muon critical energy in GeV, and $b = (0.3092 \log(E_o) + 0.8189) \cdot 10^{-4} (m^{-1})$.

At this point, knowing the traveled distance between the mediator's decay point and the sphere impact point, the muon energy is calculated. *Fluka*®⁴ simulations have been performed for muons (0.1, 0.5 and 2.5 TeV) in order to parameterize the energy spectrum vs distance and the suffered scattering along the path. Using the simulation results for these masses a parameterization, based on the muon mass and the maximum traveled distance, is proposed for the rest of muon energy cases.

- i. Parametrization of energy spectrum and angle scattering vs distance

DiMuGen generates di-muons with a fixed muon mass (0.5 TeV) as reference, which corresponds to the simulation case of $M_\chi = 1 \text{ TeV}$. For other masses under study some corrections are applied to the results of the reference case for obtaining the scattering angle, the muon energies and the travelled distance to reach the detector:

$$\sigma_1 = \frac{\sigma_{1ref}}{\sqrt{d_{max} / d_{max ref}}} \quad (6.12)$$

$$\sigma_2 = \frac{\sigma_{2ref}}{\sqrt{d_{max} / d_{max ref}}}$$

⁴ *Fluka*© is a general purpose tool for calculations of particle transport and interactions with matter. *Fluka*© can simulate with high accuracy the interaction and propagation in matter of about 60 different particles, including photons and electrons from 1 keV to thousands of TeV, neutrinos, muons of any energy, hadrons of energies up to 20 TeV and all the corresponding antiparticles, neutrons down to thermal energies and heavy ions.

$$d = d_{ref} \left(\frac{d_{max}}{d_{max ref}} \right) \quad (6.13)$$

$$E_1 = E_{1ref} \left(\frac{M_{\chi}/2}{M_{\chi ref}/2} \right) \quad (6.14)$$

$$E_2 = E_{2ref} \left(\frac{M_{\chi}/2}{M_{\chi ref}/2} \right)$$

where the terms named `**_ref` are the results for the reference case di-muons (0.5 TeV), d_{maxref} is the maximum travelled distance, for muons of 0.5 TeV, before reaching the spherical can and $M_{\chi ref} = 1\text{TeV}$, is the reference DM mass. In the following plots (Fig 6.11 and Fig 6.12) the results using *Fluka*© simulations and the new parameterization are compared. 10^4 events of $M_{\chi} = 200$ GeV and $M_{\chi} = 5$ TeV have been simulated and compared with *Fluka* simulations of muons of 100 GeV and 2.5 TeV respectively. These comparisons show good agreement between *Fluka*© simulations results and the results obtained with the parameterization.

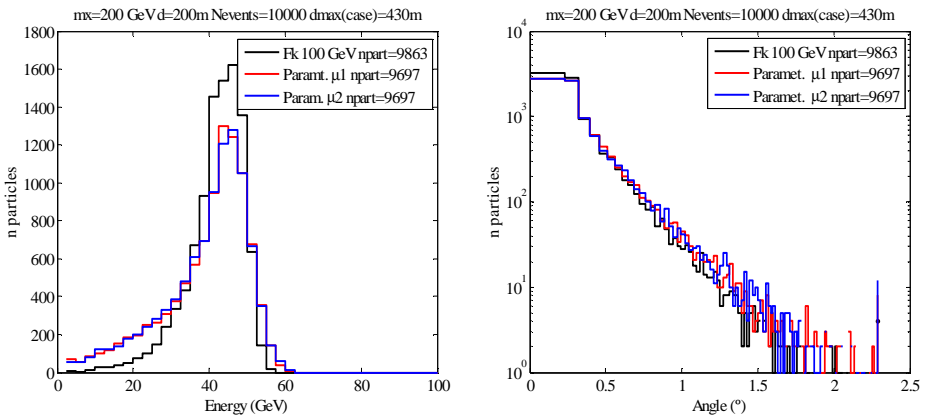


Fig 6.11. *Fluka* vs parameterization comparison for 0.1 TeV muons. Energy spectra comparison (left) and scattering angle (right).

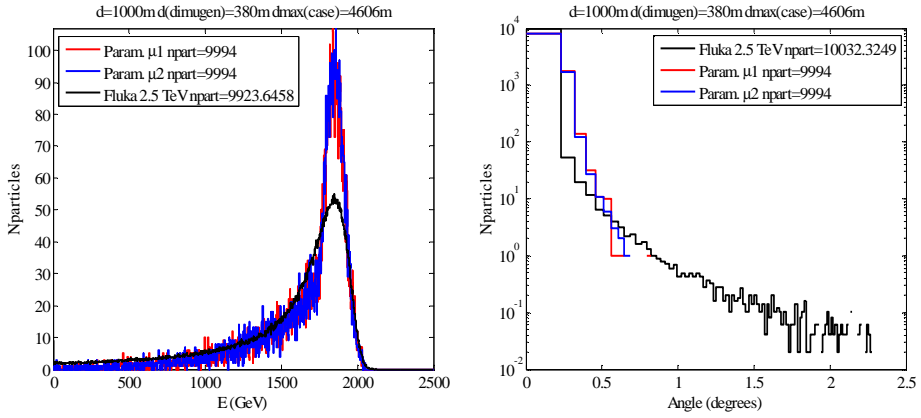
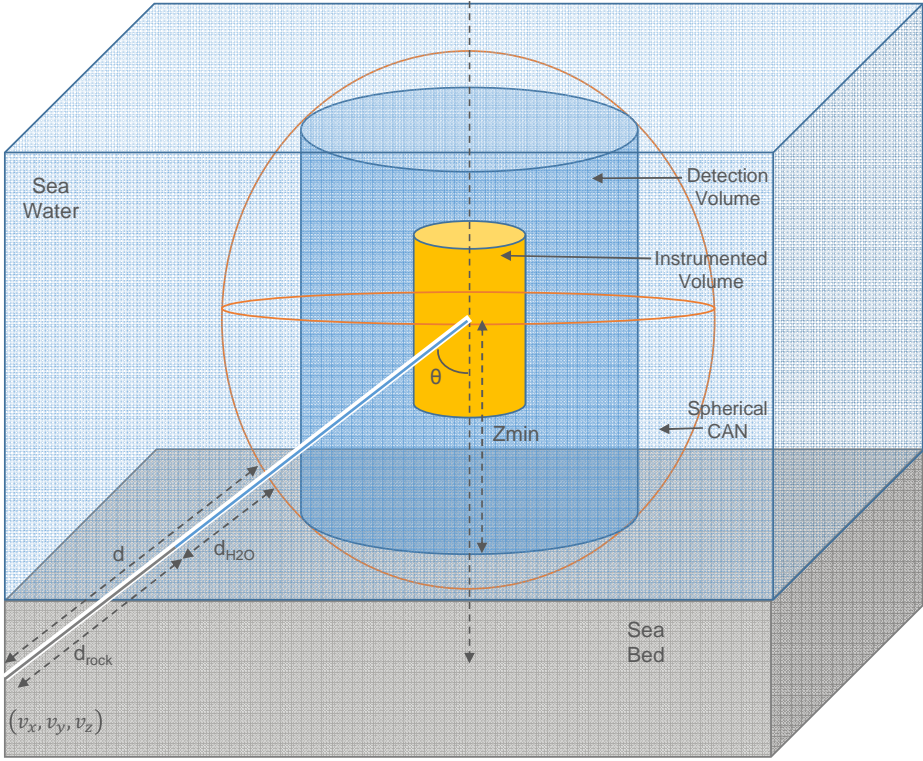


Fig 6.12. Fluka vs parameterization comparison for 2.5 TeV muons. Energy spectra comparison (left) and scattering angle (right).

Assuming that in the decay point each muon has an energy $E_o = M_\chi/2$, the energy losses and the scattering suffered in the path to reach the sphere can be obtained using these parameterizations. This affects the di-muon separation, which is most notably with the distance and consequently to the final impact point over the spherical can.

All of these parameterizations have been done simulating muon propagation in seawater but, if the arrival direction is *upgoing*, part of the propagation occurs in rock (See Fig 6.13). For these *upgoing* events an “equivalent water distance”, longer distance, is calculated in order to take into account the larger losses occurring during the rock propagation.

Fig 6.13. Propagation distances used in *DiMuGen*.

First of all, for all the *upgoing* events, it is calculated the portion of rock and sea water of the whole propagation distance as:

$$\cos \theta = \frac{|z_{\min}|}{d_{H2O_{\max}}} \quad (6.15)$$

as $V_0 = (v_x, v_y, v_z) = -(\sin \theta \cos \phi, \sin \theta \sin \phi, \cos \theta)$:

$$d_{H2O} = \frac{|z_{\min}|}{v_z} - R_{Sph} \quad (6.16)$$

and therefore $d_{rock} = d - d_{H2O}$. The equivalent water propagation distance to the rock propagation distance is calculated as:

$$d_{eq} = d_{H2O} + F d_{rock} \quad (6.17)$$

where $F=2.2$ is the average relation factor between water and rock propagations used. This value of muons has been set according to the range given by PGD (Olive et al., 2014). Fig 6.14 shows the propagation distance distribution for the example case.

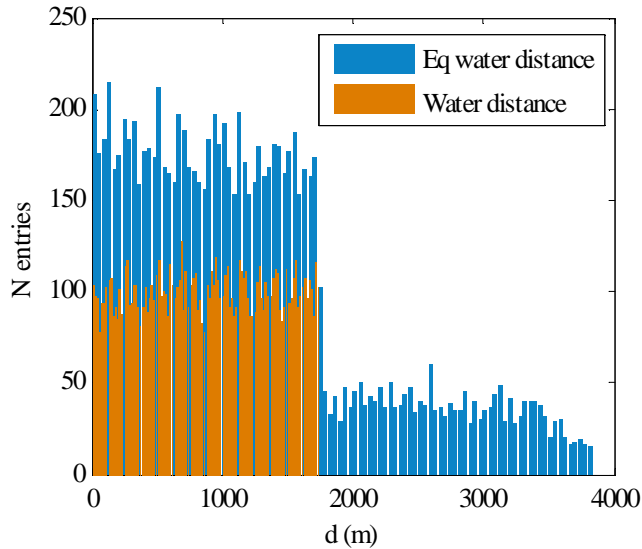


Fig 6.14. Dimuon travelled distance distributions considering only water propagation or the equivalent water distance (water+rock propagation).

After redefining the distances for the *upgoing* muons it is necessary to re-calculate their energy according to d_{eq} . This is performed using again the energy spectrum. These new energy values calculated for d_{eq} already consider losses including the propagation in rock, therefore, lowering energy values. For this reason more cases with energy equal to zero appear (meaning that the muon, finally, has not reached the can) (See Fig 6.15).

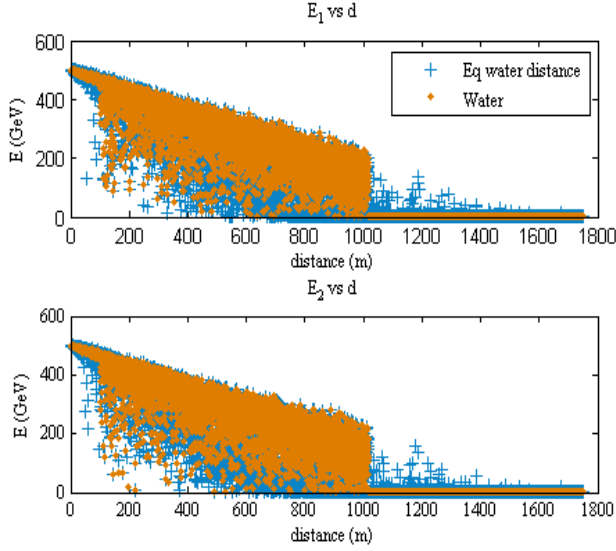


Fig 6.15. Di-muon energy distributions considering only water propagation or water+rock propagation.

IV. True impact points on the spherical can (P1,P2)

Finally, the true di-muon impact points over the sphere are calculated. For this purpose it is necessary knowing the di-muon separation at reaching the spherical can. This separation will be determined by the di-muon deviation at the decay point ($\tan\varphi$ following the same procedure as in the inside case (See Section 6.1.1.2.2.III), the traveled distance to reach the sphere (d) and the scattering suffered for each muon ($\tan\theta_{s1}, \tan\theta_{s2}$) (Fig 6.16).

$$\delta_r = d \tan \varphi \quad (6.18)$$

$$\delta_{r1} = d \tan \theta_{s1} \quad (6.19)$$

$$\delta_{r2} = d \tan \theta_{s2}$$

where δ_r represents the di-muon separation caused by boost during the mediator decay and δ_{r1} and δ_{r2} encompass the separation caused by scattering during the di-

muon propagation. d is the travelled distance, $\tan\varphi = p_T/p_L$, Θ_{s1} and Θ_{s2} are the scattering angle suffered for each muon respectively.

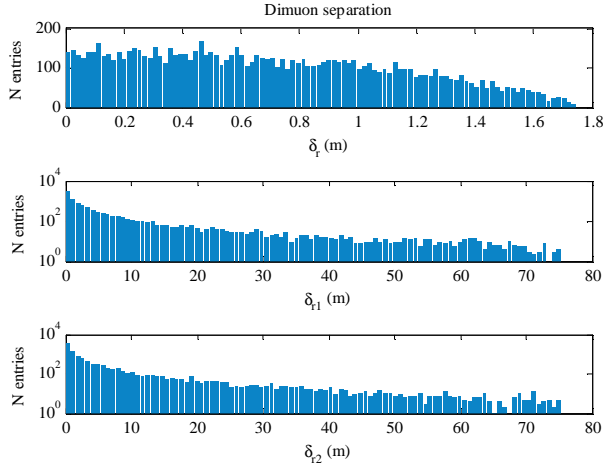


Fig 6.16. Distribution of the di-muon deviation at the decay point (δr) and the scattering suffered for each muon (δr_1 , δr_2).

These separation distances would be in a perpendicular plane to the arrival direction $V_0 = (v_x, v_y, v_z)$. To calculate the impact points on the sphere (Fig 6.17) the two orthonormal unitary vectors of the plane are calculated as:

$$V_1 = \frac{(V_y, -V_x, 0)}{(V_y^2 + V_x^2)^{1/2}} \quad (6.20)$$

As their scalar product is null and no one of them is a null vector:

$$V_0 \cdot V_1 = (V_x, V_y, V_z) \cdot (V_y, -V_x, 0) = V_x V_y - V_y V_x + 0 = 0 \quad (6.21)$$

The second vector is obtained by the vector product $V_2 = V_0 \times V_1$:

$$V_2 = V_0 \times V_1 = \frac{1}{(V_y^2 + V_x^2)^{1/2}} \begin{vmatrix} i & j & k \\ V_x & V_y & V_z \\ V_y & -V_x & 0 \end{vmatrix} = \frac{(V_x V_z, V_y V_z, -V_y^2 - V_x^2)}{(V_y^2 + V_x^2)^{3/2}} \quad (6.22)$$

To obtain the real impact point of each muon:

$$P_1 = P_o + \delta_r (a_1 V_1 + a_2 V_2) + \delta_{r1} (b_1 V_1 + b_2 V_2) \quad (6.23)$$

$$P_2 = P_o + \delta_r (a_1 V_1 + a_2 V_2) + \delta_{r2} (c_1 V_1 + c_2 V_2) \quad (6.24)$$

Being a_1 (and b_1, c_1) random numbers between 0 and 2π weighted as $f(a_1) = \cos(a_1)$ and a_2 (and b_2, c_2) between 0 and 2π weighted as $f(a_2) = \sin(a_2)$.

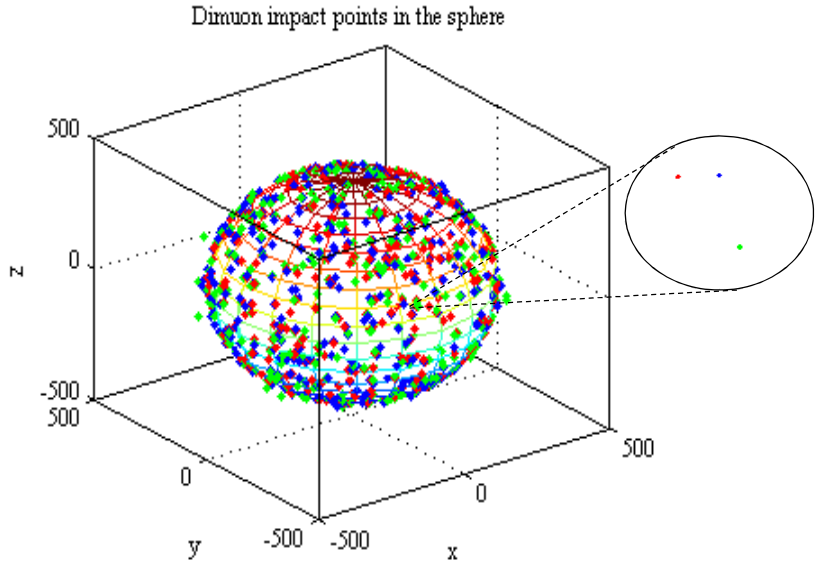


Fig 6.17. Mediator hypothetical impact point (red), blue and green points show the impact points over the sphere of the two muons (Only have been plotted 10^3 events for better visualization. In the detailed view 500X zoom has been applied.

At this point it is available all the information to complete the output file: mediator's direction, di-muon's impact points and muon's energy.

6.2 Background obtained using the scrambled data

There are two sources of muon background in ANTARES, both produced in the interactions of cosmic rays with the Earth's atmosphere:

- i. Down-going atmospheric muons resulting from the interaction of cosmic rays in the atmosphere. Almost all of this is reduced by the Deep sea location and by the reconstruction algorithms that are tuned to *upgoing* events. Cuts on the quality of the tracks are also applied to reject *downgoing* muons wrongly reconstructed as *upgoing*.
- ii. Atmospheric neutrinos produced by cosmic rays. These neutrinos can traverse the Earth, so they can be detected as *upgoing* tracks. This is an irreducible background.

Fig 6.18 shows a comparison between data and Monte Carlo (MC) simulations of:

- a) Miss-reconstructed atmospheric muons performed with the MUPAGE (Atmospheric MUons from PArametric formulas: a fast GEnerator for neutrino telescopes) package (Carminati, Margiotta, & Spurio, 2008).
- b) *Upgoing* atmospheric neutrinos performed with GENHEN (GENerator of High Energy Neutrinos) (Labbate, Montaruli, & Sokalski, 2004,) which is the ANTARES software package to simulate neutrino interaction events in the proximity of the detector.

Fig 6.18 shows the good agreement between the data-MC comparisons. However, for the background estimation scrambled data (randomizing the time) during the period under study was used. This allows to reduce the effect of systematic uncertainties (efficiency of the detector, assumed flux, etc.) from the simulation. The data used correspond to the period from 2007-2012. During almost all 2007 only 5 lines were installed. The number of operative lines was increasing until arriving to 12 in 2008.

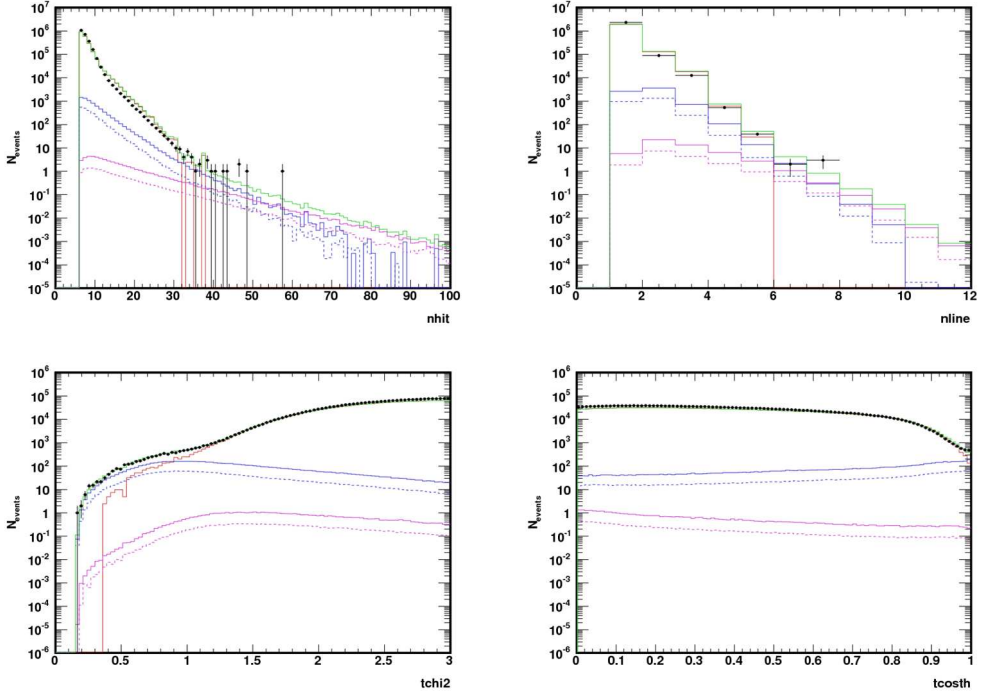


Fig 6.18. Data_MC comparisons for some of the basic cuts. Data (black), MC: miss-reconstructed atmospheric muons (red), *upgoing* neutrinos of energies comprises between $[5\text{-}20\cdot 10^3]$ GeV (blue), *upgoing* neutrinos of energies comprises between $[20\cdot 10^3 - 1^8]$ GeV (pink), all (green). The represented variables have been described in Section 6.1. *tchi2* refers to the quality parameter (Q). (plots from the standard dark matter Sun analysis (Lambard et al., 2013))

6.3 Optimization of the event selection criteria

A binned method is used in order to minimize the sensitivity of ANTARES to the di-muon flux. In this sense, the *Model Rejection Factor* (MRF) (Hill & Rawlins, 2003) is used to optimize the angular distance to the sources, ψ_{cut} , defined as the angular separation between tracks and the Sun's direction, and the track quality cut parameters, Q_{cut} (Ec.(6.1)). The sensitivity for a di-muon flux can be written as:

$$\Phi(E, \theta)_{90\%} = \Phi(E, \theta) \frac{\mu_{90}(n_{\text{obs}}, n_b)}{n_s} \quad (6.25)$$

where $\Phi(E, \theta)_{90\%}$ indicates the upper limit on the source flux calculated scaling the simulated flux $\Phi(E, \theta)$ by the ratio of the upper limit, $\mu_{90}(n_{obs}, n_b)$, and the signal expectation, n_s . The confidence interval at 90%, $\mu_{90}(n_{obs}, n_b)$, is defined as a function of the number of events observed, n_{obs} , and the expected background, n_b . Although it is not possible knowing the upper limit that will result from an experiment until looking at the data, it is possible using the MC predictions to calculate an average upper limit, $\bar{\mu}_{90}(n_b)$, that would be observed after hypothetical repetition of the experiment with expected background, n_b , and no true signal ($n_s=0$) (Feldman & Cousins, 1998). The average upper limit, is the sum of these expected upper limits weighted by their Poisson probability of occurrence:

$$\bar{\mu}_{90}(n_b) = \sum_{n_{obs}=0}^{\infty} \mu_{90}(n_{obs}, n_b) \frac{\binom{n_b}{n_{obs}} e^{-n_b}}{(n_{obs})!} \quad (6.26)$$

The strongest constrain on the expected signal flux $\Phi(E, \theta)$ corresponds to the set of cuts that minimizes the *Model Rejection Factor*, $\bar{\mu}_{90}/n_s$ which, consequently, minimizes the average flux upper limit that would be obtained over the hypothetical repetition of the experiment.

$$\bar{\Phi}(E, \theta)_{90} = \Phi(E, \theta) \frac{\bar{\mu}_{90}}{n_s} \quad (6.27)$$

In the secluded dark matter analysis, decay of mediators in the volumes inside and outside the spherical can have been simulated. To convert this into a flux, the simulated number of events in the inside case has been taken as reference, in this way, the sensitivity to di-muon flux would be given by:

$$\Phi_{di-\mu} = \frac{\left(\frac{N_{sim}}{T_{live}} \right) \bar{\mu}_{90}}{\left(\left(\frac{4}{3} \right) \pi R_{sph}^3 \right)^{2/3}} \quad (6.28)$$

where T_{live} corresponds to the live time (total number of data taking days: 1321), N_{sim} is the number of events simulated inside the can ($1 \cdot 10^5$) and R_{sph} is the radius of the spherical detection can. Notice that the events of the outside case are also considered through n_s , see Eq. (6.2).

6.4 Other interesting cases in Secluded Dark Matter

In the SDM model there are some other interesting cases that have been studied. In all cases DM is annihilated into a mediator which escapes of the dense solar core. The difference lies in the product of the mediator's decay.

6.4.1 Di-muon decay into neutrino

If the mediator decay into di-muons occurs far away to the Earth, the di-muons in turn may also decay, typically into $e^-(e^+), \nu(\bar{\nu})$, the neutrino and antineutrino are muonic and electronic (or vice versa) in each decay. As the products of these decays are three particles it is not trivial knowing the spectrum of neutrinos. For this reason, Michel's spectra have been used (Divari, Galanopoulos, & Souliotis, 2012), in the muon at rest reference frame. Moreover, their boost, taking into account the muon energy (i.e., the DM mass), has been calculated. A detailed oscillation study has not been done for neutrino propagation. The more conservative assumption in which, after oscillations, all neutrino flavours arrive to the Earth with the same ratio 1:1:1 has been considered. As an example, the final spectra of muonic and electronic neutrino, for di-muon decay from $M_\chi=1 \text{ TeV}$ $m_\phi=1 \text{ GeV}$ is shown in Fig 6.19.

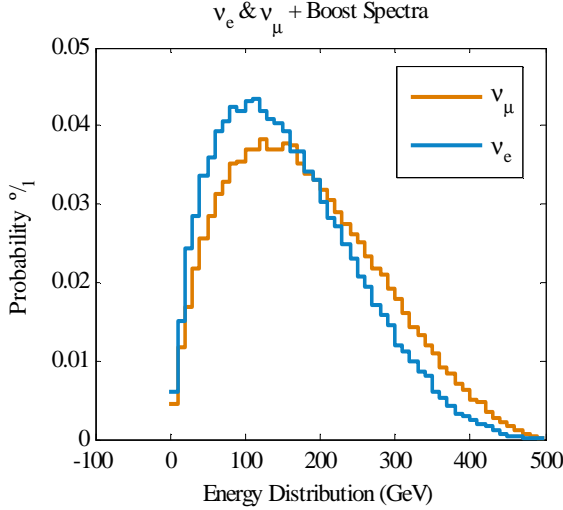


Fig 6.19. Neutrino spectra, from the initial muonic and electronic neutrino, for di-muon decay from $M\chi=1$ TeV $m\phi=1$ GeV.

For the *Di-muon decay into neutrino* case, the process of optimization and minimization of sensitivities was done working with the ANTARES Effective Areas (EffArea) for neutrinos and antineutrinos. The EffArea was calculated by the authors of the Dark Matter Sun analysis 2007-2012 using the standard ANTARES simulation tools (Lambard et al., 2013). In the SDM analysis, the only change respect to the Standard Sun Analysis, is the final energy distribution of these particles.

6.4.2 Mediator decay into neutrino

When the mediator, ϕ , escapes of the Sun core, they could decay directly into neutrinos and antineutrinos, $\phi \rightarrow \nu\bar{\nu}$ (Fig 6.20). In the standard scenario, in which neutrinos are produced at the center of the Sun, absorption is relevant for $E \geq 100 \text{ GeV}$, resulting in a significant suppression of the neutrino spectrum beyond $E \sim 1 \text{ TeV}$. The neutrino energy spectrum is damped as $e^{-E_\nu/\mathcal{E}}$, with a critical energy of $\mathcal{E} \sim 100 \text{ GeV}$. This occurs because high energy neutrinos can interact with nuclei and be absorbed before escaping the Sun. However, as the solar density decreases exponentially with

radius, if neutrinos are injected (by a mediator) at larger radii they are subject to much less absorption and finally can propagate out of the Sun. Even for ϕ decay inside the Sun, the neutrino signal can be dramatically enhanced compared to the standard scenario. It is expected that the critical energy scale for absorption increases exponentially with the neutrino injection radius, increasing rapidly once the injection point is moved outside the dense core.

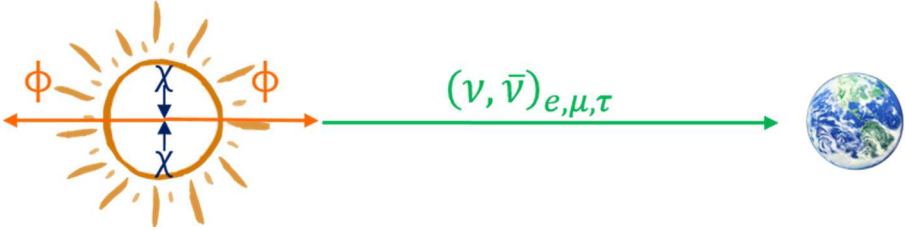


Fig 6.20. Secluded scenario diagram where the mediator escapes the solar dense core and decays into neutrino.

In the *mediator decay into ν* case, the neutrino signal at the Earth from annihilation of secluded DM in the Sun, for a range of DM masses and considering mediator lifetimes $\gamma\tau \geq 10s$ has been analyzed. For this case the spectrum of neutrinos is flat with energies from 0 to the DM mass (Bell & Petraki, 2011). It is usually also assumed that the mediators decay with equal branching ratio to each of the three neutrino flavors and will reach the Earth with ratios 1:1:1.

For the optimization of the last SDM cases: *Di-muon decay into ν* and *mediator decay into ν* the sensitivity to neutrino flux would be given by:

$$\Phi_{\nu+\bar{\nu}} = \frac{\bar{\mu}_{90}/A_{eff}^{\nu+\bar{\nu}}}{T_{live}} \quad (6.29)$$

where T_{live} corresponds to the live time (total number of data taking days: 1321), $\bar{\mu}_{90}$ is the average upper limit of the background at 90% CL computed using a Poisson

distribution in the Feldman-Cousins approach (Feldman & Cousins, 1998). $A_{eff_{\nu+\bar{\nu}}}$ is the effective area averaged over the neutrino energy defined as:

$$A_{eff_{\nu+\bar{\nu}}}(M_\chi) = \sum_{\nu, \bar{\nu}} \left(\frac{\int_{E_\nu^{th}}^{M_\chi} A_{eff}^i(E_{\nu, \bar{\nu}}) \frac{dN_{\nu, \bar{\nu}}}{dE_{\nu, \bar{\nu}}} dE_{\nu, \bar{\nu}}}{\int_0^{M_\chi} \frac{dN_\nu}{dE_\nu} dE_\nu + \frac{dN_{\bar{\nu}}}{dE_{\bar{\nu}}} dE_{\bar{\nu}}} \right) \quad (6.30)$$

where $E_\nu^{th} = 10 GeV$ is the energy threshold for neutrino detection in ANTARES, M_χ is the WIMP mass, $dN_{\nu, \bar{\nu}}/dE_{\nu, \bar{\nu}}$ is the energy spectrum of the (anti-)neutrinos at the surface of the Earth, and is the effective area of ANTARES as a function of the (anti-) neutrino energy for tracks coming from the direction of the Sun below the horizon. Due to their different cross-sections, the effective areas for neutrinos and anti-neutrinos are slightly different and therefore are considered separately. In addition, the fluxes of muon neutrinos and anti-neutrinos from the Sun and are convoluted with their respective efficiencies. (i index denotes the periods with different detector configurations (5, 9, 10 and 12 detection lines))

7

Analysis and Results

The last part of the search of SDM with ANTARES is the data unblinding, i.e., uncover the registered data for looking to the region where the best flux is expected. In order to know what is this region, simulations have been performed using the tools and following the methods described in the previous chapter. In this chapter will be presented the flux sensitivities obtained after simulation of the different scenarios. Moreover the strategy to unblind the data, fixing the angular separation between tracks and the Sun's direction (ψ_{cut}) and the track quality parameter (Q_{cut}), will be described. To finalize, the ANTARES limits for the SDM model in the Sun will be shown.

7.1 Flux sensitivities

In this analysis a blinding policy, in order to avoid biases in the event selection, has been followed. The values of the cuts (Q_{cut} and ψ_{cut}) have been chosen before looking at the region where the signal is expected. For this reason, the simulation of the different scenarios provides valuable information about the expected flux of di-muons and neutrinos coming from mediator decay or coming from di-muon decay.

Following the minimization process described in Chapter 6 section 6.3, the ANTARES flux sensitivity was obtained for the different scenarios. In the first case, di-muons as product of mediators' decay in the vicinity of the detector have been simulated. Both mediator's decay cases, inside and outside of the spherical can, have been simulated. The ANTARES sensitivity to di-muon flux (Eq.(6.27)) was obtained minimizing the MRF, $(\bar{\mu}_{90}/n_s)$, considering the number of obtained events (n_s) in the simulation. An example of the number of events distribution is shown in Fig 7.1. In the other SDM cases (Sections 6.4.1 and 6.4.2), the sensitivity to neutrino flux (Eq.(6.28)) was obtained minimizing the MRF, $(\bar{\mu}_{90}/Aeff_{\nu+\bar{\nu}})$, considering the effective area ($Aeff_{\nu+\bar{\nu}}$) for (anti-)neutrinos. An example of the effective area for (anti-)neutrinos is shown in Fig 7.2. The average upper limit in the half-cone angle parameters space used to optimize the flux sensitivity for all cases is shown in Fig 7.3.

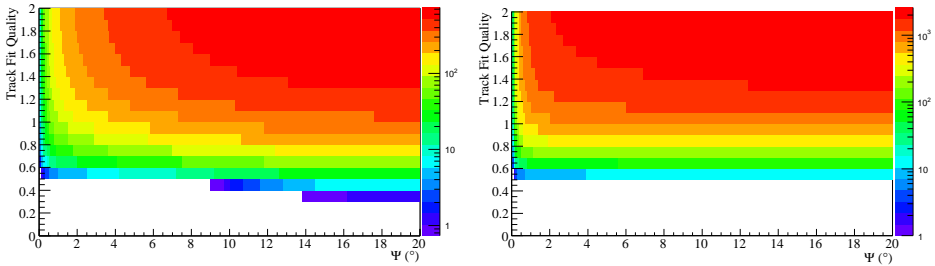


Fig 7.1. Number of detected events, n_s , amount in the Q, half-cone angle parameter space for *SingleLine* (left) and *MultiLine* (right) analysis according to simulations corresponding to $m\chi=1$ TeV $m\phi=1$ GeV. The colorbar indicates the number of events.

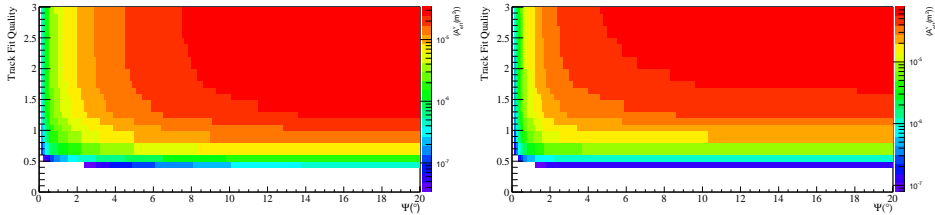


Fig 7.2. Effective area (m^2) in the Q, half-cone angle (zenith band width) parameters space for SL (left) and ML (right) analysis for the simulation

corresponding to $m\chi=1$ TeV, $m\phi=1$ GeV. The colorbar indicates the Effective area (m^2).

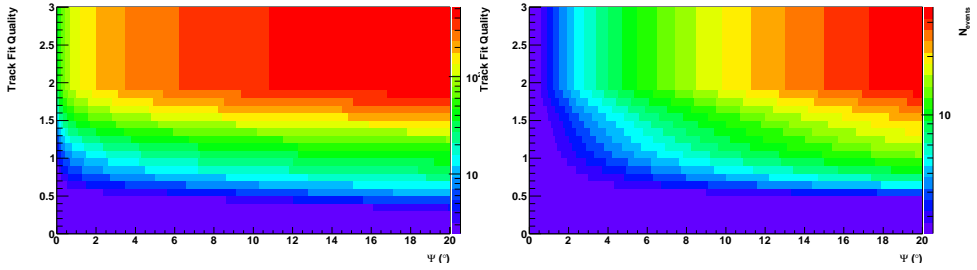


Fig 7.3. Average upper limit $\bar{\mu}_{90}(n_b)$ (Eq. 6.28) in the Q, half-cone angle parameters space for SingleLine (left) and MultiLine (right) analysis. The colorbar indicates the number of events.

The best flux sensitivity, for each DM mass and each strategy, is expected for the pair of cuts, track fit quality (Q_{cut}) and half-cone (bandwidth) angle (ψ_{cut}), which minimize the MRF. Fig 7.4 shows the di-muon flux sensitivity obtained with the two reconstruction strategies. Usually, *SingleLine* strategy is used for low energy events. Likewise, Fig 7.5 and Fig 7.6 show the neutrino flux sensitivities of the two other SDM scenarios.

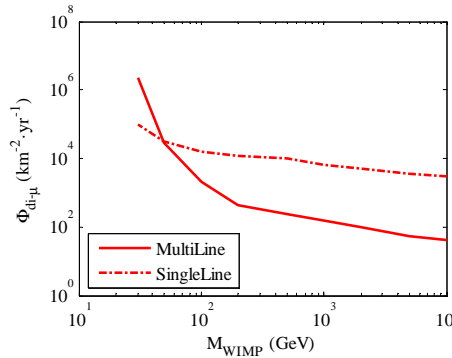


Fig 7.4. Di-muon flux sensitivities using the optimum cuts

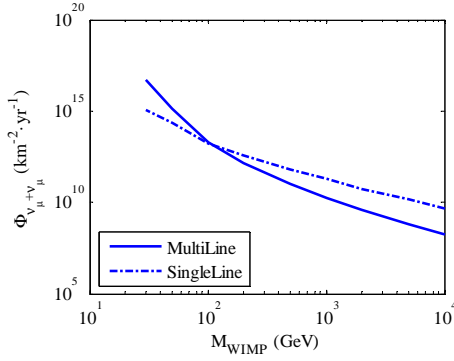


Fig 7.5. Sensitivities to $V+\bar{V}$ flux coming from di-muon decay using the optimum cuts

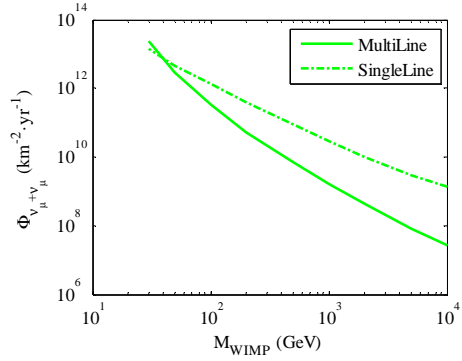


Fig 7.6. Sensitivities to $V+\bar{V}$ flux coming from mediator decay using the optimum cuts

The values of the optimum cuts for each dark matter mass, strategy and SDM scenario are presented in Annex A. The values of the MRF minimization and the di-muon (or neutrino) fluxes are also shown.

7.2 Unblinding Strategy

Optimizing for each mass, strategy (*MultiLine* and *SingleLine*) and SDM scenario results in many observation trials. Taking into account that the differences in flux sensitivities using different cuts is not large, the number of cuts to be used for the unblinding has been set to six (Table 7. 1) since they were representative enough, for simplicity, inasmuch as the losses in discovery potential were small, and in order not to increase the trial factor. The six cuts (4 for *MultiLine* (ML) and 2 for *SingleLine* (SL)) are sufficient to deal with the different energy ranges, strategy and scenario.

To enhance the sensitivity to the di-muon case, three different cases were proposed to use for ML analysis: for masses lower than $M_\chi=0.2$ TeV the optimum cuts for $M_\chi=0.1$ TeV (Cut 3: $Q_{\text{cut}}=1.6$, $\psi_{\text{cut}}=2$) are used; for masses between 0.2 TeV up to 5 TeV, the optimum cuts for $M_\chi=1$ TeV (Cut 2: $Q_{\text{cut}}=1.6$, $\psi_{\text{cut}}=1.4$) are selected and finally, for higher masses the optimum cut for $M_\chi=10$ TeV (Cut 1: $Q_{\text{cut}}=1.8$,

$\psi_{\text{cut}}=1.3$) are used. For SL analysis, the optimum cuts for $M_\chi = 0.05$ TeV ($Q_{\text{cut}} = 1$, $\psi_{\text{cut}}=12.8$) are used for all M_χ .

In order to enhance sensitivity for both neutrino cases a ML Cut 4: $Q_{\text{cut}}=1.4$ $\psi_{\text{cut}}=2.6$ are used for lower masses whereas the previous Cut 1: $Q_{\text{cut}}=1.8$ $\psi_{\text{cut}} = 1.3$ are selected at the highest masses studied. For SL analysis, it has been used $Q_{\text{cut}} = 0.7$ $\psi_{\text{cut}} = 11.3$ for all masses. Table 7.1. summarizes the final selected cuts for the correspondent energy ranges and scenarios.

<i>Reconstruction</i>	N_{cut}	Q_{cut}	$\psi_{\text{cut}}(^{\circ})$	<i>Di-μ</i>	<i>Di-μ into ν</i>	ϕ into ν
<i>MultiLine</i>	1	1.8	1.3	$M_\chi > 5\text{TeV}$	$M_\chi > 5\text{TeV}$	$M_\chi \geq 2\text{TeV}$
<i>MultiLine</i>	2	1.6	1.4	$0.2\text{TeV} \leq M_\chi \leq 5\text{TeV}$	-	-
<i>MultiLine</i>	3	1.6	2	$M_\chi < 0.2\text{TeV}$	-	-
<i>MultiLine</i>	4	1.4	2.6	-	$M_\chi \leq 5\text{TeV}$	$M_\chi < 2\text{TeV}$
<i>SingleLine</i>	1	1	12.8	All M_χ	-	-
<i>SingleLine</i>	2	0.7	11.3	-	All M_χ	All M_χ

Table 7. 1. Summary of the proposed cuts for the unblinding data evaluation.

Fig 7.7 shows the ratio between the flux sensitivity obtained using the optimum cuts (Annex A) and the flux sensitivity obtained using the proposed ones (Table 7. 1) for the Di-muon case. This factor represents the worsening in sensitivity when the proposed cuts are used with respect to optimum ones. For most of the masses values close to 1 are obtained, with some specific cuts, so it can be concluded that the effect will not be large.

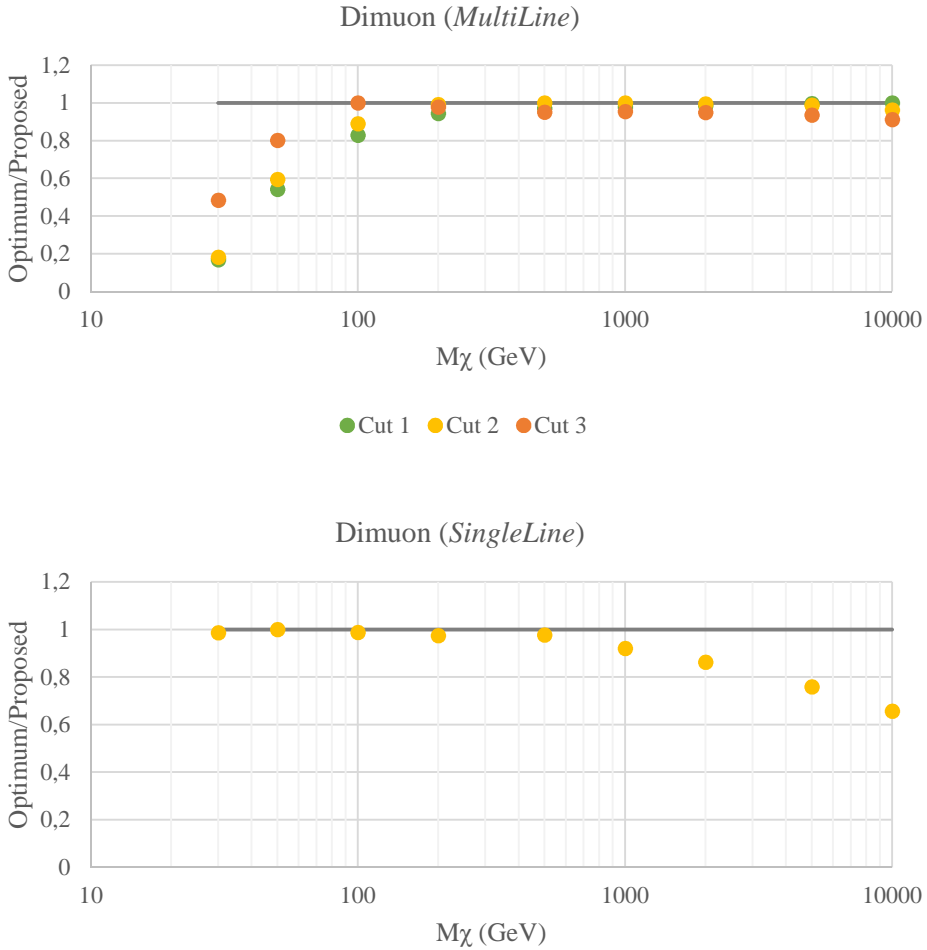


Fig 7.7. Ratio between the sensitivity obtained using the optimum cuts and the sensitivity obtained using the proposed ones. On top for ML analysis, on the bottom for SL analysis.

For each DM mass the cut which ratio value is nearest to one was selected for estimating the final flux. The comparison of flux sensitivity using the proposed cuts with the optimal ones are presented in Fig 7.8, Fig 7.9 and Fig 7.10. In these figures it is also appreciated that the effect of using these proposed ones in the final flux is small.

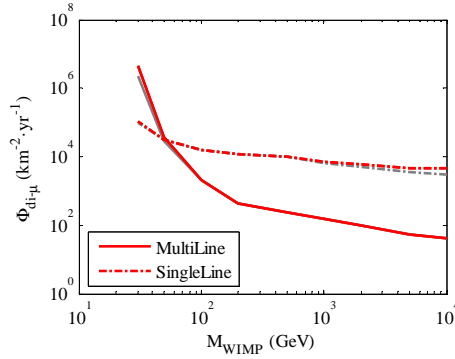


Fig 7.8. Di-muon flux sensitivities using the proposed cuts (red) and the optimum cuts (gray).

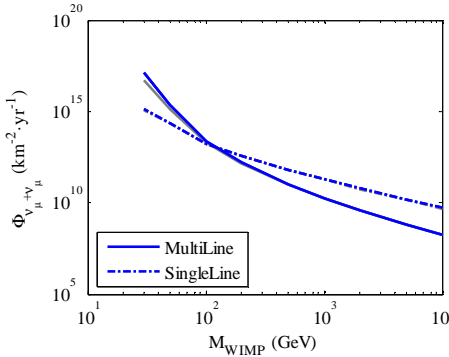


Fig 7.9. Sensitivities to $V+\bar{V}$ flux coming from di-muon decay using the proposed cuts (blue) and the optimum cuts (gray). Gray lines are difficult to appreciate because the fluxes using the proposed cuts are almost the same

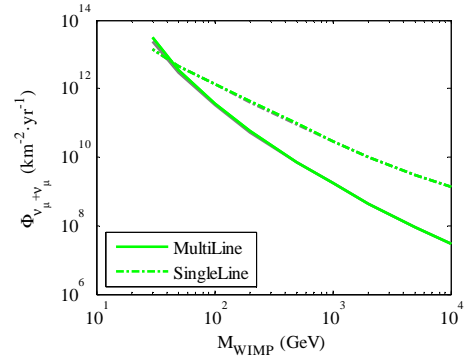


Fig 7.10. Sensitivities to $V+\bar{V}$ flux coming from mediator decay using the proposed cuts (green) and the optimum cuts (gray).

7.3 Sensitivity in terms of annihilation rates

The probability of a mediator, with a decay length $L = \gamma c \tau$, of decaying in the vicinity of a detector of size d is given by Equation (7.1) (Meade et al., 2010).

$$P_{decay} = 2\Gamma\left(\frac{d^2}{4\pi D^2}\right) e^{(-D/L)} (1 - e^{(-d/L)}) \quad (7.1)$$

where:

- $\Gamma = \Gamma_{ann} \times R_{hid} \times BR_{\mu}$: Γ_{ann} is the product of the annihilation rate, $R_{hid} = \sigma(DM DM \rightarrow \phi) / \sigma_{total}$ is the fraction of annihilations that produces mediators, and BR_{μ} , which is the branching ratio of mediators (ϕ) into muons (μ). For simplicity, branching ratios 1 for the channel considered are assumed ($R_{hid} = 1$ and $BR_{\mu} = 1$), given this the use of Γ and Γ_{ann} is equivalent.
- d : is the detector size. For simplicity, fluxes are referred to mediators which decay occurs inside of a sphere, with a characteristic distance $d = (V_{in})^{1/3}$.
- D : Is the distance between the Sun and the Earth.
- $L = \gamma c \tau$ is the mediator's decay length. γ is the relativistic factor, in this case $\gamma = M_{\chi} / m_{\phi}$.

In the first term of Eq.(7.1), two times the annihilation factor is because two mediators are produced in each annihilation of DM. In the second term the solid angle suppression is taken into account. The third one takes into account the probability of decaying before reaching the detector and in the last one the probability of decaying inside the reference detector is considered. P_{decay} can be related with the average flux upper limit (Eq.(6.27)) for each M_{χ}, m_{ϕ} simulated pair through the expression (Eq.(7.2)).

$$2\Gamma \left(\frac{d^2}{4\pi D^2} \right) e^{(-D/L)} \left(1 - e^{(-d/L)} \right) = \left(\frac{N_{sim}}{T_{live}} \right) \frac{\bar{\mu}_{90}}{n_s} = \Phi_{di-\mu} d^2 \quad (7.2)$$

Grouping the terms, the sensitivity can be defined in terms of annihilation rate as:

$$\Gamma = \frac{\Phi_{di-\mu}}{2 \left(\frac{1}{4\pi D^2} \right) e^{(-D/L)} \left(1 - e^{(-d/L)} \right)} \quad (7.3)$$

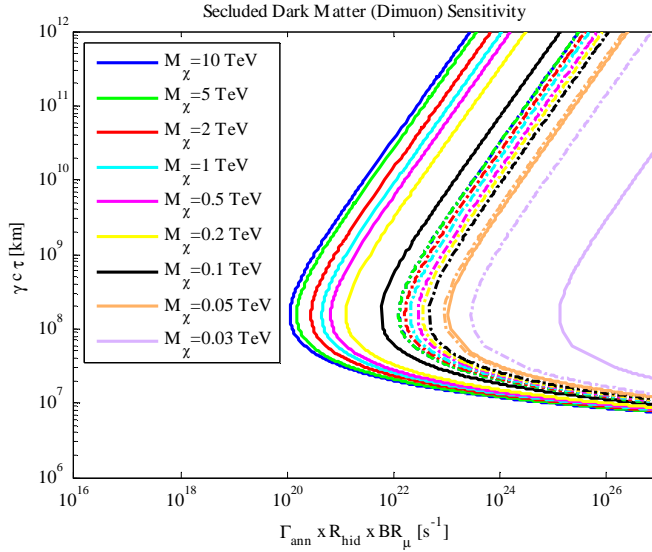


Fig 7.11. ANTARES reach for detecting mediators produced in the Sun and decaying into di-muons as a function of the DM annihilation rate and mediator decay length. Results for different DM mass and $m\phi=1$ GeV using *BBfit* Singleline (dashed) and *Multiline* (solid) reconstruction strategies are shown. Results of sensitivities obtained using the proposed cuts.

Fig 7.11 shows the reach of the ANTARES neutrino telescope to detect mediators coming from DM annihilation and decaying into di-muons, as a function of the DM annihilation rate and the decay length of the mediator. It is easily discernible that the reach of ANTARES to di-muons is limited by the solar radius ($\sim 7 \cdot 10^5$ km). Mediators which do not escape of the Sun are not detected. The detection rate is maximized when the mediator decays at or in the vicinity of the detector, i.e., when the lifetime of the mediator is enough to reach the Earth surface. Above this lifetime value, the detection probability decreases linearly with the decay length.

Similarly, sensitivity in terms of annihilation rates can be defined for the other two SDM scenarios. Equation (7.4) describes the sensitivity in terms of annihilation rates for detecting mediators which decay into di-muons between the Sun and the Earth and they, in turn, decay into neutrinos. Likewise, equation (7.5) describes the

sensitivity in terms of annihilation rates for detecting mediators which decay directly into neutrinos. The differences between the three expressions (equations: (7.3), (7.4) and (7.5)) lie in the different decay products.

$$\Gamma = \frac{\frac{\bar{\mu}_{90}}{Aeff_{\nu+\bar{\nu}}} 4\pi D^2}{\frac{8}{3} T_{live} (e^{-R_{sun}/L} - e^{-D/L})} = \frac{\Phi_{\nu+\bar{\nu}} 4\pi D^2}{\frac{8}{3} (e^{-R_{sun}/L} - e^{-D/L})} \quad (7.4)$$

$$\Gamma = \frac{\frac{\bar{\mu}_{90}}{Aeff_{\nu+\bar{\nu}}} 4\pi D^2}{\frac{4}{3} T_{live} (1 - e^{-D/L})} = \frac{\Phi_{\nu+\bar{\nu}} 4\pi D^2}{\frac{4}{3} (1 - e^{-D/L})} \quad (7.5)$$

Fig 7.12 shows the reach of the ANTARES neutrino telescope to detect mediators coming from DM annihilation which decay into di-muons and finally decay into neutrinos, as a function of the DM annihilation rate and the decay length of the mediator. Three different regions can be observed in the plot: Best sensitivity is obtained when the mediator decays in the vicinity of the Earth. The sensitivity remains almost constant while the decay length is enough to escape out of the Sun. If the decay length of the mediator is longer than the Sun Earth distance, the sensitivity decreases linearly with the decay length.

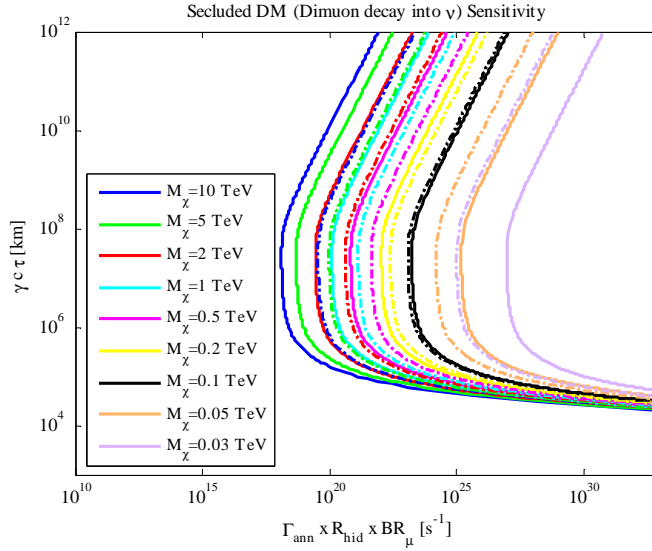


Fig 7.12. ANTARES reach for detecting mediators produced in the Sun and decaying into di-muons and finally into neutrinos (before reaching the Earth) as a function of the annihilation rate and decay length. Results for different DM mass and $m_\phi = 1$ GeV using *BBfit Singleline* (dashed) and *Multiline* (solid) reconstruction strategies are shown. Results of sensitivities obtained using the proposed cuts.

Fig 7.13 shows the ANTARES reach for detecting mediators produced in the Sun and decaying into neutrinos as a function of the annihilation rate and decay length. In this case, mediators with lifetime higher than 10 seconds have been studied, so it is assumed that the mediator escapes of the Sun. Here again, the best sensitivity is obtained when the mediator decays between the Sun and the Earth, decreasing linearly when the decay length exceed the Sun-Earth distance.

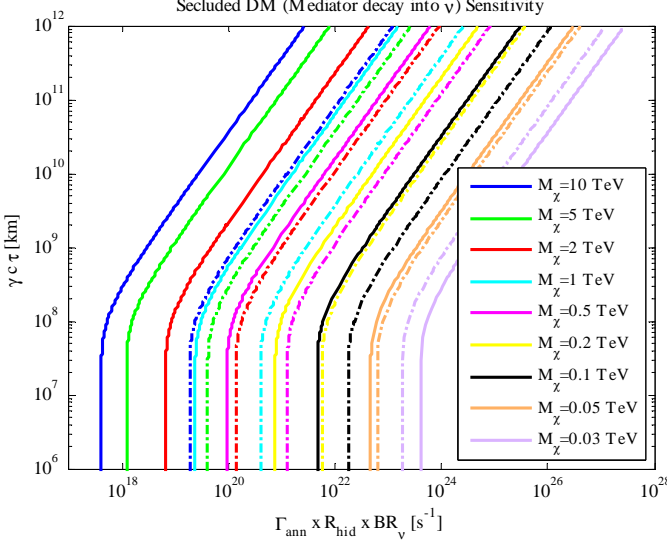


Fig 7.13. ANTARES reach for detecting mediators produced in the Sun and decaying into neutrinos as a function of the annihilation rate and decay length. Results for different DM mass and $m\phi = 1$ GeV using *BBfit Singleline* (dashed) and *Multiline* (solid) reconstruction strategies are shown.

7.4 Cross Section Sensitivities

For the study of the SDM model, the assumption whereby the annihilation balances the DM capture in the Sun has been taken into account, $\Gamma_{ann} = C_{\odot} / 2$. The capture can be approximately obtained by Eq.(5.2), where, σ_{sc} and σ_{sl} are the spin-dependent (SD) and spin-independent (SI) cross sections respectively. The limits on the SD and SI WIMP-proton scattering cross-sections are derived for the case in which one or the other is dominant. Following these assumptions, the spin-dependent cross-section will be:

$$\sigma_{SD} = \left(\frac{2\Gamma_{ann}}{10^{20} s^{-1}} \right) \frac{10^{-40} cm^2}{2.77} \left(\frac{1TeV}{M_{\chi}} \right)^{-2} \quad (7.6)$$

Likewise, the spin-independent cross-section will be:

$$\sigma_{SI} = \left(\frac{2\Gamma_{ann}}{10^{20} s^{-1}} \right) \frac{10^{-40} cm^2}{4.27 \cdot 10^3} \left(\frac{1TeV}{M_\chi} \right)^{-2} \quad (7.7)$$

Authors, in this reference (Ibarra et al., 2014), relies on assumptions on the density and velocity distributions of dark matter particles in the Solar System, as well as on the composition and density distribution of the interior of the Sun (A. Gould, 1987). These assumptions along with the model considered are the cause of little differences between the expressions obtained by different authors. For example, σ_{SD} calculated by the (Kamionkowski, 1991) proposal differs a factor about 3 to 5 (depending on the M_χ) with the (Ibarra et al., 2014) one. The case of σ_{SI} is a little bit more complex due the M_χ dependence used for diverse authors in the bibliography. Ibarra et al. consider a quadratic dependence while (Bell & Petraki, 2011) consider a lineal dependence and (Meade et al., 2010) consider $(M_\chi)^{3/2}$

The results of this work have been obtained following the capture rate proposed by (Ibarra et al., 2014).

As was presented in the previous sections, the sensitivity in terms of the annihilation rates depends on the lifetime of the mediator. For the cross-section evaluation it will be convenient to set a value of the lifetime of the mediator. To see the maximum potential for these models, lifetime values for which the sensitivities are the best have been assumed. For the di-muon case, the lifetime has to be long enough to assure that the mediator reach the vicinity of the Earth (see Fig 7.11). Following this, the best sensitivity is obtained for mediators with decay length $L = \gamma c \tau = 1.5 \cdot 10^8 km$ (distance between the Sun and the Earth). In both neutrino cases the lifetime of the mediator for best sensitivity has to be long enough to assure that the mediator escapes of the solar dense nucleus, but not too long so that it decays before reaching the Earth. It can be demonstrated, by minimization of the equation (7.1) that the lifetime of the

mediator for the best sensitivity must be forty times the solar radius ($L = \gamma c \tau = 2.7 \cdot 10^7 \text{ km}$), approximately.

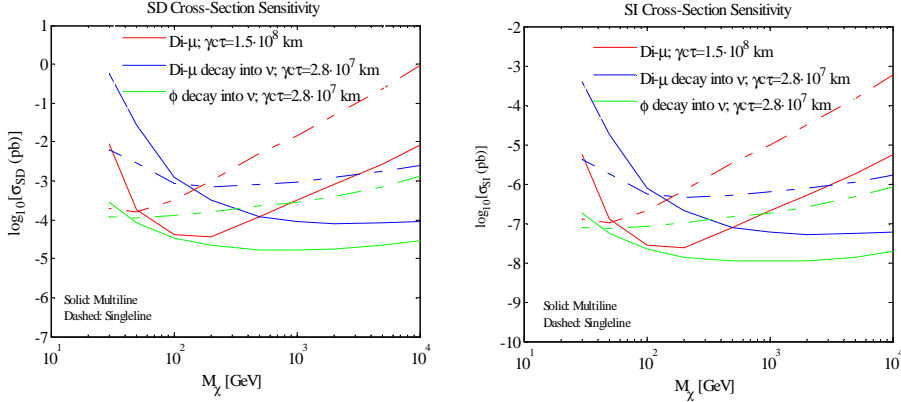


Fig 7.14. ANTARES proton-WIMP cross section sensitivities for the three Secluded DM studied cases, USING *Bfit Singleline* and *Multiline* reconstruction strategies. Results for favorable lifetime of mediators.

Fig 7.14 shows the ANTARES proton-WIMP cross section sensitivities for the different SDM scenarios (products of DM annihilation in the Sun through mediators decaying into: di-muons (red), di-muons which in turn decay into neutrinos (blue) and directly into neutrinos (Green)) for favourable mediator life time values. It is worth to mention that, for favorable lifetime of mediators, this ANTARES analysis search has better sensitivities for spin-dependent interaction than those of direct detection experiments. For SI, this is only the case for large M_χ .

7.5 Final Results after unblinding the data

After a detailed study of three different secluded dark matter scenarios and the cut optimization procedure a total of 6 cuts (on quality parameter (Q_{cut}) and angular distance to the source (ψ_{cut}) have been selected for the evaluation of all considered masses and scenarios. The proposed cuts have been summarized in Table 7. 1. After the proposed cuts were fixed, the data sample was unblinded and events coming from Sun direction during the evaluated period were studied.

7.5.1 Unblinding results following MultiLine reconstruction strategy

Table 7. 2 shows the unblinding results for the *MultiLine* analysis. In this table the obtained events in the selected cuts (N_{obs}) and the number of events expected for background, scrambled data (N_{back}), are presented. No statistical significant excess has been observed above the background in the Sun's direction for any cut.

<i>Reconstruction</i>	N_{cut}	Q_{cut}	ψ_{cut} ($^{\circ}$)	N_{obs}	N_{back}	$\mu_{90\%}$ <i>UpperLimit</i>	$\mu_{90\%}$ <i>LowerLimit</i>
<i>MultiLine</i>	1	1.8	1.3	2	1,25	4,665	0
<i>MultiLine</i>	2	1.6	1.4	2	0,892	5,02	0
<i>MultiLine</i>	3	1.6	2	3	1,82	5,605	0
<i>MultiLine</i>	4	1.4	2.6	3	2,037	5,39	0

Table 7. 2. Results of the unblinded data evaluation with the proposed cuts for *MultiLine* reconstruction.

As the significance level is not enough to evidence signal, it has been proceed to put limits for the models. Using the values obtained for the proposed cuts, 90% Confidence Level (CL) limits on the di-muon flux, ($\Phi_{di-\mu}$) and also neutrino flux ($\Phi_{\nu+\bar{\nu}}$), can be computed from the data according to Eq.(6.28) and Eq.(6.29) respectively, where the $\bar{\mu}_{90}$ average 90% CL upper limit is replaced by the upper limit at 90% CL, μ_{90} , on the number of observed events. Taking into account the number of events observed and the expected background, the upper limit can be obtained as the 90% confidence interval following the Feldman-Cousins approach (Feldman & Cousins, 1998).

$$\Phi_{di-\mu} = \frac{\left(\frac{N_{sim}}{T_{live}}\right) \mu_{90}}{\left(\left(\frac{4}{3}\right) \pi R_{sph}^3\right)^{2/3}} \quad (7.8)$$

$$\Phi_{\nu+\bar{\nu}} = \frac{\mu_{90}}{T_{live} Aeff_{\nu+\bar{\nu}}} \quad (7.9)$$

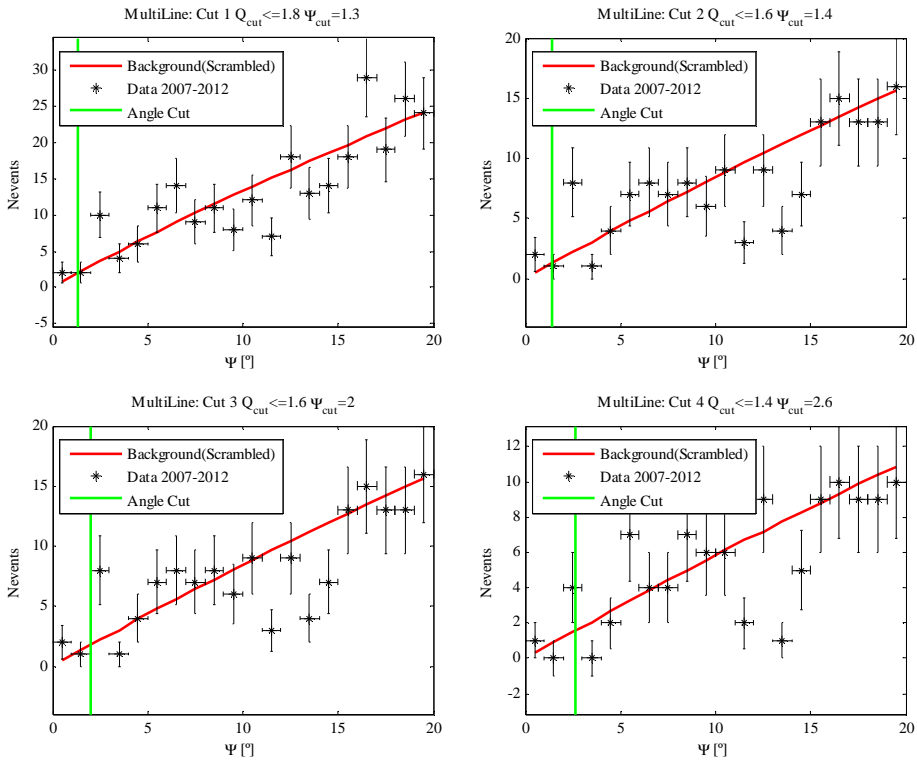


Fig 7.15. Differential distribution of the angular separation ψ of the event tracks with respect to the Sun’s direction for the expected background (red line) compared to the data (black asterisk). Results for the four cuts of *BBFit MultiLine* reconstruction.

Fig 7.15 shows the distribution of the angular separation between the events and the Sun’s direction obtained after applying the selection criteria on the zenith angle, the

minimum number of hits and lines, and the different Q_{cut} of the Table 7. 2. As remarked previously, in any cut has been observed a statistical significant excess.

7.5.2 Unblinding results following SingleLine reconstruction strategy.

Table 7. 3 shows the unblinding results for the *SingleLine* analysis. In this table the data events for the selected cuts (N_{obs}) and the number of events expected by the scrambled data (N_{back}) are presented. No excess has been observed above the background in the Sun's direction for any cut. Following the same procedure than in the previous section (7.5.1) it has been proceed to put limits for this model.

<i>Reconstruction</i>	N_{cut}	Q_{cut}	ψ_{cut} ($^{\circ}$)	N_{obs}	N_{back}	$\mu_{90\%}$ <i>UpperLimit</i>	$\mu_{90\%}$ <i>LowerLimit</i>
<i>SingleLine</i>	1	1	12.8	190	202,9	12,95	0
<i>SingleLine</i>	2	0.7	11.3	23	24,4	7,7	0

Table 7. 3. Results of the unblinded data evaluation with the proposed cuts for *SingleLine* reconstruction.

0 shows the distribution of the zenith angular separation between the events and the Sun's direction obtained after applying the selection criteria on the zenith angle, the minimum number of hits and lines, and the different Q_{cut} of the Table 7. 3. As remarked previously, in no cut has been observed signal excess using *SingleLine* reconstruction strategy.

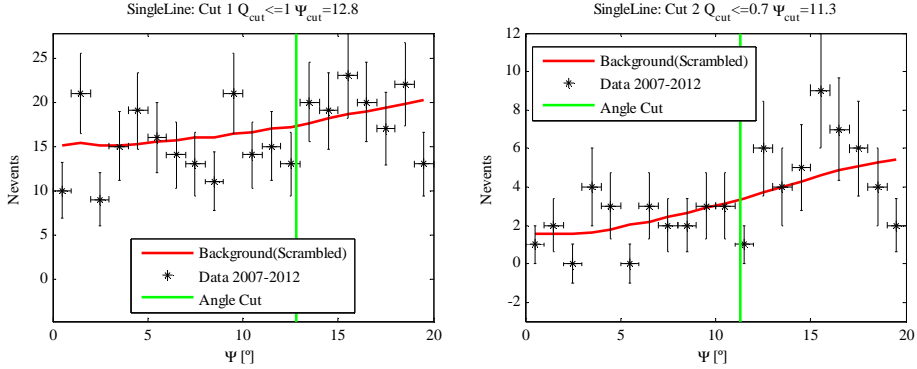


Fig 7.16. Differential distribution of the zenith angular separation ψ of the event tracks with respect to the Sun's direction for the expected background (red line) compared to the data (black asterisk). Results for *BBFit SingleLine* reconstruction.

7.6 Limits obtained for Secluded Dark Matter models

This section includes the plots of the ANTARES limits for the SDM model in terms of DM annihilation rates and cross-sections for the two final products, di-muon and neutrino. The plots show the differences between the flux ($(\Phi_{di-\mu})$ and $(\Phi_{\nu+\bar{\nu}})$) limits, calculated after unblinding the data. They are compared to the sensitivities. Notice that the limits are above sensitivities in the case of *MultiLine* since the number of events observed is larger than the expected ones. For *SingleLine*, occurs the opposite.

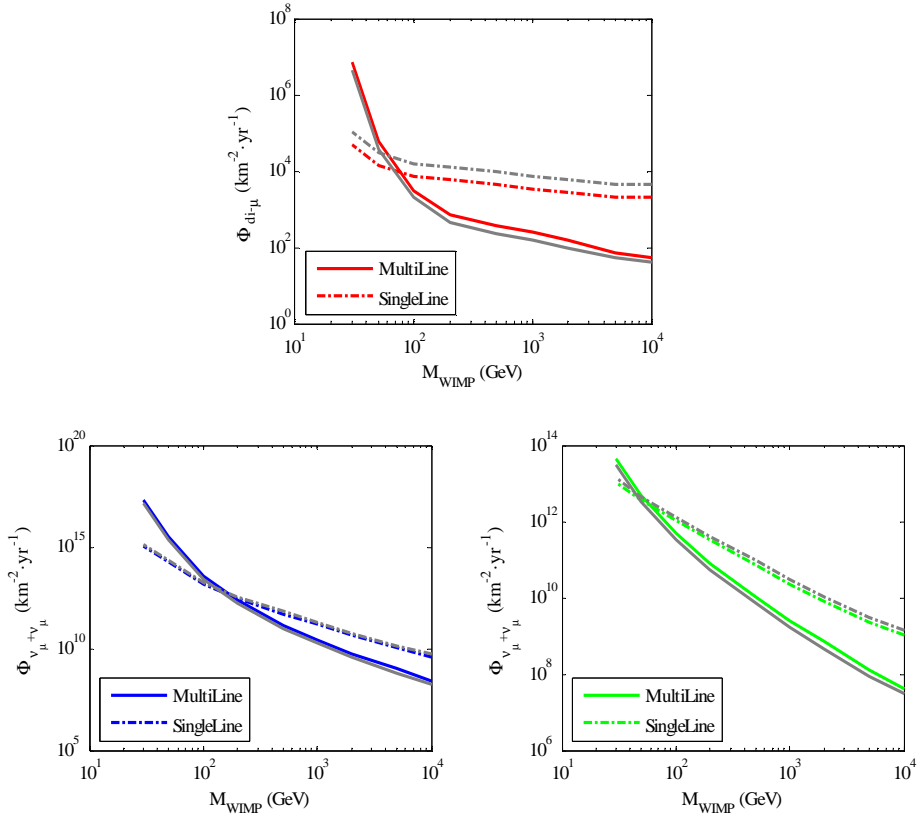


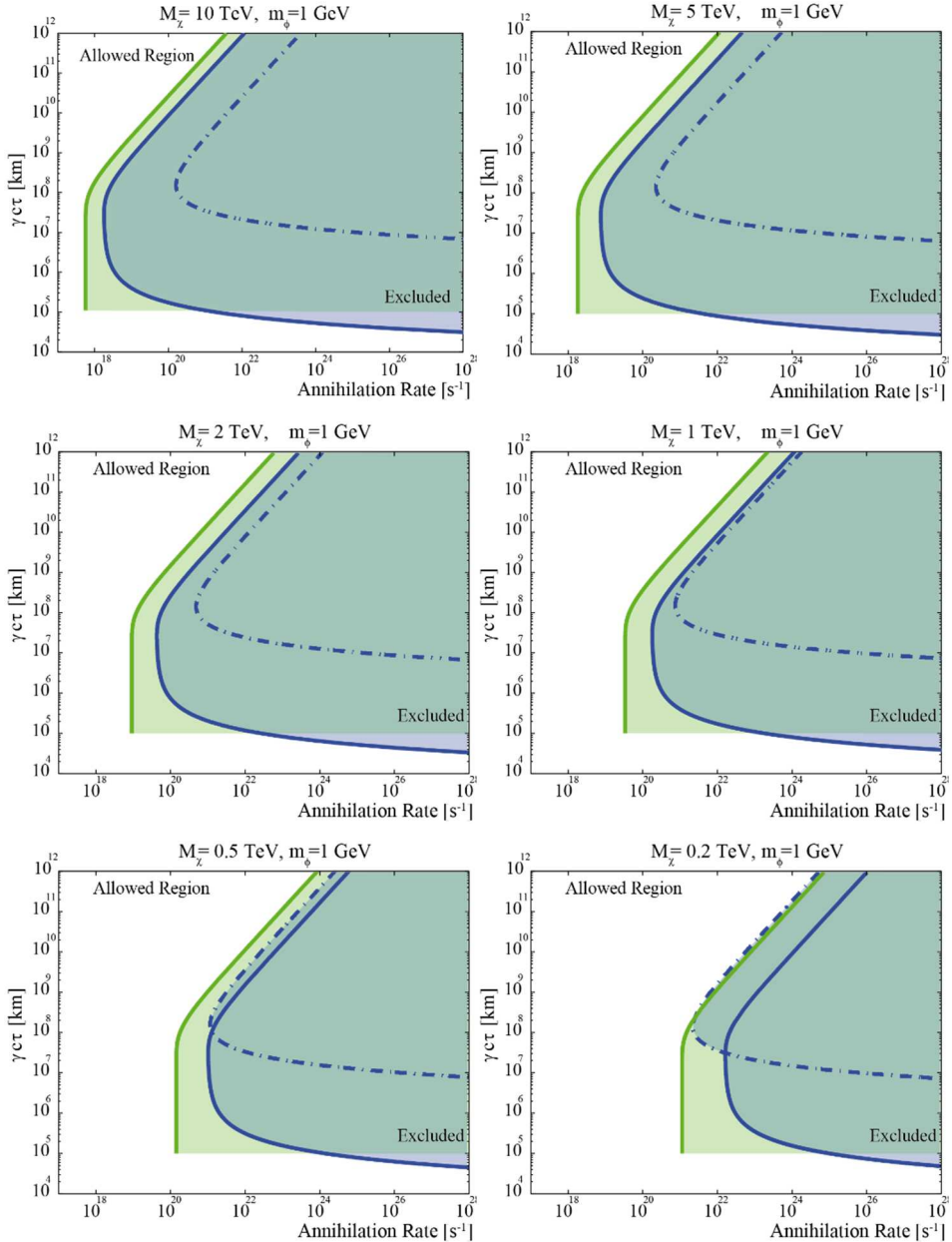
Fig 7.17. Flux limits for di-muons (top) and neutrinos coming from di-muon decay (bottom-left) and coming from mediator decay (bottom-right). In gray color the correspondent flux sensitivities.

7.6.1 Annihilation Rates

Limits of annihilation rates have been obtained through the Equations (7.3), (7.4) and (7.5) where the values of the limits on the di-muon flux ($\Phi_{di-\mu}$), and the neutrino flux ($\Phi_{di-\mu}$) have been considered for each scenario. For better comparison in Fig 7.18, the ANTARES exclusion limits for the three Secluded DM scenarios (products of DM annihilation in the Sun through mediators decaying into: di-muons (dash-dotted blue), neutrinos from di-muons (solid blue), directly into neutrinos (green)) as a function of the annihilation rate (Γ) and the decay length ($\gamma\tau$) for all dark matter

masses analysed are shown. The shadow regions would be excluded for these models.

Depending on the M_χ and the decay length different regions can be explored.



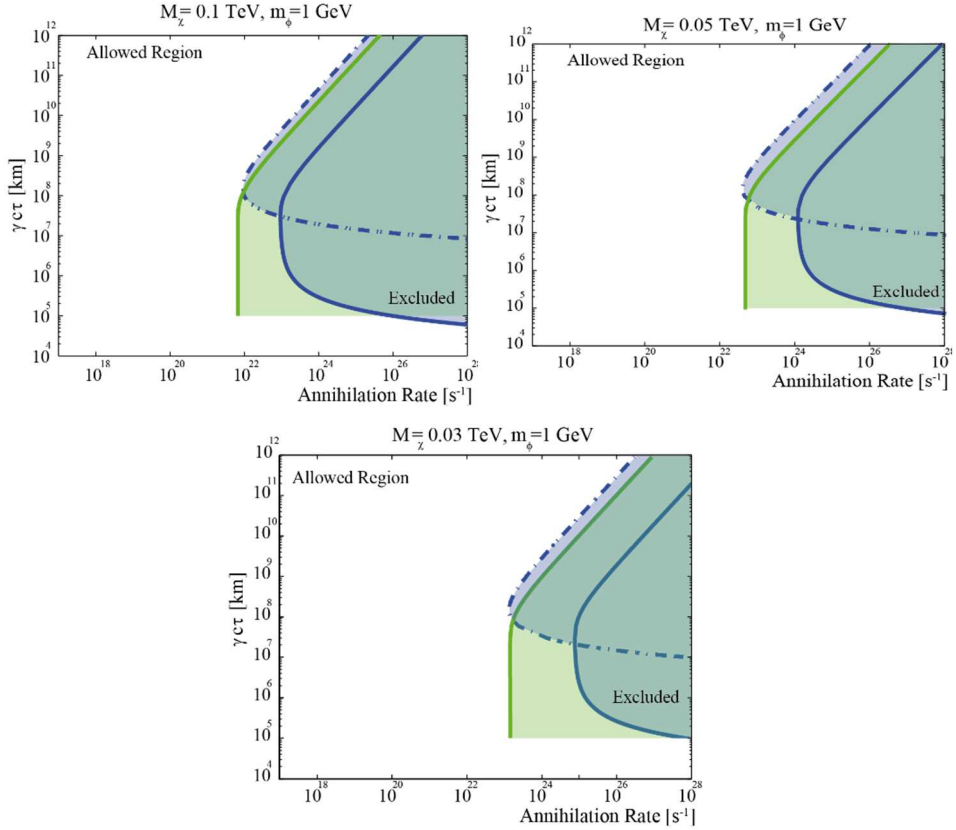


Fig 7.18. ANTARES exclusion limits for the three Secluded DM scenarios (products of DM annihilation in the Sun through mediators decaying into: di-muons (dash-dotted blue), neutrinos from di-muons (solid blue), directly into neutrinos (Green)) as a function of the annihilation rate (Γ) and the decay length ($\gamma\tau$) for three all analysed dark matter masses. The shadow regions would be excluded for these models

7.6.2 Limits on Cross Sections for SDM

To finalize, the cross section limits are presented and compared with other experiments. The spin-dependent and spin-independent cross section limits depends on the annihilation rates and these, in turn, depends on the lifetime of the mediator for the SDM model, as explained in section 7.4. Here, the cross-section limits for the three cases are presented, for the two lifetime values for which the sensitivities are the best. Fig 7.19 shows Antares proton-WIMP cross-section limits for SDM scenario

(products of DM annihilation in the Sun through mediators decaying into: di-muons (blue) and directly into neutrinos (Green)) for favourable mediator life time values. Fig 7.20 shows the limits compared to different experiments of direct search for dark matter in the Sun.

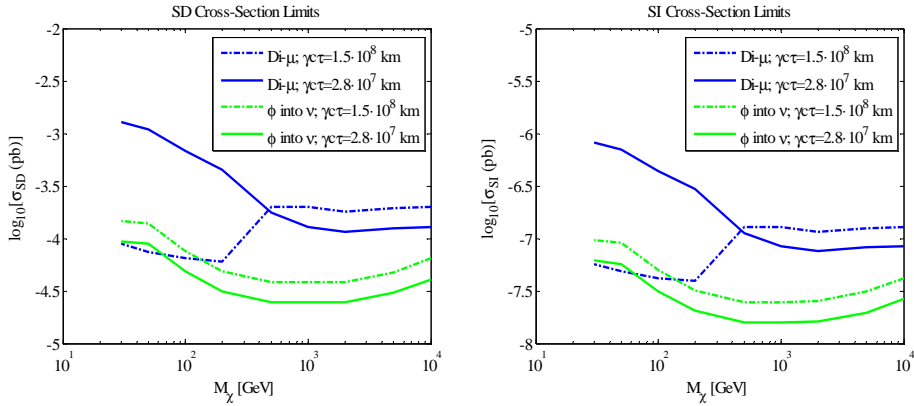


Fig 7.19. ANTARES 90% CL upper limits on the spin-dependent (left) and spin-independent (right) WIMP-proton cross-sections as a function of the WIMP mass for favourable mediator life time.

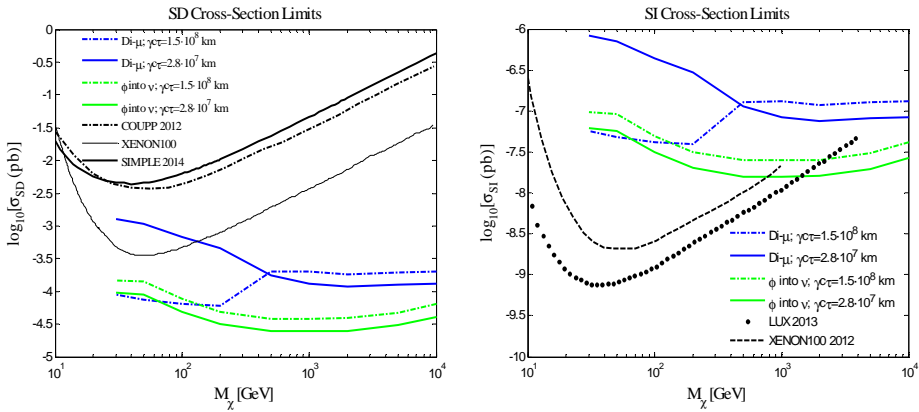


Fig 7.20. Sensitivities collection of different direct detection experiments (SIMPLE (Felizardo et al., 2014), COUPP (Behnke et al., 2012), LUX (Akerib et al., 2014) and XENON-100 (Aprile et al., 2012)) of search for dark matter in the sun (black lines). On the spin-dependent (left) and spin-independent (right) WIMP-nucleon cross-sections as a function of the WIMP mass. SDM ANTARES limits (color lines).

The limits derived in this thesis are the first experimental limits to SDM models established in neutrino telescopes. There were some previous constraints or sensitivities predicted by phenomenology physicists (Meade et al., 2010; Schuster et al., 2010), but naturally, the knowledge of the response of the detector in this kind of papers is quite limited, and therefore, the results are usually taken with caution. As shown in Fig 7.20, for sufficiently long-lived, but not stable, mediators, the imposed limits to these models are much more restrictive than the ones derived in direct detection searches for the case of spin-dependent interaction. In case of spin-independent interactions, direct detection search is more competitive for low and intermediate masses, but this search becomes to be competitive for larger masses (> 1 TeV).

Comparing with other indirect detection methods, such as gamma ray detection, roughly speaking, the limits derived here will be competitive for large dark matter masses and favorable mediator life time ($\gamma c\tau \sim 10^{11}$ m). However, the comparison is not easy, since results are usually given in terms of $\langle \sigma v \rangle$ parameter and several astrophysical assumptions have to be taken. Therefore, it will be better understood in terms of complementary information. In that sense, this analysis constrains in an alternative way these models that are one of the preferred solutions to explain, for example, the energy of the positron flux measured by AMS-II (Accardo et al., 2014; M. Aguilar et al., 2014). Although one possible interpretation of this data would be the existence of near-by pulsars, quite a lot of papers study the possibility of a DM hint. In this line, the annihilation into two mediators that results in four leptons (two di-muons, for example) is much favored than the direct annihilation into leptons (Boudaud et al., 2014; Cholis & Hooper, 2013; Lopez, Savage, Spolyar, & Adams, 2015).

Conclusions

The first part of the thesis has been dedicated to the design and development of a calibrator for the acoustic detection of neutrinos in deep sea neutrino telescopes. The parametric acoustic source technique has been tested and finally used in order to reach the high directivity of the bipolar pulse maintaining a compact design. Pioneering studies of this technique have been carried out here demonstrating its capacity for this application even for the case of cylindrical symmetry and transitory signals. Moreover, taking the advantage of the versatility of the chosen transducer, the functionality of the final calibrator prototype has been expanded, allowing working in two operation modes: low and high frequency. In one hand the low-frequency mode allows the system to deal several acoustic-related tasks in an underwater neutrino telescope such as calibration of the receiver sensors, or use it as emitter for acoustic positioning purposes. On the other hand the high-frequency mode is used for acoustic neutrino detection calibration by generating directive bipolar pulses using the parametric technique. Furthermore, a strategy for performing sea campaigns with the calibrator has been planned and a mechanical structure which

makes possible to operate the calibrator from a vessel controlling the direction of emission has been developed. A register system to monitor the position, orientation and emissions during the sea campaign has also been integrated. The prototype has been successfully tested in low-frequency mode. However, the power electronics for high frequency mode has still to be completed in order to be able to use the compact calibrator with all functionalities. All this work and results have been presented in different ANTARES meetings, Multidark Workshops and international conferences (ARENA, 2010; MARSS, 2011; VLVnT, 2011; ARENA, 2012; CIBRA, 2013;), and published in refereed journals (Adrián-Martínez et al., 2011; Ardid et al., 2012a; Ardid et al., 2012b; Adrián-Martínez et al., 2013a; Adrián-Martínez et al., 2013b).

The second part of the thesis has been dedicated to the analysis of the ANTARES data in order to constrain Secluded Dark Matter models. Specifically, these models have been tested by the detection of di-muons and/or neutrinos coming from Sun direction. In order to know the detector response to the di-muon signal, a dedicated code has been developed for the simulation of di-muon generation from mediator decay and its detection with ANTARES. In order to avoid biases in the event selection, a blinding policy has been followed in the analysis choosing the optimum cuts before looking at the Sun direction, where the signal is expected. The selection criteria have been chosen to maximize the amount of signal over the expected background, i.e. for better flux sensitivity, for a few representative cases. Finally, since no significant statistical excess has been observed above the expected background in the Sun's direction, it has been proceed to constrain the models. The limits derived in this thesis are the first experimental ones established in neutrino telescopes to SDM models. Through the comparison with other experiments, it has been drawn that the imposed limits to these models are much more restrictive than the ones derived in direct detection searches for the case of spin-dependent interaction for a wide range of lifetimes of the meta-stable mediator. In case of spin-independent

interactions, direct detection search is more competitive for low and intermediate masses, but this search becomes to be competitive for larger masses (> 1 TeV).

It is worth to mention that SDM models are one of the preferred solutions to explain some non-completely understood measurements, such as for example the rising in the positron-electron ratio spectrum measured by AMS-II. Although one possible interpretation of this data would be the existence of near-by pulsars, quite a lot of research works study the possibility of a DM hint. In this line, the annihilation into two mediators that results in four leptons (two di-muons, for example) is much favored than the direct annihilation into leptons. Recently, some constraints from gamma detectors have also been arisen for this explanation and, in this sense, the analysis of this thesis constrains it in an alternative and complementary way. This analysis and results have been presented in different ANTARES meetings, Multidark Workshops and in RICAP 2014 conference (Adrian-Martínez, RICAP). Moreover, a publication in a refereed journal is being prepared.

Bibliography

- Aartsen, M. G., Abbasi, R., Abdou, Y., Ackermann, M., Adams, J., Aguilar, J. A., . . . Bai, X. (2013a). First observation of PeV-energy neutrinos with IceCube. *Phys.Rev.Lett.*, *111*, 021103. doi:10.1103/PhysRevLett.111.021103"
- Aartsen, M. G., Abbasi, R., Abdou, Y., Ackermann, M., Adams, J., Aguilar, J. A., . . . Bai, X. (2013b). IceCube search for dark matter annihilation in nearby galaxies and galaxy clusters. *Phys.Rev.*, *D88*(12), 122001. doi:10.1103/PhysRevD.88.122001"
- Abbasi, R., Abdou, Y., Abu-Zayyad, T., Adams, J., Aguilar, J. A., Ahlers, M., . . . Baker, M. (2011a). Search for dark matter from the galactic halo with the IceCube neutrino telescope. *prd*, *84*(2), 022004. doi:10.1103/PhysRevD.84.022004
- Abbasi, R., Abdou, Y., Abu-Zayyad, T., Adams, J., Aguilar, J. A., Ahlers, M., . . . Zarzhitsky, P. (2011b). Measurement of acoustic attenuation in south pole ice. *Astroparticle Physics*, *34*(6), 382-393. doi:<http://dx.doi.org/10.1016/j.astropartphys.2010.10.003>
- Abbasi, R., Abdou, Y., Abu-Zayyad, T., Adams, J., Aguilar, J. A., Ahlers, M., . . . Zarzhitsk, P. (2012). Background studies for acoustic neutrino detection at the south pole. *Astroparticle Physics*, *35*(6), 312-324. doi:<http://dx.doi.org/10.1016/j.astropartphys.2011.09.004>
- Abbasi, R., Abdou, Y., Ackermann, M., Adams, J., Aguilar, J. A., Ahlers, M., . . . Yoshida, S. (2010). Measurement of sound speed vs. depth in south pole ice for neutrino astronomy. *Astroparticle Physics*, *33*(5-6), 277-286. doi:<http://dx.doi.org/10.1016/j.astropartphys.2010.01.012>
- Abbasi, R., & et al. (2012). Search for neutrinos from annihilating dark matter in the direction of the galactic center with the 40-string IceCube neutrino observatory.
- Abdo, A. A., Ackermann, M., Ajello, M., Atwood, W. B., Axelsson, M., Baldini, L., . . . Ziegler, M., (2009). Measurement of the cosmic ray e^+e^- spectrum from 20GeV to 1TeV with the fermi large area telescope. *Physical Review Letters*, *102*(18), 181101. doi:10.1103/PhysRevLett.102.181101

- Accardo, L., Aguilar, M., Aisa, D., Alpat, B., Alvino, A., Ambrosi, G., . . . Zurbach, C. (2014). High statistics measurement of the positron fraction in primary cosmic rays of 0.5-500~GeV with the alpha magnetic spectrometer on the international space station. *Phys.Rev.Lett.*, *113*(12), 121101.
doi:10.1103/PhysRevLett.113.121101
- Adriani, O., Barbarino, G., Bazilevskaya, G., Bellotti, R., Boezio, M., Bogomolov, E., . . . Zverev, V. (2010). PAMELA results on the cosmic-ray antiproton flux from 60 MeV to 180 GeV in kinetic energy. *Phys.Rev.Lett.*, *105*(12), 121101.
doi:10.1103/PhysRevLett.105.121101
- Adrian-Martínez, S. (In publication process). Secluded dark matter search in the sun with the ANTARES neutrino telescope. *EPJ Web of Conferences. RICAP-14 Proceedings*,
- Adrián-Martínez, S., Albert, A., Al Samarai, I., André, M., Anghinolfi, M., Anton, G., . . . Zúñiga, J. (2013). First results on dark matter annihilation in the sun using the ANTARES neutrino telescope. *Journal of Cosmology and Astroparticle Physics*, *2013*(11), 032.
- Adrián-Martínez, S., Ardid, M., Bou-Cabo, M., Felis, I., Llorens, C., Martínez-Mora, J. A., & Saldaña, M. (2015). Acoustic signal detection through the cross-correlation method in experiments with different signal to noise ratio and reverberation conditions. *Ad-Hoc Networks and Wireless*, *7*
doi:DOI:10.1007/978-3-662-46338-3_7
- Adrián-Martínez, S., Ageron, M., Aguilar, J. A., Samarai, I. A., Albert, A., André, M., . . . Zúñiga, J. (2012). The positioning system of the ANTARES neutrino telescope. *Journal of Instrumentation*, *7*(08), T08002.
- Adrián-Martínez, S., Al Samarai, I., Albert, A., André, M., Anghinolfi, M., Anton, G., . . . Zúñiga, J. (2012). Measurement of atmospheric neutrino oscillations with the ANTARES neutrino telescope. *Physics Letters B*, *714*(2-5), 224-230.
doi:<http://dx.doi.org/10.1016/j.physletb.2012.07.002>
- Adrián-Martínez, S., Ardid, M., Bou-Cabo, M., Felis, I., Larosa, G., Llorens, C., . . . Saldaña, M. (2013a). A versatile compact array calibrator for UHE neutrino acoustic detection. *AIP Conference Proceedings*, *1535*(1), 190-194.
doi:<http://dx.doi.org/10.1063/1.4807546>

- Adrián-Martínez, S., Ardid, M., Bou-Cabo, M., Larosa, G., Llorens, C. D., & Martínez-Mora, J. A. (2011). Development of a compact transmitter array for the acoustic neutrino detection calibration. *Mobile Ad-Hoc and Sensor Systems, IEEE International Conference on*, 0, 916-921.
doi:<http://doi.ieeecomputersociety.org/10.1109/MASS.2011.110>
- Adrián-Martínez, S., Ardid, M., Bou-Cabo, M., Larosa, G., Llorens, C. D., & Martínez-Mora, J. A. (2013b). A compact acoustic calibrator for ultra-high energy neutrino detection. *Nuclear Instruments and Methods in Physics Research Section A: Accelerators, Spectrometers, Detectors and Associated Equipment*, 725(0), 219. doi:<http://dx.doi.org/10.1016/j.nima.2012.11.142>"
- Ageron, M., Aguilar, J. A., Al Samarai, I., Albert, A., Ameli, F., André, M., . . . et al., . (2011). ANTARES: The first undersea neutrino telescope. *Nuclear Instruments and Methods in Physics Research A*, 656, 11-38.
doi:10.1016/j.nima.2011.06.103
- Aguilar, J. A., Al Samarai, I., Albert, A., André, M., Anghinolfi, M., Anton, G., . . . Zúñiga, J. (2011). A fast algorithm for muon track reconstruction and its application to the ANTARES neutrino telescope. *Astroparticle Physics*, 34(9), 652-662. doi:<http://dx.doi.org/10.1016/j.astropartphys.2011.01.003>
- Aguilar, J. A., Samarai, I. A., Albert, A., André, M., Anghinolfi, M., Anton, G., . . . Zúñiga, J. (2011). Time calibration of the ANTARES neutrino telescope. *Astroparticle Physics*, 34(7), 539.
doi:<http://dx.doi.org/10.1016/j.astropartphys.2010.12.004>"
- Aguilar, J. A., Samarai, I. A., Albert, A., Anghinolfi, M., Anton, G., Anvar, S., . . . Zúñiga, J. (2011). AMADEUS—The acoustic neutrino detection test system of the ANTARES deep-sea neutrino telescope. *Nuclear Instruments and Methods in Physics Research Section A: Accelerators, Spectrometers, Detectors and Associated Equipment*, 626–627(0), 128.
doi:<http://dx.doi.org/10.1016/j.nima.2010.09.053>"
- Aguilar, M., Aisa, D., Alvino, A., Ambrosi, G., Andeen, K., Arruda, L., . . . Zurbach, C. (2014). Electron and positron fluxes in primary cosmic rays measured with the alpha magnetic spectrometer on the international space station. *Phys.Rev.Lett.*, 113(12), 121102.
doi:10.1103/PhysRevLett.113.121102

- Aharonian, F., & et al. (2008). The energy spectrum of cosmic-ray electrons at TeV energies. *Phys.Rev.Lett.*, *101*, 261104. doi:10.1103/PhysRevLett.101.261104"
- Ainslie, M. A., & McColm, J. G. (1998). A simplified formula for viscous and chemical absorption in sea water. *The Journal of the Acoustical Society of America*, *103*(3), 1671-1672. doi:<http://dx.doi.org/10.1121/1.421258>
- Akerib, D. S., Bai, X., Bedikian, S., Bernard, E., Bernstein, A., Bolozdynya, A., . . . Zhang, C., (2013). The large underground xenon (LUX) experiment. *Nuclear Instruments and Methods in Physics Research A*, *704*, 111-126. doi:10.1016/j.nima.2012.11.135
- Akerib, D. S., et al., (2014). First results from the LUX dark matter experiment at the sanford underground research facility. *Phys.Rev.Lett.*, *112*(9), 091303. doi:10.1103/PhysRevLett.112.091303"
- Amole, C., Ardid, M., Asner, D. M., Baxter, D., Behnke, E., Bhattacharjee, P., . . . Zhang, J., (2015). Dark matter search results from the PICO-2L C₃F₈ bubble chamber. *ArXiv e-Prints*,
- ANTARES Collaboration. (In publication process). Indirect dark matter search into the galactic center with ANTARES.
- Aprile, E., Alfonsi, M., Arisaka, K., Arneodo, F., Balan, C., Baudis, L., . . . Weinheimer, C., (2012). Dark matter results from 225 live days of XENON100 data. *Physical Review Letters*, *109*(18), 181301. doi:10.1103/PhysRevLett.109.181301
- Ardid, M. (2009). Calibration in acoustic detection of neutrinos. *Nuclear Instruments and Methods in Physics Research Section A: Accelerators, Spectrometers, Detectors and Associated Equipment*, *604*(1-2, Supplement), S203-S207. doi:<http://dx.doi.org/10.1016/j.nima.2009.03.071>
- Ardid, M. (2014). Dark matter searches with the ANTARES neutrino telescope.
- Ardid, M., Adrián, S., Bou-Cabo, M., Larosa, G., Martínez-Mora, J. A., Espinosa, V., . . . Ferri, M. (2012a). R&D studies for the development of a compact transmitter able to mimic the acoustic signature of a UHE neutrino interaction. *Nuclear Instruments and Methods in Physics Research Section A: Accelerators, Spectrometers, Detectors and Associated Equipment*, *662*, Supplement 1(0), S206. doi:<http://dx.doi.org/10.1016/j.nima.2010.11.139>"

- Ardid, M., Bou-Cabo, M., Camarena, F., Espinosa, V., Larosa, G., Martínez-Mora, J. A., & Ferri, M. (2009). Use of parametric acoustic sources to generate neutrino-like signals. *Nuclear Instruments and Methods in Physics Research Section A: Accelerators, Spectrometers, Detectors and Associated Equipment*, 604(1â€“2, Supplement), S208. doi:<http://dx.doi.org/10.1016/j.nima.2009.03.196>"
- Ardid, M., Martínez-Mora, J. A., Bou-Cabo, M., Larosa, G., Adrián-Martínez, S., & Llorens, C. D. (2012b). Acoustic transmitters for underwater neutrino telescopes. *Sensors*, 12(4), 4113-4132. doi:10.3390/s120404113
- ARENA. (2010). 4th international workshop on acoustics and ReV neutrino detection activities. ARENA2010. Nantes, France.
- ARENA. (2012). 5th international workshop on acoustics and ReV neutrino detection activities. ARENA2012. Erlangen, Germany. doi:ISBN: 978-0-7354-1159-3
- Arkani-Hamed, N., Finkbeiner, D. P., Slatyer, T. R., & Weiner, N. (2009). A theory of dark matter. *Phys.Rev.*, D79, 015014. doi:10.1103/PhysRevD.79.015014"
- Askariyan, G. A., Dolgoshein, B. A., Kalinovsky, A. N., & Mokhov, N. V. (1979). Acoustic detection of high energy particle showers in water. *Nuclear Instruments and Methods*, 164(2), 267-278. doi:[http://dx.doi.org/10.1016/0029-554X\(79\)90244-1](http://dx.doi.org/10.1016/0029-554X(79)90244-1)
- Askaryan, G. (1957). Hydrodynamic radiation from the tracks of ionizing particles in stable liquids. *Sov.,J.,Atom.,Energy*, 3, 921.
- Atkins, R., Benbow, W., Berley, D., Blaufuss, E., Bussons, J., Coyne, D. G., . . . Yodh, G. B. (2004). Search for very high energy gamma rays from WIMP annihilations near the sun with the milagro detector. *Phys.Rev.D*, 70(8), 083516. doi:10.1103/PhysRevD.70.083516
- Aynutdinov, V., Avrorin, A., Balkanov, V., Belolaptikov, I., Budnev, N., et al. (2008). The baikal neutrino experiment: Status, selected physics results, and perspectives. *Nucl.Instrum.Meth.*, A588, 99-106. doi:10.1016/j.nima.2008.01.011"
- Aynutdinov, V., Avrorin, A., Belolaptikov, I., Bogorodsky, D., Budnev, N., et al. (2012). Acoustic search for high-energy neutrinos in the lake baikal: Results

- and plans. *Nucl.Instrum.Meth.*, A662, S210-S215.
doi:10.1016/j.nima.2010.11.153"
- Barr, M. (2001). Introduction to pulse width modulation. *Embed. Syst. Program.*, 14, 103-104.
- Batell, B., Pospelov, M., Ritz, A., & Shang, Y. (2010). Solar gamma rays powered by secluded dark matter. *Phys.Rev.*, D81, 075004.
doi:10.1103/PhysRevD.81.075004"
- Behnke, E., Behnke, J., Brice, S. J., Broemmelsiek, D., Collar, J. I., Conner, A., . . . Vázquez-Jáuregui, E., (2012). First dark matter search results from a 4-kg CF₃I bubble chamber operated in a deep underground site. *\prd*, 86(5), 052001. doi:10.1103/PhysRevD.86.052001
- Bell, N. F., & Petraki, K. (2011). Enhanced neutrino signals from dark matter annihilation in the sun via metastable mediators. *Journal of Cosmology and Astroparticle Physics*, 2011(04), 003.
- Bergström, L., Edsö, J., & Zaharijas, G., (2009). Dark matter interpretation of recent electron and positron data. *Physical Review Letters*, 103(3), 031103. doi:10.1103/PhysRevLett.103.031103
- Bergstrom, L. (2000). Nonbaryonic dark matter: Observational evidence and detection methods. *Rept.Prog.Phys.*, 63, 793. doi:10.1088/0034-4885/63/5/2r3"
- Bernabei, R., Belli, P., Di Marco, A., Cappella, F., d'Angelo, A., Incicchitti, A., . . . Ye, Z. P.,. (2013). DAMA/LIBRA results and perspectives. *ArXiv e-Prints*,
- Bertone, G., Hooper, D., & Silk, J. (2005). Particle dark matter: Evidence, candidates and constraints. *Physics Reports*, 405(5–6), 279-390.
doi:<http://dx.doi.org/10.1016/j.physrep.2004.08.031>
- Bevan, S., Brown, A., Danaher, S., Perkin, J., Rhodes, C., Sloan, T., . . . Waters, D. (2009). Study of the acoustic signature of UHE neutrino interactions in water and ice. *Nuclear Instruments and Methods in Physics Research Section A: Accelerators, Spectrometers, Detectors and Associated Equipment*, 607(2), 398. doi:<http://dx.doi.org/10.1016/j.nima.2009.05.009>"

- Bevan, S. (2009). Data analysis techniques for UHE acoustic astronomy. *Nuclear Instruments and Methods in Physics Research Section A: Accelerators, Spectrometers, Detectors and Associated Equipment*, 604(1–2, Supplement), S143-S148. doi:<http://dx.doi.org/10.1016/j.nima.2009.03.059>
- Bou-Cabo, M. (In publication process). Dark matter searches using superheated liquid detectors *EPJ Web of Conferences. RICAP-14 Proceedings*,
- Boudaud, M., Aupetit, S., Caroff, S., Putze, A., Belanger, G., Genolini, Y., . . . Vecchi, M., (2014). A new look at the cosmic ray positron fraction. *ArXiv e-Prints*,
- Carminati, G., Margiotta, A., & Spurio, M. (2008). Atmospheric MUons from PArametric formulas: A fast GEnerator for neutrino telescopes (MUPAGE). *Comput.Phys.Commun.*, 179, 915-923. doi:10.1016/j.cpc.2008.07.014"
- Chang, J., Adams, J. H., Ahn, H. S., Bashindzhagyan, G. L., Christl, M., Ganel, O., . . . Zatsepin, V. I. (2008). An excess of cosmic ray electrons at energies of 300-800[thinsp]GeV. *Nature*, 456(7220), 362-365. doi:http://www.nature.com/nature/journal/v456/n7220/supinfo/nature07477_S1.html
- Chen, F., Cline, J. M., & Frey, A. R. (2009). Nonabelian dark matter: Models and constraints. *Phys.Rev.*, D80, 083516. doi:10.1103/PhysRevD.80.083516"
- Cholis, I., & Hooper, D., (2013). Dark matter and pulsar origins of the rising cosmic ray positron fraction in light of new data from the AMS. *\prd*, 88(2), 023013. doi:10.1103/PhysRevD.88.023013
- CIBRA. (2013). 30th international workshop cetacean echolocation and outer space neutrinos: Ethology and physics for an interdisciplinary approach to underwater bioacoustics and astrophysical particles detection. Erice, Italy.
- Cirelli, M. (2012). Indirect searches for dark matter: A status review. *Pramana*, 79, 1021-1043. doi:10.1007/s12043-012-0419-x"
- Cirelli, M., Fornengo, N., Montaruli, T., Sokalski, I. A., Strumia, A., et al. (2005). Spectra of neutrinos from dark matter annihilations. *Nucl.Phys.*, B727, 99-138. doi:10.1016/j.nuclphysb.2005.08.017 10.1016/j.nuclphysb.2007.10.001 10.1016/j.nuclphysb.2005.08.017 10.1016/j.nuclphysb.2007.10.001"

- Clowe, D., & et al. (2006). A direct empirical proof of the existence of dark matter. *Astrophys.J.*, 648, 109-113.
- Clowe, D., Gonzalez, A., & Markevitch, M. (2004). Weak-lensing mass reconstruction of the interacting cluster 1E 0657–558: Direct evidence for the existence of dark matter. *The Astrophysical Journal*, 604(2), 596.
- Cronin, J. W., Gaisser, T. K., & Swordy, S. P. (1997). Cosmic rays at the energy frontier. *Scientific American*, 276, 32-37. doi:10.1038/scientificamerican0197-44
- Danaher, S. (2007). First data from ACoRNE and signal processing techniques. *Journal of Physics: Conference Series*, 81(012011), 1-8. doi:doi:10.1088/1742-6596/81/1/012011
- Danaher, S. (2012). In Communication (Ed.), *A linear array hydrophone transmitter for the calibration of acoustic UHE neutrino telescopes* (5TH INTERNATIONAL WORKSHOP ON ACOUSTIC AND RADIO EEV NEUTRINO DETECTION ACTIVITIES: ARENA 2012 ed.). ARENA 2012:
- Del Grosso, V. A. (1974). New equation for the speed of sound in natural waters (with comparisons to other equations). *The Journal of the Acoustical Society of America*, 56(4), 1084-1091. doi:<http://dx.doi.org/10.1121/1.1903388>
- Desai, S., et al. (2004). Search for dark matter WIMPs using upward through-going muons in super-kamiokande. *Phys.Rev.*, D70, 083523. doi:10.1103/PhysRevD.70.083523 10.1103/PhysRevD.70.109901"
- Desai, S., et al. (2008). Study of TeV neutrinos with upward showering muons in super-kamiokande. *Astropart.Phys.*, 29, 42-54. doi:10.1016/j.astropartphys.2007.11.005"
- Divari, P., Galanopoulos, S., & Souliotis, G. (2012). Coherent scattering of neutral-current neutrinos as a probe for supernova detection. *Journal of Physics G: Nuclear and Particle Physics*, 39(9), 095204.
- EDELWEISS Collaboration. (2011). Final results of the EDELWEISS-II WIMP search using a 4-kg array of cryogenic germanium detectors with interleaved electrodes. *Physics Letters B*, 702, 329-335. doi:10.1016/j.physletb.2011.07.034

- Elsaesser, D., & Mannheim, K. (2005). MAGIC and the search for signatures of supersymmetric dark matter. *New Astron.Rev.*, 49, 297-301. doi:10.1016/j.newar.2005.01.019"
- European Space Agency. (2014). Retrieved from <http://www.cosmos.esa.int/web/planck>
- Faber, S. M., & Dressler, A. (1977). Radial velocities for galaxies in 11 clusters. *aj*, 82, 187-192. doi:10.1086/112028
- Faber, S. M., & Jackson, R. E. (1976). Velocity dispersions and mass-to-light ratios for elliptical galaxies. *apj*, 204, 668-683. doi:10.1086/154215
- Feldman, G. J., & Cousins, R. D. (1998). Unified approach to the classical statistical analysis of small signals. *Phys.Rev.D*, 57(7), 3873-3889. doi:10.1103/PhysRevD.57.3873
- Felizardo, M., Girard, T., A., Morlat, T., Fernandes, A., C., Ramos, A., R., Marques, J., G., . . . Marques, R. (2014). The SIMPLE phase II dark matter search. *Phys.Rev.D*, 89(7), 072013. doi:10.1103/PhysRevD.89.072013
- Fisher, F. H., & Simmons, V. P. (1977). Sound absorption in sea water. *The Journal of the Acoustical Society of America*, 62(3), 558-564. doi:<http://dx.doi.org/10.1121/1.381574>
- Francois, R. E., & Garrison, G. R. (1982a). Sound absorption based on ocean measurements. part II: Boric acid contribution and equation for total absorption. *The Journal of the Acoustical Society of America*, 72(6), 1879-1890. doi:<http://dx.doi.org/10.1121/1.388673>"
- Francois, R. E., & Garrison, G. R. (1982b). Sound absorption based on ocean measurements: Part I: Pure water and magnesium sulfate contributions. *The Journal of the Acoustical Society of America*, 72(3), 896-907. doi:<http://dx.doi.org/10.1121/1.388170>"
- Gandhi, R., Quigg, C., Reno, M. H., & Sarcevic, I. (1998). Neutrino interactions at ultrahigh energies. *Phys.Rev.D*, 58(9), 093009. doi:10.1103/PhysRevD.58.093009
- Gould, R. J., & Schreder, G. (1966). Opacity of the universe to high-energy photons. *Phys.Rev.Lett.*, 16(6), 252-254. doi:10.1103/PhysRevLett.16.252

- Gould, A. (1987). Resonant enhancements in WIMP capture by the earth. *Astrophys.J.*, 321, 571. doi:10.1086/165653"
- Graf, K. (2008). Experimental studies within ANTARES towards acoustic detection of ultra-high energy neutrinos in the deep-sea.
- Grasso, D., Profumo, S., Strong, A. W., Baldini, L., Bellazzini, R., Bloom, E. D., . . . Stephens, T. E.,. (2009). On possible interpretations of the high energy electron-positron spectrum measured by the fermi large area telescope. *Astroparticle Physics*, 32, 140-151. doi:10.1016/j.astropartphys.2009.07.003
- Greisen, K. (1966). End to the cosmic-ray spectrum? *Phys.Rev.Lett.*, 16(17), 748-750. doi:10.1103/PhysRevLett.16.748
- H.E.S.S. Collaboration. (2014). H.E.S.S: High energy stereoscopic system. Retrieved from <https://www.mpi-hd.mpg.de/hfm/HESS/>
- Hamilton, M. F., & Blackstock, D. T. (1998). *Nonlinear acoustics* Academic Press.
- Hill, G. C., & Rawlins, K. (2003). Unbiased cut selection for optimal upper limits in neutrino detectors: The model rejection potential technique. *Astropart.Phys.*, 19, 393.
- Hirata, K. S., Kajita, T., Koshiba, M., Nakahata, M., Oyama, Y., Sato, N., . . . Cortez, B. G. (1988). Observation in the kamiokande-II detector of the neutrino burst from supernova SN1987A. *Phys.Rev.D*, 38(2), 448-458. doi:10.1103/PhysRevD.38.448
- Ibarra, A., Totzauer, M., & Wild, S. (2014). Higher order dark matter annihilations in the sun and implications for IceCube. *JCAP*, 1404, 012. doi:10.1088/1475-7516/2014/04/012"
- IceCube Collaboration. (2012). Search for dark matter annihilations in the sun with the 79-string IceCube detector. *ArXiv e-Prints*,
- IceCube Collaboration. (2013). Evidence for high-energy extraterrestrial neutrinos at the IceCube detector. *Science*, 342, 1. doi:10.1126/science.1242856
- IceCube Collaboration. (2014). IceCube neutrino observatory. Retrieved from <http://icecube.wisc.edu/>

- Jungman, G., Kamionkowski, M., & Griest, K. (1996). Supersymmetric dark matter. *Phys.Rept.*, 267, 195-373. doi:10.1016/0370-1573(95)00058-5"
- Kamionkowski, M. (1991). Energetic neutrinos from heavy-neutralino annihilation in the sun. *Phys.Rev.D*, 44(10), 3021-3042. doi:10.1103/PhysRevD.44.3021
- Karg, T. (2012). Status and recent results of the south pole acoustic test setup. *Nuclear Instruments and Methods in Physics Research Section A: Accelerators, Spectrometers, Detectors and Associated Equipment*, 662, Supplement 1(0), S36-S41. doi:<http://dx.doi.org/10.1016/j.nima.2010.10.122>
- Katz, U. F. (2014). The ORCA option for KM3NeT. *ArXiv e-Prints*,
- Kowalski, M., Rubin, D., Aldering, G., Agostinho, R. J., Amadon, A., Amanullah, R., . . . Yun, J. L. (2008). Improved cosmological constraints from new, old, and combined supernova data sets. *The Astrophysical Journal*, 686(2), 749.
- Kurahashi, N., & Gratta, G. (2008). Oceanic ambient noise as a background to acoustic neutrino detection. *Phys.Rev.D*, 78(9), 092001. doi:10.1103/PhysRevD.78.092001
- Kurahashi, N., Vandenbroucke, J., & Gratta, G. (2010). Search for acoustic signals from ultrahigh energy neutrinos in 1500 km³ of sea water. *Phys.Rev.D*, 82(7), 073006. doi:10.1103/PhysRevD.82.073006
- Kuzmichev, L., et al. (2006). The baikal neutrino experiment: From NT200 to NT200+. *Nucl.Instrum.Meth.*, A567, 433-437.
- Labbate, A., Montaruli, T., & Sokalski, I. A. (2004,). GENHEN v6: ANTARES neutrino generator extension to all neutrino flavors and inclusion of propagation through the earth.
- Lahmann, R. (2011). *Ultra-High_Energy neutrinos and their acoustic detection in the sea*
- Lahmann, R. (2012). The neutrino telescope of the \KM3NeT\ deep-sea research infrastructure. *Physics Procedia*, 37(0), 1209. doi:<http://dx.doi.org/10.1016/j.phpro.2012.02.457>"
- Lambard, G., Zornoza, J., & Hernandez-Rey, J. (2013). *Indirect dark matter search into the sun and the galactic center*. ANTARES Internal notes:

- Larosa, G., Ardid, M., Llorens, C. D., Bou-Cabo, M., Martínez-Mora, J. A., & Adrián-Martínez, S. (2013). Development of an acoustic transceiver for the KM3NeT positioning system. *Nuclear Instruments and Methods in Physics Research Section A: Accelerators, Spectrometers, Detectors and Associated Equipment*, 725(0), 215. doi:<http://dx.doi.org/10.1016/j.nima.2012.11.167>"
- Learned, J. G. (1979). Acoustic radiation by charged atomic particles in liquids: An analysis. *Phys.Rev.*, D19, 3293. doi:10.1103/PhysRevD.19.3293"
- Liebermann, L. N. (1948). The origin of sound absorption in water and in sea water. *The Journal of the Acoustical Society of America*, 20(6), 868-873. doi:<http://dx.doi.org/10.1121/1.1906450>
- LLorens, C. D. (In process). *Diseño y desarrollo de la electrónica de los emisores acústicos para los sistemas de calibracion de telescopios submarinos de neutrinos*. (Unpublished)
- Llorens, C. D., Ardid, M., Sogorb, T., Bou-Cabo, M., Martínez-Mora, J. A., Larosa, G., & Adrián-Martínez, S. (2012). The sound emission board of the KM3NeT acoustic positioning system. *Journal of Instrumentation*, 7(01), 01001.
- Lopez, A., Savage, C., Spolyar, D., & Adams, D. Q.,. (2015). Fermi/LAT observations of dwarf galaxies highly constrain a dark matter interpretation of excess positrons seen in AMS-02, HEAT, and PAMELA. *ArXiv e-Prints*,
- Mackenzie, K. V. (1981). Nine-term equation for sound speed in the oceans. *The Journal of the Acoustical Society of America*, 70(3), 807-812. doi:<http://dx.doi.org/10.1121/1.386920>
- MAGIC Collaboration. (2015). The MAGIC telescopes. Retrieved from <https://magic.mpp.mpg.de/>
- MARSS. (2011). 1st international workshop on marine sensors and systems (MARSS2011). Valencia, Spain.
- Meade, P., Nussinov, S., Papucci, M., & Volansky, T. (2010). Searches for long lived neutral particles. *Journal of High Energy Physics*, 2010(6), 1-25. doi:10.1007/JHEP06(2010)029

- Medwin, H. (1975). Speed of sound in water: A simple equation for realistic parameters. *The Journal of the Acoustical Society of America*, 58(6), 1318-1319. doi:<http://dx.doi.org/10.1121/1.380790>
- Menon, A., Morris, R., Pierce, A., & Weiner, N. (2010). Capture and indirect detection of inelastic dark matter. *Phys.Rev.*, D82, 015011. doi:10.1103/PhysRevD.82.015011"
- MILAGRO Collaboration. (2007). TeV all-sky gamma ray observatory. Retrieved from <http://umdgrb.umd.edu/cosmic/milagro.html>
- Milgrom, M. (1983). A modification of the newtonian dynamics as a possible alternative to the hidden mass hypothesis. *apj*, 270, 365-370. doi:10.1086/161130
- Moffett, M. B., & Mellen, R. H. (1977). Model for parametric acoustic sources. *The Journal of the Acoustical Society of America*, 61(2), 325-337. doi:<http://dx.doi.org/10.1121/1.381310>"
- Moffett, M. B., Mellen, R. H., & Konrad, W. L. (1978). Parametric acoustic sources of rectangular aperture. *The Journal of the Acoustical Society of America*, 63(5), 1326-1331. doi:<http://dx.doi.org/10.1121/1.381885>
- Moffett, M. B., & Mello, P. (1979). Parametric acoustic sources of transient signals. *The Journal of the Acoustical Society of America*, 66(4), 1182-1187. doi:<http://dx.doi.org/10.1121/1.383312>
- Muir, T. G., & Willette, J. G. (1972). Parametric acoustic transmitting arrays. *The Journal of the Acoustical Society of America*, 52(5B), 1481-1486. doi:<http://dx.doi.org/10.1121/1.1913264>
- National Aeronautics and Space Administration. (2008). Cosmic background exproler. Retrieved from <http://lambda.gsfc.nasa.gov/product/cobe/>
- Navarro, J. F., Frenk, C. S., & White, S. D. M. (1996). The structure of cold dark matter halos. *Astrophys.J.*, 462, 563-575. doi:10.1086/177173"
- Neff, M. (2013). *Studies on the selection of neutrino-like signals for the acoustic detection test device AMADEUS*

- Niess, V., & Bertin, V. (2006). Underwater acoustic detection of ultrahigh energy neutrinos. *Astropart.Phys.*, 26, 243-256.
doi:10.1016/j.astropartphys.2006.06.005"
- Nosengo, N. (2009, 3 December-2009). The neutrino and the whale. *Nature*, 426, 560. doi:10.1038/462560a
- Nussinov, S., Wang, L., & Yavin, I. (2009). Capture of inelastic dark matter in the sun. *JCAP*, 0908, 037. doi:10.1088/1475-7516/2009/08/037"
- Olive, K. A., et al. (2014). Review of particle physics. *Chin.Phys.*, C38, 090001. doi:10.1088/1674-1137/38/9/090001"
- Ooppakaew, W., Danaher, S., & Saldana, M. (2011). Acoustic array calibration and signal processing for UHE neutrinos generation. *Mobile Adhoc and Sensor Systems (MASS), 2011 IEEE 8th International Conference on*, 910-915. doi:10.1109/MASS.2011.109
- Percival, W. J., Cole, S., Eisenstein, D. J., Nichol, R. C., Peacock, J. A., et al. (2007). Measuring the baryon acoustic oscillation scale using the SDSS and 2dFGRS. *Mon.Not.Roy.Astron.Soc.*, 381, 1053-1066. doi:10.1111/j.1365-2966.2007.12268.x"
- Pospelov, M., & Ritz, A. (2009). Astrophysical signatures of secluded dark matter. *Phys.Lett.*, B671, 391-397. doi:10.1016/j.physletb.2008.12.012"
- Pospelov, M., Ritz, A., & Voloshin, M. B. (2008). Secluded WIMP dark matter. *Phys.Lett.*, B662, 53-61. doi:10.1016/j.physletb.2008.02.052"
- Press, W. H., & Spergel, D. N. (1985). Capture by the sun of a galactic population of weakly interacting, massive particles. *apj*, 296, 679-684. doi:10.1086/163485
- Reda, I., & Andreas, A. (2008). *Solar position algorithm for solar radiation applications (revised)*. (Technical No. NREL/TP-560-34302).
- Refregier, A. (2003). Weak gravitational lensing by large-scale structure. *Ann.Rev.Astron.Astrophys.*, 41, 645-668.
- Riccobene, G. (2009). Long-term measurements of acoustic background noise in very deep sea. *Nuclear Instruments and Methods in Physics Research Section*

-
- A: *Accelerators, Spectrometers, Detectors and Associated Equipment*, 604(1–2, Supplement), S149-S157. doi:<http://dx.doi.org/10.1016/j.nima.2009.03.195>
- Rothstein, I. Z., Schwetz, T., & Zupan, J. (2009). Phenomenology of dark matter annihilation into a long-lived intermediate state. *Journal of Cosmology and Astroparticle Physics (JCAP)*, 7, 18. doi:10.1088/1475-7516/2009/07/018
- Roy, D. P. (2000). Basic constituents of the visible and invisible matter - A microscopic view of the universe. *ArXiv Physics e-Prints*,
- Rubin V.C., & Ford Jr., W. K. (1970). Rotation of the andromeda nebula from a spectroscopic survey of emission regions. *apj*, 159, 379. doi:10.1086/150317
- Rubin, V. C., Thonnard, N., & Ford, W. K., Jr. (1980). Rotational properties of 21 SC galaxies with a large. *Astrophys.J.*, 238, 471. doi:10.1086/158003"
- Sander, J., Ahmed, Z., Anderson, A. J., Arrenberg, S., Balakishiyeva, D., Thakur, R. B., . . . Zhang, J. (2013). SuperCDMS status from soudan and plans for SNOLab. *AIP Conference Proceedings*, 1534(1), 129-135. doi:<http://dx.doi.org/10.1063/1.4807350>"
- Schulkin, M., & Marsh, H. W. (1963). Absorption of sound in sea-water. *Radio and Electronic Engineer*, 25(6), 493-500(7).
- Schuster, P., Toro, N., Weiner, N., & Yavin, I. (2010). High energy electron signals from dark matter annihilation in the sun. *Phys.Rev.*, D82, 115012. doi:10.1103/PhysRevD.82.115012"
- Serpico, P. D. (2012). Astrophysical models for the origin of the positron "excess". *Astroparticle Physics*, 39, 2-11. doi:10.1016/j.astropartphys.2011.08.007
- Sherman, C., & Butler, J. (2007). Transducers as projectors., 76-151. doi:10.1007/978-0-387-33139-3_3
- Simmonds, J., & MacLennan, D. N. (2005). Underwater sound. In Wiley-Blackwell (Ed.), *Fisheries acoustics: Theory and practice* (2nd ed., pp. 20). Oxford. UK: Blackwell Science Ltd. doi:ISBN-13: 978-0-632-05994-2
- SuperKamiokande Collaboration. (2013). Super kamiokande. Retrieved from <http://www-sk.icrr.u-tokyo.ac.jp/sk/index-e.html>

- Tanaka, T., Abe, K., Hayato, Y., Iida, T., Kameda, J., Koshio, Y., . . . e Collaboration, . (2011). An indirect search for weakly interacting massive particles in the sun using 3109.6 days of upward-going muons in super-kamiokande. *apj*, 742, 78. doi:10.1088/0004-637X/742/2/78
- Taylor, A. N., Dye, S., Broadhurst, T. J., Benitez, N., & van Kampen, E. (1998). Gravitational lens magnification and the mass of abell 1689.
- Tempel, E., Hektor, A., & Raidal, M. (2012). Fermi 130 GeV gamma-ray excess and dark matter annihilation in sub-haloes and in the galactic centre. *JCAP*, 1209, 032. doi:10.1088/1475-7516/2012/09/032 10.1088/1475-7516/2012/11/A01"
- Tjøtta, J. N., & Tjøtta, S. (1980). Nonlinear interaction of two collinear, spherically spreading sound beams. *The Journal of the Acoustical Society of America*, 67(2), 484-490. doi:<http://dx.doi.org/10.1121/1.383912>
- Torii, S., et al. (2008). High-energy electron observations by PPB-BETS flight in antarctica.
- Vandenbroucke, J., Gratta, G., & Lehtinen, N. (2005). Experimental study of acoustic ultra-high-energy neutrino detection. *The Astrophysical Journal*, 621(1), 301.
- Vander Velde, J. C. (Personal web). The IBM experiment. Retrieved from <http://www-personal.umich.edu/~jcv/imb/imb.html>
- VERITAS Collaboration. (2014). Very energetic radiation imaging telescope array system. Retrieved from <http://veritas.sao.arizona.edu/>
- Viel, M., Bolton, J. S., & Haehnelt, M. G. (2009). Cosmological and astrophysical constraints from the lyman *alpha* forest flux probability distribution function. *mnras*, 399, 39-43. doi:10.1111/j.1745-3933.2009.00720.x
- Vikhlinin, A., Kravtsov, A., Forman, W., Jones, C., Markevitch, M., Murray, S. S., & Speybroeck, L. V. (2006). Chandra sample of nearby relaxed galaxy clusters: Mass, gas fraction, and mass-temperature relation. *The Astrophysical Journal*, 640(2), 691.
- Vivier, M. (2011). Indirect searches for dark matter annihilations toward dwarf spheroidal galaxies with VERITAS.

- VLVnT. (2011). Very large volume neutrino telescope. VLVnT. Erlangen, Germany.
- Volders, L. M. J. S. (1959). Neutral hydrogen in M 33 and M 101. *\bain*, 14, 323.
- Walsh, D., Carswell, R. F., & Weymann, R. J. (1979). 0957 + 561 A, B: Twin quasistellar objects or gravitational lens? *Nature*, 279(5712), 381-384.
- Weniger, C. (2012). A tentative gamma-ray line from dark matter annihilation at the fermi large area telescope. *JCAP*, 1208, 007. doi:10.1088/1475-7516/2012/08/007"
- Westervelt, P. J. (1963). Parametric acoustic array. *The Journal of the Acoustical Society of America*, 35(4), 535-537. doi:<http://dx.doi.org/10.1121/1.1918525>
- Wright.E.L, B. C. L., Bay.M, Halpern.M, Hinshaw.G, Jackson.C, Jarosik.N, . . . Wollack.E. (2003). The microwave anisotropy probe mission. *The Astrophysical Journal*, 583(1), 1.
- Zatsepin, G. T., & Kuz'min, V. A. (1966). Upper limit of the spectrum of cosmic rays. *Soviet Journal of Experimental and Theoretical Physics Letters*, 4, 78.
- Zornoza, J. D. (2014). Overview of ANTARES results on dark matter searches.

Acknowledgements / Agradecimientos

En primer lugar quiero dar las gracias a mi director de tesis, *Miquel Ardid*, por confiar en mí para su equipo, por su dedicación tanto a la supervisión de mi trabajo como a mi formación y por su empeño en llevarme allá donde yo pensaba que no podría llegar.

A *Manu*, por su labor como co-director, pero sobretodo como amigo. Por todos los viajes que hemos hecho juntos, por todas las veces que me has animado a seguir adelante. Quiero que sepas que sin tus palabras en determinados momentos no hubiera llegado hasta aquí.

También quiero expresar mi gratitud a los miembros del *Departamento de Física Aplicada* de l'Escola Politècnica Superior de Gandía, siempre dispuestos a compartir sus conocimientos y experiencias, en especial a mis compañeros de batallas del *E201*, sin olvidarme de *Laura* y *Charli*.

Mención especial quiero dedicarle a *Vicent*, mi amigo, mi confidente. Porque sin ti estos años no hubiesen sido lo mismo. *Perdi*, gracias por ser, gracias por estar.

No podría olvidarme de mi familia y mis amigas que durante este tiempo me han mostrado su apoyo y han estado animándome, sobretodo en la recta final del trabajo.

Ni de mi nueva familia, *Pabe* y *Pepe*. Gracias por recordarme lo que muchas veces yo no soy capaz de ver.

Gracias *Vicen* por estar a mi lado todo este tiempo, por compartir tu espacio y tus inquietudes enseñándome otra forma de disfrutar la vida. Aquí empieza otro capítulo en mi vida, en nuestra vida.

Para finalizar quiero dar las gracias a mis padres. Gracias por vuestro apoyo incondicional e incansable en todas mis decisiones. Gracias por haberme enseñado tanto. Son tantas las cosas que os tengo que agradecer que no podría expresarlo en tan pocas líneas, así que he decidido hacerlo bien grande: GRACIAS. Os quiero.

I would like to thank the members of *Multidark project* and *ANTARES Collaboration*, especially to the *Dark Matter group*.

My acknowledge to the financial support of the Spanish Ministerio de Ciencia e Innovación (MICINN) and Ministerio de Economía y Competitividad (MINECO), Grants: Consolider MultiDark CSD2009-00064, FPA2009-13983-C02-02 and FPA2012-37528-C02-02. As well as to the Generalitat Valenciana, Grants ACOMP/2014/153 and PrometeoII/2014/079.

Table List

Table 2.1	Overview of the acoustic detection test sites.	41
Table 3.1	See conditions in the ANTARES site used for the signal propagation	78
Table 4.1	Register report example	101
Table 6.1	Different configuration periods used in the simulation and for the background estimation using scrambled data	149
Table 7.1	Summary of the proposed cuts for the unblinding data evaluation	181
Table 7.2	Results of the unblinded data evaluation with the proposed cuts for <i>MultiLine</i> reconstruction	192
Table 7.3	Results of the unblinded data evaluation with the proposed cuts for <i>SingleLine</i> reconstruction	193

Figure List

Fig 1.1	Scheme of the different messengers that can reach the Earth from astrophysical sourced and its possible interaction with the medium during their travel.	19
Fig 1.2	Infographic view of the two different origin of the neutrinos detected on the Earth: atmospheric neutrinos and astrophysical neutrinos	20
Fig 1.3	Spectral Flux of Cosmic Rays observed on Earth. Figure adapted from (Cronin, Gaisser, & Swordy, 1997).	21
Fig 1.4	Principle of detection of high energy muon neutrinos in an underwater neutrino telescope. The incoming neutrino interacts with the material around the detector to create a muon. The muon gives Cherenkov light in the sea water which is then detected by a matrix of light sensors. The original spectrum of light emitted from the muon is attenuated in the water such that the dominant wavelength range detected is between 350 and 500 nm.	24
Fig 1.5	Zenith angular distribution of the muon flux above 1 TeV from atmospheric muons and atmospheric neutrino induced muons at 2300 m water equivalent depth.	25
Fig 1.6	Schematic view of the ANTARES detector which consists in 885 OMs set along 12 lines connected to shore by an electro-optical cable.	26
Fig 1.7	Schematic view of the ANTARES detector. The six acoustic storeys are highlighted and their three different setups are shown. This is the configuration after the last redeployment of the IL in November 2013.	30
Fig 1.8	Drawing of a standard acoustic storey with hydrophones in the AMADEUS system.	31
Fig 1.9	Images of the three different storeys of the AMADEUS system during its deployment. On the left a standard storey equipped with hydrophones pointing up is shown. In the middle the acoustic storey on L12 with the hydrophones pointing down. On the right the lowermost acoustic storey on L12 equipped with Acoustic Modules.	32
Fig 1.10	Left: KM3NeT digital optical module. Right: Detection Unit of KM3NeT.	34

Fig 2.1	Grüneissen parameter β for different oceans and seas as a function of depth. Polar areas (dashed), oceans in tropical (dash-dotted) and tempered (solid, bottom line) areas and the Mediterranean Sea (solid upper line). The dotted horizontal line indicates the value used by (Askariyan et al., 1979)	44
Fig 2.2	Illustration of the cascade produced by neutrino interaction in water and the directive pressure pulse generated. Typical dimensions of the implicated parts for acoustic detection are indicated.	46
Fig 2.3	Sketch of a typical acoustic signal pulse. On the left the time pattern. On the right the frequency spectrum. From (Niess & Bertin, 2006)	47
Fig 2.4	Simulated acoustic pulse for a 10^{20} eV shower at 1 km distance from the shower centre. Left: the contribution of the radial distribution for up to 1 cm and 2 cm from the shower core and for the contribution of the whole shower are shown, in time domain. Right: Relative power spectrum at 100 and 1000 m from the shower.	47
Fig 2.5	Illustration of acoustic energy propagating away from a transducer. (a) Spherical spreading reduces the intensity at large ranges. (b) This causes the intensity of a point source to follow the inverse-square law (curve 1) at any range. For a finite transducer near-field effect limits the intensity near the face of a finite transducer (curve 2). From (Simmonds & MacLennan, 2005)	49
Fig 2.6	Sound attenuations in sea water for the SAUND/Learned (f^2 approximation, Niess and Bertin, Francois and Garrison, Ainslie and McColm and the ACORNE parameterisations). Since the Ainslie & McColm/ACORNE and Francois & Garrison results match very closely they are depicted as the same curve in the figure. The attenuation in Antarctic ice is shown for comparison. Inset: the phase shifts at 1 km for the two complex attenuation models. Plot extracted from (S. Bevan et al., 2009).	51
Fig 2.7	Left: temperature variation with the depth from sea surface. Right: Sound propagation velocity variation with the depth from sea surface. For both plots: measurement from the ANTARES site in August 2007 (solid blue line) and in March 2010 (dashed red line). Figure from (Lahmann, 2011)	53
Fig 2.8	Ray tracing of acoustic signals for the speed of sound profile of Fig 2.7 (summer values). It is assumed open water models with a constant depth (2478 m). The shaded area indicates the region from which signals cannot reach the receiver located 410 m above sea floor.	53

Fig 2.9	Summary of the principal background sources and the affected frequency band. The orange part is the most relevant one for neutrino detection	54
Fig 2.10	Fig 2.10. Power spectral density (PSD) of the ambient noise recorded with one HTI sensor on the topmost storey of the IL. Occurrence rate in arbitrary units (shades of grey), where dark colours indicate higher rates. Median value of the in-situ PSD (white dotted line) and the noise level recorded in the laboratory prior to deployment (black solid line).	55
Fig 2.11	Left: Relative variation of the wind speed and of the ambient noise level at ANTARES site over the first half of 2008. Acoustic data measured on the topmost acoustic storey of the IL. The plot is the relative variation for better comparison. The values represent the daily averages divided by the yearly average. Right: Ambient noise in the 1-50 kHz frequency range as a function of the time of the day. It is shown the noise relative to the mean noise recorded during about two years.	56
Fig 2.12	Illustration of the virtual array in the water interaction region of the two primary beams where the parametric effect takes place.	59
Fig 2.13	Directivity pattern of a parametric source. (a) Primary 418 kHz, (b) Primary 482 kHz, (c) Beam pattern of difference frequency, 64 kHz.	60
Fig 3.1	Experimental set-up	67
Fig 3.2	Top: Signal used for emission (1 MHz emitter). Bottom: Received signal (solid line) and bipolar signal obtained after applying the low-pass filter (dashed line)	68
Fig 3.3	Amplitude of the received (primary beam) and filtered (bipolar, secondary beam) vs amplitude of the input signal	69
Fig 3.4	Directivity patterns (left) and distance dependence (right) of the primary and secondary (parametric) beams	70
Fig 3.5	a) Transmitting voltage response. b) FFR SX83. c) Directivity pattern. d) Electrical admittance	71
Fig 3.6	Left: Receiving voltage response (sensitivity) of the ITC-1042 + CCA1000 set using the measurement configuration (10 kHz, 10 nF, 20dB). Right top: CCA1000, bottom: ITC-1042	73
Fig 3.7	Examples of different signals used for emission to study the shape dependences of the secondary parametric bipolar pulse. Left: the default signal with 5 μ s sigma. Centre: signal with 10 μ s sigma. Right: signal with 5 μ s sigma and with 50 μ s length of constant amplitude in the middle	74

Fig 3.8	Received signals (gray), primary beam (black) and parametric secondary beam, i.e. bipolar signal (blue) for the emitted signals shown in Fig 3.7. The bipolar signal (blue) has been multiplied by a factor of three for a better visual comparison. The maximum and minimum of the bipolar signal used to calculate δt and δV are highlighted (orange). Notice that for the last signal, the constant amplitude between the rise and fall of the primary beam results in a separation of the positive and negative parts of the bipolar pulse	75
Fig 3.9	Left: Normalized amplitude of the received primary beam and the secondary (bipolar) signal as function of the transducer input amplitude. Right: Amplitude dependence with the distance of the primary and secondary (parametric) beams. The results of the data fits are also shown in both plots	76
Fig 3.10	Directivity pattern of the primary beam and the secondary beam measured in the water tank at 60 cm distance between emitter and receiver	77
Fig 3.11	Amplitude of the primary and secondary signals as a function of the distance and directivity pattern for both beams. Normalization values (a) Primary beam: 166 kPa, Secondary beam: 200 Pa; (b) Primary beam: 27 kPa, Secondary beam: 80 Pa.	78
Fig 3.12	Schematic view of the propagation algorithm	79
Fig 3.13	Sound absorption coefficient in the ANTARES site	80
Fig 3.14	Signal obtained by the propagation of the received signal to distances beyond 1 km. Notice that received and propagated signal are shown in different units.	80
Fig 3.15	Pressure signal obtained at different angles for a three-element array	82
Fig 3.16	Photography of the array during the initial tests and geometric configuration of the array	83
Fig 3.17	a) Example of a received signal and the primary and secondary beams obtained after applying the band-pass filters (the secondary beam has been amplified by a factor 3 for a better observation). b) Directivity patterns of primary and secondary beam emitted with the array	84
Fig 3.18	Signal obtained by the received signal (Fig 3.17a) propagation. Notice that the received and the propagated signal have different magnitude orders	85
Fig 4.1	Diagram of the three step calibration strategy	90

Fig 4.2	Emitted and received signal for the parametric sweep test. The correlated signal is the result of correlation between parametric expected signal and received signal	91
Fig 4.3	Directivity comparison of the three different kind of signals generated with the selected transducer. These signals are proposed for the different steps of the strategy for a Sea Campaign	92
Fig 4.4	Constructional drawings and photo of the array with the holding system. Dimensions in mm	93
Fig 4.5	Artistic view of the array operated from a boat during a Sea campaign calibration in mm	94
Fig 4.6	Constructional drawings of the head of the fastening structure. Real view of the rudder is shown in the perspective view. Dimensions	95
Fig 4.7	Conceptual block diagram of the EEB	97
Fig 4.8	A simple method to generate the PWM pulse train corresponding to a given signal is the intersective PWM: the signal (here the red sinewave) is compared with a sawtooth waveform (blue). When the latter is less than the former, the PWM signal (magenta) is in high state (1). Otherwise it is in the low state (0)	99
Fig 4.9	Envelope of the signal to be used for emission	100
Fig 4.10	Square signal after applying PWM modulation	100
Fig 4.11	Expected signal at the amplifier output	101
Fig 4.12	Screenshots of the APP and the register system	102
Fig 4.13	Transmitting voltage response of the array connected in parallel and for the central element for the low frequency range	104
Fig 4.14	Experimental setup (left), emitter (middle) and receiver (right) transducers	107
Fig 4.15	Pure tone emitted: 20 kHz, 0.3 ms duration signal (left). Received signal (middle).Emitted-received signal correlation (right).	107
Fig 4.16	Sine sweep emitted: 10 kHz – 40 kHz, 2 ms duration (left). Received signal (middle).Emitted-received signal correlation (right).	107
Fig 4.17	MLS emitted: 2.5 ms duration (left). Received signal (middle).Emitted-received signal correlation (right)	108
Fig 4.18	Left: Comparison of the received amplitude in time domain and using the cross-correlation method. Right: Comparison of the S/N ratio	108

Fig 4.19	Evolution of the amplitude of the different received signals during propagation up to 3 km	109
Fig 4.20	Left: HTI-08 Receiving Voltage Response. Right: Example of background registered by the same receiver	110
Fig 4.21	Signal to noise ratio of the received signals in time domain (left) and signal to noise ratio of the received signal after correlation (right).	110
Fig 4.22	Aerial view of the experimental setup disposition	112
Fig 4.23	Left: Registered signal when the array had emitted a pure tone of 30 kHz and 4 ms duration. In grey is represented the registered signal (masked by noise), Band-pass filtered signal has been plotted in orange, also has been magnified for better visualization. Right: Result of the correlation between the emitted and the received signal	112
Fig 4.24	Left: Emitter-Receiver distance obtained with correlation method for each emitted signal tested. Dot-dashed line indicates the mean value and dashed lines indicates the deviation of the results obtained with all emitted signals. Error bars indicates the measurement uncertainty of each particular signal. Right: Signal to noise ratio of the correlated signal for each emitted signal tested	113
Fig 4.25	Left: Normalized pressure amplitude measured along a parallel plane to the array axis. Right: Extrapolation with the distance of the pressure maximum evolution offered by each element of the array	117
Fig 5.1	Estimated composition of the Energy-Matter of the Universe	122
Fig 5.2	Observed rotation curve of the nearby dwarf spiral galaxy M33, superimposed on its optical image (from (Roy, 2000))	124
Fig 5.3	Gravitational Lensing phenomena diagram. Light coming from a faraway galaxy is deflected due the dark matter located in its travel path. Dark matter gravity acts as a lens and at the observer point (Earth) is appreciated various images of the same galaxy. (Figure adapted from ©Infn-Asimmetrie)	126
Fig 5.4	Schematic view of Universe evolution following the Standard Model in cosmology. On the bottom the temporal scale of the events since the Big Bang until now is shown. On the top flap the estimated DM distribution is represented. (Figure adapted from ©Infn-Asimmetrie)	128
Fig 5.5	Summary of the direct detection experiments classified by their detection mechanism	132

Fig 5.6	Preliminary limits on $\langle\sigma v\rangle$ for the Galactic Centre for the $\tau - \tau +$ channel (red solid line) with IC40 for the GC (brown solid line), IC59 for dwarf galaxies (dashed black line), IC79 for the Galactic Halo (magenta solid line), IC59 for the VIRGO cluster (black solid line), DeepCore+IC79 for the GC (blue solid line) and Fermi for dwarf galaxies (green solid line). The grey/green area represent leptophilic dark matter models which would explain the PAMELA (grey) and Fermi+PAMELA+HESS (green) excess in the Galactic Centre. Adapted from ((ANTARES Collaboration, In preparation)) 136
Fig 5.7	Preliminary Spin-independent cross section sensitivity (90% CL) for the Earth analysis, assuming $\langle\sigma v\rangle \sim 3 \cdot 10^{-26} \text{ cm}^3 \text{ s}^{-1}$ for three different channels: $\tau\bar{\tau}$ (dash, blue), W^+W^- (dot, green) and $b\bar{b}$ (dash-dot, magenta). This sensitivity is also compared with the results of XENON-100 (solid, red). Plot from (Zornoza, 2014). 137
Fig 5.8	Preliminary Spin-dependent (left) and Spin-independent (right) cross-section limits for the search on the Sun: ANTARES 2007-2012 (thick solid) lines): $\tau - \tau +$ (red), W^+W^- (blue), (green), IceCube-79 (dashed lines), SuperKamiokande (colored dash-dotted lines), SIMPLE (black short dash-dotted line), COUPP (black long dash-dotted line) and XENON-100 (black long dashed line). The results are compared with a scan in MSSM-7. (Figure from (Zornoza, 2014). 139
Fig 5.9	Secluded scenario diagram where the mediator decays in the vicinity of the Earth as two co-linear muons which could be detected by neutrino telescopes. 143
Fig 5.10	Energy deposited for stopping a di-muon event (black), a single muon (red) and a more energetic single (muon blue) 143
Fig 5.11	Secluded scenario diagram where the mediator decays far from the detector as two co-linear muons which, in turn, decay into neutrinos and could be detected by neutrino telescopes 144
Fig 5.12	The purple curves show the current bounds from Super-Kamiokande on the annihilation rate of DM in the Sun into mediators assuming 100% branching ratio and decaying into di-muons. The red (orange) curves are the expected bounds from ANTARES (Ice-Cube). (Plot adapted from (Schuster et al., 2010)) 145
Fig 5.13	Secluded scenario diagram where the mediator decays inside or near the Sun's surface into neutrinos which could be detected by neutrino telescopes 146

Fig 6.1	Secluded scenario diagram where the mediator decays in the vicinity of the Earth as two co-linear muons. These could be detected by neutrino telescopes	150
Fig 6.2	Schematic view of the different considered volumes for inside and outside decays	154
Fig 6.3	Relations between instrumented volume, detection volume and spherical detection can used in <i>DiMuGen</i>	155
Fig 6.4	Block diagram of the <i>DiMuGen</i> main program	156
Fig 6.5	Θ and ϕ distributions to assign the mediator direction arriving from all incoming directions	158
Fig 6.6	Θ and ϕ distributions to assign the mediator direction arriving from Sun direction	159
Fig 6.7	Decay points inside the sphere	160
Fig 6.8	Mediator decay point (red) after the direction assignment, blue and green points show the trajectory deviation of the two muons. In the detailed view, a 500X zoom has been applied	161
Fig 6.9	Schematic view of the outside decay case	162
Fig 6.10	α and β distributions to assign the hypothetical mediator impact point over the sphere	163
Fig 6.11	Fluka vs parameterization comparison for 0.1 TeV muons. Energy spectra comparison (left) and scattering angle (right).	165
Fig 6.12	Fluka vs parameterization comparison for 2.5 TeV muons. Energy spectra comparison (left) and scattering angle (right)	166
Fig 6.13	Propagation distances used in <i>DiMuGen</i>	167
Fig 6.14	Dimuon travelled distance distributions considering only water propagation or the equivalent water distance (water+rock propagation).	168
Fig 6.15	Dimuon energy distributions considering only water propagation or water+rock propagation. Di-Muon deviation at decay point.	169
Fig 6.16	Distribution of the di-muon deviation at the decay point (δr) and the scattering suffered for each muon ($\delta r_1, \delta r_2$)	170
Fig 6.17	Mediator hypothetical impact point (red), blue and green points show the impact points over the sphere of the two muons (Only have been plotted $1e3$ events for better visualization. In the detailed view 500X zoom has been applied	171
Fig 6.18	Data_MC comparisons for some of the basic cuts. Data (black), MC: mis-reconstructed atmospheric muons (red), <i>upgoing</i> neutrinos of energies comprises between $[5-20 \cdot 10^3]$ GeV (blue), <i>upgoing</i> neutrinos of energies comprises between $[20 \cdot 10^3 - 1^8]$	173

	GeV (pink), all (green).(plots from the standard dark matter Sun analysis (Lambard et al., 2013))	
Fig 6.19	Neutrino spectra, from the initial muonic and electronic neutrino, for di-muon decay from $M\chi=1$ TeV $m\phi=1$ GeV	176
Fig 6.20	Secluded scenario diagram where the mediator escapes the solar dense core and decays into neutrino	177
Fig 7.1	Number of detected events, ns, amount in the Q, half-cone angle parameter space for <i>SingleLine</i> (left) and <i>MultiLine</i> (right) analysis according to simulations corresponding to $m\chi=1$ TeV $m\phi=1$ GeV. The colorbar indicates the number of events	180
Fig 7.2	Effective area (m^2) in the Q, half-cone angle (zenith band width) parameters space for SL (left) and ML (right) analysis for the simulation corresponding to $m\chi=1$ TeV, $m\phi=1$ GeV. The colorbar indicates the Effective area (m^2).	180
Fig 7.3	Average upper limit (Eq. 6.28) in the Q, half-cone angle parametersspace for <i>SingleLine</i> (left) and <i>MultiLine</i> (right) analysis. The colorbar indicates the number of events	181
Fig 7.4	Di-muon flux sensitivities using the optimum cuts	181
Fig 7.5	Sensitivities to $V+\bar{V}$ flux coming from di-muon decay using the optimum cuts	182
Fig 7.6	Sensitivities to $V+\bar{V}$ flux coming from mediator decay using the optimum cuts	182
Fig 7.7	Ratio between the sensitivity obtained using the optimum cuts and the sensitivity obtained using the proposed ones. On top for ML analysis, on the bottom for SL analysis	184
Fig 7.8	Di-muon flux sensitivities using the proposed cuts (red) and the optimum cuts (gray)	185
Fig 7.9	Sensitivities to $V+\bar{V}$ flux coming from di-muon decay using the proposed cuts (blue) and the optimum cuts (gray). Gray lines are difficult to appreciate because the fluxes using the proposed cuts are almost the same	185
Fig 7.10	Sensitivities to $V+\bar{V}$ flux coming from mediator decay using the proposed cuts (green) and the optimum cuts (gray).	185
Fig 7.11	ANTARES reach for detecting mediators produced in the Sun and decaying into di-muons as a function of the DM annihilation rate and mediator decay length. Results for different DM mass and $m\phi=1$ GeV using <i>BBfit</i> Singleline (dashed) and <i>Multiline</i>	187

	(solid) reconstruction strategies are shown. Results of sensitivities obtained using the proposed cuts	
Fig 7.12	ANTARES reach for detecting mediators produced in the Sun and decaying into di-muons and finally into neutrinos (before reaching the Earth) as a function of the annihilation rate and decay length. Results for different DM mass and $m\phi= 1$ GeV using <i>BBfit Singleline</i> (dashed) and <i>Multiline</i> (solid) reconstruction strategies are shown. Results of sensitivities obtained using the proposed cuts	189
Fig 7.13	ANTARES reach for detecting mediators produced in the Sun and decaying into neutrinos as a function of the annihilation rate and decay length. Results for different DM mass and $m\phi= 1$ GeV using <i>BBfit Singleline</i> (dashed) and <i>Multiline</i> (solid) reconstruction strategies are shown	190
Fig 7.14	ANTARES proton-WIMP cross section sensitivities for the three Secluded DM studied cases, USING <i>BBfit Singleline</i> and <i>Multiline</i> reconstruction strategies. Results for favorable lifetime of mediators	192
Fig 7.15	Differential distribution of the angular separation ψ of the event tracks with respect to the Sun's direction for the expected background (red line) compared to the data (black asterisk). Results for the four cuts of <i>BBFit MultiLine</i> reconstruction	194
Fig 7.16	Differential distribution of the zenith angular separation ψ of the event tracks with respect to the Sun's direction for the expected background (red line) compared to the data (black asterisk). Results for <i>BBFit SingleLine</i> reconstruction	196
Fig 7.17	Flux limits for di-muons (top) and neutrinos coming from di-muon decay (bottom-left) and coming from mediator decay (bottom-right). In gray the correspondent flux sensitivities	197
Fig 7.18	ANTARES exclusion limits for the three Secluded DM scenarios (products of DM annihilation in the Sun through mediators decaying into: di-muons (dash-dotted blue), neutrinos from di-muons (solid blue), directly into neutrinos (Green)) as a function of the annihilation rate (Γ) and the decay length ($g\tau$) for three all analysed dark matter masses. The shadow regions would be excluded for these models	199
Fig 7.19	ANTARES 90% CL upper limits on the spin-dependent (left) and spin-independent (right) WIMP-proton cross-sections as a function of the WIMP mass for favourable mediator life time	200

Fig 7.20	Sensitivities collection of different direct detection experiments (SIMPLE (Felizardo et al., 2014), COUPP (Behnke et al., 2012), LUX (Akerib et al., 2014) and XENON-100 (Aprile et al., 2012)) of search for dark matter in the sun (black lines). On the spin-dependent (left) and spin-independent (right) WIMP-nucleon cross-sections as a function of the WIMP mass. SDM ANTARES limits (color lines). 199
----------	--	-----------

Acronyms

ANTARES	Astronomy with a Neutrino Telescope and Abyss environmental RESEARCH
ACORNE	Acoustic Cosmic Ray Neutrino Experiment
AGN	Active Galactic Nuclei
AMADEUS	ANTARES Modules for the Acoustic DETECTION Under the Sea
Ams	Acoustic Modules
AMS	Alpha Magnetic Spectrometer
APP	Application Software
AUTEC	Atlantic Undersea Test and Evaluation Center
BDUNT	Baikal Deep Underwater Neutrino Telescope
CBM	Cosmic Microwave Background
CC	Charged Current
CL	Confidence Level
DAQ	Data Acquisition
DIMUGEN	Di-muon Generator
DM	Dark Matter
DOM	Digital Optical Module
ECAP	Erlangen Centre for Astroparticle Physics
EEB	Electronic Emission Board
EPSCG	Escola Politècnica Superior de Gandi
FFR	Free Flooded Ring
FWHM	Full Width Half Maximum
GC	Galactic Center
GENHEN	GENERATOR of High Energy Neutrinos
GRBs	Gamma Ray Bursts
GZK	Greisen-Zatsepin-Kuz'min
HESS	High Energy Stereoscopic System
HTI	High Technology Incorporation
IBM	Irvine-Michigan-Brookhaven
IGIC	Intituto de Investigación para la Gestión Integrada de Zonas Costeras
IL	Instrumentation Line

INFN-LNS	Istituto Nazionale di Fisica Nucleare - Laboratori Nazionale del Sud
KM3NeT	Cubic Kilometre Neutrino Telescope
L12	Line number 12
LED	Light-Emitting Diode
LHC	Large Hadron Collider
MAGIC	Major Atmospheric Gamma-ray Imaging Cherenkov Telescope
MC	Monte Carlo
MLS	Maximum Length Sequence
MOSFET	Metal Oxide Semiconductor Field Effect Transistor
MRF	Model Rejection Factor
MUPAGE	Atmospheric MUons from PArametric formulas: a fast GEnerator for neutrino telescopes
NC	Neutral Current
NEMO	Neutrino Ettore Majorana Observatory
NFW	Navarro Frenk White
OMs	Optical Modules
ORCA	Oscillation Research with Cosmics in the Abyss
OvDE	Ocean Noise Detection Experiment
PCI	Peripheral Component Interconnect
PIC	Peripheral Interface Controller
PMTs	Photomultipliers
PSD	Power Spectral Density
PWM	Pulse Width Modulation
PXI	PCI eXtensions for Instrumentation
RF	Radio Frequency
RMS	Root Mean Square
SAUND	Study of Acoustic Ultra-high Neutrino Detection
SPATS	South Pole Acoustic Test Setup
UDP	User Datagram Protocol
UHE	Ultra High Energy
UPV	Universidad Polit3cnica de Valencia
VERITAS	Very Energetic Radiation Imaging Telescope Array System
WIMPs	Weakly Interacting Massive Particles

Annex A

Cut values which minimizes the flux sensitivities for each DM mass and strategy.

m_χ (TeV)	Optimum Cuts							
	Dimuon (<i>MultiLine</i>)				Dimuon (<i>SingleLine</i>)			
	MRF	Q_{cut}	Ψ_{cut} (°)	$\Phi_{\text{Di-}\mu}$ ($\text{km}^{-2}\text{yr}^{-1}$)	MRF	Q_{cut}	Ψ_{cut} (°)	$\Phi_{\text{Di-}\mu}$ ($\text{km}^{-2}\text{yr}^{-1}$)
10	5,8E-04	1,8	1,3	3,9E+01	4,3E-02	1,2	1	2,9E+03
5	7,7E-04	1,7	1,4	5,3E+01	4,9E-02	1,1	1,9	3,4E+03
2	1,4E-03	1,7	1,4	9,8E+01	7,3E-02	1,1	1,9	4,9E+03
1	2,3E-03	1,6	1,4	1,6E+02	9,6E-02	1	3,2	6,6E+03
0,5	3,4E-03	1,6	1,4	2,3E+02	1,4E-01	1	8,2	9,0E+03
0,2	6,4E-03	1,6	1,6	4,4E+02	1,7E-01	1	9,8	1,2E+04
0,1	2,9E-02	1,6	2	2,0E+03	2,3E-01	1	11,1	1,6E+04
0,05	4,3E-01	1,5	4,1	2,9E+04	4,6E-01	1	12,8	3,1E+04
0,03	3,3E+01	1,5	6,2	2,2E+06	1,5E+00	1	16	1,0E+05

Table 1. Di-muon flux sensitivities obtained using the optimum cuts values of Q_{cut} and Ψ_{cut} which minimized the *Model Rejection Factor*.

m_χ (TeV)	Optimum Cuts							
	Dimuon into ν (<i>MultiLine</i>)				Dimuon into ν (<i>SingleLine</i>)			
	MRF	Q_{cut}	Ψ_{cut} (°)	$\Phi_{\nu+\bar{\nu}}$ ($\text{km}^{-2}\text{yr}^{-1}$)	MRF	Q_{cut}	Ψ_{cut} (°)	$\Phi_{\nu+\bar{\nu}}$ ($\text{km}^{-2}\text{yr}^{-1}$)
10	1,3E+03	1,8	1,3	1,8E+08	3,6E+04	0,7	8,2	4,9E+09
5	4,8E+03	1,8	1,4	6,6E+08	9,6E+04	0,7	8,2	1,3E+10
2	2,9E+04	1,4	2,1	3,9E+09	4,2E+05	0,7	8,2	5,7E+10
1	1,3E+05	1,4	2,6	1,8E+10	1,3E+06	0,7	8,7	1,9E+11
0,5	6,9E+05	1,4	3,1	9,6E+10	4,4E+06	0,7	8,7	6,0E+11
0,2	1,0E+07	1,4	4,2	1,4E+12	2,5E+07	0,7	9,2	3,5E+12
0,1	1,4E+08	1,4	4,6	1,9E+13	1,3E+08	0,7	11,2	1,7E+13
0,05	9,9E+09	1,4	5	1,4E+15	1,6E+09	0,7	12,7	2,2E+14
0,03	3,4E+11	1,3	3,1	4,6E+16	8,7E+09	0,9	14,7	1,2E+15

Table 2. Neutrino flux sensitivities obtained using the optimum cuts values of Q_{cut} and ψ_{cut} which minimized the *Model Rejection Factor*.

m_χ (TeV)	Optimum Cuts							
	Mediator into ν (<i>MultiLine</i>)				Mediator into ν (<i>SingleLine</i>)			
	MRF	Q_{cut}	Ψ_{cut} (°)	$\Phi_{\nu+\bar{\nu}}$ ($\text{km}^{-2}\text{yr}^{-1}$)	MRF	Q_{cut}	Ψ_{cut} (°)	$\Phi_{\nu+\bar{\nu}}$ ($\text{km}^{-2}\text{yr}^{-1}$)
10	2,2E+02	1,8	1,3	2,9E+07	9,5E+03	0,9	5,6	1,3E+09
5	6,4E+02	1,8	1,4	8,8E+07	2,1E+04	0,7	8,9	2,9E+09
2	3,2E+03	1,8	1,4	4,5E+08	7,1E+04	0,7	8,7	9,8E+09
1	1,2E+04	1,4	1,9	1,7E+09	2,0E+05	0,7	8,2	2,8E+10
0,5	5,0E+04	1,4	2,3	6,9E+09	6,4E+05	0,7	8,2	8,9E+10
0,2	3,9E+05	1,4	3,1	5,5E+10	2,9E+06	0,7	8,7	4,1E+11
0,1	2,3E+06	1,4	3,8	3,2E+11	9,2E+06	0,7	8,7	1,3E+12
0,05	2,2E+07	1,4	4,7	2,9E+12	3,3E+07	0,7	9,9	4,6E+12
0,03	1,7E+08	1,4	5,1	2,4E+13	9,8E+07	0,7	11,4	1,4E+13

Table 3. Neutrino flux sensitivities obtained using the optimum cuts values of Q_{cut} and ψ_{cut} which minimized the *Model Rejection Factor*.